Journal of
Mechanics of
Materials and Structures

TRUSS WAVINESS EFFECTS IN CELLULAR LATTICE STRUCTURES

DOUGLAS T. QUEHEILLALT, VIKRAM S. DESHPANDE AND HAYDN N. G. WADLEY

Methods have emerged for making metallic lattice structures either by the lay up of collinear wire arrays or by stacking woven textile meshes. The two fabrication routes result in similar lattice topologies: the collinear lattice has straight struts while those in the textile lattice are wavy. Wire waviness in the textile lattice results in a knockdown in both the stiffness and strength compared to the collinear lattice. Analytical estimates and finite element (FE) predictions of the through thickness compressive responses of collinear and textile lattices indicate that the stiffness and strength of lattices oriented to form a diamond structure are specimen aspect ratio dependent. By contrast, the stiffness of the collinear and textile lattices oriented to form a square structure is independent of both specimen aspect ratio and height while the strength depends on the sandwich height. Experimental measurements on specimens fabricated from 304L stainless steel are in good qualitative agreement with the elastic ideally-plastic analytical estimates while FE predictions incorporating the full strain hardening response of the parent material give accurate quantitative predictions of the measurements.

1. Introduction

Lightweight metallic sandwich panel structures that utilize low density cores and solid face sheets are widely used in aerospace and other transportation applications where high specific stiffness and/or strength is required. Hexagonal honeycomb structures are frequently used for the cores of sandwich panels [Bitzer 1997]. However, sandwich panels with metal foam cores, which might be structurally less efficient, are also of interest as they facilitate various multifunctional applications [Ashby et al. 2000]. The lower specific strength of metal foam cores is a consequence of the fact that their stiffness and strengths are primarily governed by bending of the constituent struts and cell walls and thus scale as $\bar{\rho}^2$ and $\bar{\rho}^{1.5}$, respectively, where $\bar{\rho}$ is the relative density [Gibson and Ashby 1997]. In contrast, the stiffness and strength of lattice materials are governed by the stretching of the constituent struts and scale with $\bar{\rho}$ [Deshpande and Fleck 2001]. It follows that a *stretching-dominated* cellular material with $\bar{\rho} = 0.1$ is predicted to be about ten times stiffer and about three times stronger than the equivalent relative density (weight) foam [Deshpande and Fleck 2001].

A variety of stretching-dominated cellular metal topologies have recently been proposed for cores of sandwich panels, and simple methods for their fabrication from high performance alloys have been identified, as reviewed by Wadley et al. [2003]. These include pyramidal, tetrahedral and Kagomé lattice trusses [Deshpande and Fleck 2001; Sypeck and Wadley 2002; Hyun et al. 2003; Wang et al. 2003;

Kooistra et al. 2004; Zok et al. 2004], the prismatic diamond lattice [Valdevit et al. 2004; Cote et al. 2006] and a square-honeycomb lattice [Berggren et al. 2001; Cote et al. 2004; Meidell 2005; Liang and Chen 2006]. Besides these recent examples, there exist well established theories for analyzing sandwich panels. The reader is referred to [Noor et al. 1995; Buannic et al. 2003] and the references therein for additional information regarding computational modeling of sandwich panels and shells. Simple brazing methods can also be used to bond together metallic wire meshes resulting in periodic metal lattice structures with a woven or textile topology [Sypeck and Wadley 2001; Zupan et al. 2004]. These structures can then be cut and brazed to facesheets resulting in sandwich structures. The lattice core structures can be oriented such that they have their struts aligned parallel-to and perpendicular-to the sandwich panel facesheets (a square orientation) or rotated at say ±45° to the faces (a diamond orientation). Recently, a method for fabricating a cellular lattice structure with an analogous topology using collinear arrays of solid wires or hollow tubes has also been reported [Queheillalt and Wadley 2005]. From a mechanics perspective, the main difference between the two topologies is that while the textile lattice is comprised of wavy wires, the collinear lattice consists of straight struts. This study explores the consequences of waviness on the mechanical properties of these similar topologies.

The effects of various structural defects or imperfections on the mechanical properties of regular honeycomb and bending-dominated foam structures have been extensively investigated using a combination of finite element and analytical techniques. Simone and Gibson [1998b], Grenestedt and Tanaka [1998], and Grenestedt and Bassinet [2000] reported that plateau borders (cell walls with a nonuniform wall thickness) had only a minor effect on the mechanical properties of hexagonal honeycombs and closed-cell foams with tetrakaidecahedral cells. On the other hand, Grenestedt [1998], Simone and Gibson [1998a], Chen et al. [1999], and Grenestedt and Bassinet [2000] found that wavy cell walls significantly reduce both the Young's modulus and compressive yield strength of cellular materials.

Strut waviness is also expected to play a role in determining the mechanical properties of the stretching-dominated textile and collinear lattice materials. However, limited data is available on the effects of defects on the strength of lattice materials. Wallach and Gibson [2001] used finite element methods to look at the effect of randomly removing truss members of an *octet* truss structure. They determined that both the Young's modulus and strength in compression decrease linearly ~15–20% after randomly removing only 10% of the constituent struts. Here we use analytical, finite element, and experimental techniques to investigate the through thickness compressive response of collinear and textile lattices with cores oriented in both a diamond and square orientation. The issues of specimen size dependent mechanical properties and the influence of strut waviness in these sandwich core materials are addressed.

2. Analytical mechanical property relationships

Four lattices of interest have been identified based on two orientations of brazed collinear and textile materials configured as the core of a sandwich structure (Figure 1): (i) collinear lattice in a diamond orientation; (ii) collinear lattice in a square orientation; (iii) textile lattice in the diamond orientation; and (iv) textile lattice in the square orientation.

The schematic illustrations in Figure 1 indicate that while the topology of the collinear and textile lattices are similar, the collinear lattices consist of straight struts (Figure 1(a) and (b)), while the textile lattices have wavy struts with a peak-to-peak amplitude equal to the wire diameter (Figures 1(c) and 1(d)).

We also note that the angle of inclination of the struts in a diamond orientation is $\omega = \pm 45°$ ($x_1 - x_2$ plane) with respect to the sandwich faces and are 0° and 90° for the square orientation.

Neglecting the added mass of braze material used during fabrication, geometrical considerations give the relative density, $\bar{\rho}$, of the collinear and textile lattice materials (to first order in a/l) as

$$\bar{\rho} = \frac{\pi}{2 \sin 2\omega} \left(\frac{a}{l} \right), \tag{1}$$

where ω is the half weave angle, a is the radius of the wire strut, and l is the cell size (center-to-center wire spacing) as defined in Figure 1(a).

2.1. *Diamond orientation.* Approximate analytical expressions have been developed for the through thickness compressive stiffness and strength of lattices made from an elastic ideally-plastic solid material with a Young's modulus E_s, Poisson's ratio ν and yield strength σ_{ys} [Sypeck and Wadley 2001; Zupan et al. 2004]. We begin by reviewing expressions for the stiffness and strength of a collinear (nonwavy) structure and then modify these expressions to account for the waviness of the wires in the textile structure.

2.1.1. *Collinear lattice.* Consider a sandwich plate of length L with rigid facesheets and a collinear diamond lattice core of thickness H (Figure 1). Note that in the diamond orientation, some of the struts are attached to both facesheets while near the edge of the sandwich panel; some of the struts are attached to only one of the facesheets. Zupan et al. [2004] derived lower bound estimates for the mechanical properties of such a structure loaded in the through thickness direction. In their derivation, they assumed
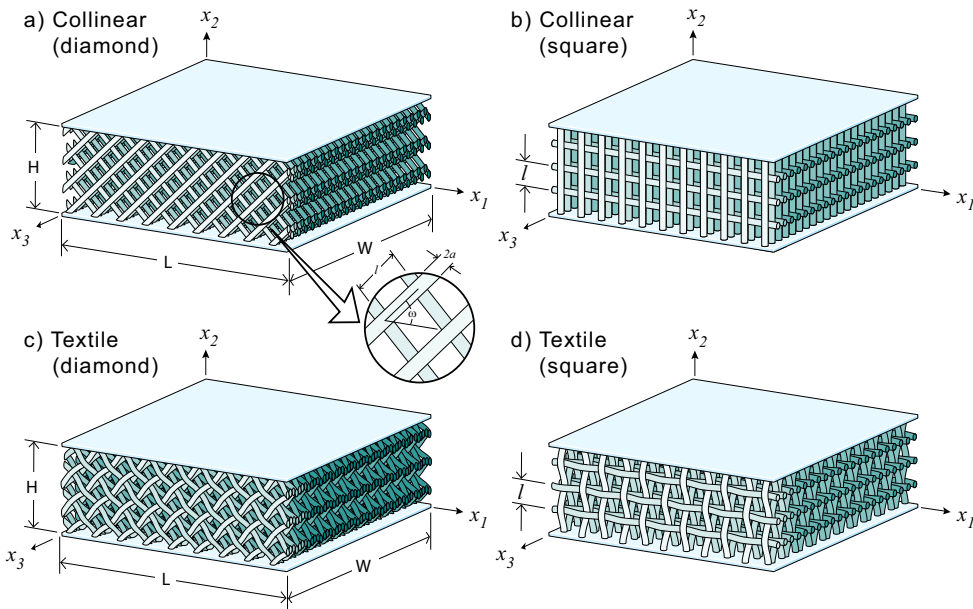

Figure 1. Schematic illustrations of (a) the collinear core in the diamond orientation, (b) the collinear core in the square orientation, (c) the textile core in the diamond orientation and (d) the textile core in the square orientation.

that wires attached to only one facesheet carried no load (i.e. do not contribute to the mechanical response) while wires attached to both facesheets are subject to an axial stress, σ_f, established by equilibrium with an applied macroscopic compressive stress in the x_2-direction. Using this approach, they showed that the normalized Young's modulus E of the lattice is given by

$$\frac{E}{E_s} = \left(1 - \frac{1}{A \tan \omega}\right) \sin^4 \omega \cdot \bar{\rho}, \tag{2}$$

where $A \equiv L/H$ is the aspect ratio of the sandwich plate. Note that the term $1 - 1/A \tan \omega \to 1$ as $A \to \infty$ and the normalized Young's modulus of the lattice asymptotically reaches a maximum of $E/E_s = \sin^4 \omega \cdot \bar{\rho}$ for samples that are long compared to their thickness. In other words, edge effects due to the struts that are attached to only one facesheet become negligible. Note also that deformation in the x_3 direction has been neglected in this analysis and thus Equation (2) is accurate for $W \gg H$.

The yield strength σ of the lattice can similarly be determined directly from equilibrium conditions [Zupan et al. 2004]. It is assumed that each strut attached to both facesheets is at the yield point, and the macroscopic compressive yield strength of the lattice in the x_2-direction is given by

$$\frac{\sigma}{\sigma_{ys}} = \left(1 - \frac{1}{A \tan \omega}\right) \sin^2 \omega \cdot \bar{\rho}. \tag{3}$$

Again, it should be noted that Equations (2) and (3) neglect the contribution to the stiffness and strength from bending of the constituent wires: these contributions become increasingly important for small aspect ratio specimens and thus Equations (2) and (3) are expected to underpredict the stiffness and strength of sandwich structures with low values of A.

The collinear lattice collapses by elastic buckling of the constituent struts if the Euler buckling load P_{euler} of the constituent struts is less than or equal to their plastic yield strength. The Euler buckling load of a cylindrical column is given by

$$P_{\text{euler}} = \frac{k^2 \pi^3 E_s a^4}{4l^2}, \tag{4}$$

while the plastic yield load $P_{\text{yield}} = \pi a^2 \sigma_{ys}$. The factor k in Equation (4) depends on the rotational stiffness of the end nodes of the strut. The lowest strength buckling mode under uniaxial compression corresponds to struts of length l buckling as pin-ended (freely rotating) struts as sketched in Figure 2(c). Thus, we take $k = 1$ in Equation (4) and it follows that the collinear lattice collapses by elastic buckling of the constituent struts if the relative density

$$\bar{\rho} \leq \frac{1}{\sin 2\omega} \sqrt{\varepsilon_y}, \tag{5}$$

where the yield strain $\varepsilon_y \equiv \sigma_{ys}/E_s$. In the regime of relative densities where elastic buckling dominates, the collapse strength is given by

$$\frac{\sigma}{\sigma_{ys}} = \frac{1}{\varepsilon_y} \left(1 - \frac{1}{A \tan \omega}\right) \sin^2 \omega \cdot \bar{\rho}^3. \tag{6}$$

a) Diamond orientation
   (undeformed)

b) Square orientation
   (undeformed)

c) Diamond orientation
   (deformed)

d) Square orientation
   (deformed)
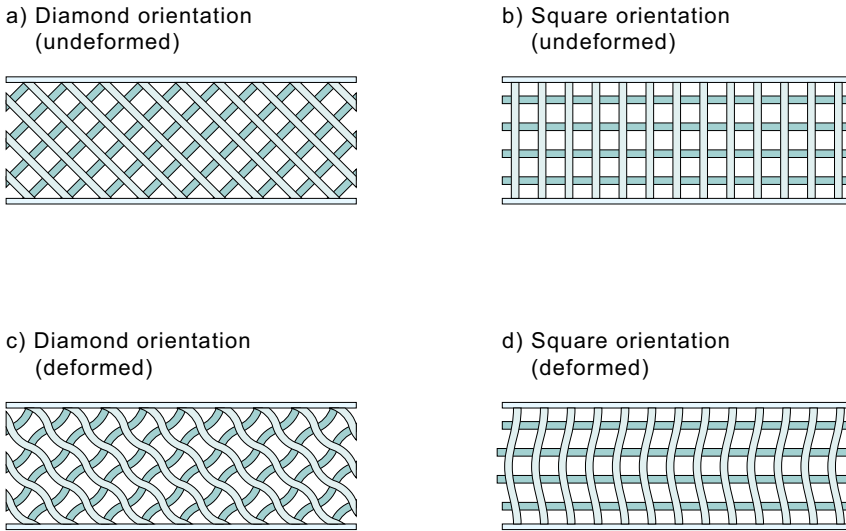
Figure 2. Sketches of the buckling modes of the collinear and textile sandwich cores in the diamond and square orientations.

2.1.2. *Textile lattice.* Unlike the collinear lattice, the wires in a textile are wavy with the transverse (in the x_3-direction) profile $w(s)$ of each wire approximated by

$$w = a\left(1 - \cos\frac{\pi s}{l}\right), \tag{7}$$

where s is the axial coordinate along one strut of a cell measured from a node. This waviness results in a reduction in the axial stiffness and load carrying capacity of each wire and thus the textile lattice is anticipated to have a lower stiffness and strength compared to an equivalent collinear lattice material.

We first analyze the effective stiffness and strength of a long wavy wire as sketched in Figure 3(a). The transverse profile of this wire is assumed to be described by Equation (7). The supports in Figure 3(a) prevent the transverse deflection (in the x_3-direction) of the wire and represent the constraint imposed by successive layers of the wire meshes which are all brazed together at the nodes. A free-body diagram of a wire segment between two supports is sketched in Figure 3(b), where P is the applied axial load and R the horizontal reaction from the supports. Antisymmetry considerations dictate that the bending moment vanishes at the supports. Thus, moment equilibrium implies that

$$R = 2P\left(\frac{a}{l}\right). \tag{8}$$

For $a/l \ll 1$, we can assume that the axial load P and shear force R are approximately constant through the length of the strut. Then the total elastic strain energy, U, in a wavy strut of length l is given by the sum of the stretching, bending and shearing energies

$$U = \frac{1}{2E_s}\frac{P^2 l}{\pi a^2} + \frac{1}{2}\int_0^l \frac{M^2}{E_s I}ds + \frac{1+\nu}{E_s}\frac{R^2 l}{\pi a^2}, \tag{9}$$
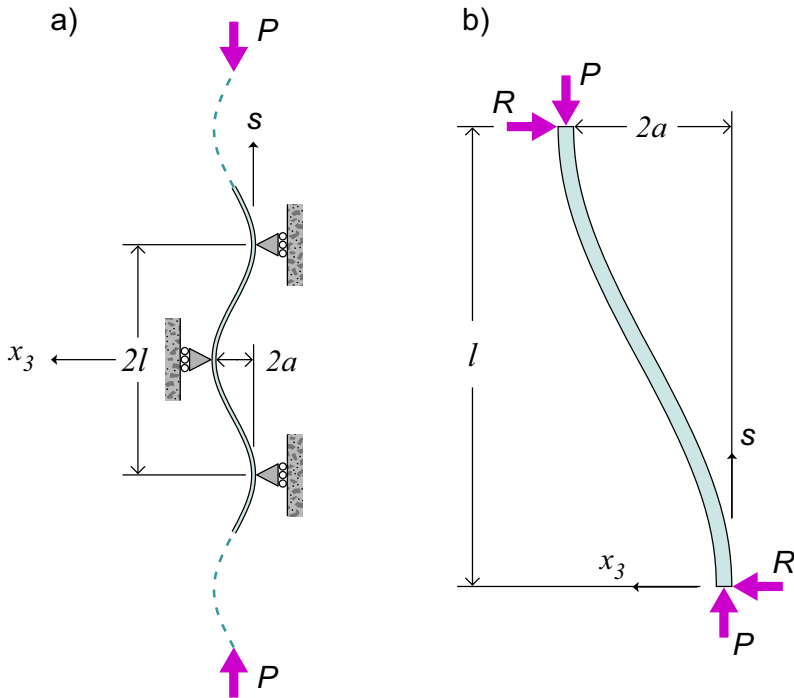
Figure 3. (a) Sketch of the loading on a single wavy wire in the textile core and (b) a free-body diagram of the representative wavy wire.

where the bending moment

$$M(x) = Pa\left(1 - \cos\frac{\pi s}{l}\right) + Pa\left(\frac{a}{l}\right)s, \tag{10}$$

and the second moment of area of the cylindrical wire $I = \pi a^4/4$.

A work balance gives the effective modulus E_w of the wavy strut as

$$\frac{E_w}{E_s} = \frac{1}{1.09 + 8(1 + \nu)\left(\frac{a}{l}\right)^2}. \tag{11}$$

Note that the decrease in E_w with increasing a/l is a result of the contribution of shear deflections to the compliance of the wavy struts.

The yield locus of a beam element under combined bending and tension is given by (see for example [Prager 1959])

$$\left(\frac{P}{P_o}\right)^2 + \left(\frac{M}{M_o}\right) = 1, \tag{12}$$

where for a strut of circular cross-sectional radius a, $P_o = \pi a^2 \sigma_{ys}$ and $M_o = 4a^3\sigma_{ys}/3$. Since the axial load is constant through the strut length, yielding of the strut is expected to commence at the point of

maximum bending moment. Equation (10) dictates that the maximum bending moment is

$$M_{\max} = \left[\left(1 - \sqrt{1 - \frac{4}{\pi^2}} \right) - \frac{2}{\pi} \sin^{-1} \left(\frac{2}{\pi} \right) \right] \cdot Pa = \lambda Pa, \tag{13}$$

and thus the collapse stress σ_w of the wavy strut follows from the yield locus, Equation (12), as

$$\frac{\sigma_w}{\sigma_{ys}} = \frac{\pi \lambda + \sqrt{\pi^2 \lambda^2 + 64/9}}{8/3}. \tag{14}$$

The normalized modulus and plastic yield strength of the textile sandwich lattice material may then be estimated by replacing E_s and σ_{ys} by E_w and σ_w, respectively, in Equation (2) and Equation (3). The effect of strut waviness on the elastic buckling strength of the textile material is not explored in detail here. However, as the wires buckle as pin-ended struts in the plane of each wire mesh, the wavy imperfections in the $x_2 - x_3$ plane are expected to have only a minor effect upon the elastic buckling strength of the textile sandwich lattice [Zupan et al. 2004].

2.2. *Square orientation.* In this section, we derive approximate formulae for the Young's modulus and compressive strength of the collinear and textile lattices in the square orientation. The lattices are again assumed to be made from an elastic ideally-plastic solid material with a Young's modulus E_s and yield strength σ_{ys}.

2.2.1. *Stiffness.* Under out-of-plane compression (in the x_2-direction), only the vertical wires carry load and the normalized Young's modulus of the collinear sandwich lattice is given by

$$\frac{E}{E_s} = \frac{\pi}{4} \left(\frac{a}{l} \right) = \frac{\bar{\rho}}{2}. \tag{15}$$

The Young's modulus of the textile material is obtained by replacing E_s in the above equation with E_w from Equation (11).

2.2.2. *Strength.* The horizontal wires do not contribute to the compressive strength of the sandwich lattices in the square orientation. Assuming that vertical wires (aligned along the x_2-direction) undergo compressive yield, the effective yield strength of the collinear lattice follows as

$$\frac{\sigma}{\sigma_{ys}} = \frac{\pi}{4} \left(\frac{a}{l} \right) = \frac{\bar{\rho}}{2}, \tag{16}$$

while the strength of the textile lattice is obtained by replacing σ_{ys} in the above equation with σ_w from Equation (14).

In the square orientation, experimental studies [Queheillalt and Wadley 2005] indicate the lattice collapses by cooperative Euler buckling of the constituent struts over the full height of the sandwich; see Figure 2. Assuming that the struts are built into the sandwich faces, the elastic buckling collapse load of a square lattice made from either the collinear or textile materials is given by

$$\frac{\sigma}{\sigma_{ys}} = \frac{\pi^3}{4\varepsilon_y} \left(\frac{a}{l} \right)^3 \left(\frac{l}{H} \right)^2 = \frac{2\bar{\rho}^3}{\varepsilon_y} \left(\frac{l}{H} \right)^2, \tag{17}$$

where we have assumed that the waviness of the trusses in the textile lattice does not substantially affect the elastic buckling loads of the trusses. Comparing Equation (16) and Equation (17), we see that elastic buckling is the operative collapse mode for lattice relative densities satisfying the inequality

$$\bar{\rho}^2 < \frac{\pi^2 \varepsilon_y}{4} \left(\frac{H}{l} \right)^2. \tag{18}$$

It is important to note that the elastic buckling strength of the sandwich lattice materials in the square orientation is not an intrinsic material property; it decreases with increasing lattice height for a fixed value of the relative density.

3. Finite element simulations

The analytical expressions for the stiffness and strength of the lattice materials in the diamond orientation is checked by performing finite element (FE) calculations with the general purpose finite element package ABAQUS. Here the intent is only to compare the FE and analytical predictions and not study a specific parent material. In these FE calculations, the collinear and textile materials were rigidly jointed at the nodes and hence the FE calculations include contributions from the bending of the struts, which were neglected in the analytical calculations. We note that the compression of the square lattice is simply equivalent to the uniaxial compression of the vertical trusses and hence excellent agreement between the FE and analytical calculations was obtained and for the sake of brevity those comparisons are omitted here.

Two types of FE calculations were performed for both the collinear and textile lattices with a diamond topology:

- periodic unit cell calculations to determine the effective properties of the lattice materials,

- calculations on a sandwich beam with a finite aspect ratio.

The waviness of the mesh wires in the textile material was assumed to be of the form specified by Equation (7) with each wire modeled using 3-dimensional Timoshenko beam elements (B32 element in the ABAQUS notation) of size $l/20$. At each node of the cellular material (the wire crossover points), no relative displacement or rotation of one wire with respect to the other was permitted. This models a rigidly brazed joint. To reduce the size of the computations, only one layer of the wire mesh was modeled in the FE calculations with symmetry boundary conditions (i.e. displacement $u_3 = 0$ and the rotations $\theta_1 = \theta_2 = 0$) imposed on the nodes (wire crossover points) of the cellular material. Thus, the FE calculation models a plane strain limit which is valid for a cellular material comprising a large number of wire mesh layers with $W \gg H$. The FE models for the collinear material were essentially the same as those of the textile material, except that the wire waviness term was set to zero in this case. Imperfections were not included in the $x_1 - x_2$ plane in the FE calculations as the large waviness in the x_3-direction dominates the buckling strength of the struts of these textile cores.

In the linear elastic calculations used to determine the Young's modulus, the solid wire material was modeled as linear elastic with a Poisson's ratio $\nu = 0.3$. For the strength calculations, the solid material was assumed to be a J2 flow theory elastic ideally-plastic solid with a yield strain $\varepsilon_y = 0.5\%$ and an elastic Poisson's ratio $\nu = 0.3$.

3.1. *Effective properties of the infinite material.* In order to determine the effective properties of the collinear and textile lattice materials, a unit cell of the material was analyzed in the FE calculations. Periodic boundary conditions were specified through

$$\Delta u_i = \bar{\varepsilon}_{ij} \Delta x_j \qquad \text{and} \qquad \Delta \theta_i = 0, \tag{19}$$

where Δu_i and $\Delta \theta_i$ are the differences in the displacements and rotations on opposites sides of the unit cell specified by the position difference vector Δx_j. Here we consider compression in the x_2-direction and thus specify the strain components $\bar{\varepsilon}_{11} = \bar{\varepsilon}_{12} = 0$ and $\bar{\varepsilon}_{22} = \varepsilon$, where ε is the applied strain. The work conjugate applied stress is

$$\sigma_{ij} = \frac{1}{2(4l \cos \omega)^2} \sum \left(F_i x_j + F_j x_i \right), \tag{20}$$

where $4l \cos \omega$ is the size of the unit cell analyzed, F_i is the force acting on the boundary nodes and the summation is over all these boundary nodes with coordinates x_i. The stress $\sigma = \sigma_{22}$ (work-conjugate to the applied strain $\bar{\varepsilon}_{22} = \varepsilon$) is evaluated in these simulations.

Finite element predictions of the effective Young's modulus of the diamond topology collinear and textile cellular materials are plotted in Figure 4(a) as a function of the relative density $\bar{\rho}$. The corresponding analytical predictions in the infinite aspect ratio limit ($A \rightarrow \infty$) are also included in Figure 4(a) and agree well with the FE predictions, especially for the collinear material. The FE and analytical predictions of the effect of the weave angle ω on the Young's modulus of a $\bar{\rho} = 0.16$ collinear and textile material is shown in Figure 4(b). The effective Young's modulus of these materials increases with increasing ω and good agreement is seen between the analytical and FE predictions.

Finite deformation FE simulations were performed to determine the peak compressive strength of the diamond topology collinear and textile cellular materials assuming elastic ideally-plastic solid wires with a yield strain $\varepsilon_y = 0.5\%$. These peak compressive strength predictions are plotted in Figure 5

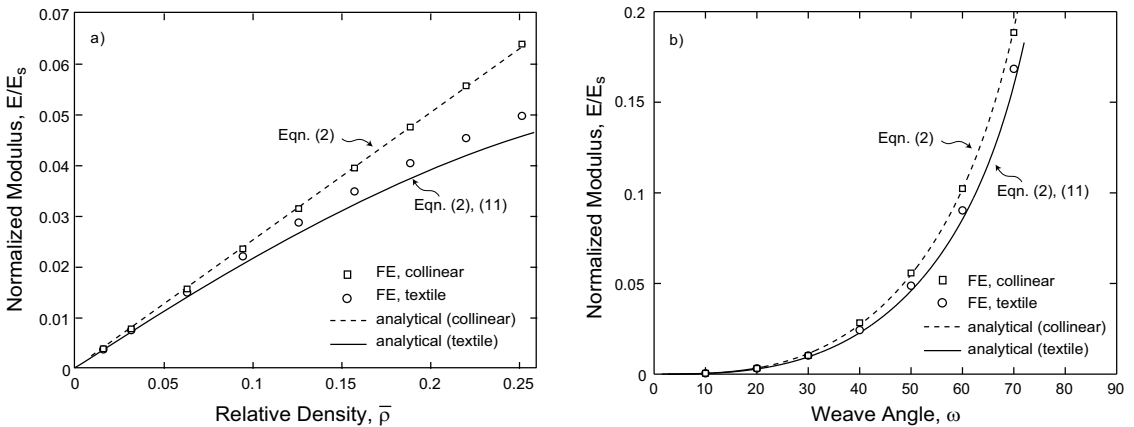**Figure 4.** Analytical and finite element predictions of the normalized Young's modulus of the collinear and textile sandwich core materials in the diamond orientation ($A \rightarrow \infty$). (a) Effect of relative density $\bar{\rho}$ for the $\omega = \pm 45°$ diamond lattice structures and (b) the effect of the strut inclination angle ω on the modulus for $\bar{\rho} = 0.16$ lattice materials.
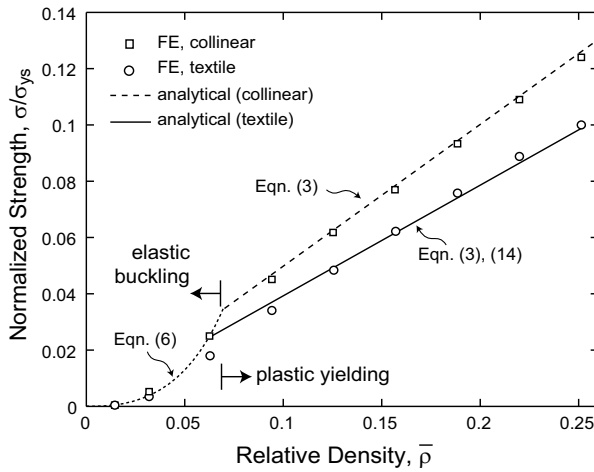
Figure 5. Analytical and finite element predictions of the peak compressive strength of the diamond topology collinear and textile cellular materials ($A \to \infty$) as a function of the relative density $\bar{\rho}$. The struts were assumed to be made from an elastic ideally-plastic solid with yield strain $\varepsilon_y = 0.5\%$ in these predictions.

along with the corresponding analytical estimates. For a yield strain $\varepsilon_y = 0.5\%$, elastic buckling of the constituent struts is the operative failure mode for relative densities less than approximately 0.06. The finite element calculations are in good agreement with the analytical predictions for both the collinear and textile materials in the elastic buckling as well as plastic yielding regimes.

3.2. *Effective properties of the material in sandwich configuration.* Finite element and analytical predictions of the Young's modulus and compressive strength of the collinear and textile materials in the
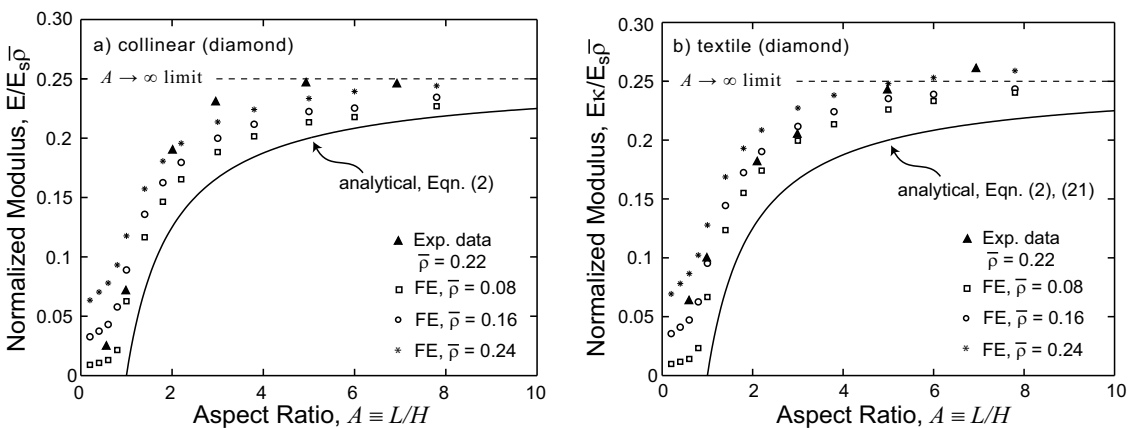
Figure 6. Analytical and finite element predictions of the aspect ratio dependence of the normalized Young's modulus in the diamond orientation of the (a) collinear and (b) textile sandwich core materials. Measurements on lattice materials made from 304 stainless steel are also included.

sandwich configuration are reported in this section. In all the FE calculations, a sandwich beam with 5 cells along the height H of the specimen was analyzed. The specimen aspect ratio was varied by changing the specimen length L. All displacement and rotational degrees of freedom of the nodes along the bottom surface were completely constrained while on the top surface, a uniform compressive displacement in the x_2-direction was specified with the other displacement and rotational degrees of freedom constrained to zero. The work-conjugate force to the applied uniform displacement was employed to define the applied nominal stress.

Analytical and FE predictions of the variation of the normalized Young's moduli with sandwich aspect ratio $A \equiv L/H$ are plotted in Figures 6 (a) and (b) for the collinear and textile lattices, respectively. The normalization factors in Figure 6 have been chosen such that the analytical predictions give a unique curve (for all values of $\bar{\rho}$) for the collinear and textile materials. Thus, for the collinear materials we plot the normalized Young's modulus $E/(E_s\bar{\rho})$ while for the textile materials we plot $E\kappa/(E_s\bar{\rho})$, where

$$\kappa = 1.09 + 8(1+\nu)\left(\frac{a}{l}\right)^2, \tag{21}$$

is a factor due to wire waviness in the textile material, see Equation (11).

There is a rapid reduction in the normalized modulus of both collinear and textile topologies as the specimen aspect ratio $A \to 1$. It is observed that the analytical model consistently underestimates the FE predictions with the deviation between the FE and analytical predictions increasing in magnitude with higher relative densities. As previously stated, the analytical expressions assume that only struts connected to both sandwich faces carry load. However, the FE calculations indicate that struts connected to only one facesheet are able to carry load via bending at the rigidly brazed nodes. This phenomena is clearly seen in the FE predictions of the deformation of the $\bar{\rho} = 0.16$ textile sandwich lattice material with aspect ratio $A = 4$ (Figure 7). These bending effects are neglected in the analytical predictions and hence these estimates are lower than the FE predictions.

A comparison between the analytical and FE predictions of the variation of the peak compressive strength of the collinear and textile sandwich lattices as a function of aspect ratio is shown in Figures 8 (a) and (b) for relative densities of $\bar{\rho} = 0.16$ and 0.24, respectively. Plastic yielding of the lattice trusses
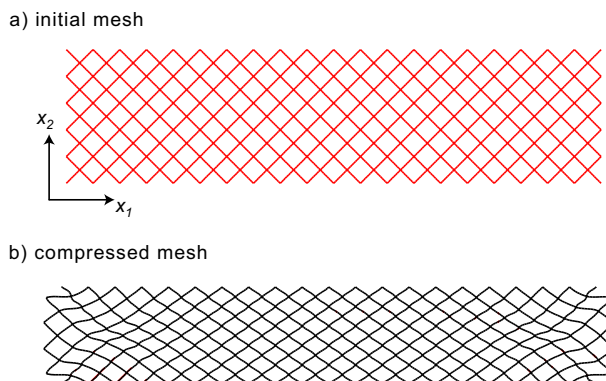

Figure 7. Deformed finite element mesh for an $A = 4$, $\bar{\rho} = 0.16$ diamond topology textile sandwich core. Note that edge effects are clearly visible in the deformed mesh.

is the operative collapse mode for these relative densities and thus we have normalized the strength as $\sigma/(\sigma_{ys}\bar{\rho})$ so that the analytical predictions give a unique curve for both relative densities. Similar to the comparisons presented in Figure 6, the analytical calculations underpredict the strength, because the contribution to the strength from edge wires that carry some load by bending is neglected in those calculations. Included in Figure 8 are best fits to the FE data for aspect ratios $A > 1$. Relations of the form

$$\frac{\sigma}{\sigma_{ys}} \equiv \left(1 - \frac{0.8}{A \tan \omega}\right) \sin^2 \omega \cdot \bar{\rho}, \tag{22}$$

and

$$\frac{\sigma}{\sigma_w} \equiv \left(1 - \frac{0.6}{A \tan \omega}\right) \sin^2 \omega \cdot \bar{\rho}, \tag{23}$$

accurately capture the finite element predictions in Figure 8 for the collinear and textile materials, respectively.

Analogous finite element calculations also confirmed the accuracy of the simple analytical formulae presented in Section 3 for the stiffness and strength of the collinear and textile materials in the square orientation. Explicit comparisons are omitted for the sake of brevity.

4. Experimental assessments

The through thickness compressive stress versus strain responses of the collinear and textile sandwich lattice materials in the diamond and square orientations were examined in the experimental investigation. The compressive responses of the sandwich lattice specimens were measured at a nominal applied strain rate $4 \times 10^{-2} \, \text{s}^{-1}$. The measured load cell force was used to define the nominal applied stress and the nominal through thickness strain in the lattice was estimated using a laser extensometer to monitor the relative displacements of the facesheets.
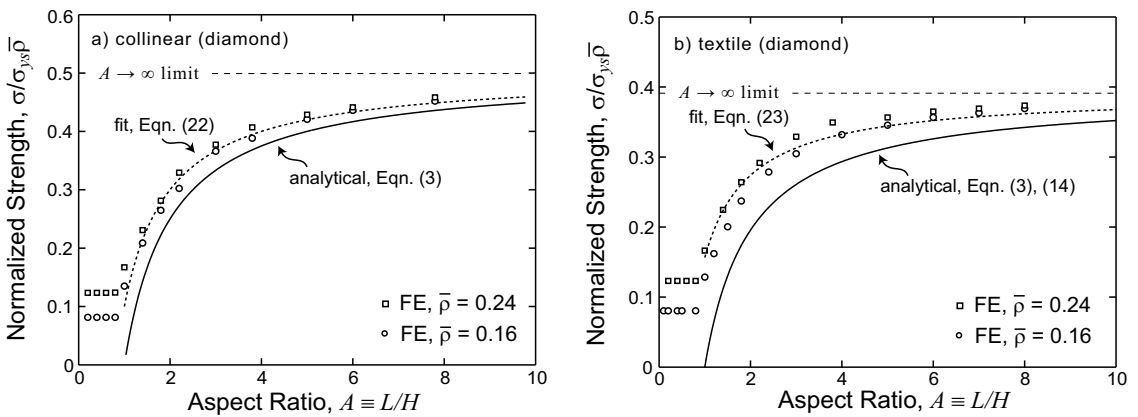

Figure 8. Analytical and finite element predictions of the aspect ratio dependence of the peak compressive strength in the diamond orientation of the (a) collinear and (b) textile sandwich core materials. The struts were assumed to be made from an elastic ideally-plastic solid with yield strain $\varepsilon_y = 0.5\%$ in these predictions.

4.1. *Materials and testing.* Schematics of the assembly method of the collinear and textile lattices made from solid 304 stainless steel wires and plain weave textiles are shown in Figure 9. These assemblies were then bonded by vacuum brazing as described by Queheillalt and Wadley [2005]. Sandwich panel specimens were produced by brazing 2.5 mm thick, 304L stainless steel sheets to the top and bottom faces of the as-cut specimens. Collinear sandwich lattice specimens were manufactured from solid 304 stainless steel wires of radius $a = 0.73$ mm spaced $l = 5$ mm apart while the textile sandwich lattices were manufactured from 304L stainless steel wire meshes of wire radius $a = 0.69$ mm and cell size $l = 5$ mm. The measured $\bar{\rho}$ for the collinear lattice was 0.23 ± 0.005, while the measured $\bar{\rho}$ for the textile lattice was 0.22 ± 0.005.

The specimens in the diamond orientation had a height $H = 21.2$ mm and width $W = 28.3$ mm. A series of through thickness compression tests on specimens with aspect ratios $0.5 \leq A \leq 7.0$ were conducted by varying the length L of the specimens. The effects of both aspect ratio A and height H were investigated for the specimens in the square lattice orientation with $W = 29.5$ mm. The following two series of tests were conducted on the square-orientation lattices assuming similar behavior exists between the two core topologies:

- The aspect ratio dependence was investigated via a series of through thickness compression tests on textile specimens with height $H = 15$ mm and aspect ratio A in the range $2.0 \leq A \leq 7.0$.

- The effect of specimen height was explored via a series of through thickness compression tests on $A = 3$ collinear specimens with heights H in the range 12.3 mm $\leq H \leq 27.3$ mm.

We note here that the width W of the specimens in all cases was sufficiently large such that negligible deformation was observed in the x_3-direction consistent with the plane strain assumption made in the analysis reported above.

Tensile tests were conducted on the 304L stainless wires subjected to the same brazing cycle as that used to manufacture the textile and collinear sandwich lattice specimens. The measured true stress versus logarithmic strain response revealed that the parent material is adequately approximated as an

a) collinear lay-up   b) textile lay-up
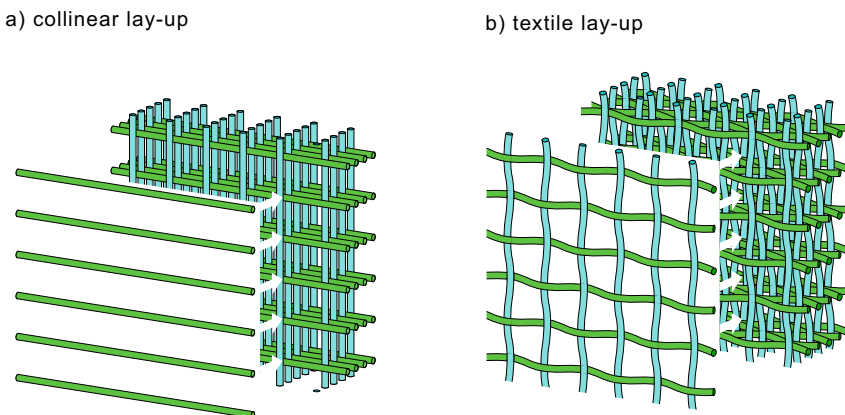
Figure 9. Sketches illustrating the manufacture of the (a) collinear and (b) textile cores.

Figure 10. Measured compressive stress versus strain responses of (a) the $\bar{\rho} = 0.23$ collinear and (b) the $\bar{\rho} = 0.22$ textile diamond oriented cellular sandwich cores. Results are plotted for selected values of the specimen aspect ratio, A.

elastic-plastic solid with Young's modulus $E_s = 200\,\text{GPa}$, 0.2% offset yield strength $\sigma_{ys} = 189\,\text{MPa}$ and a linear hardening modulus $E_t \equiv d\sigma/d\varepsilon \approx 2450\,\text{MPa}$.

4.2. *Results and discussion.*

4.2.1. *Diamond orientation.* The through thickness nominal compressive stress versus nominal strain responses of the diamond topology collinear and textile lattices are plotted in Figure 10 for samples with aspect ratios $0.5 \leq A \leq 7.0$. The modulus was measured via unload/reload curves within the elastic loading regime and are plotted versus aspect ratio in Figure 6. (The unload/reload modulus portions
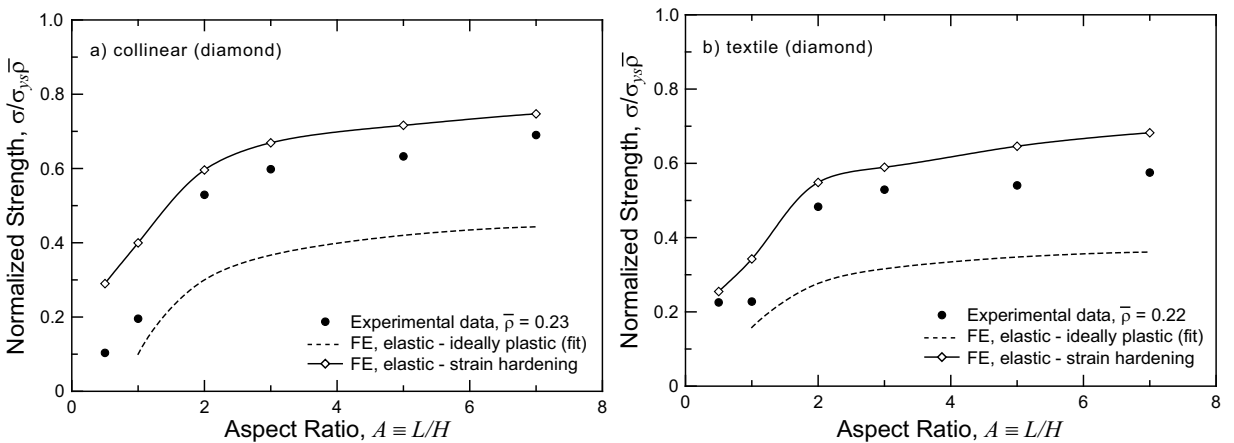
Figure 11. Finite element predictions and measured values of the peak compressive strengths for the diamond orientation (a) $\bar{\rho} = 0.23$ collinear and (b) the $\bar{\rho} = 0.22$ textile sandwich core materials. Also included are the fits (Equations (22) and (23)) derived from the ideally-plastic finite element simulations.

of the stress-strain curves were removed from Figure 10 for the sake of clarity.) The measured Young's moduli agree well with FE predictions while the analytical calculations slightly underpredict the stiffness because bending of the edge wires is neglected in the analytical estimates.

The peak compressive strength of both the collinear and textile lattices is plotted in Figure 11 as a function of the specimen aspect ratio A. The peak compressive strength of both diamond lattices increases with increasing specimen aspect ratio. The peak strength was achieved at compressive strains in the range 5% to 10% indicating that the peak strengths of these stainless steel cellular material are governed by plastic buckling of the constituent wires with the strain hardening of the 304 stainless steel playing a significant role.

Finite element simulations of these experiments were repeated using a solid material having the measured characteristics of the as-brazed 304L stainless steel. A comparison between the strain hardening finite element predictions and the measured peak compressive strength values is shown in Figure 11 for the two diamond lattices. Also included in Figure 11 are the elastic perfectly-plastic FE estimates (Equations (22) and (23)) using $\sigma_{ys} = 189$ MPa. Good agreement between the measurements and strain hardening FE predictions (especially for $A > 1$) are observed whereas the ideally plastic simulations significantly underpredict the peak strength at the highest aspect ratios. This confirms our expectation that the strain hardening of the 304 stainless steel plays a significant role in establishing the peak strength of these cellular materials. Note that some deviation is seen for $A < 1$. This is due to the FE simulation assuming a perfectly rigid bond between nodes, whereas the brazed joint has a lower strength than the parent material: node fractures were observed especially in the specimens with aspect ratios $A < 1$.

4.2.2. *Square orientation.* The through thickness compressive nominal stress versus nominal strain responses of the square lattices are shown in Figure 12. In Figure 12(a), the compressive responses of collinear cores with an aspect ratio $A = 3$ are shown for three sandwich core heights, H. In Figure 12(b), the effect of aspect ratio on the stress versus strain responses of the square textile lattices is investigated
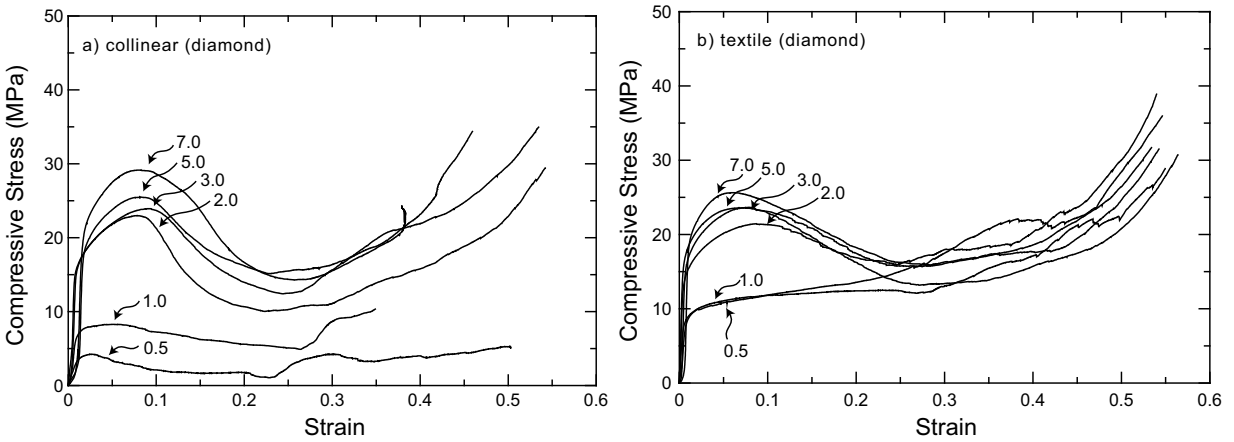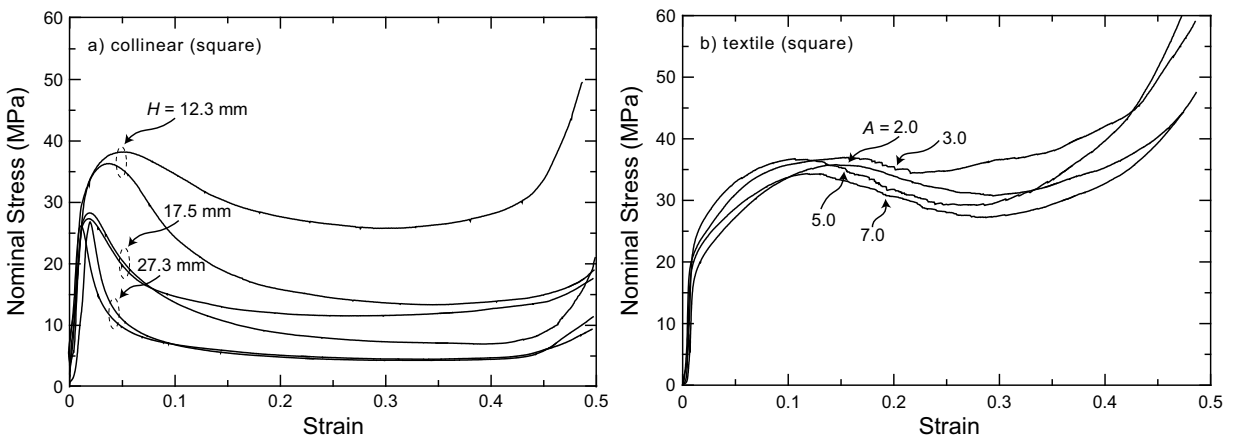

Figure 12. Measured compressive stress versus strain responses of (a) the $\bar{\rho} = 0.23$ collinear ($A = 3.0$) and (b) the $\bar{\rho} = 0.22$ textile square oriented ($H = 15.0$ mm) cellular sandwich core materials.
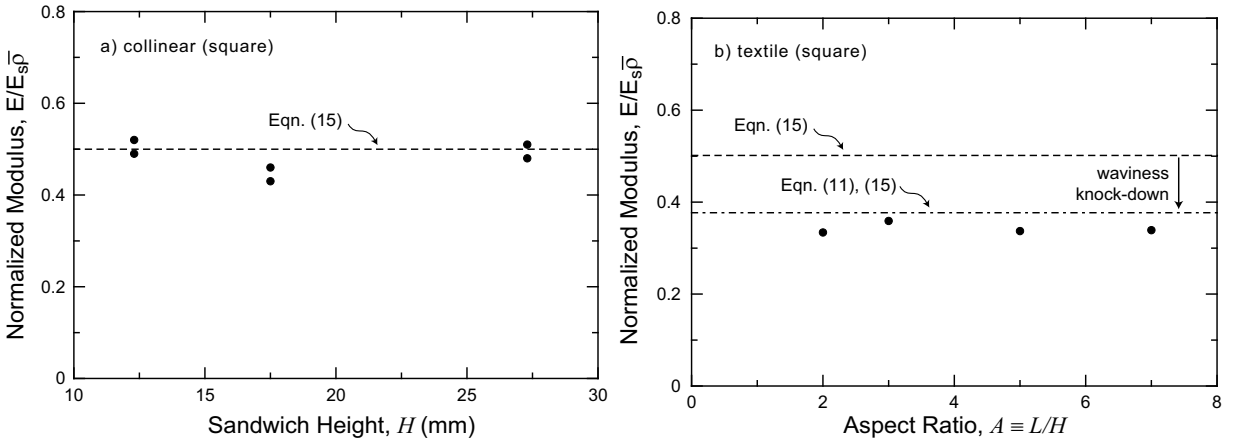
Figure 13. Analytical predictions and measured values of the normalized Young's modulus for the (a) $\bar{\rho} = 0.23$ square collinear and (b) the $\bar{\rho} = 0.22$ square textile sandwich core materials as a function of specimen height H and aspect ratio A, respectively.

for a specimen height $H = 15.0$ mm. The peak compressive strength of the square collinear lattice is seen to decrease with increasing core height while the specimen aspect ratio has a negligible effect.

The effective Young's moduli were evaluated from unload/reload cycles prior to the onset of plastic yielding of the square lattices. This data is plotted in Figure 13(a) as a function of sample height H and in Figure 13(b) as a function of sample aspect ratio $A \equiv L/H$. The analytical predictions are included as dashed horizontal lines in both figures. The analytical predictions are in good agreement with the square collinear lattice data. A significant knock-down in the modulus of the textile material compared to that of the collinear material was observed, and this *waviness* effect is well predicted by Equation (11).

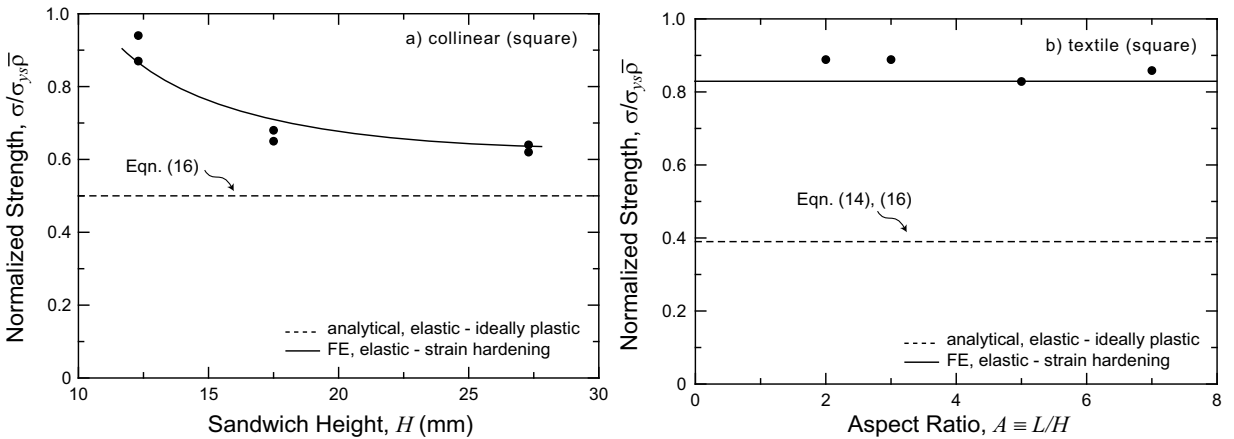**Figure 14.** Analytical and FE predictions and measured values of the normalized compressive strengths for the (a) $\bar{\rho} = 0.23$ square collinear and (b) $\bar{\rho} = 0.22$ square textile sandwich core materials as a function of specimen height H and aspect ratio A, respectively.

The variation of the peak compressive strength of the $A = 3$ square collinear sandwich core with core height H is plotted in Figure 14(a). The normalized peak strengths $\sigma/(\sigma_{ys}\bar{\rho})$ exceed 0.5 which indicates that plastic buckling is the operative collapse mode in this case. Finite element predictions (which include the strain hardening of the 304 stainless steel) of the peak strengths are also included in Figure 14(a) and agree well with the experimental measurements. Experimental measurements and FE as well as analytical predictions of the peak strengths for the $H = 15$ mm square textile lattice are compared in Figure 14(b) for specimen aspect ratios in the range $2.0 \leq A \leq 7.0$. Again, plastic buckling is the operative collapse mode (the normalized peak strength $\sigma/(\sigma_{ys}\bar{\rho})$ exceeds 0.5) and the FE predictions with material strain hardening included agree well with the measurements.

5. Conclusions

Metallic cellular materials are manufactured by laying-up either collinear arrays of solid wires (alternating the direction of successive layers) or woven (textile) meshes. These two routes result in similar lattice truss topologies which differ in the fact that the collinear lattice comprises straight struts while the corresponding struts in the textile material are wavy. Analytical and finite element (FE) calculations show that waviness of the struts results in about a 20% reduction in the stiffness and strength of the textile lattice materials compared to the corresponding collinear materials.

Through-thickness compression tests were conducted on the collinear and textile cores in the diamond and square orientations. In the diamond orientation the stiffness and strength are sensitive to the specimen aspect ratio for aspect ratios less than about 4. By contrast, the properties of sandwich cores in the square orientation are reasonably independent of the specimen aspect ratio but the strength decreases with increasing core height due to buckling of the wires across the entire height of the sandwich core. This mode is suppressed in the diamond orientation and thus the diamond orientation is considered more useful from a practical standpoint.

References

[Ashby et al. 2000] M. F. Ashby, T. Evans, N. A. Fleck, L. J. Gibson, J. W. Hutchinson, and H. N. G. Wadley, *Metal foams: a design guide*, Butterworth-Heinemann, Boston, 2000.

[Berggren et al. 2001] S. A. Berggren, D. Lukkassen, A. Meidell, and L. Simula, "On stiffness properties of square honeycombs and other unidirectional composites", *Compos. B Eng.* **32**:6 (2001), 503–511.

[Bitzer 1997] T. N. Bitzer, *Honeycomb technology: materials, design, manufacturing, applications and testing*, Chapman & Hall, London, 1997.

[Buannic et al. 2003] N. Buannic, P. Cartraud, and T. Quesnel, "Homogenization of corrugated core sandwich panels", *Compos. Struct.* **59**:3 (2003), 299–312.

[Chen et al. 1999] C. Chen, T. J. Lu, and N. A. Fleck, "Effect of imperfections on the yielding of two-dimensional foams", *J. Mech. Phys. Solids* **47**:11 (1999), 2235–2272.

[Cote et al. 2004] F. Cote, V. S. Deshpande, N. A. Fleck, and A. G. Evans, "The out-of-plane compressive behavior of metallic honeycombs", *Mater. Sci. Eng. A* **380**:1-2 (2004), 272–280.

[Cote et al. 2006] F. Cote, V. S. Deshpande, N. A. Fleck, and A. G. Evans, "The compressive and shear responses of corrugated and diamond lattice materials", *Int. J. Solids Struct.* **43**:20 (2006), 6220–6242.

[Deshpande and Fleck 2001] V. S. Deshpande and N. A. Fleck, "Collapse of truss core sandwich beams in 3-point bending", *Int. J. Solids Struct.* **38**:36-37 (2001), 6275–6305.

[Gibson and Ashby 1997] L. J. Gibson and M. F. Ashby, *Cellular solids: structure and properties*, 2nd ed., Cambridge solid state science series, Cambridge University Press, Cambridge, 1997.

[Grenestedt 1998] J. L. Grenestedt, "Influence of wavy imperfections in cell walls on elastic stiffness of cellular solids", *J. Mech. Phys. Solids* **46**:1 (1998), 29–50.

[Grenestedt and Bassinet 2000] J. L. Grenestedt and F. Bassinet, "Influence of cell wall thickness variations on elastic stiffness of closed-cell cellular solids", *Int. J. Mech. Sci.* **42**:7 (2000), 1327–1338.

[Grenestedt and Tanaka 1998] J. L. Grenestedt and K. Tanaka, "Influence of cell shape variations on elastic stiffness of closed cell cellular solids", *Scripta Mater.* **40**:1 (1998), 71–77.

[Hyun et al. 2003] S. Hyun, A. M. Karlsson, S. Torquato, and A. G. Evans, "Simulated properties of Kagomé and tetragonal truss core panels", *Int. J. Solids Struct.* **40**:25 (2003), 6989–6998.

[Kooistra et al. 2004] G. W. Kooistra, V. S. Deshpande, and H. N. G. Wadley, "Compressive behavior of age hardenable tetrahedral lattice truss structures made from aluminium", *Acta Mater.* **52**:14 (2004), 4229–4237.

[Liang and Chen 2006] S. Liang and H. L. Chen, "Investigation on the square cell honeycomb structures under axial loading", *Compos. Struct.* **72**:4 (2006), 446–454.

[Meidell 2005] A. Meidell, "On some new formulae for in-plane elastic moduli of square honeycomb structures", *Int. J. Comput. Civil Struct. Eng.* **1**:1 (2005), 79–88.

[Noor et al. 1995] A. K. Noor, W. S. Burton, and C. W. Bert, "Computational model for sandwich panels and shells", *Appl. Mech. Rev.* **155** (1995), 155–199.

[Prager 1959] W. Prager, *An introduction to plasticity*, Addison-Wesley, Reading, MA, 1959.

[Queheillalt and Wadley 2005] D. T. Queheillalt and H. N. G. Wadley, "Cellular metal lattices with hollow trusses", *Acta Mater.* **53**:2 (2005), 303–313.

[Simone and Gibson 1998a] A. E. Simone and L. J. Gibson, "The effects of cell face curvature and corrugations on the stiffness and strength of metallic foams", *Acta Mater.* **46**:11 (1998), 3929–3935.

[Simone and Gibson 1998b] A. E. Simone and L. J. Gibson, "Effects of solid distribution on the stiffness and strength of metallic foams", *Acta Mater.* **46**:6 (1998), 2139–2150.

[Sypeck and Wadley 2001] D. J. Sypeck and H. N. G. Wadley, "Multifunctional microtruss laminates: textile synthesis and properties", *J. Mater. Res.* **16**:3 (2001), 890–897.

[Sypeck and Wadley 2002] D. J. Sypeck and H. N. G. Wadley, "Cellular metal truss core sandwich structures", *Adv. Eng. Mater.* **4**:10 (2002), 759–764.

[Valdevit et al. 2004] L. Valdevit, J. W. Hutchinson, and A. G. Evans, "Structurally optimized sandwich panels with prismatic cores", *Int. J. Solids Struct.* **41**:18-19 (2004), 5105–5124.

[Wadley et al. 2003] H. N. G. Wadley, N. A. Fleck, and A. G. Evans, "Fabrication and structural performance of periodic cellular metal sandwich structures", *Compos. Sci. Technol.* **63**:16 (2003), 2331–2343.

[Wallach and Gibson 2001] J. C. Wallach and L. J. Gibson, "Defect sensitivity of 3D truss material", *Scripta Mater.* **45**:6 (2001), 639–644.

[Wang et al. 2003] J. Wang, A. G. Evans, K. Dhamasena, and H. N. G. Wadley, "On the performance of truss panels with Kagomé cores", *Int. J. Solids Struct.* **40**:25 (2003), 6981–6988.

[Zok et al. 2004] F. W. Zok, S. A. Waltner, Z. Wei, H. J. Rathbun, R. M. McMeeking, and A. G. Evans, "A protocol for characterizing the structural performance of metallic sandwich panels: application to pyramidal truss cores", *Int. J. Solids Struct.* **41**:22-23 (2004), 6249–6271.

[Zupan et al. 2004] M. Zupan, V. S. Deshpande, and N. A. Fleck, "The out-of-plane compressive behaviour of woven-core sandwich plates", *Eur. J. Mech. A Solid* **23**:3 (2004), 411–421.

DOUGLAS T. QUEHEILLALT: dougq@virginia.edu
Department of Materials Science and Engineering, University of Virginia, 140 Chemistry Way, Charlottesville, VA 22904, United States

VIKRAM S. DESHPANDE: vsd@engineering.ucsb.edu
Department of Mechanical Engineering, University of California, Santa Barbara, Santa Barbara, CA 93106, United States

HAYDN N. G. WADLEY: haydn@virginia.edu
Department of Materials Science and Engineering, University of Virginia, 140 Chemistry Way, Charlottesville, VA 22904, United States

PLASTIC HINGES AS PHASE TRANSITIONS IN STRAIN SOFTENING BEAMS

Gianni Royer-Carfagni and Giovanni Buratti

A jump between the upper yield point and lower yield point is well evident in strain driven tests on low-carbon steel bars. However, in the constitutive equations commonly used to model the elastic-plastic flexure of beams this jump is usually neglected. Here, we show instead that such jump, albeit small, may drastically vary the structural response, because it renders the moment-curvature relationship of the beam strain-softening in type and with horizontal asymptotes. Because of this, with a process analogous to a phase transition within the solid state itself, strain may suddenly localize in the form of concentrated rotations of the beam axis, indeed forming a *plastic hinge* in the classical sense of limit analysis. Therefore, the formation of plastic hinges, usually indicated as an approximate or technical model, is now rigorously predicted by this approach. Experimental observations corroborate this finding.

1. Introduction

The elastic-plastic design of civil structures is classically associated with the *plastic-hinge* model which allows the technical analysis of the bending of beams in a relatively simple manner. Following this rationale, when a beam made of a ductile material, such as steel, is gradually loaded, plastic hinges are assumed to develop at those sections where the bending moment reaches a certain threshold, that is, at those sections rotations of any amount may occur while the bending moment remains fixed at the threshold value [Neal 1963]. However, the plastic hinge model is traditionally considered an approximate or technical model because, even when the material is idealized as elastic-perfectly plastic, regardless of the shape of beam cross-section the bending moment M is a monotonically increasing function of the beam curvature χ asymptotically approaching, but never reaching, the full plastic moment as $\chi \to \infty$. Thus, the development of a plastic hinge can be read as a borderline case, never attained in practice, but a very useful simplification in the structural analysis.

There are, however, some interesting but perhaps forgotten old experiments by Nakanishi et al. [1934], which have provided a wealth of evidence describing how the plastic hinge model may indeed be more accurate than expected. To illustrate, Figure 1 represents the bending moment $\bar{M}$ versus sag δ relationship measured from tests on simple supported beams with various cross-sections, loaded as in Figure 2. If the material is considered elastic-perfectly plastic and, according to the Bernoulli–Navier hypothesis, cross-sections remain planar in the deformation, then the flexure is uniform in the central portion A-B of Figure 2, and the bending moment is a monotonically increasing function of the beam curvature χ, asymptotically approaching the full plastic threshold. However, this trend is not confirmed by experiments. In fact, if the flexure were uniform, the $\bar{M}$-δ diagrams of Figure 1 would also represent, by a
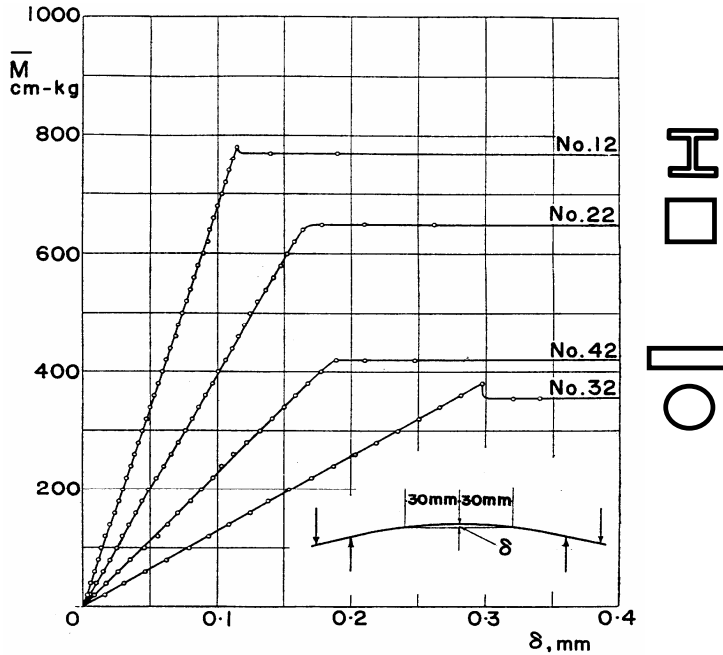
Figure 1. Experimental $\bar{M}$-δ relationships for beams with different cross-sections [Nakanishi et al. 1934].

proper change of scale, the moment-curvature response of the beam. This is because the curvature of its centroid line could be expressed, with the usual first-order approximation, as

$$\chi(z) \cong \frac{8\delta}{l^2}. \tag{1}$$

Quite surprisingly, the graphs of Figure 1 do not show monotonically increasing curves, but rather exhibit a horizontal *plateau*, revealing that the bending moment remains constant while the beam sag increases indefinitely as if a classical *plastic hinge* had developed.

In order to solve the apparent discrepancy between theoretical predictions and experimental results, we simply propose to consider in the constitutive stress-strain law the jump between the so called *upper yield*
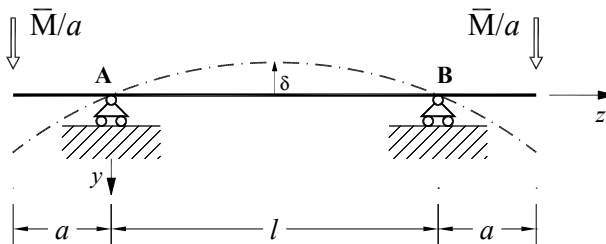
Figure 2. Layout of the experimental configuration for tests of Figure 1 [Nakanishi et al. 1934].

point (Oberestreckgrenze) and *lower yield point* (Unterestreckgrenze). Such jump is usually neglected in the constitutive equations, although it is well evident in strain driven tests on low-carbon steel bars [Neal 1963]. For example, in Figure 3, which shows the engineering stress σ versus the engineering strain ε diagrams as measured in one of the tests recorded in [Froli and Royer-Carfagni 1999], the ratio between *Oberestreckgrenze* and *Unterestreckgrenze* is of the order of 1.12; this value may vary according to the carbon level in the steel. In fact, at the nanoscale, the stress drop can be attributed to the pinning of the dislocations (Peierls–Nabarro effect) due to the presence of solute atoms of carbons in the metallic lattice [Cottrell 1953]. It has been demonstrated [Froli and Royer-Carfagni 2000] that the consideration of such a jump is of crucial importance for the orderly formation, at the microscale, of slip (Lüder) bands in stretched bars of mild steel.

For the case of bending, consideration of this jump is not without consequences because it renders the elastic-plastic moment-curvature relationship $M(\chi)$ nonmonotone in type. Indeed, the nonmonotone character of $M(\chi)$, analogously to the classical loops in the pressure versus volume isotherms of a Van der Waals fluid, may produce a transition in the beam strain reminiscent of the sudden volume change associated with the transition from the liquid to the vapor phase in the fluid. The extension of Van der Waals model to solids has received much attention recently; see [Müller and Villaggio 1977; Dunn and Fosdick 1980]. The relevant theories, which allow for stress- and deformation-induced phase transitions within the solid state itself, predict discontinuous strain fields in reasonable agreement with the experimental observations. Another characteristic feature of the $M(\chi)$ function that will be deduced from the proposed constitutive σ-ε law, is that it exhibits a horizontal asymptote. Truskinovsky [1996] has perhaps been the first to consider the consequences of assuming constitutive relationships with horizontal *plateaux* for the one-dimensional case of a tensile bar, evidencing the consequent possibility of strain localization, similar in type to the nucleation of passing through a crack.

Figure 3. Local σ-ε relationship in a stretched bar of mild steel [Froli and Royer-Carfagni 1999]. Local strain measured with strain gauges.

In this paper we will show that the loops and the horizontal asymptotes of the $M(\chi)$ constitutive law may imply, similarly to phase transitions, 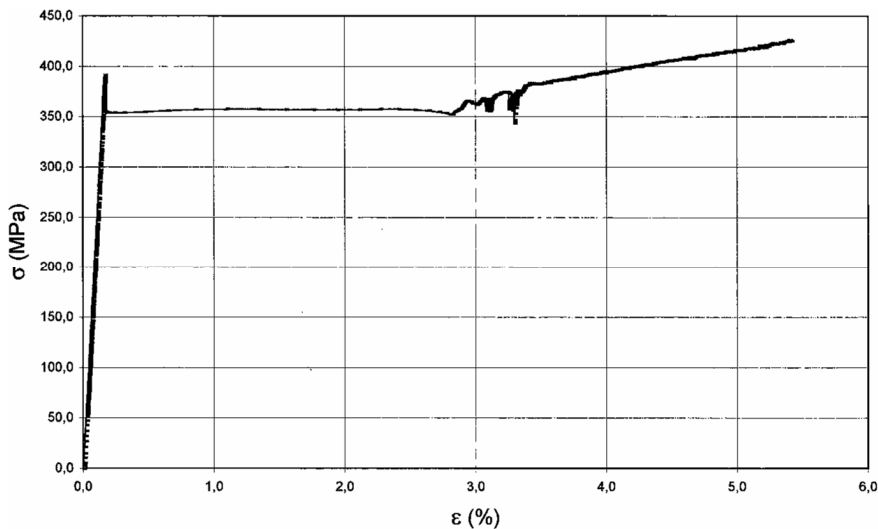a sudden strain localization in the beam, that is, a discontinuity in the rotation field of the centroid line, analogous to the formation of a *plastic hinge* in the classical meaning of limit analysis. An accurate reworking of the traditional technical theories from this novel approach may be of importance, especially in the seismic design of civil engineering works, where the plastic resources in terms of ductility play a decisive role in the structural performance.

2. Moment versus curvature relationships for elastic-plastic beams

To illustrate the consequences of considering a jump between the upper and lower yield points in the stress-strain constitutive law, consider the case of a beam with constant cross-section under flexure. According to the Bernoulli–Navier hypothesis we assume that cross-sections remain planar during bending, so that the elongation of each longitudinal fiber is directly proportional to the distance y from the neutral axis by a coefficient χ, representing the curvature of the centroid line of the beam. In particular, consider the simplest relationship between engineering stress σ and engineering strain ε of the type reported in Figure 4. Clearly, the material is elastic-perfectly plastic, symmetric in tension and compression. Nevertheless, it exhibits a well marked jump from *Oberestreckgrenze* to *Unterestreckgrenze*. For the constitutive law $\sigma(\varepsilon)$ can be written in the form

$$\sigma(\varepsilon) = \begin{cases} -\sigma_0, & \varepsilon < -\varepsilon_0, \\ \alpha\frac{\sigma_0}{\varepsilon_0}\varepsilon, & -\varepsilon_0 \leq \varepsilon \leq \varepsilon_0, \\ \sigma_0, & \varepsilon > \varepsilon_0, \end{cases}$$

where $\alpha\sigma_0$, with $\alpha > 1$, is the *Oberestreckgrenze* and σ_0 the *Unterestreckgrenze*.

Let us now examine beams with cross-sections of three different shapes. Consider first a rectangular cross section of depth h and width b. As the beam curvature χ is gradually increased, the distribution of normal stress along the depth of the cross-section is of the type sketched in Figure 5, where χ_I denotes the curvature corresponding to the elastic limit. When the curvature is increased beyond χ_I, the most distant fibers from the neutral axis are strained beyond ε_0 and, consequently, in these overstrained regions
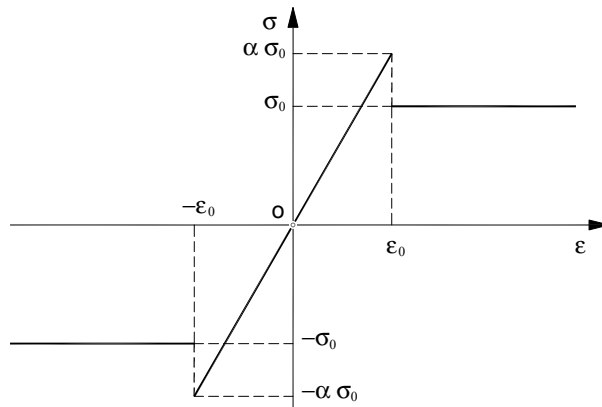
Figure 4. Stress-strain relationship with stress jump at yielding.
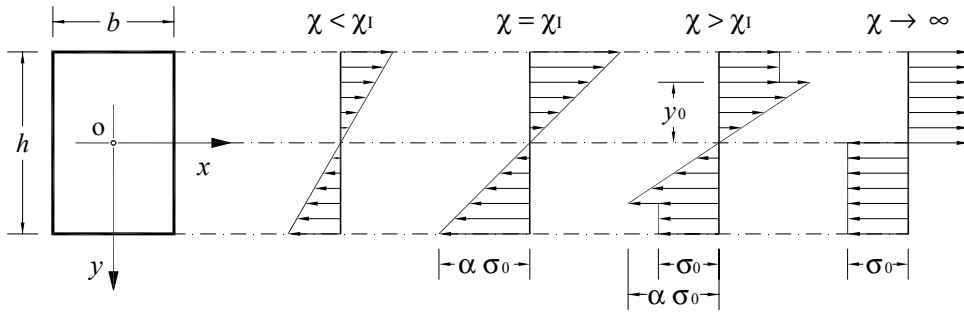
Figure 5. Rectangular cross-section: stress distribution with discontinuous σ-ε relationship.

the stress remains constant and equal to the lower yield point stress, σ_0. Further increasing the curvature, more and more fibers reach the yield point until the entire beam, with the exception of a thin layer at the neutral axis, becomes plastic. In Figure 5 this condition is referred to as the stage $\chi \to \infty$.

Denoting by y_0 the distance from the fiber neutral axis at which the strain reaches the limit value ε_0, the relationship between bending moment and curvature is $M(\chi) = \frac{2}{3}Eby_0^3\chi + \sigma_0 b\left(\frac{1}{4}h^2 - y_0^2\right)$, where

$$y_0 = \begin{cases} h/2, & \chi \leq \chi_{\mathrm{I}}, \\ \alpha\sigma_0/(\chi E), & \text{otherwise,} \end{cases}$$

and E denotes the Young's modulus. The corresponding moment-curvature M-χ relationship is represented in Figure 6 for different values of the parameter α. In particular, observe that for $\alpha > 3/2$ the M-χ curve exhibits a well-recognizable strain-softening branch. In this latter case, under a strain history monotonically increasing the curvature χ, the work U consumed in deforming the beam per unit beam length defined as

$$U(\chi) = \int_0^\chi M(\eta)d\eta \tag{2}$$

is a nonconvex function with oblique asymptotes of the type schematically represented in Figure 7.

As a second example consider a beam whose cross-section is rhomboidal with depth b_R and height h_R. The stress diagram for gradually increasing curvatures is shown in Figure 8, while the corresponding M-χ relationship is qualitatively sketched in Figure 9. Again, when $\alpha > 3/2$, the bending moment attains
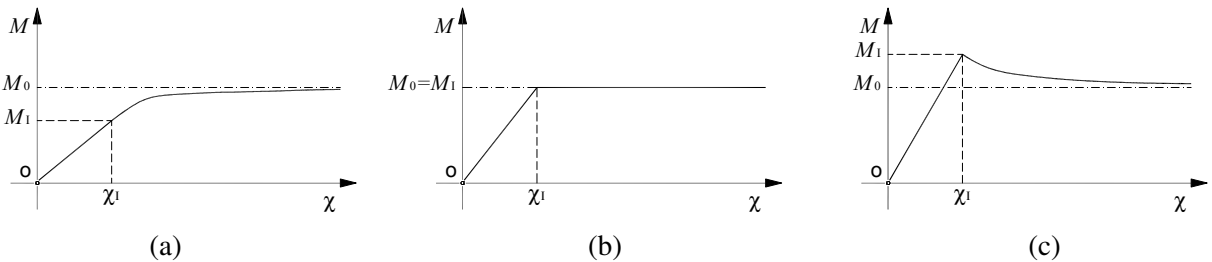
Figure 6. Bending moment versus curvature of beams with rectangular cross-section for (a) $1 < \alpha < 3/2$, (b) $\alpha = 3/2$, (c) $\alpha > 3/2$.
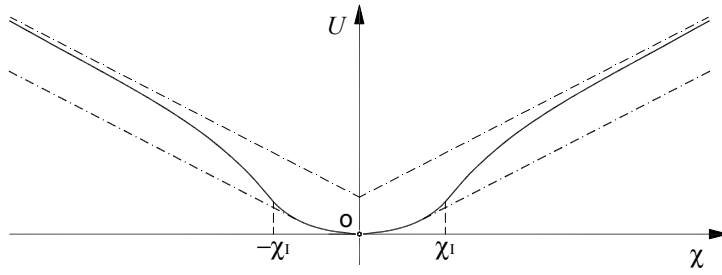
Figure 7. Rectangular cross section. Elastic-plastic work per unit length $U(\chi)$ for $\alpha > 3/2$.
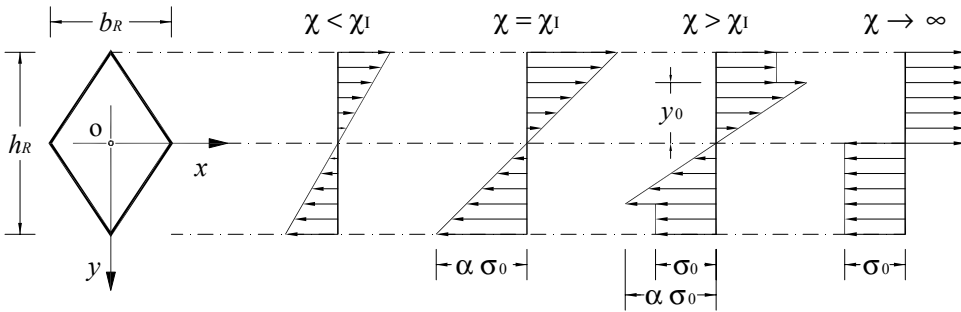
Figure 8. Stress distribution for rhomboidal cross-sections.
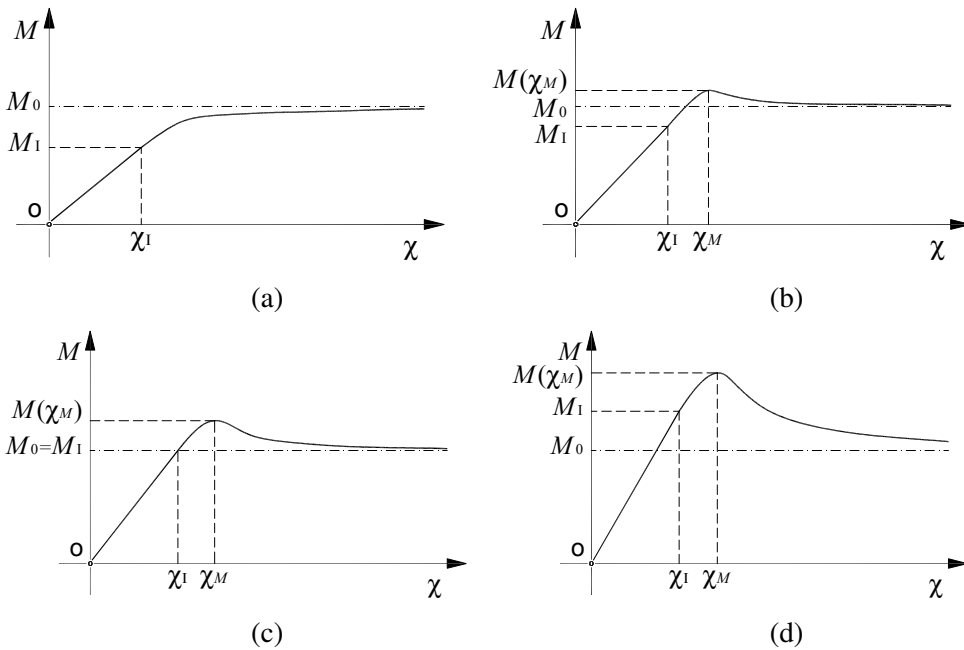
Figure 9. Bending moment versus curvature for rhomboidal cross-sections for (a) $1 < \alpha \leq 3/2$, (b) $3/2 < \alpha \leq 2$, (c) $\alpha = 2$, (d) $\alpha > 2$.
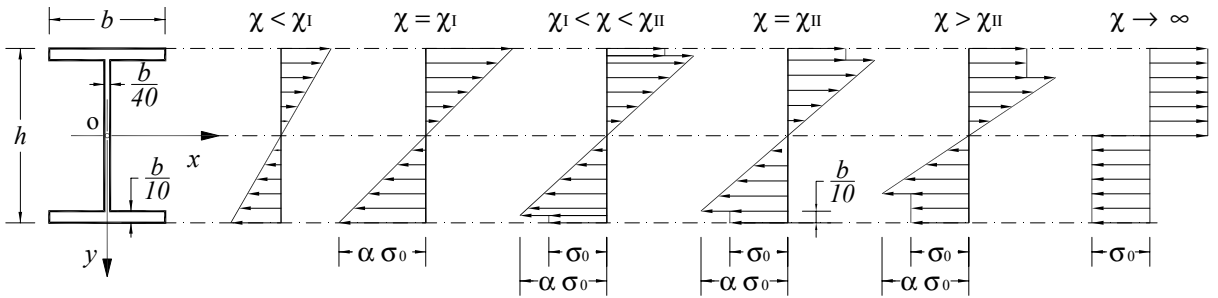
Figure 10. I-shaped cross-section: stress distribution with discontinuous σ-ε relationship.

its maximum value at the (finite) curvature given by

$$\chi_M = \frac{3}{2h_R}\frac{3\alpha - 4}{2\alpha - 3}, \qquad M(\chi_M) = \frac{(128\alpha^2 - 333\alpha + 216)\alpha}{324(4 - 3\alpha)^2}b_R h_R^2,$$

but such value is greater than the full plastic moment M_0. Consequently, the $M(\chi)$ curve becomes nonmonotone, with a strain softening branch. Correspondingly, the work consumed in deforming the beam $U(\chi)$ results again in a nonconvex type when $\alpha > 3/2$.

As a third, and perhaps most practically relevant example, consider an I-shaped cross section. The stress-distribution at different values of the curvature is schematically represented in Figure 10, where χ_I denotes again the elastic limit curvature and χ_{II} the curvature at which the flanges become plastic.
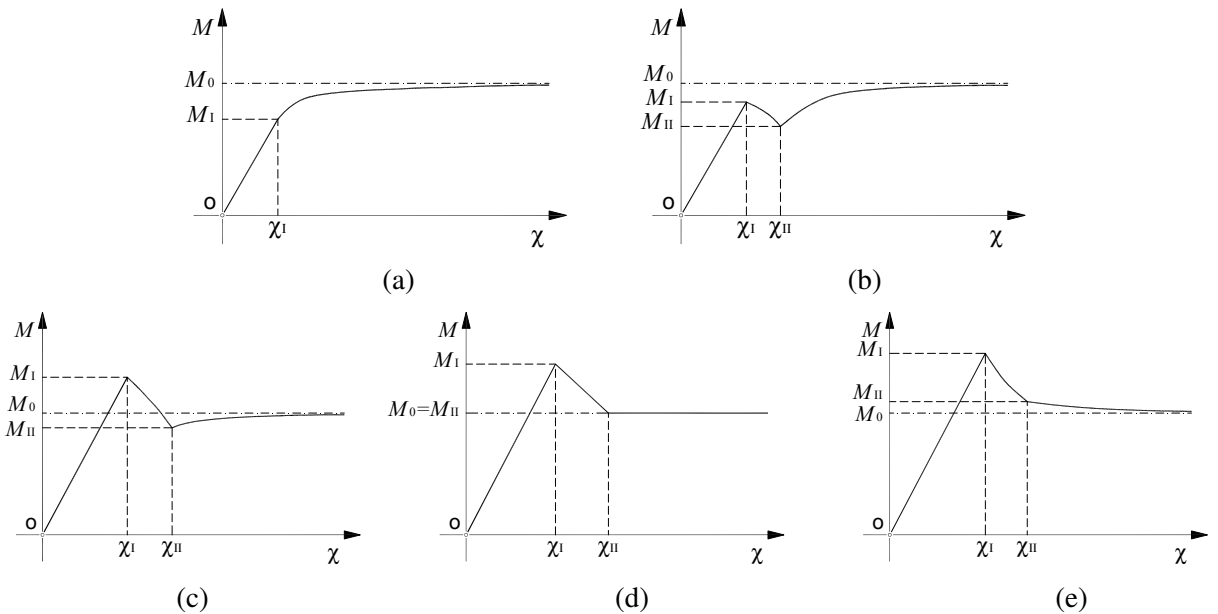
Figure 11. Bending moment versus curvature for I-shaped beams for (a) $\alpha \leq 60/59$, (b) $60/59 < \alpha \leq 12615/11569$, (c) $12615/11569 < \alpha < 3/2$, (d) $\alpha = 3/2$, (e) $\alpha > 3/2$.

The M-χ curves obtained for different choices of the parameter α are schematically represented in Figure 11. Remarkably, in the third example the dependence of the M-χ relationship on α is quite nonlinear, and the nonmonotone character is observed also for very small values of α. This finding is crucial for the forthcoming analysis, where a nonmonotone (strain-softening) character for the moment-curvature relationship will be systematically assumed. The corresponding diagrams for the elastic-plastic work $U(\chi)$ are sketched in Figure 12.

Note that in this case the nonmonotone character of the bending M-χ relationship is attained also for small jumps in the stress-strain curve, specifically for $\alpha > 60/59$. A value of this order is certainly reached in practice; experimental tests on mild steel show that $\alpha \cong 1.1$ [Froli and Royer-Carfagni 1999]. Moreover, as the parameter α is varied within this range, the corresponding graphs of $M(\chi)$ and $U(\chi)$ may exhibit loops that are different in kind. Thus, at least for I-shaped profiles, the discussion of the cases when the moment-curvature relationship is of the type represented in Figure 11 acquires a practical interest.

3. The energy functional

Consider a simply supported beam subject to a transversally distributed load $q(z)$ and two couples, W_A and W_B, acting at its ends (considered positive if oriented as in Figure 13). Let $v(z)$ denote the displacement component in the y-direction of the beam centroid axes at z, $\varphi(z)$ the corresponding rotation which is positive if counterclockwise, and define the curvature χ through the relationship $\chi(z) = \varphi'(z)$, where the prime indicates a derivative with respect to z.
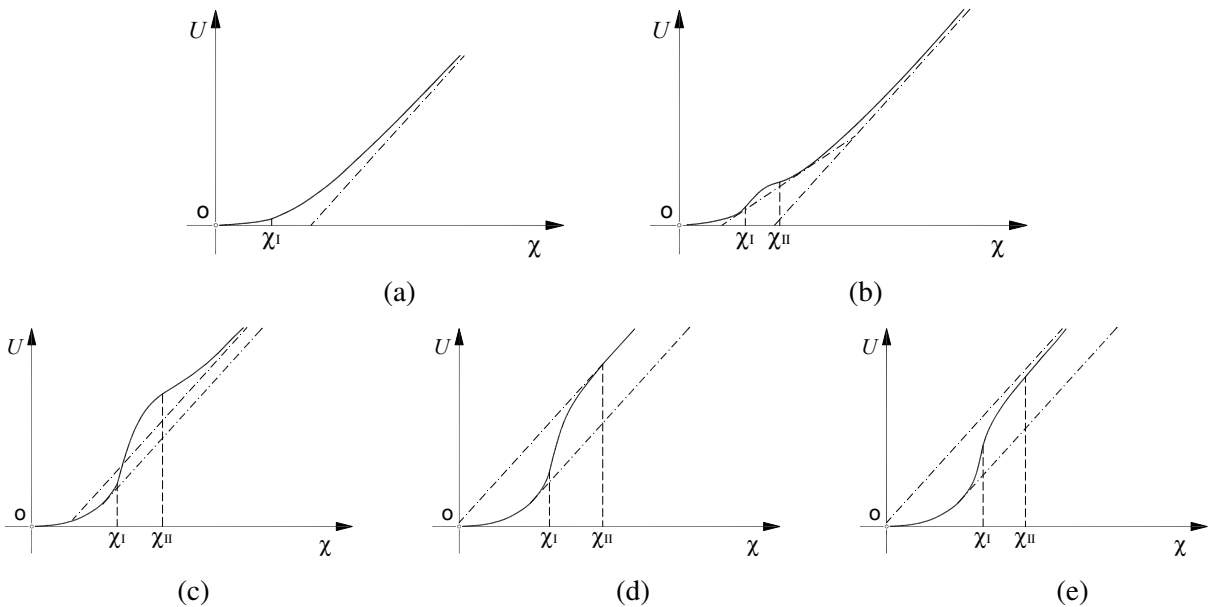
Figure 12. Elastic-plastic work per unit length $U(\chi)$ in I-shaped beams for (a) $\alpha \le 60/59$, (b) $60/59 < \alpha \le 12615/11569$, (c) $12615/11569 < \alpha < 3/2$, (d) $\alpha = 3/2$, (e) $\alpha > 3/2$.

At this stage, the analysis will be limited to the case of holonomic plasticity only, so that a strain energy functional can be defined. This produces noteworthy simplifications because the beam stable equilibrium configurations will be associated with absolute minimizers of the energy functional. This allows modern techniques in the calculus of variations to be applied to the corresponding nonconvex minimization problem. Under these assumptions, the energy functional associated with the sum of the strain energy and the potential energy of the applied loads can be written in the form

$$E[\varphi, v] = \int_0^L U\big(\varphi'(z)\big)dz - \int_0^L q(z)v(z)dz - \big[W\varphi(z)\big]_{z=0}^{z=L}, \tag{3}$$

where $U(\varphi') = U(\chi)$ is the bulk energy density, defined as in Equation (2). In general, for the reasons discussed in Section 2, U is an even, nonconvex function whose qualitative form will represented by one of the graphs in Figure 12.

It is useful to introduce the quantity

$$T(z) = -\int_0^z q(z)dz + C_1, \tag{4}$$

where C_1 is a constant whose value will be determined afterward. It is easy to recognize that when the constant C_1 represents the vertical reaction at point A of Figure 13, then $T(z)$ denotes the shear force acting at section z. The importance of Equation (4) is that it allows us to write a convenient expression for the work of the external load. In fact, by setting

$$\varphi(z) \cong -\frac{d}{dz}v(z) \tag{5}$$

as customary in the technical theory of beams, upon integrating by parts one obtains

$$\int_0^L q(z)v(z)dz = \int_0^L T(z)v'(z)dz - \big[T(z)v(z)\big]_{z=0}^{z=L} = -\int_0^L T(z)\varphi(z)dz, \tag{6}$$

that, once introduced into Equation (3), provides a simpler form of the total energy functional to be minimized. In particular,

$$\pi[\varphi] = \int_0^L U\big(\varphi'(z)\big)dz + \int_0^L T(z)\varphi(z)dz - \big[W(z)\varphi(z)\big]_{z=0}^{z=L}, \tag{7}$$
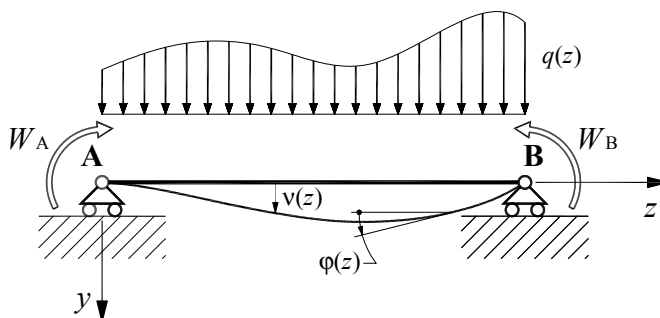
Figure 13. Generic layout of beam under flexure.

since now only the rotation field φ comes into play. Using Equation (5) the boundary conditions $v(0) = v(L) = 0$ can be equivalently restated in terms of φ only via

$$\int_0^L \varphi(z)dz = 0. \tag{8}$$

Solutions of the variational problem have to be sought in the space of function of bounded variation on $[0, L]$, usually referred to as $BV[0, L]$. For our derivations we will need to use some notions of functional analysis; see [Kolmogorov and Fomin 1975] for details and notation. The necessity of considering a space of functions allowing for discontinuities such as the space BV comes essentially from the presence of the oblique asymptotes in the strain energy function $U(\chi)$. In fact, due to the linear growth of $U(\chi)$ at infinity, a finite value of the energy is associated with infinite curvatures.

To illustrate this point, let us take a step function of the type

$$H(z) = \begin{cases} 0, & 0 \le z < z_0, \\ \varphi_0, & z_0 \le z \le L, \end{cases}$$

where φ_0 is a fixed number. Consider then the sequence $\varphi_{(n)}^H(z)$ defined by

$$\varphi_{(n)}^H(z) = \begin{cases} 0, & 0 \le z < z_0, \\ \varphi_0 \, n(z - z_0), & z_0 \le z \le z_0 + 1/n, \\ \varphi_0, & z_0 < z \le L, \end{cases}$$

converging to $H(z)$ when $n \to \infty$. The derivative of $\varphi_{(n)}^H(z)$ with respect to the variable z is not null in the interval $z_0 \le z \le z_0 + 1/n$ only, where it is constant and directly proportional to n. But $U(\varphi'(z))$ has oblique asymptotes with slope $\pm M_0$; consequently, the strain energy remains bounded also when $n \to \infty$ because

$$\lim_{n \to \infty} \int_0^L U\big(\varphi_{(n)}^{H'}(z)\big)dz \cong \lim_{n \to \infty} \left(\mathrm{sgn}(\varphi_0) \mathrm{M}_0 \frac{\varphi_0}{1/n} \frac{1}{n} \right) = \mathrm{M}_0 \, \varphi_0 \, \mathrm{sgn}(\varphi_0) = \mathrm{M}_0 |\varphi_0|, \tag{9}$$

where $\mathrm{sgn}(\varphi_0)$ denotes the sign of φ_0. Therefore, since by Equation (9) the total energy is also limited for functions with discontinuous rotation fields, the possibility of discontinuities must be contemplated in a proper class of function in which minimizers have to be sought. Moreover, the energy functional given in Equation (3) must be modified to account for the energy associated with the singularities of the rotation field.

The energy contribution due to concentrated rotations has been evaluated with a limit procedure by Royer-Carfagni [2001]. Here we only recall the main results, which were also discussed in [Del Piero 2003]. First of all, recall by Lebesgue decomposition [Kolmogorov and Fomin 1975] that any function φ of bounded variation can written in the form

$$\varphi(\cdot) = \varphi_a(\cdot) + \varphi_s(\cdot) + \varphi_d(\cdot), \tag{10}$$

that is, the sum of a function φ_a whose derivative, in the sense of distributions, is absolutely continuous with respect to the Lebesgue measure, a singular Cantor-like function φ_s and a jump function φ_d. Then, the new energy functional $\Pi[\varphi]$ to be considered [Royer-Carfagni 2001] has the property that $\Pi[\varphi]$

coincides with $\pi[\varphi]$ of Equation (7) whenever $d\varphi(z)$ is absolutely continuous, that is, $d\varphi_s = d\varphi_d \equiv 0$. Furthermore, $\liminf_{n\to\infty} \pi[\varphi_{(n)}] = \Pi[\varphi]$ for any sequence $\varphi_{(n)}$ converging in a suitable topology [1] onto a singular function φ with null absolutely continuous part, that is, with $\varphi_a \equiv 0$.

The result is as follows. Recalling that any function in $BV: \mathbb{R} \to \mathbb{R}$ can be written as the sum of a nondecreasing function and a nonincreasing function [Kolmogorov and Fomin 1975], using Equation (6) and writing φ_s as the sum of a nondecreasing and nonincreasing functions φ_s^+ and φ_s^- acting in their domains of definition J_+ and J_-, respectively, the energy stored in the beam, obtained by augmenting Equation (3) of the contribution due to possible irregularities in the rotation field, can be written in the form [Royer-Carfagni 2001; Del Piero 2003]

$$\Pi[\varphi] = \int_0^L U(\varphi_a')dz + M_0\Big(\int_{J_+} d\varphi_s^+ - \int_{J_-} d\varphi_s^-\Big) + M_0 \sum_{z\in\Gamma(\varphi)} |[\![\varphi]\!](z)|$$
$$+ \int_0^L T(z)\varphi(z)dz - \big[W(z)\varphi(z)\big]_{z=0}^{z=L}, \quad (11)$$

where $\Gamma(\varphi)$ is the (countable) set of discontinuity points of φ and $[\![\varphi]\!](z) := \varphi(z^+) - \varphi(z^-)$ is the jump of φ at $z \in \Gamma(\varphi)$. It should be remarked that in addition to a bulk term Equation (11) also consists of a surface or interfacial part, that is, the part associated with the Cantor part $d\varphi_s$ and jump part $[\![\varphi]\!]$ of φ. Such parts take into account of the energy consumed at those points where the beam curvature becomes infinite.

The energy functional has to be minimized in the class $\varphi \in BV[0, L] \to \mathbb{R}$ subject to the condition

$$\int_0^L \varphi(z)dz = \int_0^L \varphi_a(z)dz + \int_0^L \varphi_s(z)dz + \int_0^L \varphi_d(z)dz = 0, \quad (12)$$

analogous to Equation (8). In what follows, we will consider the variational problem of minimizing $\Pi[\varphi]$ for two specific cases.

4. Simple supported beam under uniform bending

Consider first the bending of an originally straight beam loaded by bending moments at its ends, that is, $W(z = 0) = W_A$, $W(z = L) = W_B$ and $q(z) \equiv 0$ in the notation of Figure 13. To analyze the stationary points of the energy functional Equation (11), observe first that $q(z) = 0$ and Equation (6) imply $\int_0^L T(z)\varphi(z)dz = 0$. Let then $\varphi^*(z) \in BV : [0, L] \to \mathbb{R}$ be a minimizer of $\Pi[\varphi]$ of Equation (11), and consider the variation $\varphi^* + \varepsilon\psi$. Lebesgue's decomposition (10) gives

$$\psi = \psi_a + \psi_s + \psi_d \in BV : [0, L] \to \mathbb{R}, \quad (13)$$

with $d\psi$ consisting of the absolutely continuous part $d\psi_a$, the singular part $d\psi_s$ and the jump part $d\psi_d$. Then, by the boundary condition (8), ψ has to satisfy

$$\int_0^L \psi(z)dz = \int_0^L \psi_a(z)dz + \int_0^L \psi_s(z)dz + \int_0^L \psi_d(z)dz. \quad (14)$$

---

[1] The weak* topology in the space of measures [Buttazzo 1989].

The necessary conditions for equilibrium, yielded by a standard procedure of calculus of variation, are given by the inequality

$$\lim_{\varepsilon \to 0^+} \frac{\Pi[\varphi^* + \varepsilon \psi] - \Pi[\varphi^*]}{\varepsilon} \geq 0, \qquad \text{for all } \psi. \tag{15}$$

For the following, it is convenient to introduce the function

$$M^*(z) = U'\big(\varphi_a^{*\prime}(z)\big), \tag{16}$$

representing the bending moment in the beam. Three classes of perturbations will be considered.

In the first case, let $d\psi = d\psi_a$, $d\psi_s = d\psi_d = 0$, that is, the perturbation is represented by a rotation field whose distributional derivative is absolutely continuous with respect to the Lebesgue measure. Since two-sided variations are allowed, the inequality (15) reduces to the equality

$$0 = d\Pi[\psi] = \int_0^L U'\big(\varphi_a^{*\prime}(z)\big)\psi_a'(z)dz - \big[W(z)\psi_a(z)\big]_{z=0}^{z=L},$$

that, after integrating by parts and using Equation (16), can be rewritten in the form

$$0 = d\Pi[\psi] = \big[U'\big(\varphi_a^{*\prime}(z)\big)\psi_a(z)\big]_{z=0}^{z=L} - \int_0^L \frac{d}{dz}U'\big(\varphi_a^{*\prime}(z)\big)\psi_a(z)dz - \big[W(z)\psi_a(z)\big]_{z=0}^{z=L}$$

$$= -\int_0^L \frac{d}{dz}M^*(z)\psi_a(z)dz + \big[\big(M^*(z) - W(z)\big)\psi_a(z)\big]_{z=0}^{z=L}. \tag{17}$$

Because of the arbitrariness of ψ_a and Equation (14), this is satisfied if and only if

$$-\frac{d}{dz}M^*(z) = C = \text{const}, \qquad M^*(z=0,L) = W(z=0,L). \tag{18}$$

These are the standard equilibrium equations at the interior points and at the ends of the beam, respectively. Consequently, integrating the first equation of (18), with the natural conditions given in the second part of (18) one gets

$$M^*(z) = \frac{W_B - W_A}{L}z + W_A. \tag{19}$$

In the particular case of uniform bending whence $W_A = W_B$ as in Figure 2, Equation (19) reduces to

$$M^*(z) = W_A. \tag{20}$$

As a second case, consider the variation $d\psi = d\psi_a + d\psi_s$, $d\psi_d = 0$. Condition (15) yields

$$\int_0^L M^*(z)\psi_a'(z)dz + M_0\left(\int_{J_+} d\psi_s - \int_{J_-} d\psi_s + \int_{J_0} |d\psi_s|\right) - \big[W(z)\psi(z)\big]_{z=0}^{z=L} \geq 0, \tag{21}$$

with $J_0 = \text{Supp}[d\psi_s] \backslash \{J_+ \cup J_-\}$, where $\text{Supp}[d\psi_s]$ denotes the support of $d\psi_s$. Consequently, integrating by parts the first integral and recalling that $\psi_a = \psi - \psi_s$, we get

$$-\int_0^L \frac{d}{dz} M^*(z)\psi(z)dz + \int_0^L \frac{d}{dz} M^*(z)\psi_s dz + \left[M^*(z)\psi_a(z)\right]_{z=0}^{z=L}$$
$$+ M_0\left(\int_{J_+} d\psi_s - \int_{J_-} d\psi_s + \int_{J_0} |d\psi_s|\right) - \left[W(z)\psi(z)\right]_{z=0}^{z=L} \geq 0. \quad (22)$$

However, from the conditions (14) and (18) the first term vanishes. Thus, integrating by parts once more and using Equation (18), Equation (22) can be put into the equivalent form

$$-\int_0^L M^*(z)d\psi_s + M_0\left(\int_{J_+} d\psi_s - \int_{J_-} d\psi_s + \int_{J_0} |d\psi_s|\right) + \left[(M^*(z) - W(z))\psi(z)\right]_{z=0}^{z=L}$$
$$= -\int_0^L M^*(z)d\psi_s + M_0\left(\int_{J_+} d\psi_s - \int_{J_-} d\psi_s + \int_{J_0} |d\psi_s|\right) \geq 0.$$

From this inequality, after subdividing the first integral into the same portions, J_+, J_- and J_0 and using the arbitrariness of $d\psi_s$, one gets the following conditions

$$\begin{aligned}
M(z) &= M_0, & &\text{for all } z \in J_+, \\
M(z) &= -M_0, & &\text{for all } z \in J_-, \\
-M_0 &\leq M(z) \leq M_0, & &\text{for all } z \in J_0.
\end{aligned} \quad (23)$$

In words, the bending moment cannot take values outside the interval $[-M_0, M_0]$. Moreover, where the rotation field presents positive or negative discontinuities, the bending moment must be equal to M_0 or $-M_0$, respectively.

Finally, assume a perturbation $d\psi = d\psi_a + d\psi_d$, $d\psi_s = 0$, such that the term ψ_d satisfies the condition

$$\psi_d = \begin{cases} 0, & 0 \leq z < z_0, \\ [\![\psi_d]\!](z_0) \neq 0, & z_0 \leq z < L. \end{cases} \quad (24)$$

If $[\![\varphi^*]\!](z_0) = 0$ one obtains $\int_0^L M^*(z)\psi_a'(z)dz + M_0|[\![\psi_d]\!](z_0)| - [W(z)\psi(z)]_{z=0}^{z=L} \geq 0$, that, due to Equations (14) and (18), similarly to the second case, can be rewritten as

$$-\int_0^L M^*(z)d\psi_d + \left[M^*(z)\psi_d(z)\right]_{z=0}^{z=L} + \left[M^*(z)\psi_a(z)\right]_{z=0}^{z=L} + M_0\big|[\![\psi_d]\!](z_0)\big| - \left[W(z)\psi(z)\right]_{z=0}^{z=L}$$
$$= -M^*(z_0)[\![\psi_d]\!](z_0) + M_0\big|[\![\psi_d]\!](z_0)\big| + \left[(M^*(z) - W(z))\psi(z)\right]_{z=0}^{z=L}$$
$$= -M^*(z_0)[\![\psi_d]\!](z_0) + M_0\big|[\![\psi_d]\!](z_0)\big| \geq 0,$$

giving the condition $-M_0 \leq M^*(z_0) \leq M_0$. Otherwise, if $[\![\varphi^*]\!](z_0) \neq 0$, one finds

$$\int_0^L M^*(z)\psi_a'(z)dz + M_0\big([\![\psi_d]\!](z_0)\big)\text{sgn}\big([\![\varphi^*]\!](z_0)\big) - \left[W(z)\psi(z)\right]_{z=0}^{z=L} \geq 0.$$

Consequently, $-M^*(z_0)[\![\psi_d]\!](z_0) + M_0\big([\![\psi_d]\!](z_0)\big)\mathrm{sgn}\big([\![\varphi^*]\!](z_0)\big) \geq 0$. Since $[\![\psi_d]\!](z_0)$ is arbitrary, this is equivalent to the condition

$$M^*(z_0) = M_0\mathrm{sgn}\big([\![\varphi^*]\!](z_0)\big), \tag{25}$$

from which it follows that at the jump points of φ^* the function M^* can assume the values M_0 or $-M_0$. The sign of the bending moment is consistent with the sign of the jump, as stated by Equation (25).

The analysis of the second variation for the energy functional (11) provides the simple inequality

$$U''\big(\varphi_a^{*\prime}\big) \geq 0. \tag{26}$$

It is then clear that any field that solves the Euler equations, but attains the softening branches of the moment curvature relationship, that is, the concave portion of the strain potential, corresponds to an *unstable* equilibrium configuration.

Finally, for a complete characterization of minimizers it is convenient to introduce an auxiliary problem known as the relaxed problem. After a well known procedure in the calculus of variations [Buttazzo 1989], the relevant procedure consists of the minimization of the *relaxed* strain energy functional

$$\Pi^{**}[\varphi] = \int_0^L U^{**}(\varphi_a')dz + M_0\Big(\int_{J+} d\varphi_s^+ - \int_{J-} d\varphi_s^-\Big) + M_0 \sum_{z\in\Gamma(\varphi)} \big|[\![\varphi]\!](z)\big|$$
$$+ \int_0^L T(z)\varphi(z)dz - \big[W(z)\varphi(z)\big]_{z=0}^{z=L}. \tag{27}$$

This functional is identical to $\Pi[\varphi]$ of Equation (11) except for the strain energy density U that has been substituted with its lower-convex envelope U^{**}, that is, the lower convex function which supports U from below. Observe that U^{**} is identified by the envelope of the lines that are tangent but not intersecting the graph of U and, for the cases shown in Figure 12, such envelope is delimited by those tangent lines which are parallel to the oblique asymptotes of U. Correspondingly, the graph of $U^{**\prime}$ presents a *horizontal plateau* in correspondence with the horizontal asymptote of U'.

As discussed at length by Royer-Carfagni [2001], the relationship between the original energy (11) and the relaxed energy (27) consists of the fact that minimizers φ^* of $\Pi[\varphi]$ enjoy the properties that $U^{**}(\varphi_a^{*\prime}(z)) \equiv U(\varphi_a^{*\prime}(z))$, $\forall z \in (0, L)$. In other words, the beam curvature $\chi^*(z) \equiv \varphi_a^{*\prime}(z)$ can only attain those values at which U coincides with its lower convex envelope U^{**}. This finding, first observed by Truskinovsky [1996], represents the natural extension to localized deformations of the well known Ericksen's problem of a tensile bar with nonconvex strain energy [Ericksen 1975]. In conclusion, solutions of the nonconvex minimization problem can be equivalently investigated by considering the associated *relaxed* minimization problem that, in the one-dimensional case, is obtained by substituting the strain energy function with its lower convex envelope.

In order to characterize the equilibrium states of the beam, one has to consider the conditions (18), (23) and (25). One of the main results due to Equation $(23)_3$, is that deformation paths made of stable equilibrium configurations cannot attain values of the bending moment outside the interval $[-M_0, M_0]$, whose extremities are defined by the levels of the horizontal asymptotes of the moment-curvature relationship. For the cases represented in Figure 11 it follows, in particular, that those parts of the linear elastic path passing through the origin that are outside the interval $[-M_0, M_0]$ are inaccessible via stable configurations and should be regarded as points of metastable equilibrium.

Now, let a beam be gradually strained according to the static scheme of Figure 2, corresponding to the Nakanishi experimental condition referred to in Section 1. The central portion A-B of the beam is uniformly bent, that is, $W_A = W_B \equiv \bar{M}$ and $q = 0$ in the scheme of Figure 13, so that Equation (20) holds. Imagine now that a closed loop control of the loading device allows to gradually increase the sag δ by controlling applied force $\bar{M}/a$ of Figure 2 (strain driven test), and consider the beam response for various forms of the M-χ constitutive relationships, of the type represented in Figure 11.

Consider first the case of part (a) of Figure 11, where the M-χ law is strain-hardening in type and the associated strain potential strictly convex. Then, whenever $\bar{M} < M_0$, by Equation (23) the rotation field $\varphi^*(z)$ must be absolutely continuous, that is, $\varphi_s^*(z) = \varphi_d^*(z) \equiv 0$. Consequently, the curvature is uniform and, by Equation (1), a unique value of the sag δ corresponds to each value of $\bar{M}$. According to Equation (25), strain localization in the form of concentrated rotations may occur when $\bar{M}$ reaches the threshold value M_0, but before reaching such a value the beam curvature has to become, at least in theory, infinite. In other words, whenever the constitutive relationship M-χ is monotonically increasing, the beam is bent with uniform curvature. Consequently, because of Equation (1), the experimental tests of Figure 1 should provide a M versus δ response that should be similar, at the qualitative level, to the M versus χ graph of Figure 11 in part (a). However, Nakanishi's results do not corroborate this finding.

As a second case, assume that the constitutive law of the bar is the one of part (b) of Figure 11. What should be observed now is that whenever the bending moment $\bar{M}$ satisfies $M_{\mathrm{II}} < \bar{M} < M_{\mathrm{I}}$, there are three values of the curvature that correspond to the same value of $\bar{M}$. In this situation, the characterization of minimizers is analogous to that recorded by James and Fosdick [1981], even if the energy they considered, though nonconvex, exhibited a superlinear growth at infinity that prevented the formation of singularities in the minimizing field. Introducing the Maxwell line $M = M_{\mathrm{M}}$ in the graph of the function $M(\chi)$ determined by the equal area rule as in part (a) of Figure 14 and the lower convex envelope of the potential $U(\chi)$ as in part (b), and recalling Equation (1), the $\bar{M}$-δ relationship resulting from the corresponding nonconvex minimization problem takes the form

$$\bar{M} = \begin{cases} M(8\delta/l^2), & \delta \leq \delta_A = \chi_A l^2/8, \\ M_{\mathrm{M}}, & \delta_A \leq \delta \leq \delta_B = \chi_B l^2/8, \\ M(8\delta/l^2), & \delta \geq \delta_B = \chi_B l^2/8. \end{cases}$$
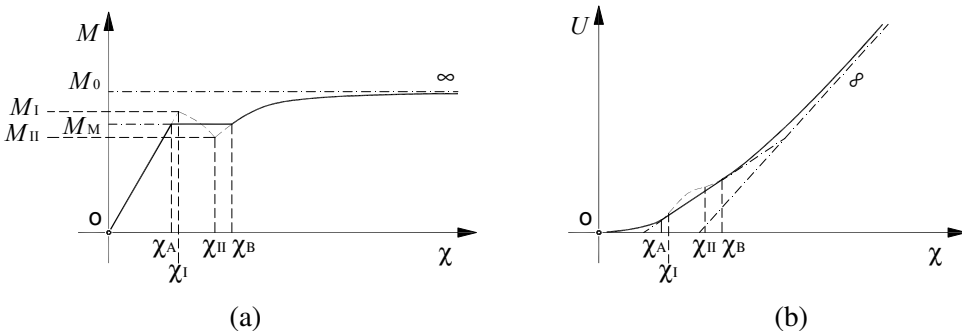

Figure 14. Equilibrium configuration path for case (b) in Figure 11: (a) M-χ relationship, (b) U-χ relationship.

In particular, similarly to phase transitions [Ericksen 1975], provided the test is strain driven, when $\bar{M} = M_M$ the beam curvature may take the constant value $\chi = \chi_A$ on a portion of length l_A and the constant value $\chi = \chi_B$ on a portion of length $l_B = l - l_A$ satisfying $8\delta_A/l \le \chi_A l_A + \chi_B l_B \le 8\delta_B/l$. Consequently, the $\bar{M}$-δ response exhibits a plastic plateau in correspondence of the Maxwell line, followed by a work-hardening branch. Likewise, in the previous case, by Equation (25) concentrated rotations may develop when $\bar{M}$ approaches M_0, but only after that the beam curvature has attained very large uniform curvatures. However, this response again does not match the experimental results of Figure 1.

The situation becomes more involved when the moment-curvature relationship $M(\chi)$ is as in part (c) of Figure 11. Clearly, when $\bar{M} \le M_{II}$ to each value of the bending moment corresponds one and only one value of the beam curvature. Therefore, the central portion A-B of Figure 2 becomes uniformly bent and, by Equation (1), the corresponding sag ends up being $\delta = M^{-1}(\bar{M})l^2/8$. Moreover, by Equation (23) one finds that stable equilibrium states must satisfy $0 \le \bar{M} \le M_0$. Consequently, any equilibrium configuration attaining the branches with $\bar{M} \ge M_0$ has to be considered metastable.

It should be noticed, however, that when $M_{II} \le \bar{M} \le M_0$ there are still three different values of the curvature which correspond to the same value of the applied bending moment. On the one hand, the second variation condition (26) rules out the possibility of attaining the strain softening branch, which corresponds to unstable equilibrium states. On the other hand, it is possible to find equilibrium states for which the beam curvature takes two distinct values, one in the interval $(\chi_I M_{II}/M_I, \chi_I M_0/M_I)$, that is, on the first linear elastic branch, the other in the strain hardening branch $(\chi_{II}, +\infty)$, both corresponding to the same value of the bending moment $\bar{M}$. In order to recognize if such states are of stable equilibrium, it is necessary to consider the relaxed problem and the minimization of the relaxed energy (27), obtained by introducing the lower convex envelope of the strain energy $U(\chi)$ in part (c) of Figure 12. The lower convex envelope is represented with bold face in part (b) of Figure 15 and the corresponding moment-curvature relationship $M(\chi)$, which follows the Maxwell line at $M = M_0$, in part (a) of Figure 15. The result is that curvatures attaining the branch $(\chi_{II}, +\infty)$ do not correspond to minimizers because $U(\chi) \ne U^{**}(\chi)$ when $\chi \in (\chi_{II}, +\infty)$ [Royer-Carfagni 2001]. In particular, Royer-Carfagni [2001] demonstrated that it would be possible to lower the energy by considering curvature in the branch $(0, \chi_A)$.
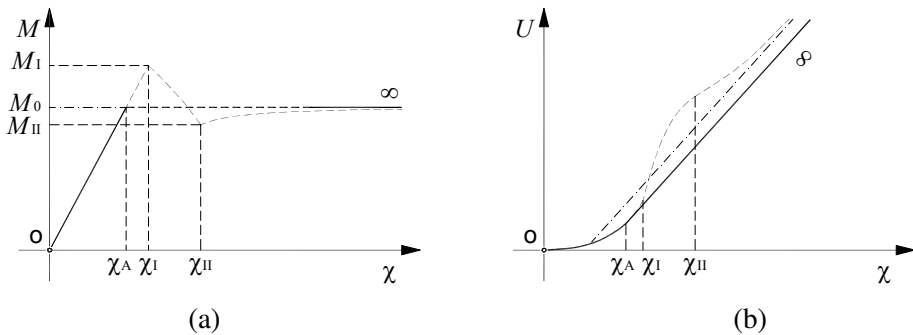
Figure 15. Equilibrium configuration path for case (c) of Figure 11: (a) M-χ relationship, (b) U-χ relationship.
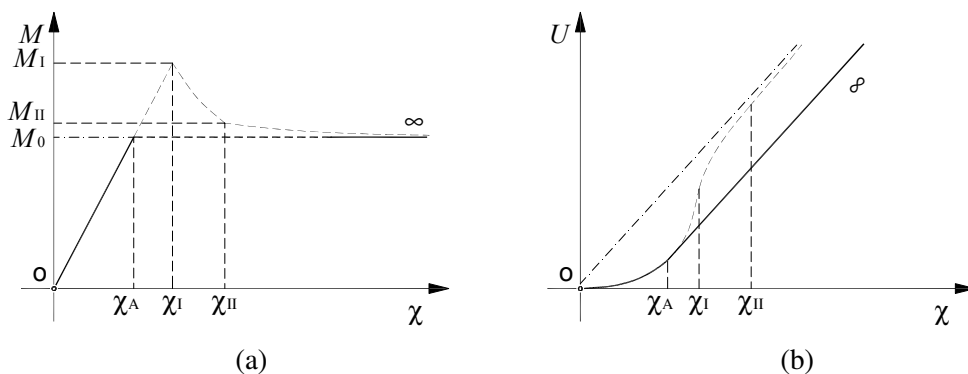
Figure 16. Equilibrium configuration path for case (e) of Figure 11: (a) M-χ relationship, (b) U-χ relationship.

In conclusion, when Equation (1) holds, the $\bar{M}$-δ relationship takes the form

$$\bar{M} = \begin{cases} M(8\delta/l^2), & \delta \leq \delta_{\mathrm{A}} = \chi_{\mathrm{A}} l^2/8, \\ M_{\mathrm{M}}, & \delta > \delta_{\mathrm{A}}. \end{cases} \tag{28}$$

It is important to remark that with a process similar to a phase transition when the moment approaches M_0, the strain is instantaneously localized at some point of the beam axis under the form of a concentrated rotation. At that point the curvature increases infinitely, and the corresponding kinematic characterization is analogous to the nucleation of a perfectly plastic hinge. One of the surprising results of this analysis is the predicted $\bar{M}$ versus δ response of Equation (28) matches surprisingly well with the diagrams of Figure 1. In particular, the plastic *plateau* has to be associated with the formation of a plastic hinge which may indefinitely increase the value of the sag δ while keeping fixed the value of the bending moment $\bar{M}$. Moreover, the apparent transition from an upper to a lower yield point in some of the diagrams of Figure 1 may be associated with the attainment of metastable equilibrium states which touch those points in the first linear elastic branch of Figure 15, above the threshold value $M = M_0$.

A similar response can be obtained when the bending moment-curvature relationship is of the type indicated in parts (d) or (e) of Figure 11. The main difference with the previous case (c) is that now
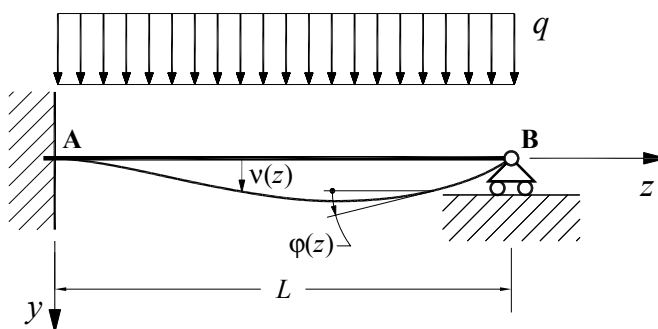
Figure 17. The propped cantilever layout.

there is no strain hardening branch for $\chi \geq \chi_{\mathrm{I}}$. Therefore, by Equation (23), stable equilibrium states can only attain the curvature interval $(\chi, \chi_{\mathrm{A}})$ when $\bar{M} < M_0$. Strain localization occurs at $\bar{M} = M_0$ and neither M_{I} nor M_{II} can be attained (see Figure 16). The form of the energy minimizers is analogous to that expressed in Equation (28).

5. The propped cantilever

To discuss a statically undetermined structure, let us consider the propped cantilever of Figure 17 under the uniform transverse load q. Such a problem has been already recorded in [Royer-Carfagni 2001; Del Piero 2003] for a particular form of a moment-curvature relationship, analogous to that of part (e) of Figure 11, but now the analysis is extended to the remaining cases of that figure. Obviously, if the material response is symmetric in tension and compression, the beam M-χ response is symmetric when the bending moment changes its sign. As a result, the properties of Figure 11 are extended symmetrically with respect to the origin in order to account for this possibility.

Let us briefly recall the main equations of [Royer-Carfagni 2001]. Keeping the notation of Section 4, and once more taking the rotation φ as the independent variable, the functional to be minimized is $\Pi[\varphi]$ of Equation (11) with $W(0) = W(L) = 0$. Using Equations (5) and (10), the boundary conditions $v(0) = v(L)$ give again Equation (12), to which the additional condition $\varphi(0) = 0$ has to be applied. If $\varphi^*(z) \in BV : [0, L] \to \mathbb{R}$ is a minimizer of $\Pi[\varphi]$, then considering the variation $\varphi^* + \varepsilon\psi$ with ψ satisfying Equation (13), one obtains again Equation (14) subject to the additional restriction $\psi(0) = 0$.

We now consider particular variations. First, let $d\psi = d\psi_a$, $d\psi_s = d\psi_d = 0$. Defining the bending moment $M^*(z)$ as in Equation (16), the first variation condition (15) gives, after an integration by parts analogous to Equation (17), the condition

$$d\Pi[\psi] = \int_0^L M^*(z)\psi_a'(z)dz + \int_0^L T(z)\psi_a(z)dz = \left[M^*(z)\psi_a(z)\right]_{z=0}^{z=L} + \int_0^L \left(-\frac{d}{dz}M^*(z) + T(z)\right)\psi_a(z)dz = 0.$$

Since the sign of ψ_a is not restricted and $\psi_a(0) = 0$, this is satisfied if and only if

$$M^*(L) = 0, \qquad -M^{*\prime}(z) + T(z) = \text{const.} \tag{29}$$

Evaluation of Equation $(29)_2$ at $z = 0$ gives $C = -M^{*\prime}(0) + T(0)$ or equivalently, using Equation (4), $C = -M^{*\prime}(0) + C_1$, where C_1 represents the vertical reaction at the clamped section A, considered positive if upwards oriented. Without loss of generality, assuming $C_1 = M^{*\prime}(0)$ gives $C = 0$. Then from Equations (4) and $(29)_2$, the equilibrium equations may be written as

$$-M^{*\prime}(z) + T(z) = 0, \quad T(z) = M^{*\prime}(0) - \int_0^z q(t)dt. \tag{30}$$

As a second case consider the variation $d\psi = d\psi_a + d\psi_s$, $d\psi_d = 0$. Defining J_+, J_-, and J_0 as in Equation (21), condition (15) yields

$$\int_0^L M^*(z)\psi_a'(z)dz + M_0\left(\int_{J_+} d\psi_s - \int_{J_-} d\psi_s + \int_{J_0} |d\psi_s|\right) + \int_0^L T(z)(\psi_a + \psi_s)dz$$

$$= \left[M^*(z)\psi_a(z)\right]_{z=0}^{z=L} + M_0\left(\int_{J_+} d\psi_s - \int_{J_-} d\psi_s + \int_{J_0} |d\psi_s|\right) + \int_0^L T(z)\psi_s(z)dz$$

$$= \left[M^*(z)\big(\psi_a(z) + \psi_s(z)\big)\right]_{z=0}^{z=L} + M_0\left(\int_{J_+} d\psi_s - \int_{J_-} d\psi_s + \int_{J_0} |d\psi_s|\right) - \int_0^L M^*(z)d\psi_s$$

$$= M_0\left(\int_{J_+} d\psi_s - \int_{J_-} d\psi_s + \int_{J_0} |d\psi_s|\right) - \int_0^L M^*(z)d\psi_s \geq 0,$$

where we have integrated by parts, used Equation $(30)_1$, and in the last line used the fact that $\psi_a(0) + \psi_s(0) = 0$ and $M^*(L) = 0$. Because of the arbitrariness of $d\psi_s$, this again yields condition (23).

Finally, assume a perturbation $d\psi = d\psi_a + d\psi_d$, $d\psi_s = 0$, with ψ_d of the form (24). If $[\![\varphi^*]\!](z_0) = 0$,

$$\int_0^L M^*(z)\psi_a'(z)dz + \int_0^L T(z)\big(\psi_a(z) + \psi_d(z)\big)dz + M_0\big|[\![\psi_d]\!](z_0)\big| \geq 0,$$

which, in view of Equation (30), gives

$$\left[M^*(z)\psi_a(z)\right]_{z=0}^{z=L} + \int_0^L \big(-M^*(z) + T(z)\big)\psi_a dz + \left[M^*(z)\psi_d(z)\right]_{z=0}^{z=L} - \int_0^L M^*(z)d\psi_d + M_0\big|[\![\psi_d]\!](z_0)\big|$$

$$= -M^*(z_0)[\![\psi_d]\!](z_0) + M_0\big|[\![\psi_d]\!](z_0)\big| \geq 0,$$

and, consequently, the condition $-M_0 \leq M^*(z_0) \leq M_0$. Otherwise, if $[\![\varphi^*]\!](z_0) \neq 0$, one obtains

$$\int_0^L M^*(z)\psi_a'(z)dz + \int_0^L T(z)\big(\psi_a(z) + \psi_d(z)\big)dz + M_0\big([\![\psi_d]\!](z_0)\big)\text{sgn}\big([\![\varphi^*]\!](z_0)\big)$$

$$= -M^*(z_0)[\![\psi_d]\!](z_0) + M_0\big([\![\psi_d]\!](z_0)\big)\text{sgn}\big([\![\varphi^*]\!](z_0)\big) \geq 0,$$

and, since $[\![\psi_d]\!](z_0)$ is arbitrary, condition (25) follows.

The complete characterization of minimizers of the energy functional (11) again requires the second variation inequality (26) and the additional condition coming from the relaxed energy functional (27), that is, the beam curvature $\chi^*(z) \equiv \varphi_a^{*\prime}(z)$ can only attain those values at which U and its lower convex envelope U^{**} coincide.

The detailed derivation of the solution follows that in [Royer-Carfagni 2001; Del Piero 2003]. The starting point is the equilibrium equation $(30)_1$. Considering Equation (4) from which we have $T(z) = qz + C_1$, the differential equation $(30)_1$ can be easily integrated and, by introducing the natural condition $M^*(L) = 0$, it provides the expected parabolic dependence of M^* upon z, that is,

$$M^*(z) = \tfrac{1}{2}q(L^2 - z^2) - C_1(L - z). \tag{31}$$

However, because of Equation (23), M^* can take values only within the admissible range $[-M_0, M_0]$. Such a state coincides with the equilibrium states of a properly defined elastic-perfectly plastic beams, for

which the plastic *plateau* is defined by the horizontal asymptotes of the M-χ curve. We notice that, due to the parabolic dependence of M^* on z, the first two equations of (23)) exclude the presence of plastic zones of finite length along the beam, so that if a plastic deformation occurs, it has to be concentrated at isolated points. In addition, condition (25) at the jump points of φ^* is analogous to that associated with a plastic hinge in the classical sense. Let us then consider, more in detail, the various possibilities.

Consider first the strain hardening M-χ law of part (a) of Figure 11. Assume that the load q and the constant C_1 in Equation (31) are such that $-M_0 < M^*(z) < M_0$. Then, by Equation (23) the rotation field $\varphi^*(z)$ is absolutely continuous, that is, $\varphi_s^*(z) = \varphi_d^*(z) \equiv 0$, and the corresponding curvature $\chi^*(z) \equiv \varphi_a^{*'}(z)$ can be found from the assumed M-χ constitutive relationship with Equation (31), as a function of C_1. The value of the constant C_1 is found by imposing Equation (12) and the boundary condition $\varphi(0) = 0$, and checking *a posteriori* that indeed $-M_0 < M^*(z) < M_0$. If the applied load q is gradually augmented, using the aforementioned procedure there will be a value of q such that $|M^*(z)|$ reaches first the threshold value M_0 at some point, say z_R, usually coinciding with the constrained extremity A of Figure 17. However, before reaching such a value, the beam curvature becomes infinitely large in a neighborhood of such a point. Further increasing the load q, the bending moment cannot increase any more at z_R, but the effect of the resultant rotation is that of producing a redistribution of the bending moments along the beam axis. Eventually, the threshold value M_0 is reached at a second point; infinitely large deflection of the beam may now occur because of the formation of a collapse mechanism.

As the second case, let the M-χ relationship be the one of part (b) of Figure 11. When $|M^*| < M_{\mathrm{II}}$, the rotation field $\varphi^*(z)$ and the value of the constant C_1 in Equation (31) can be found as already discussed. If q is further augmented, then in a certain portion of the beam axis $M_{\mathrm{II}} < |M^*| < M_{\mathrm{M}}$, being $M = M_{\mathrm{M}}$ the Maxwell line as part (a) of Figure 14. In this portion there are three values of the curvature that may correspond to the same value of the sectional bending moment, but minimizers of the energy can only take values on the first linear branch, that is, $|\chi^*| < \chi_{\mathrm{A}}$ because on this branch only the strain potential U of Equation (11) and its lower convex envelope U^{**} of Equation (27) coincide. Increasing q, then at some section, say again z_R, $|M^*(z_R)| = M_{\mathrm{M}}$. It is well known [Ericksen 1991] that in this case, analogously to a stress driven test, the beam curvature $|\chi^*(z_R)|$ jumps from the value χ_{A} to the value χ_{B} along the Maxwell line of part (a) of Figure 14. Increasing q, the bending moment also increases, but the beam curvature can never attain values in the interval $(\chi_{\mathrm{A}}, \chi_{\mathrm{B}})$. In other words, the moment-curvature relationship is that corresponding to the points where U and its lower convex envelope U^{**} coincide, represented as well in part (b) of Figure 14. Eventually, like the previous cases, Equation (25) tell us that concentrated rotations may develop at those sections where $|M^*|$ approaches M_0, but only after the beam curvature has reached very large uniform curvatures. The beam collapses when the threshold value M_0 is reached at two distinct sections of the beam.

When the M-χ relationship is that of part (c) of Figure 11, the rotation field $\varphi^*(z)$ and the constant C_1 in Equation (31) can be found as in the previous cases provided the load q is so small that $|M^*(z)| < M_{\mathrm{II}}$ for all $z \in (0, L)$, that is, when one and only one value of the beam curvature corresponds to each value of the bending moment. If q is increased so that $M_{\mathrm{II}} \le |M^*(z)| \le M_0$ for some z, then it is possible to find equilibrium states for which the absolute value of the beam curvature takes two distinct values, one in the interval $(\chi_{\mathrm{I}} M_{\mathrm{II}}/M_{\mathrm{I}}, \chi_{\mathrm{I}} M_0/M_{\mathrm{I}})$, that is, on the first linear elastic branch, and the other in $(\chi_{\mathrm{II}}, +\infty)$, both corresponding to the same value of the bending moment. Again, the possibility of attaining the strain softening branches is ruled out by the second variation condition (26). Moreover, consideration of the

relaxed energy (27), represented in this case in part(b) of Figure 15, implies that only the linear elastic branch can be attained by minimizers, because if $|\chi^*(z)| \in (\chi_{\mathrm{II}}, +\infty)$ then $U(\chi^*(z)) \neq U^{**}(\chi^*(z))$.

The process of formation of a plastic hinge deserves some comments (see [Royer-Carfagni 2001] for more details). Let us assume the beam is progressively loaded. Eventually, the bending moment approaches the limit thresholds M_0 (or $-M_0$) at some points. A further increase of q involves the instantaneous formation of a concentrated rotation, that is, the point representative of M and χ immediately reaches an infinite curvature corresponding to the point at infinity of the horizontal asymptotes of part (c) of Figure 11.

Indeed, neither the softening branches of the moment-curvature relationship nor bending moments in absolute value greater than M_0 are accessible via deformation paths made of stable equilibrium configurations. The beam collapses when the threshold value M_0 is reached at two distinct sections of the beam.

The beam response is very similar to the one just presented when the bending moment versus curvature relationship is of the type indicated in parts (d) or (e) of Figure 11 As discussed in Section 4, the main difference from case (c) is that now there is no strain hardening branch for $\chi \geq \chi_{\mathrm{I}}$. Therefore, by Equation (23) stable equilibrium states can only attain the curvature interval $(\chi, \chi_{\mathrm{A}})$ when $|M^*(z)| < M_0$. Strain localization occurs when $|M^*(z)| = M_0$ at a certain cross section; the value of the bending moment remains fixed at that section, while concentrated rotations are allowed. When q is further increased, this produces a redistribution of the bending moment along the beam axis until, eventually, M_0 is reached at another cross section and we achieve collapse.

6. Discussion and conclusions

The main result of this work consists in having observed that the notion of plastic hinge, usually referred to as an approximate or technical model in the classical plastic methods of structural analysis may be, as a matter of fact, more accurate than traditionally reputed. In the classical approach, when the material is modeled to be elastic-perfectly plastic and cross sections are assumed to remain planar in the deformation, the bending moment M is a monotonically increasing function of the beam curvature χ, asymptotically approaching, but never reaching, the full plastic moment M_0 as $\chi \to \infty$. Ingenious solution methods, such as the approach by Neal and Symonds in limit analysis [Neal 1963] have been developed under the simplifying assumption that the bending moment remains a linear function of the beam curvature up to the attainment of the full plastic moment, at which strain localization under the form of concentrated rotations of the beam axis may indefinitely occur; this is the so-called plastic hinge model. Traditionally, such methods are considered approximate since the transitory stage when the cross section is only partially yielded is neglected.

On the other hand, here we have shown that a response that matches the static-kinematic response of the plastic hinge model can be reproduced by maintaining the most classical Bernoulli–Navier hypothesis, that is, that cross sections remain planar in the deformation, but simply considering the stress jump from an upper to a lower yield point in the material stress-strain constitutive law. Indeed, such a jump is well evident in strain driven experimental tests [Froli and Royer-Carfagni 1999] and is responsible for the orderly formation of Lüder's bands [Froli and Royer-Carfagni 2000]. This jump is usually neglected in the elastic-plastic technical theories, but once it is considered, the moment-curvature relationship,

deduced under the same hypotheses of the classical theories of beams, exhibits a strain-softening branch, while the associated flexural strain potential becomes nonconvex and with oblique asymptotes. The nonconvex character of the potential, together with its linear growth at infinity, are sufficient to provoke a phenomenon presenting a strict similarity with a phase transition in the classical thermodynamic sense within the solid state itself: when a threshold value, coinciding with the value of the full plastic moment, is approached, the beam curvature exhibits a sudden transition. In particular, the beam cross section immediately passes from a state where it is completely elastic to a state where it is completely plasticized, and concentrated rotation may indefinitely occur while the cross sectional bending moment remains constant. In other words, the response predicted upon considering the dichotomy between the upper and lower yield points is surprisingly similar to that referred to as approximate in the technical theories. It should be recalled that the pioneering experimental observations by Nakanishi et al. [1934] seemed to confirm the approximate rather than the ideal response. As such, one may wonder why the results of such tests have been completely forgotten and are not mentioned, to the authors' knowledge, in the majority of famous treatises.

Unfortunately, the present analysis is to some extent limited by the variational approach, which presupposes the hypothesis of reversibility of deformation proper of holonomic plasticity, that is, inelastic unloading can only occur along the same loading path so that the possibility of irreversible unloading, following a path possibly different from the first loading branch, is ruled out. Thus, this approach is certainly not exhaustive and, in a certain sense, even unrealistic. Nevertheless, it certainly greatly facilitates the search of stable equilibrium configurations because they can be investigated as energy minimizers. For this goal recent results in the calculus of variations on space of functions allowing for discontinuities have been conveniently used. On the other hand, consideration of irreversible unloading would require a much more complicated treatment, at least from a mathematical point of view. In any case, although unloading remains the essential aspect of the problem on the side of the localizing damage band, for the case of stable bifurcation (at increasing load) it certainly plays no role for the initial postbifurcation response.

A definite attempt to compare the proposed theory with the experimental observations is still lacking at this stage. Unfortunately, the details of the experimental studies by Nakanishi have not been recorded in the literature so that, in order to investigate the process leading to the strain localization at the mesoscopic scale, an ad hoc experimental campaign is still needed. In particular, it will be important to evaluate the actual width of the plastic *hinge* in order to interpret the sectional (mesoscopic) consequences of strain localization. At the present time the theory seems to suggests that the thickness of the beam cross section may be considered the characteristic length scale of the elastic-plastic transition, but this is certainly a consequence of the orderly formation, at the microscale, of slip (Lüder) bands in a neighborhood of the yielded cross sections. The relationship between the complex phenomena occurring at the meso and microscale and their consequences in the macroscopic interpretation of the proposed theory are presently under investigation and will be the subject of further work.

Another possible criticism could be that the strain hardening branch in the stress-strain response, though well evident in the experiments, is not considered. The material is consequently assumed to be able to withstand indefinitely large strain at constant stress. However, our main goal here has been to show the (quite surprising in our opinion) consequences on the gross structural response of considering just a small stress jump in the constitutive relationship, while maintaining all the other hypotheses of the

classical structural technical theories. Indeed, it is the stress jump from the upper to the lower yield point that induces the peculiarities of the strain energy, that is, its nonconvexity and linear growth at infinity, and it is precisely this that allows for the possibility of sudden discontinuities in the rotation of the beam axis, with a process similar in kind to a phase transition.

References

[Buttazzo 1989] G. Buttazzo, *Semicontinuity, relaxation, and integral representation in the calculus of variations*, Pitman research notes in mathematics **207**, Longman, 1989.

[Cottrell 1953] S. Cottrell, Alan Haward, *Dislocations and plastic flow in crystals*, Claredon Press, Oxford, 1953.

[Del Piero 2003] G. Del Piero, "Structured deformation in plasticity", in *Proceedings of 16th AIMETA Congress*, Ferrara, 2003. In CD-ROM.

[Dunn and Fosdick 1980] J. E. Dunn and R. L. Fosdick, "The morphology and stability of material phases", *Arch. Ration. Mech. An.* **74**:1 (1980), 1–99.

[Ericksen 1975] J. L. Ericksen, "Equilibrium of bars", *J. Elasticity* **5**:3-4 (1975), 191–201.

[Ericksen 1991] J. L. Ericksen, *Introduction to the thermodynamics of solids*, Chapman and Hall, London, 1991.

[Froli and Royer-Carfagni 1999] M. Froli and G. Royer-Carfagni, "Discontinuous deformation of tensile steel bars: experimental results", *J. Eng. Mech. ASCE* **125**:11 (1999), 1243–1250.

[Froli and Royer-Carfagni 2000] M. Froli and G. Royer-Carfagni, "A mechanical model for elastic-plastic behavior of metallic bars", *Int. J. Solids Struct.* **37**:29 (2000), 3901–3918.

[James and Fosdick 1981] R. James and R. L. Fosdick, "The elastica and the problem of pure bending for a nonconvex stored energy function", *J. Elasticity* **11**:2 (1981), 165–186.

[Kolmogorov and Fomin 1975] A. N. Kolmogorov and S. V. Fomin, *Introductory real analysis*, Dover, New York, 1975.

[Müller and Villaggio 1977] I. Müller and P. Villaggio, "A model for an elastic-plastic body", *Arch. Ration. Mech. An.* **65**:1 (1977), 25–56.

[Nakanishi et al. 1934] F. Nakanishi, M. Ito, and K. Kitamura, "On the yield point of mild steel beams under uniform bending", *ARIR* **8**:104 (1934), 273–290. Also in *Selected papers by F. Nakanishi*, Department of Aeronautics, University of Tokyo Press, 1966.

[Neal 1963] B. G. Neal, *The plastic methods of structural analysis*, Wiley, New York, 1963.

[Royer-Carfagni 2001] G. Royer-Carfagni, "Can a moment-curvature relationship describe the flexion of softening beams?", *Eur. J. Mech. A Solid* **20**:2 (2001), 253–276.

[Truskinovsky 1996] L. Truskinovsky, "Fracture as a phase transition", pp. 322–332 in *Contemporary research in the mechanics and mathematics of materials*, edited by R. C. Batra and M. F. Beatty, CIMNE, Barcelona, 1996.

GIANNI ROYER-CARFAGNI: gianni.royer@unipr.it
Dipartimento di Ingegneria Civile, dell'Ambiente, del Territorio e Architettura, Università di Parma, Parco Area delle Scienze 181/A, I 43100 Parma, Italy

GIOVANNI BURATTI: g.buratti@ing.unipi.it
I.T.C.G. Campedelli, Castelnuovo di Garfagnana, Lucca, Italy
and
Dipartimento di Ingegneria Strutturale, Università di Pisa, 56126 Pisa, Italy

SHOCK-INDUCED DETONATION OF HIGH EXPLOSIVES BY HIGH VELOCITY IMPACT

J. K. CHEN, HSU-KUANG CHING AND FIROOZ A. ALLAHDADI

We investigate shock-induced detonation of high explosives confined in an open-ended steel cylinder by a normal impact to the cylindrical surface using three-dimensional finite element analysis. Three types of steel projectiles are considered: a cube, a sphere and a square plate. For the encased LX-17 explosive the calculated threshold impact velocities that lead to deflagration and detonation are higher for a sphere than for a cube of the same mass. It is found that detonation of the encased PBXN-110 explosive with the cubical projectile could occur immediately once a full reaction is initiated in the region near the impact site. The threshold detonation velocity is much lower for PBXN-110 than for LX-17. In addition, we discuss the threshold conditions of detonation predicted by different equations of state and failure models for the steel casing and projectile.

1. Introduction

When a confined explosive is impacted by a projectile with sufficiently high speed, the energy deposited into the explosive could cause thermal decomposition, and subsequently, initiation of explosion. The two initiation mechanisms are usually shock and shear, depending on the confinement of the explosive and impact conditions. In general, the induced reaction can be classified to be either low-order detonation (deflagration) or high-order detonation (prompt explosion). The latter can massively destroy the assembly of the explosive, whereas the former would merely damage the confinement.

High explosive safety is one of the most important research areas in the field of energetic materials. To meet the safety requirements, a no-reaction event, or at least deflagration, is desired and should be ensured so that no catastrophic accident will occur. Therefore, there is a need for understanding and reliably predicting dynamic response of confined explosives, such as a warhead impacted accidentally by high speed fragments. Although an experimental approach can offer the most accurate results, it is expensive, and sometimes, difficult in implementation due to too many scenarios of warhead design, storage of munitions, and operation deployment. Alternatively, a combined numerical simulation and experiment approach can achieve the goal with a much reduced cost. In this approach firing tests can be conducted with bare or confined explosives impacted by a projectile. Besides predicting the threshold deflagration and detonation conditions, the computer simulation can give detailed information of temporal and spatial impact-to-shock-to-deflagration-to-detonation transition that provides an insight for

understanding the complicated physical processes. Once the numerical solutions are validated with test results, the numerical tool can be used for the safety assessment of real armors.

A great number of numerical studies on detonation of high explosives by projectile impact have been reported so far. Most of them are performed at the coupon level – a projectile impacting onto a flat surface of a bare, front-covered, or totally confined high explosive. Bahl et al. [1981] first used a hydrocode with the nucleation and growth model to compute the threshold impact velocities for bare and slightly covered explosives. This was followed by other hydrocode simulations [Starkenberg et al. 1984; Cook et al. 1989; Chou et al. 1991]. Later, the projectile nose shape effects on impact-induced detonation of energetic materials were investigated [James et al. 1991; James et al. 1996; Peugeot et al. 1998; Cook et al. 2001; Shin and Lee 2003a; 2003b; 2003c]. It was found that the threshold detonation velocity is higher for a hemispherical nosed projectile than for a flat-end projectile. For the nose of projectiles with a relatively small cone angle, detonation could occur in a zone of the central axis [Shin and Lee 2003b]. Since all the studies above considered normal impact on the flat surface of bare or confined explosives, the analyses were carried out with either a one-dimensional or two-dimensional axisymmetric model.

On the other hand, only a few numerical investigations on shock initiation of armor are found in the open literature. Allahdadi et al. [1998] utilized the SPH method to simulate sympathetic detonation of an acceptor warhead caused by the impact of fragments resulting from a similar donor warhead. The SPH method was also used by Lattery et al. [2005] to model detonation of a warhead mockup impacted by different fragments. Davison [1997] adopted the AUTODYN hydrocode [Autodyn 2005] to calculate the threshold impact velocity for Octol 70/30 explosive initiation in a 6 inch warhead by a 50 caliber fragment.

In this paper we perform a three-dimensional finite element analysis to model dynamic response of a steel cylinder filled with an LX-17 explosive caused by high velocity projectile impact, using the AUTODYN hydrocode [Autodyn 2005]. The primary goal is to determine the threshold condition that causes detonation of the encased energetic material. Three different shape projectiles are considered: a cube, a sphere, and a square plate. Depending on the projectile investigated, either the threshold detonation velocity or the critical size of the projectile is calculated.

For comparison, shock-induced detonation of an encased PBXN-110 explosive by the cubical projectile impact is also studied. The resulting high rate deformation and perforation of the steel cylinder as well as the shock wave and burn fraction in the explosives are presented and discussed.

It should be pointed out that, due to the complicated physics phenomena involved in the high velocity impact, the computational results presented herein may hinge on the choice of material models. To this end, we also adopt two different equations of state and three failure models in the analysis. The results are compared in terms of threshold detonation.

The paper is organized as follows. Section 2 briefly describes the ignition and growth model for shock detonation of solid explosives, the equation of state for unreacted solid explosives and the reacted gaseous product, and the constitutive models for structural response of the steel casing and projectiles. In Section 3 two different sets of two-dimensional finite element models are studied for generating adequate three-dimensional finite element models for the present numerical analysis. In Section 4 three-dimensional simulations of the shock-to-deflagration-to-detonation transition of the explosives caused by high velocity impact are presented. Conclusions are drawn in Section 5.

2. Material models

A mockup consisting of an open-ended steel cylinder filled with an LX-17 or PBXN-110 explosive subjected to steel projectiles is considered in this work. To describe the expansion and detonation of the explosives, the Lee–Tarver ignition and growth model [Lee and Tarver 1980] is employed. As with the forest fire model [Forest 1978], the Lee–Tarver model is based on the assumption that ignition starts at local hot spots and grows outward from these sites. The reaction rate for the conversion of unreacted explosive to gaseous product is given by

$$\frac{\partial F}{\partial t} = I(1-F)^b\left(\frac{\rho}{\rho_o}-1\right)^x + G(1-F)^c F^d p^y, \tag{1}$$

where F is the reaction ratio, p is the pressure, ρ_0 and ρ are the initial and current densities, respectively, and I, b, x, G, c, d, and y are constants.

Both the unreacted solid and the reacted gaseous product of LX-17 explosive are characterized with the Jones–Wilkins–Lee (JWL) equation of state [Lee et al. 1968]. The pressure in either phase is defined in terms of volume and internal energy as

$$p = A\left(1-\frac{\omega}{R_1 V}\right)e^{-R_1 V} + B\left(1-\frac{\omega}{R_2 V}\right)e^{-R_2 V} + \frac{\omega e}{V}, \tag{2}$$

where $V = \rho/\rho_o$ is the relative volume, e is the internal energy, and A, B, R_1, R_2, and ω are constants. The values of the above constants for a reacted gaseous product are different from those for the unreacted solid explosive.

For the PBXN-110 explosive the JWL equation (2) is employed for the reacted gaseous product while the Mie–Gruneisen form of equation of state is used for the unreacted solid, which is given by

$$p = p_H + \Gamma\rho(e-e_H), \quad p_H = \frac{\rho_0 c_0 \mu(1+\mu)}{[1-(s-1)\mu]^2}, \quad e_H = \frac{p_H}{2\rho_0}\left(\frac{\mu}{1+\mu}\right), \quad \rho\Gamma = \rho_0\Gamma_0, \quad \mu = \frac{\rho}{\rho_0}-1, \tag{3}$$

where Γ_0, c_0, and s are constants.

Both the cylinder and all the projectiles are modeled as 4340 steel. With the high impact pressure and the blast force resulting from explosive detonation, the shock equation of state for most metals [Meyers 1994] and the Johnson–Cook plasticity model [Johnson and Cook 1983] that accounts for the effects of strain hardening, strain-rate hardening, and thermal softening are adopted to describe the dynamic response of the steel. They are expressed as

$$U = c_0 + s u_p, \qquad Y = \left[A_0 + B_0\varepsilon_p^n\right]\left[1 + C_0 \log \dot{\varepsilon}_p^*\right][1 - T^*], \tag{4}$$

where U and u_p are the shock and particle velocities, respectively, Y is the yield stress, ε_p is the effective plastic strain, $\dot{\varepsilon}_p^* = \dot{\varepsilon}_p/\dot{\varepsilon}_p^0$ is the normalized effective plastic strain rate, $T^* = (T - T_{\text{room}})/(T_{\text{melt}} - T_{\text{room}})$ is the homologous temperature, and A_0, B_0, C_0, m, and n are constants.

The values of the material parameters in Equations (1)–(3) for the LX-17 and PBXN-110 explosives and in Equation (4) for the 4340 steel used in the present analysis are given in Tables 1 and 2, respectively.

Material Constants	LX-17	PBXN-110
ρ_0 (g/cm^3)	1.905	1.67
I (/μs)	50	33
b	0.222	0.667
x	4.0	4.0
G	500	600
c	0.222	0.667
d	0.667	0.222
y	3	3
A_r (Mbar)	6.5467	4.69924
B_r (Mbar)	0.071236	0.00106
$R_{1,r}$	4.45	3.86
$R_{2,r}$	1.2	1.0
ω_r	0.35	0.40
A_u (Mbar)	778.09999	
B_u (Mbar)	−0.05031	
$R_{1,u}$	11.3	
$R_{2,u}$	1.13	
ω_u	0.8939	
Γ_0		0.8
c_0		0.199
s		3.05

Table 1. Material constants in Equations (1)–(3) for the Lee–Tarver ignition and growth model, JWL equation and shock EOS for LX-17 [Tarver and Hallquist 1981] and PBXN-110 [Miller 1996] explosives. Subscripts u and r denote the unreacted explosive and reacted product, respectively.

Shock EOS		JC plasticity model		JC damage model	
ρ_0 (g/cm^3)	7.83	A_0 (Mbar)	0.0051	D_1	0.05
Γ_0	2.17	B_0	0.26	D_2	3.44
c_0	0.4569	C_0	0.014	D_3	−2.12
s	1.49	m	1.03	D_4	0.002
		T_{melt} ($^{\text{o}}$K)	1793	D_5	0.61

Table 2. For 4340 steel, values of material constants used in Equation (4) for the shock EOS [Meyers 1994] and the Johnson–Cook plasticity model [Johnson and Cook 1983], and in Equation (6) for the Johnson–Cook damage model [Johnson and Cook 1985]. Shear modulus is 0.818 mbar.

3. Computational modeling

A schematic sketch for the mockup impacted by a cubical projectile is depicted in Figure 1. The open-ended steel cylinder is 10 cm long and 0.9525 cm thick; the encased explosive is 6.6675 cm in radius. The projectile is assumed to strike normally on the cylindrical surface at time $t = 0$ and directly toward the centroid of the mockup. For convenience, we use a rectangular Cartesian coordinate system with origin located at the centroid of the mockup and the z-axis parallel to the axial axis. Thus, the central line of the projectile trajectory is along the positive x-axis.

The shock-induced detonation of the confined explosives by the steel projectile impact is simulated with the AUTODYN finite element processor. To ensure the accuracy of the three-dimensional numerical solutions, analyses with two sets of plane strain finite element models, namely, two-dimensional case I and two-dimensional case II, are first performed for the convergence study. The former is selected for the circular cross-section of the mockup at $z = 0$, and the latter is selected for the rectangular cross-section perpendicular to the y-axis at $y = 0$. We chose the two cross-sections for the convergence study because the most severe deformation is present in these areas. Due to the symmetry of the structural geometry and the impact loading, only half of each cross-section is analyzed. Each finite element model includes the corresponding two-dimensional portion of the cubical projectile of 7 g. For plotting the time history of the desired variables, points A and B in the explosive are assigned at $(-6.2, 0, 0)$ cm and $(-6.6675, 0, 0)$ cm, respectively. Point B is the intersection point between the central line of the projectile trajectory and the cylindrical interface between the casing and explosive.
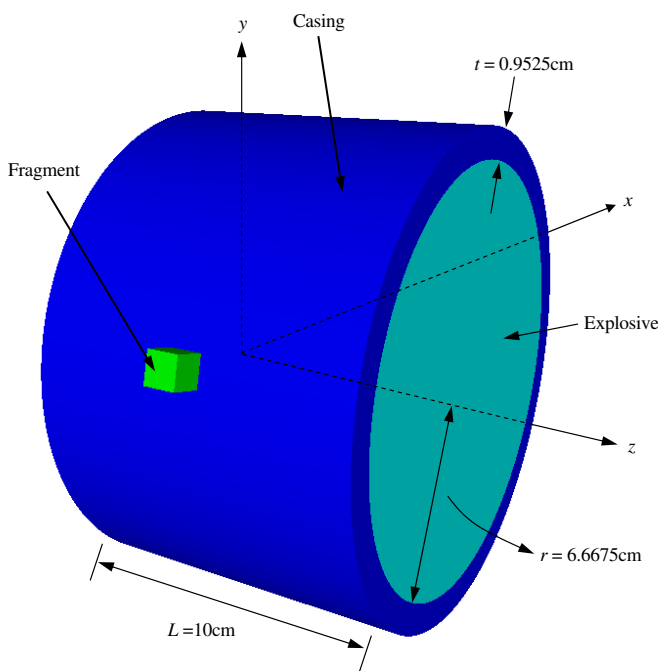

Figure 1. Schematic sketch of a mockup impacted by a single projectile.
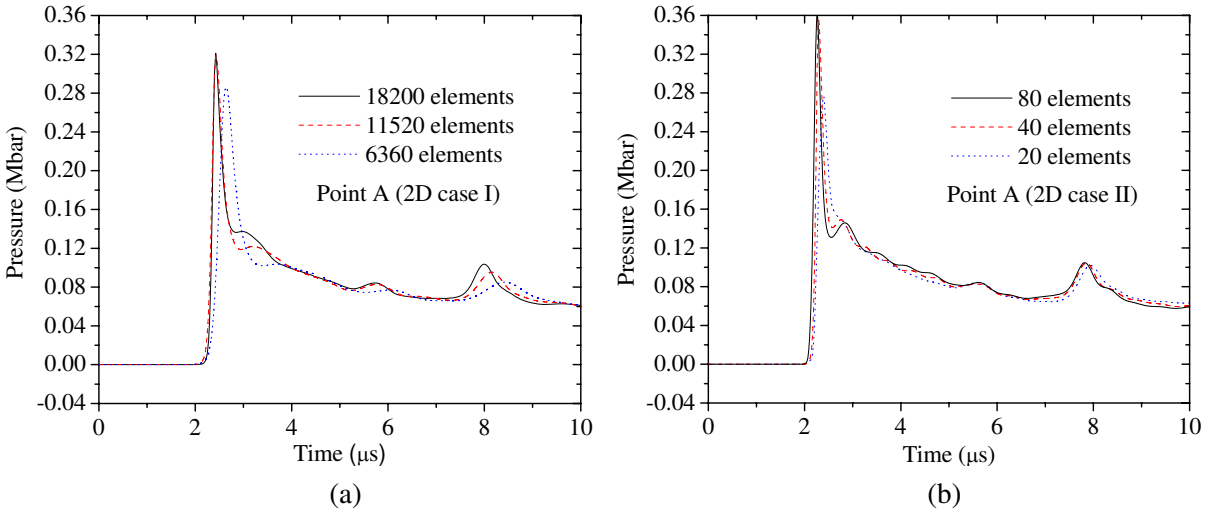
Figure 2. Time histories of the shock pressure at point A computed with different mesh densities for (a) two-dimensional case I and (b) two-dimensional case II; the impact velocity is 3.0 km/s.

Figure 2(a) shows the time history of shock pressure p at point A caused by the 7 g cubical projectile impact at a speed of 3.0 km/s, calculated with three different meshes for the two-dimensional case I. It appears that the results obtained with the finite element models of 11,520 and 18,200 elements are close to each other, thereby indicating that the mesh of 11,520 elements is sufficient to discretize the circular cross-section. For the two-dimensional case II, the number and size of the elements along the x-axis are identical to those in the mesh of 11,520 elements tested in the two-dimensional case I. The nodes along the z-direction are nonequally spaced with a smaller spacing for those located near the x-axis. Comparing the results in Figure 2(b) shows no appreciable difference in pressure at point A between the two models in which 40 elements and 80 elements are meshed in the axial direction. Therefore, the mesh with the 40 elements in the z-direction is adequate for the discretization of the model.

The mesh of 11,520 elements for the circular cross-section at $z = 0$ and the one with 40 elements in the z-direction for the rectangular cross-section perpendicular to the y-axis at $y = 0$ are the two bases in constructing the adequate three-dimensional finite element models. Figure 3 depicts a three-dimensional model generated for a quadrant of the mockup and the cubical projectile, in which a total of 461,824 elements are employed. It is used in the simulations of the mockup impacted by the cubical projectile in Sections 4.1 and 4.4. When the other shape projectiles are studied, only the projectile portion of the finite element model is modified.

During the calculation, some of the elements may become grossly distorted. A so-called erosion criterion is adopted to remove such elements from the analysis. This criterion considers an element to have failed if a predefined strain such as the instantaneous geometrical strain or the effective plastic strain exceeds a specified limit. In this study an element is removed when the instantaneous effective
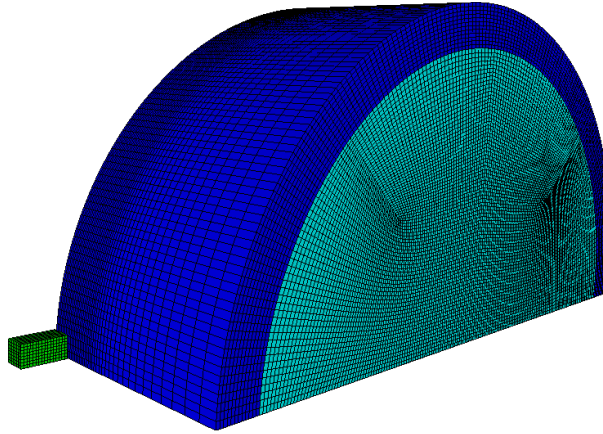
Figure 3. Three-dimensional finite element model for mockup impacted by a 0.96 cm cubical steel projectile.

geometrical strain $\bar{\varepsilon}_{\text{eff}}$ 250%. $\bar{\varepsilon}_{\text{eff}}$ is defined as the integral of the incremental effective geometric strain

$$\bar{\varepsilon}_{\text{eff}} = \int \Delta \bar{\varepsilon}_{\text{eff}} dt, \qquad \Delta \bar{\varepsilon}_{\text{eff}} = \Delta t \sqrt{\tfrac{2}{3}\left(\dot{\varepsilon}_{xx}^2 + \dot{\varepsilon}_{yy}^2 + \dot{\varepsilon}_{zz}^2 + \dot{\varepsilon}_{xy}^2 + \dot{\varepsilon}_{yz}^2 + \dot{\varepsilon}_{zx}^2\right)},$$

where $\dot{\varepsilon}_{ij}$ are the strain rates and Δt the time increment.

4. Results and discussion

The shock-induced detonation of LX-17 explosive studied in Sections 4.1–4.3 is for the impact by the three different shapes of projectile, and the PBXN-110 explosive studied in Section 4.4 is for the impact by the cubical projectile. Depending on the projectile investigated, either the threshold detonation velocity or the critical size of the projectile is determined.

4.1. *Impact by a 7 g cubical steel projectile.* This case is to determine the threshold impact velocities that leads to deflagration and detonation of the encased LX-17 explosive by the 7 g cubical steel projectile of 0.96 cm on each side. To do so, successive numerical analyses are performed by varying impact speeds.
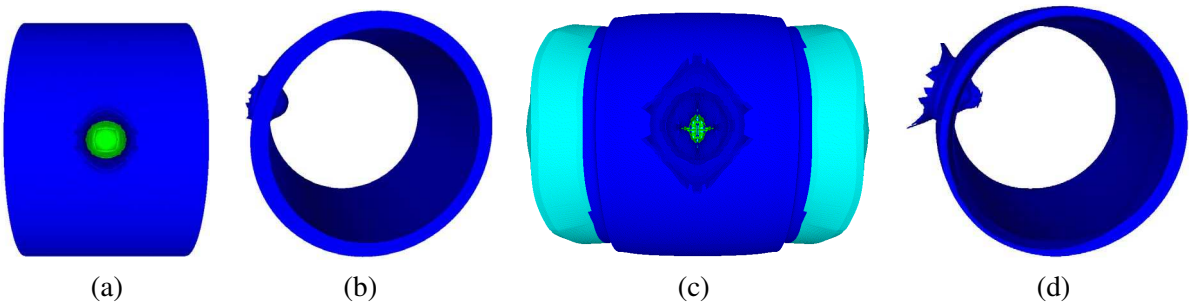

| (a) | (b) | (c) | (d) |

Figure 4. Mockup, cubical fragment and deformed outer casing at $t = 20\,\mu$s; (a,b): $V_p = 2.3$ km/s and (c,d): $V_p = 4.6$ km/s.

First, dynamic behaviors of the steel casing and the encased explosive are investigated for two simulated impact velocities, $V_p = 2.3$ km/s and 4.6 km/s. Figure 4 shows the configurations of the mockup and projectile as well as the deformation of the casing at $t = 20\,\mu$s. Apparently, the structural and explosive responses respectively are quite different between the two impact speeds. The rapid expansion of the explosive outward from both ends of the cylinder shown in Figure 4(c) for the impact at $V_p = 4.6$ km/s indicates that the explosive is undergoing a violent detonation. On the other hand, for the lower impact velocity of 2.3 km/s there is no discernible expansion of the explosive (Figure 4(a)) but a crater-like damage in the steel casing (Figure 4(b)). The overall damage to the casing is not so severe as that caused by the impact speed of 4.6 km/s, for which not only the casing is perforated, but the outer rim of the crater buckles as well; see Figure 4(d). Accordingly, it can be deduced that the threshold detonation speed of the encased LX-17 explosive must lie in between 2.3 km/s and 4.6 km/s.

Figure 5(a) compares the time histories of burn fraction α at point A for four impact speeds ranging from 2.3 km/s to 4.6 km/s. For the speed of 2.3 km/s the burn fraction is quite small, only about 2.5%. This confirms the statement made previously that the explosive is not fully ignited yet. As the speed increases to 3.8 km/s, the explosive at point A accounts for about 92% of burn fraction. It then fully reacts ($\alpha = 1$) at 3.9 km/s. This suggests that the speed of the 7 g cubical steel projectile be at least about 3.9 km/s for full ignition. The corresponding shock pressures at point A are given in Figure 5(b). For all four impact speeds a sharp pressure spike is present while the shock wave is passing through point A. As expected, the strength of the shock wave increases as the impact velocity increases. It is worth noting that the maximum shock pressure induced by the impact at 3.9 km/s is 0.325 Mbar, which is the minimum pressure needed for the LX-17 explosive to fully react. The fact that the peak pressure at point B shown in Figure 5(b) is higher than 0.325 Mbar reveals that for the impact velocity 4.6 km/s the detonation
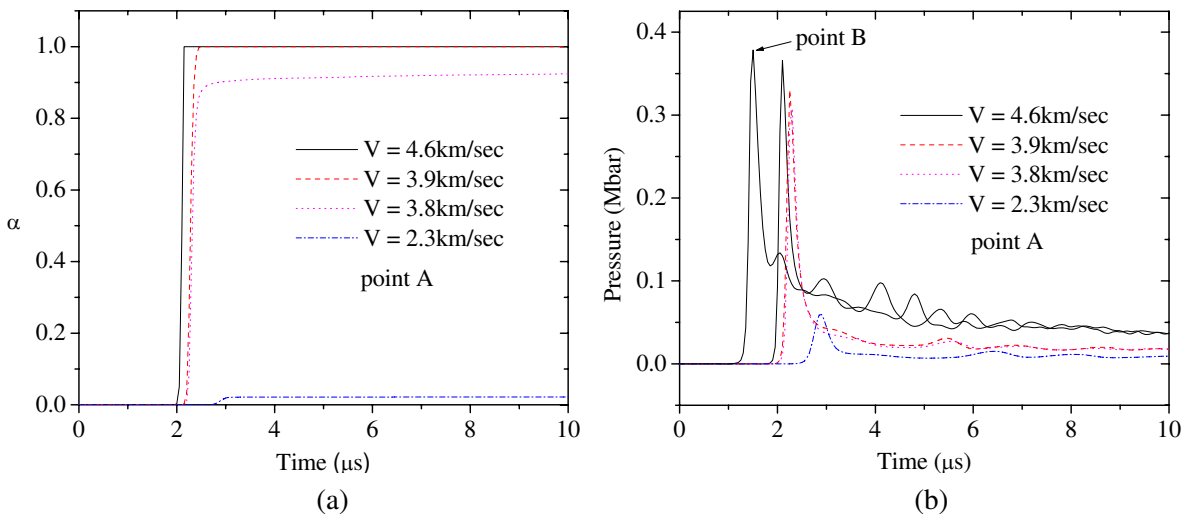

Figure 5. Time histories of (a) burn fraction and (b) shock pressure at point A $(-6.2, 0, 0)$ cm for four impact velocities; the shock pressure at point B $(-6.6675, 0, 0)$ cm for $V_p = 4.6$ km/s is also included in (b).

directly results from the pressure transmitted from the impact. Recall that point B is the intersection point between the central line of the projectile trajectory and the cylindrical interface between the steel casing and explosive.

Although the critical impact velocity for full reaction at a point such as, for example, A has been identified, initiation of explosion may not be claimed unless the succeeding pressure is strong enough to sustain the fast growth of detonation. During the shock wave propagation in a reactive material two processes are competing with each other for the shock strength. One is the rarefaction of the stress wave that is transmitted from the impact, and the other is the buildup of gas pressure from partial and/or full reaction of the solid explosive. If the latter prevails over the former, the shock wave will be amplified and, in turn, will lead to detonation after it travels a certain distance in the explosive. Otherwise, the shock wave will become weaker and weaker, and eventually will lose its ability to react with the explosive charge.

Continuing our numerical search for high-order detonation Figure 6 shows shock wave propagation in the circular cross-section at $z = 0$ for the impact speed of 4.4 km/s at $t = 3\,\mu s$, $5\,\mu s$, $10\,\mu s$, and $20\,\mu s$. It is clearly seen that the shock wave continues rarefying as it propagates outward radially from the impact region. A different shock wave evolution resulting from for the impact speed 4.5 km/s is shown in Figure 7. Early on the shock waves generated by the two impact speeds are similar and the peak pressures are also close. For example, at $t = 2\,\mu s$ the peak pressures are 0.364 Mbar caused by the impact at 4.4 km/s and 0.365 Mbar by 4.5 km/s. Similar results are seen in Figures 6(a) and 7(a) for $t = 3\,\mu s$. At later times, however, the shock wave induced by the impact speed of 4.5 km/s not only is intensified continuously, but its profile changes as well; see the rest of Figure 7. The strengthening of the shock wave implies that the buildup of the gas pressure is the dominating mechanism for this case. As indicated in Figure 7(c), the shock wave front hits the interface between the explosive and the casing at about $12\,\mu s$.

Afterwards, parts of the shock wave are reflected from both the top and low interfaces and then travel back to the impact side along the cylindrical interface, while the rest part of the wave continues moving toward the other side at $x = 6.6675$ cm. The two shock waves that travel back to the impact side interfere with each other after they reflect from the interface near the impact site. As a result of the constructive interference, the strength of the superposed shock wave in the vicinity of the x-axis increases; see Figures 7(e) and (f).

The burn fraction α is an indicator for explosive detonation, with which an explosive is said to be fully reacted when $\alpha = 1$, inert when $\alpha = 0$, and partially reacted when $0 < \alpha < 1$. Figure 8 displays the burn fraction distribution over the circular cross-section at $z = 0$ for the two impact speeds 4.4 km/s and 4.5 km/s at four different instants, $t = 5\,\mu s$, $10\,\mu s$, $15\,\mu s$ and $20\,\mu s$. At $t = 2\,\mu s$ the maximum burn fraction is 0.15 for the impact speed of 4.4 km/s and 0.23 for 4.5 km/s, occurring near point B. For both speeds the onset of the full reaction starts sometime in between $2\,\mu s$ and $3\,\mu s$. It is clearly visible in Figures 8(a)–(d) for the impact speed of 4.4 km/s that the explosive only deflagrates since the reaction does not grow, but is instead confined to a small volume. For the impact speed of 4.5 km/s, however, a full reaction rapidly grows and spreads as illustrated by the evolved contours of the burn fraction shown in Figures 8(e)–(h). The entire cross-section detonates at about $t = 20\,\mu s$, when the reflected shock waves superpose at the x-axis. The average detonation rate in the x-direction estimated from Figures 8(f) and (g) for the time interval $t = 10\text{-}15\,\mu s$, for instance, is about 0.752 cm/μs.

Figure 6. Shock wave propagation in the explosive circular cross-section at $z = 0$ for impact speed of 4.4 km/s for $t =$ (a) $3\,\mu$s, (b) $5\,\mu$s, (c) $10\,\mu$s, (d) $20\,\mu$s.

The results above indicate that for the open-ended steel cylinder of 10 cm in length and 0.9525 cm in thickness filled with the LX-17 explosive of 6.6675 cm in radius under a normal impact to the cylindrical surface by a 7 g cubical steel projectile, the simulated threshold impact velocity is 3.9 km/s for deflagration and 4.5 km/s for detonation.

4.2. *Impact by a spherical steel projectile of 7 g.* For comparison we discuss the detonation of the same mockup induced by a spherical projectile of the same mass as the cubical one, namely, 7 g. The calculated threshold velocity is about 4.5 km/s for deflagration and about 4.8 km/s for detonation. Both threshold velocities are higher than those found for the cubical projectile. The resulting shock waves are similar to those in Figure 7 for the cubical projectile; we omit them for brevity. The higher threshold detonation
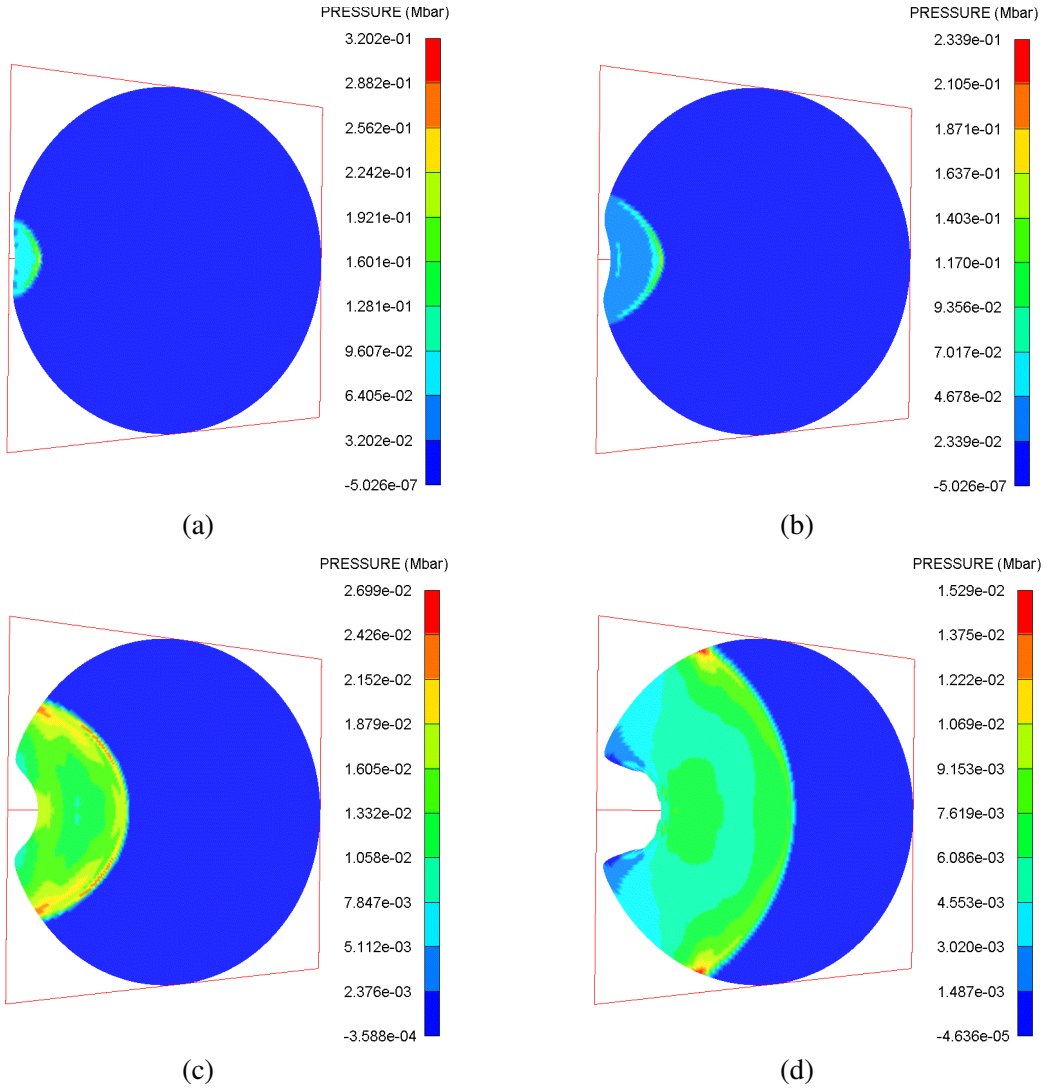
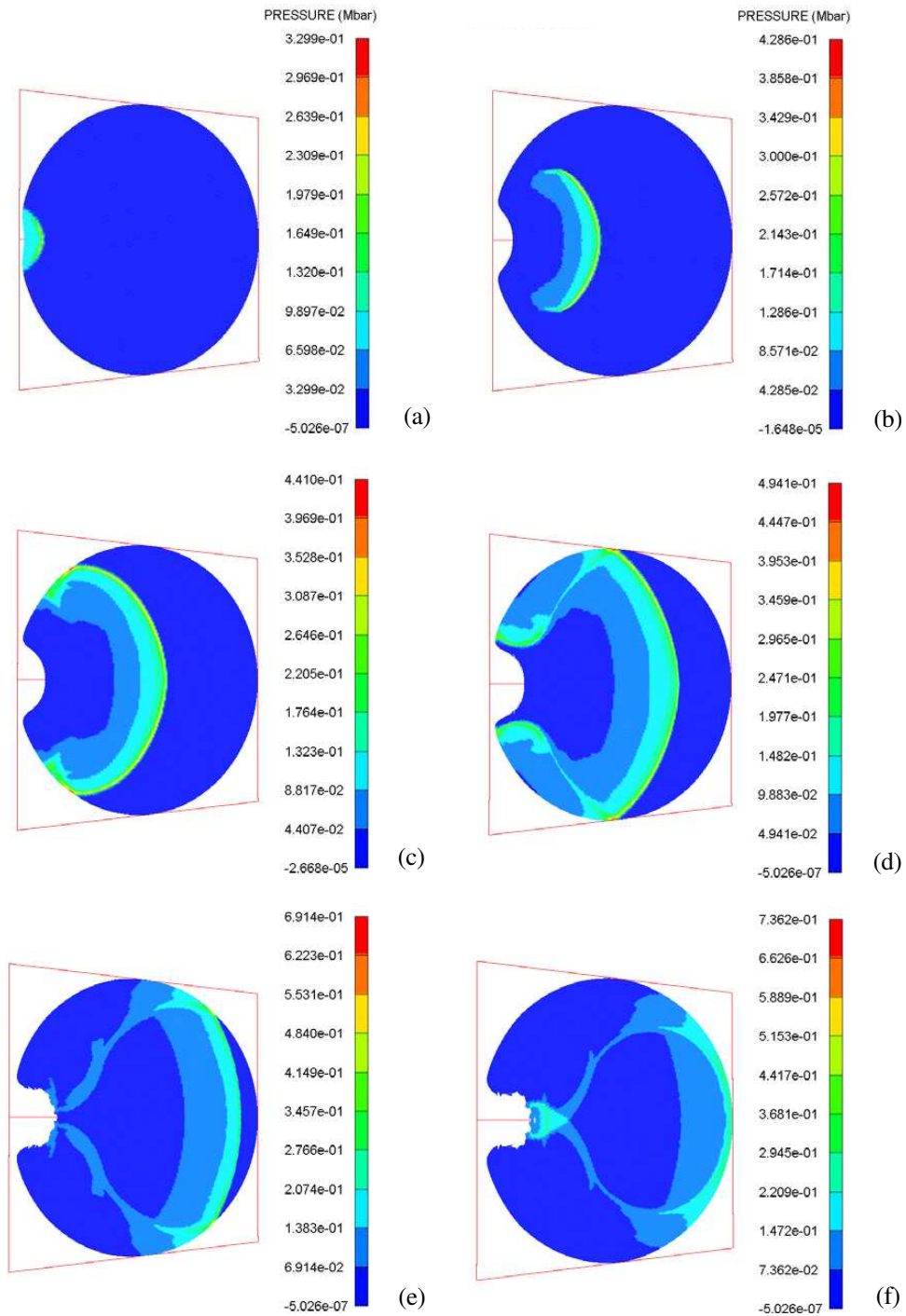**Figure 7.** Shock wave propagation in the explosive circular cross-section at $z = 0$ for impact speed 4.5 km/s for $t =$ (a) 3 μs, (b) 9 μs, (c) 12 μs, (d) 15 μs, (e) 18 μs, (f) 20 μs.
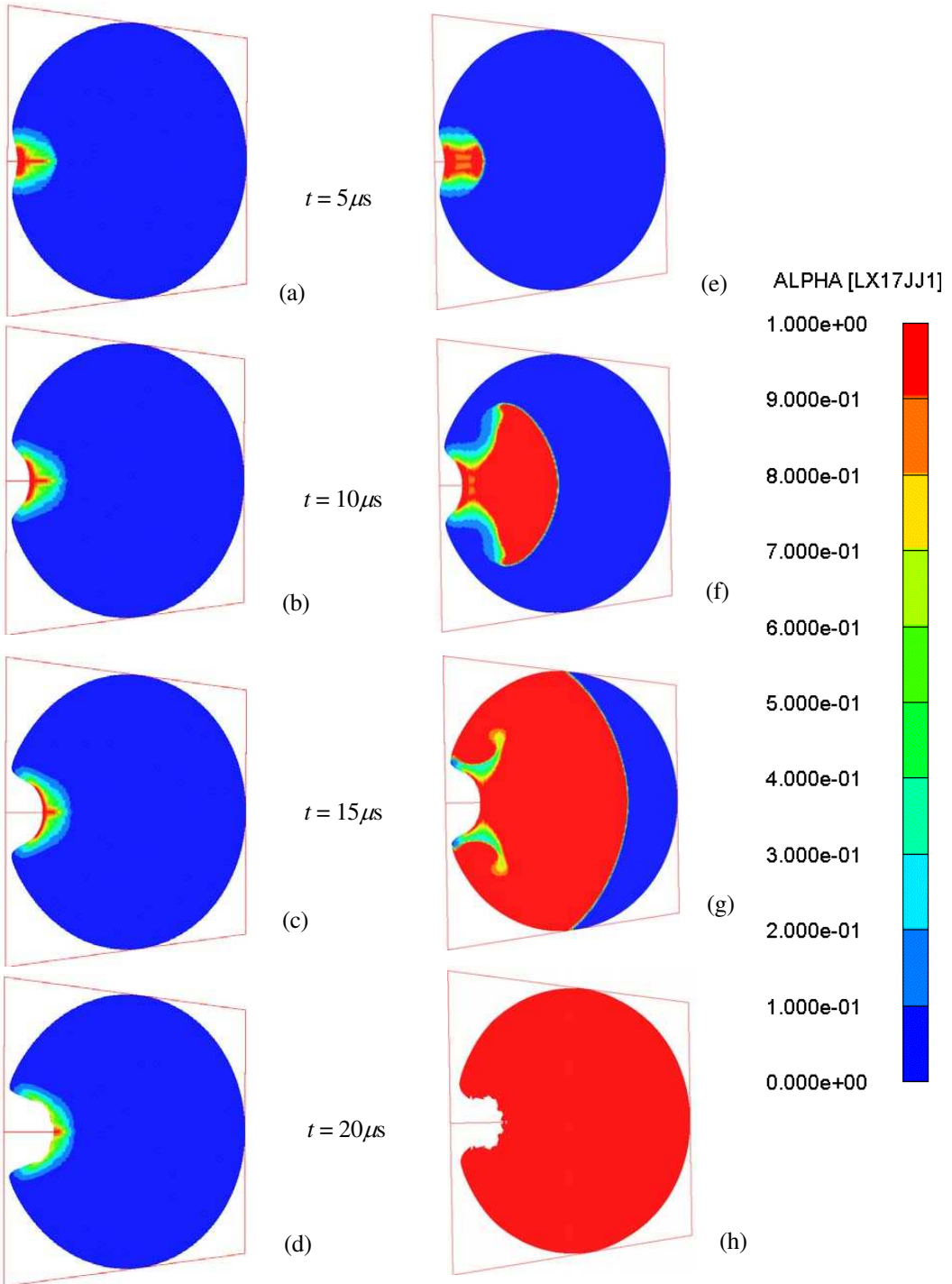
Figure 8. Burn fraction of the explosive in the circular cross-section at $z = 0$ at $t = 5$ μs, 10 μs, 15 μs and 20 μs; (a-d): $V_p = 4.4$ km/s and (e-h): $V_p = 4.5$ km/s.

velocity for the spherical projectile found here is consistent with those found for the projectiles impacting on a flat surface of a bare, front-covered, or totally confined high explosive [Hull et al. 2002].

4.3. *Impact by a square plate at constant velocity of 2.3 km/s.* Here we study the detonation of the encased LX-17 explosive caused by a square plate projectile of thickness 0.96 cm, same as the cubical projectile. The impact speed is kept constant at 2.3 km/s. The aim is to determine the threshold detonation in-plane dimensions of the plate. Successive numerical simulations are performed with the three-dimensional finite element models modified according to the change of the in-plane dimensions of the square plate.

Figure 9 shows the deformed configurations of the mockup at $t = 20 \, \mu$s simulated for the impact by two projectiles with the in-plane square dimensions of 1.73 cm and 1.74 cm, respectively. Prompt detonation caused by the latter is evidenced by the significant, rapid expansion of the explosive in Figure 9(b), while the former may only cause deflagration as per the inconsequential expansion indicated in Figure 9(a). The burn fractions in the circular cross-section of the explosive at $z = 0$ shown in Figure 10 further verify the above conjecture. The widths of the crater in and the regions of the reaction of the explosive are slightly larger than those found in the case of the cubical projectile due to the larger in-plane size, but otherwise the evolutions of the explosive reaction are similar. The lower threshold detonation velocity for a wider projectile of the same thickness as the cubic projectile calculated here is as expected.

4.4. *PBXN-110 explosive impacted by a 7 g cubical steel projectile.* Figure 11 depicts the burn fractions in the encased PBXN-110 explosive at $t = 20 \, \mu$s caused by the 7 g cubical steel projectile for the impact velocities of 2.9 km/s and 3.0 km/s. The explosive does not fully react when impacted by the cube at 2.9 km/s, since the maximum burn fraction is 0.927. It is interesting to note, however, that as we increase the impact speed by only 0.1 km/s to 3.0 km/s, violent detonation now occurs. Besides the lower threshold detonation velocity (3.0 km/s here versus 4.5 km/s for the LX-17 explosive), the direct shock-to-detonation transition found here is different than the shock-to-deflagration-to-detonation transition found for the LX-17 explosive in Section 4.1.

(a)   (b)
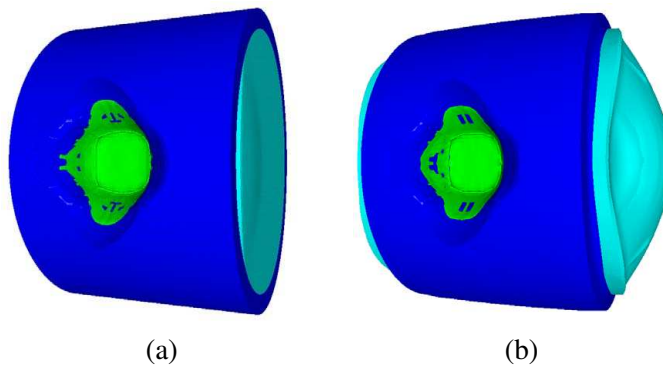
Figure 9. Mockup and projectile at $t = 20 \, \mu$s resulting from impact of two flat projectiles with $V_p = 2.3$ km/s; (a) 1.73 cm × 1.73 cm × 0.96 cm and (b) 1.74 cm × 1.74 cm × 0.96 cm.
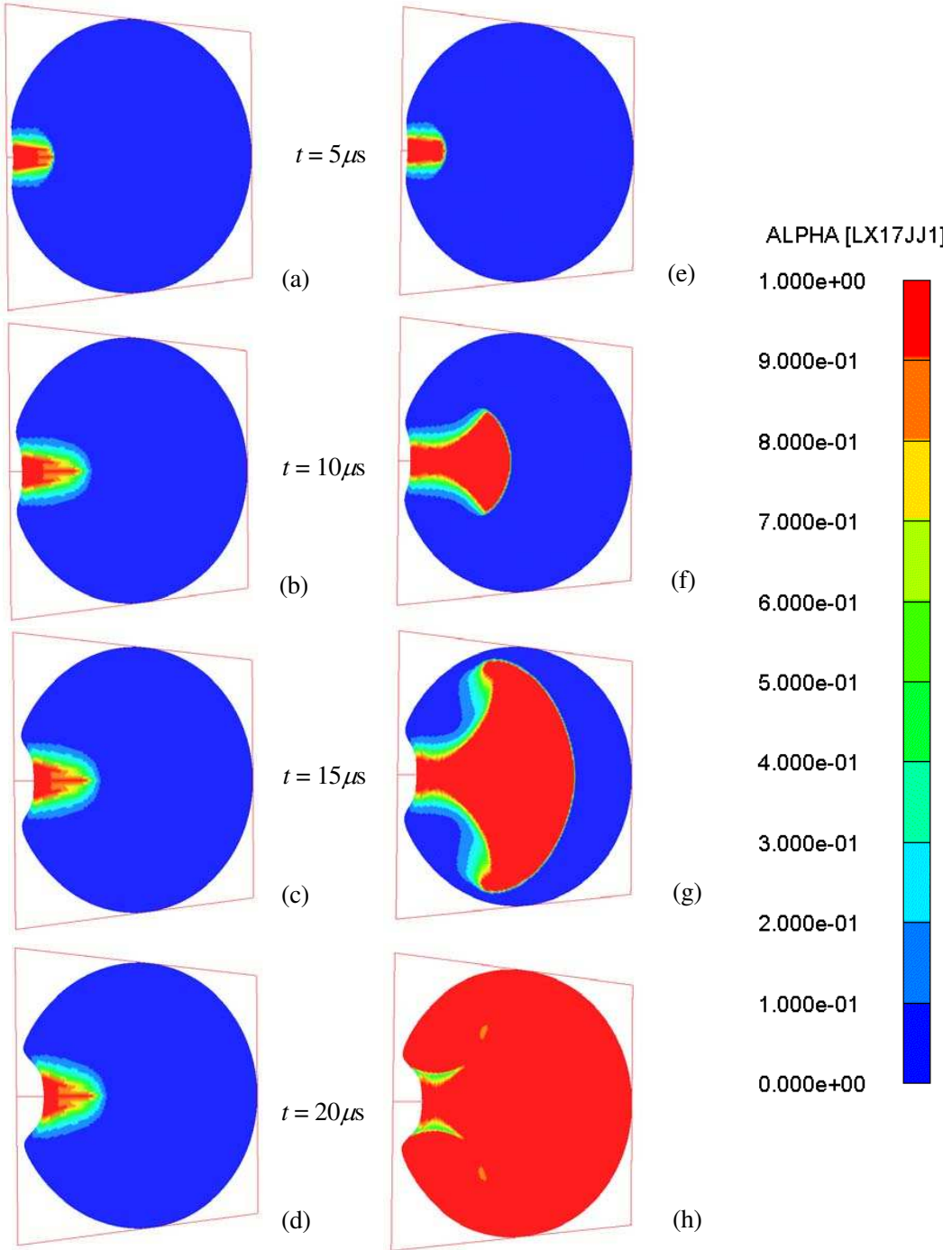
Figure 10. Burn fraction of the explosive in the circular cross-section at $z = 0$ caused by two flat projectiles at $V_p = 2.3$ km/s for $t = 5\,\mu$s, $10\,\mu$s, $15\,\mu$s and $20\,\mu$s; (a-d): 1.73 cm $\times$ 1.73 cm $\times$ 0.96 cm and (e-h): 1.74 cm $\times$ 1.74 cm $\times$ 0.96 cm.
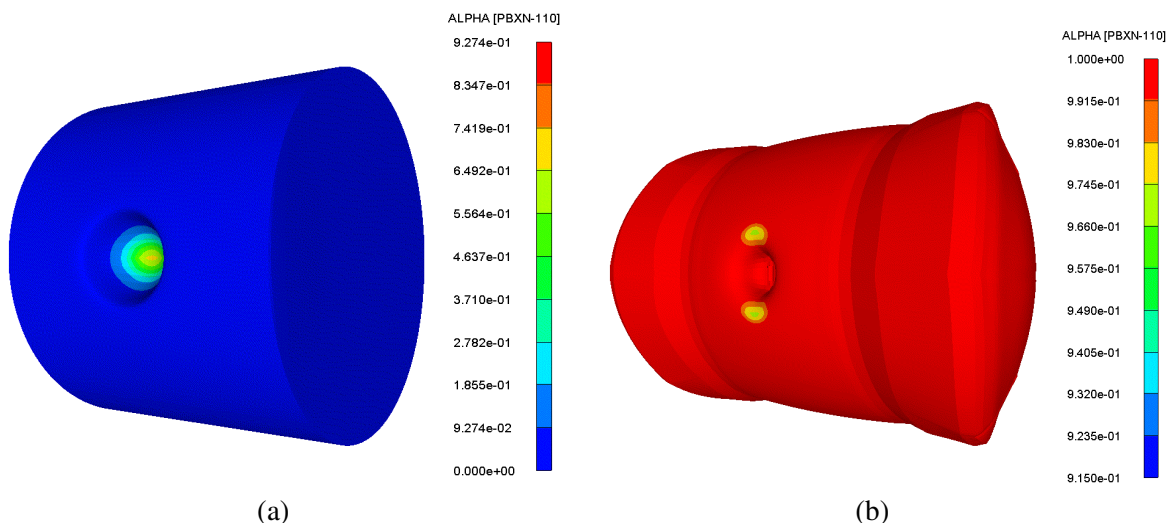
Figure 11. Burn fraction of the encased PBXN-110 explosive at $t = 20\,\mu$s for (a) $V_p = 2.9$ km/s and (b) $V_p = 3.0$ km/s.

Figure 12 shows the shock wave propagation in the circular cross-section at $z = 0$ for $V_p = 2.9$ km/s and 3.0 km/s at $t = 5\,\mu$s, $8\,\mu$s, $10\,\mu$s and $15\,\mu$s. Clearly, the shock wave is getting stronger with time for the case of 3.0 km/s. This is again attributed to the rapid pressure buildup from the explosive reaction. Note that, except for early time, the wave profiles in Figures 12(e)–(h) are different from those in Figure 7. The shock wave front hits the interface between the explosive and the casing much earlier at about $7\,\mu$s compared to $12\,\mu$s as seen in Figure 7(c). It then takes about $3\,\mu$s for the two reflected waves to superpose in the vicinity of the central axis of the projectile trajectory; compare this to $8\,\mu$s shown in Figure 7(f).

The burn fraction in the circular cross-section at $z = 0$ is presented in Figure 13. A full reaction of the explosive takes place in the region near the impact site at about $t = 5\,\mu$s where the peak pressure is 0.369 Mbar. The estimated average detonation rate in the x-direction is 0.830 cm/$\mu$s for $t = 6\text{-}8\,\mu$s, 0.850 cm/μs for $t = 8\text{-}10\,\mu$s, and 0.862 cm/μs for $t = 10\text{-}15\,\mu$s. Comparison of the results in Figure 13 and Figures 8(e)–(h) reveals the different detonation growth behavior between the encased PBXN-110 and LX-17 explosives. Moreover, the detonation rate of the PBXN-110 explosive is higher than that of the LX-17 explosive. Recall that the average detonation rate in the x-direction is about 0.752 cm/μs for the time interval $t = 10\text{-}15\,\mu$s.

4.5. *Effect of material models and parameters on the shock-induced detonation.* We have used the shock equation of state (EOS) $(4)_1$ applicable for most metals, Johnson–Cook plasticity model to describe the high velocity impact response of steel casing and projectile, and the Lee–Tarver ignition and growth model to calculate the reaction rate of the explosive materials. The erosion criterion serves not only as a material failure model, but also to ensure the completion of the analysis. Note that the results we have obtained may depend on the choice of the material models as well as the material parameters. In this section, we delineate the effect of material models and parameters on the shock-induced detonation.
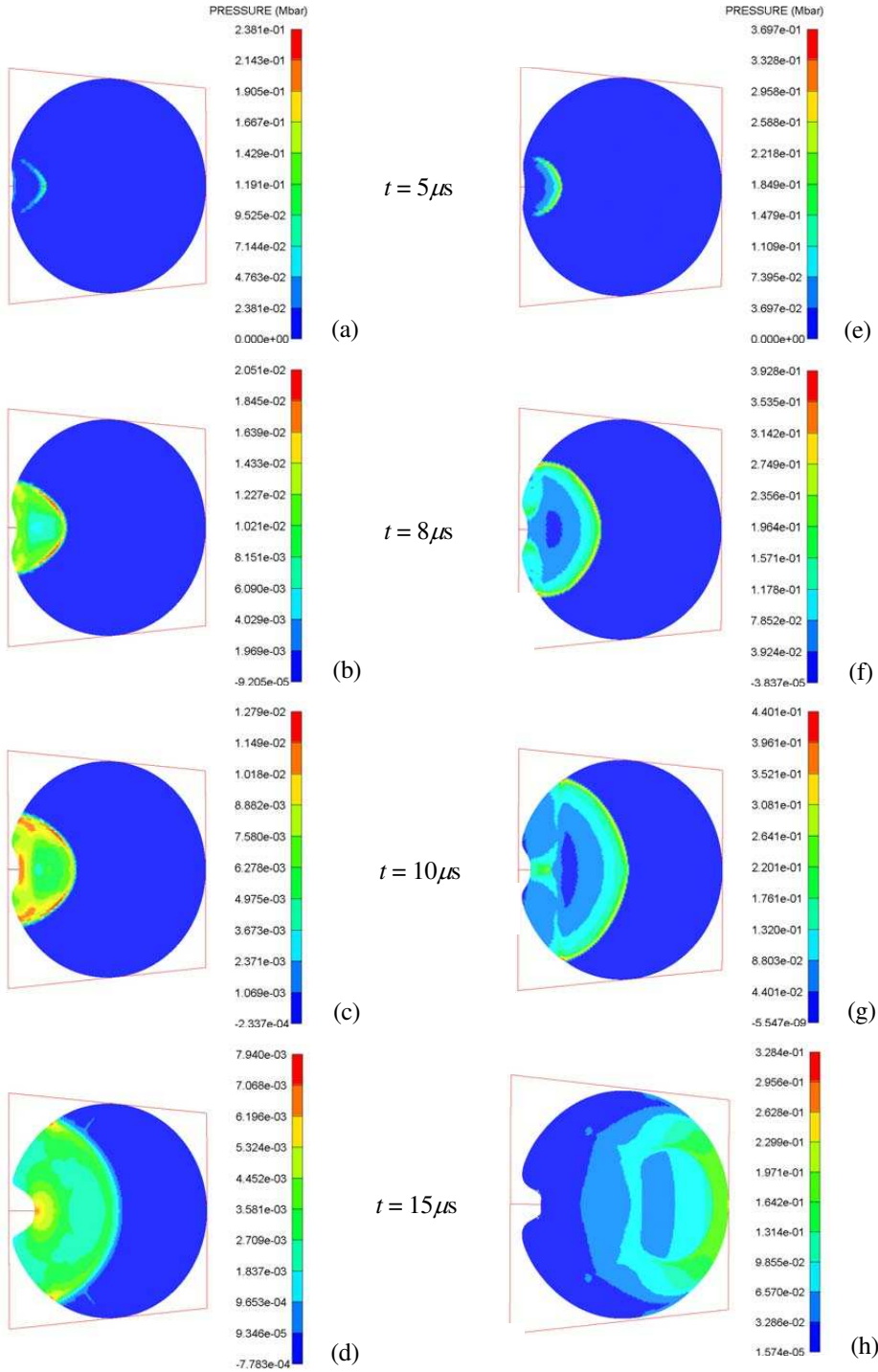
Figure 12. Shock wave in circular cross-section at $z = 0$ of the encased PBXN-110 explosive at $t = 5\,\mu s$, $8\,\mu s$, $10\,\mu s$ and $15\,\mu s$; (a-d): $V_p = 2.9\,\text{km/s}$, (e-h): $V_p = 3.0\,\text{km/s}$.
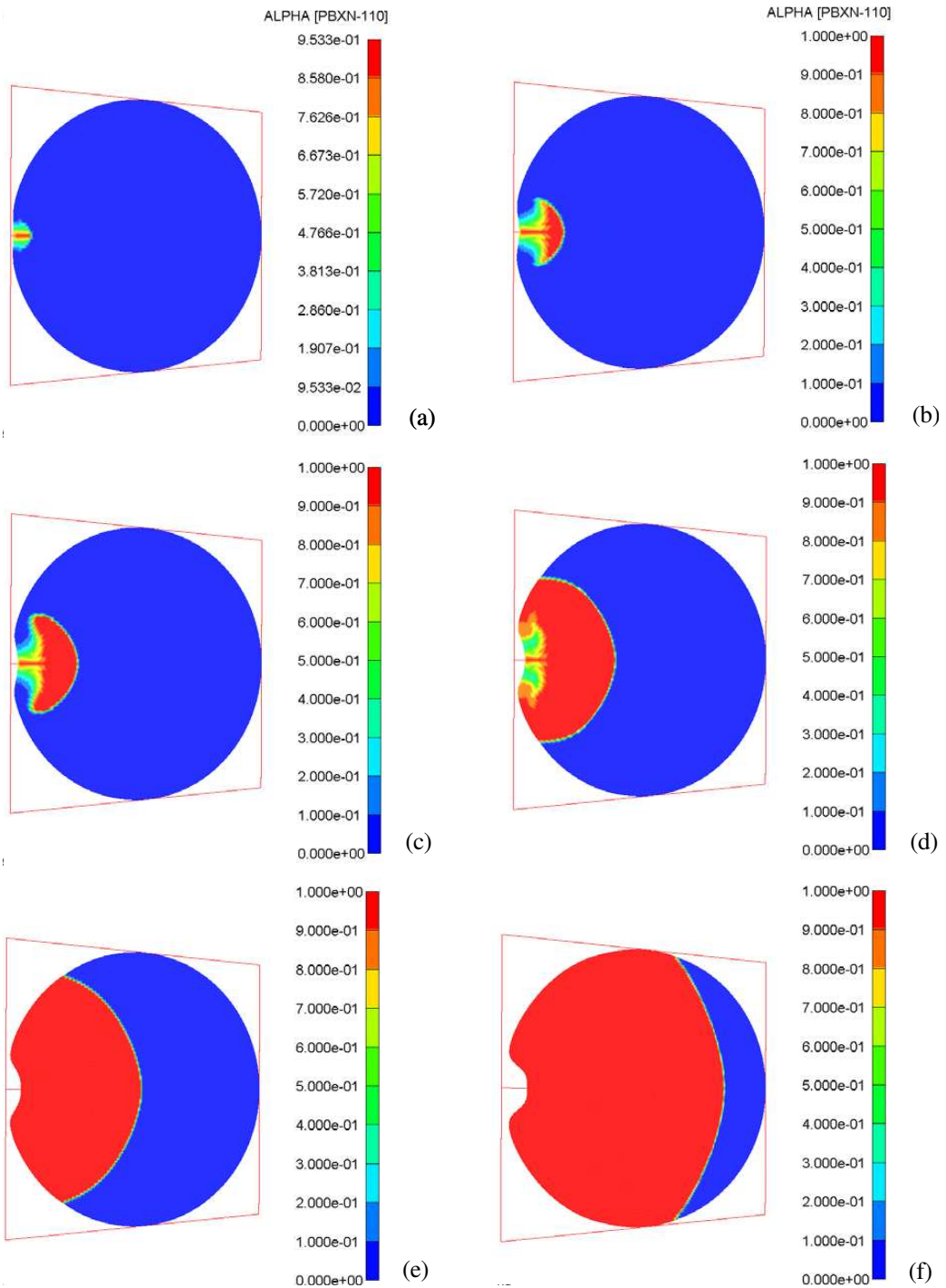
Figure 13. Burn fraction in the circular cross-section at $z = 0$ of the encased PBXN-110 explosive at $t =$ (a) $3\,\mu s$, (b) $5\,\mu s$, (c) $6\,\mu s$, (d) $8\,\mu s$, (e) $10\,\mu s$, (f) $15\,\mu s$ for $V_p = 3.0\,\text{km/s}$.

	Cube		Sphere	Plate
	PBXN-110	LX-17		
Shock EOS	3.0 km/s	4.5 km/s	4.8 km/s	1.74 cm × 1.74 cm
Linear EOS	2.8 km/s	3.9 km/s	4.3 km/s	1.64 cm × 1.64 cm

Table 3. Comparison of threshold conditions leading to detonation for cases from Sections 4.1–4.4 for steel casing using the shock and linear EOS.

Table 3 compares the threshold values of the projectile velocity or size leading to detonation, calculated with the shock EOS $(4)_1$ and the linear EOS given by

$$p = K\mu, \tag{5}$$

where p is the hydrostatic pressure, K is the material bulk modulus, and μ is the material compression defined in Equation (3); for steel considered in this work $K = 1.59$ Mbar. In every case the threshold value obtained by the linear EOS (5) is lower than that obtained by the shock EOS $(4)_1$. For example, the threshold velocity of the cubical projectile calculated with the shock EOS is 4.5 km/sec, while it is 3.9 km/s when the linear EOS is used. This suggests that a proper EOS for the case material and projectiles be used in the simulation of shock-induced detonation of energetic explosives.

In order to delineate the effect of material failure on the shock-induced detonation, we also implement the Johnson–Cook damage model in the steel casing and projectile. The progress of failure is defined by the cumulative damage law $D = \sum(\Delta\varepsilon/\varepsilon_f)$, where $\Delta\varepsilon$ is the increment in effective plastic strain with an increment in loading, and ε_f is the failure strain at the current state of the loading which is a function of the mean stress, the effective stress, the strain state and homologous temperature. The expression for the failure strain is given by

$$\varepsilon_f = \left[D_1 + D_2 e^{D_3\sigma^*}\right]\left[1 + D_4 \log |\dot{\varepsilon}_p^*|\right]\left[1 + D_5 T^*\right], \tag{6}$$

where σ' is the mean stress normalized by the effective stress, D_i are material constants whose values are listed in Table 2. Failure is assumed to occur when $D = 1$.

Figure 14 depicts the time histories of pressure at points of A and B in the encased LX-17 caused by the cubical projectile, computed with (a) the Johnson–Cook damage model only, (b) the erosion criterion only, and (c) both. The numerical calculation without the erosion criterion stops at about $t = 4.3\,\mu$s. As shown in Figure 14, the time histories of the pressures have no discernible variation among the three cases, other than the fact that no further calculation can be continued for case (a). Further numerical analysis finds that the threshold impact speeds of the projectile obtained with and without the Johnson–Cook damage model are identical, namely, 4.5 km/sec. As far as the threshold condition for shock detonation is concerned, use of the erosion criterion for the failure model for the casing and projectile could be sufficient.
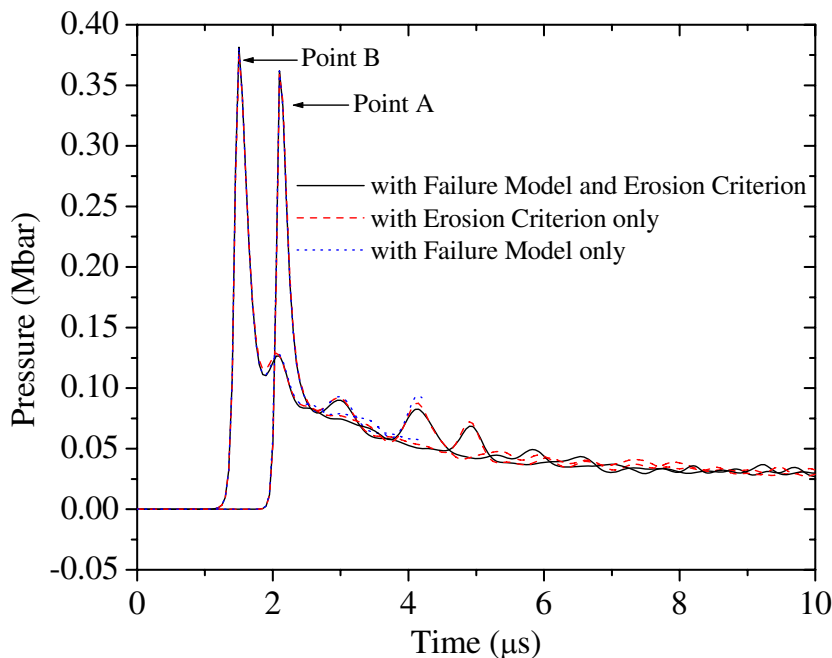
Figure 14. Time histories of shock pressure at *A* and *B* in the encased LX-17 explosive for $V_p = 4.5$ km/s, computed by combining Johnson–Cook damage model and erosion criterion, Johnson–Cook damage model only, and erosion criterion only.

5. Summary and conclusions

We have performed a three-dimensional finite element analysis for shock-induced detonation in a mockup consisting of an open-ended steel cylinder filled with LX-17 or PBXN-110 explosive by a normal impact to the cylindrical surface. Three steel projectiles of different shape are examined: (1) a cube of constant mass of 7 g, (2) a sphere of same mass, and (3) a square plate with a constant impact velocity of 2.3 km/s. The thickness of the cube and the flat square projectile is the same. The Lee–Tarver ignition and growth model is employed to describe the reaction rate of the energetic materials. Both the unreacted solid explosive and reacted gaseous product are modeled by the JWL equation of state. The shock equation of state and the Johnson–Cook plasticity model are adopted to describe structural response of the steel casing and projectile. Depending on the projectile investigated, either the threshold detonation velocity or the critical size of the projectile is calculated. The resulting high rate deformation and perforation of the steel cylinder as well as the shock wave and burn fraction in the explosives are presented and discussed.

For the LX-17 explosive encased in the cylinder of 10 cm in length, 0.9525 cm in thickness, and 6.6675 cm in the inner radius, the calculated threshold velocities of the cubical projectile that lead to deflagration and detonation are 3.9 km/s and 4.5 km/s, respectively. The threshold deflagration and detonation velocities are 4.5 km/s and 4.8 km/s for the spherical projectile. The higher threshold detonation velocity for the spherical projectile found here is consistent with those found for the projectiles impacting on a flat surface of a bare, front-covered, or totally confined high explosive. For the square plate projectile

the calculated threshold detonation in-plane dimension is 1.74 cm. For the encased PBXN-110 explosive impacted by the cubical projectile a violent detonation could occur immediately as long as a full reaction in the explosive is initiated in the region near the impact site. The calculated threshold detonation velocity is 3.0 km/s, which is much lower than that for the encased LX-17 explosive. The direct shock-to-detonation transition mechanism simulated is different from the shock-to-deflagration-to-detonation transition found for the LX-17 explosive.

There are some physics missing in the simulations in this work. For instance, cracks in the high explosive may open upon the fragment entering through the container, which may change a slow burn scenario to a full detonation. Further investigations on these issues and detonation tests are suggested.

Acknowledgements

References

[Allahdadi et al. 1998] F. A. Allahdadi, D. F. Medina, E. T. Olson, and S. R. Jeffers, "Simulation of impact induced detonation of AIM-120: a novel approach", Technical report AFSC-TR-2000-0002, Air Force Safety Center — Weapons, Space, and Nuclear Safety Division, Kirtland Air Force Base, NM, 1998, Available at http://handle.dtic.mil/100.2/ADA379702.

[Autodyn 2005] Century Dynamic Inc., *AUTODYN Theory Manual*, Century Dynamic Inc., 2005. Revision 4.3.

[Bahl et al. 1981] K. L. Bahl, H. C. Vantine, and R. C. Weingart, "The shock initiation of bare and covered explosives by projectile impact", pp. 325–335 in *Proceedings Seventh International Symposium on Detonation* (Annapolis, MD), vol. 1, NSWC MP 82-334, Naval Surface Weapons Center, Silver Spring, MD, 16–19 June 1981.

[Chou et al. 1991] P. C. Chou, D. Liang, and W. J. Flis, "Shock and shear initiation of explosive", *Shock Waves* **1**:4 (1991), 285–292.

[Cook et al. 1989] M. D. Cook, P. J. Haskins, and H. R. James, "Projectile impact initiation of explosive charges", pp. 1441–1450 in *9th Symposium International on Detonation* (Portland, OR), 27 Aug–1 Sept 1989.

[Cook et al. 2001] M. D. Cook, P. J. Haskins, R. Briggs, and C. Stennett, "Fragment impact characterization of melt and pbx explosives", pp. 1047–1050 in *Shock compression of condensed matter meeting* (Atlanta, GA), American Institute of Physics, June 24–29 2001.

[Davison 1997] D. Davison, "Three-dimensional analysis of the explosive initiation threshold for side impact on a shaped charge warhead", Technical report, Shock Transients, Inc., Hopkins, MD, 1997, Available at http://www.shocktrans.com/DownloadableFiles/STI.InsensitiveMunitions.1997.p% df.

[Forest 1978] C. A. Forest, "Burning and detonation", Technical report LA-7245, Los Alamos Scientific Laboratory, Los Alamos, NM, 1978.

[Hull et al. 2002] L. M. Hull, J. R. Faulkner, G. T. Gray III, C. M. Caddy, and W. R. Blumenthal, "Initiation experiments on PBXN-110", Technical report LA-UR-02-5024, Los Alamos National Laboratory, Los Alamos, NM, 2002.

[James et al. 1991] H. R. James, P. J. Haskins, and M. D. Cook, "Effect of case thickness and projectile geometry on the shock initiation threshold for a given explosive", pp. 18:1–15 in *AGARD Conference Proceedings 511* (Neuilly sur Seine, France), NATO Specialists Meeting, 21-23 Oct 1991. p.18/1-15.

[James et al. 1996] H. R. James, P. J. Haskins, and M. D. Cook, "Prompt shock initiation of cased explosives by projectile impact", *Propell. Explos. Pyrot.* **21**:5 (1996), 251–257.

[Johnson and Cook 1983] G. R. Johnson and W. H. Cook, "A constitutive model and data for metals subjected to large strains, high strain rates and high temperatures", pp. 541–547 in *Proc. 7th Int Symp Ballistics*, The Hague, The Netherlands, 1983.

[Johnson and Cook 1985] G. R. Johnson and W. H. Cook, "Fracture characteristics of three metals subjected to various strains, strain rates, temperature and pressures", *Eng. Fract. Mech.* **21**:1 (1985), 31–48.

[Lattery et al. 2005] J. Lattery, R. Abernathy, and K. Christopherson, "Progress Report", Technical report N60921-93-D-A109, Air Force Safety Center, 2005.

[Lee and Tarver 1980] E. L. Lee and C. M. Tarver, "Phenomenological model of shock initiation in heterogeneous explosives", *Phys. Fluids* **23**:12 (1980), 2362–2372.

[Lee et al. 1968] E. L. Lee, H. C. Hornig, and J. W. Kury, "Adiabatic expansion of high explosive detonation products", Technical report UCRL-50422, Lawrence Livermore National Laboratory, Livermore, CA, 1968.

[Meyers 1994] M. A. Meyers, *Dynamic behavior of materials*, Wiley, New York, 1994.

[Miller 1996] P. J. Miller, "A simplified method for determining reactive rate parameters for reaction ignition and growth in explosives", Technical report, Naval Air Warfare Center, Weapons Division, China Lake, CA, 1996.

[Peugeot et al. 1998] F. Peugeot, M. Quidot, and H. N. Presles, "An analytical extension of the critical energy criterion used to predict bare explosive response to jet attack", *Propell. Explos. Pyrot.* **23**:3 (1998), 117–122.

[Shin and Lee 2003a] H. Shin and W. Lee, "Interactions of impact shock waves in a thin-walled explosive container, I: impact by a flat-ended projectile", *Shock Waves* **39**:4 (2003), 470–478.

[Shin and Lee 2003b] H. Shin and W. Lee, "Interactions of impact shock waves in a thin-walled explosive container, II: impact by a cone-nosed projectiles", *Shock Waves* **39**:4 (2003), 479–486.

[Shin and Lee 2003c] H. Shin and W. Lee, "A numerical study on the detonation behavior of double reactive casettes by impact of projectiles with different nose shapes", *Int. J. Impact Eng.* **28**:4 (2003), 349–362.

[Starkenberg et al. 1984] J. Starkenberg, Y. Huang, and A. Arbuckle, "Numerical modeling of projectile impact shock initiation of bare and covered composition-B, ARBRL-TR-02576", US Army Ballistic Research Laboratory, 1984.

[Tarver and Hallquist 1981] C. M. Tarver and J. O. Hallquist, "Modeling two-dimensional shock initiation and detonation wave phenomena in PBX 9404 and LX 17", pp. 488–497 in *Proceedings Seventh International Symposium on Detonation* (Annapolis, MD), NSWC MP 82-334, Naval Service Weapons Center, Silver Spring, MD, 1981.

J. K. CHEN: ChenJnK@missouri.edu
Department of Mechanical and Aerospace Engineering, University of Missouri, Columbia, Missouri, United States

HSU-KUANG CHING: hching@vt.edu
Department of Mechanical and Aerospace Engineering, University of Missouri, Columbia, Missouri, United States

FIROOZ A. ALLAHDADI: Firooz.Allahdadi@kirtland.af.mil
Air Force Safety Center, Kirtland AFB, New Mexico, United States

STONELEY SIGNALS IN PERFECTLY BONDED DISSIMILAR THERMOELASTIC HALF-SPACES WITH AND WITHOUT THERMAL RELAXATION

Louis Milton Brock

The governing equations for each of two perfectly bonded, dissimilar thermoelastic half-spaces include as special cases the Fourier heat conduction model and models with either one or two thermal relaxation times. An exact solution in transform space for the problem of line loads applied in one half-space is obtained.

Study of the Stoneley function shows that conditions for existence of roots are more restrictive than in the isothermal case, and that both real and imaginary roots are possible. For the limit case of line loads applied to the interface, an analytical expression for the time transform of the corresponding residue contribution to interface temperature change is derived.

Asymptotic expressions for the inverses that are valid for either very long or very short times after loading occurs show that long-time behavior obeys Fourier heat conduction. Short-time results are sensitive to thermal relaxation effects. In particular, a time step load produces a propagating step in temperature for the Fourier and double-relaxation time models, but a propagating impulse for the single-relaxation time model.

1. Introduction

Joined dissimilar elastic materials occur in geological formations [Cagniard 1962] and as structural elements [Jones 1999]. Transient analyses [Stoneley 1924; Cagniard 1962] show that dynamic loading of these can produce, in addition to dilatational and rotational waves, interface (Stoneley) waves. Such waves are similar to Rayleigh surface waves [Lamb 1904] and so may be important in assessing interface integrity.

Studies such as [Stoneley 1924; Cagniard 1962] focus on isothermal materials. Studies such as [Brock 1997a; 1997b] consider both Stoneley and Rayleigh waves for materials that satisfy equations for coupled thermoelasticity [Chadwick 1960]. However, the equations are based on classical Fourier heat conduction [Carrier and Pearson 1988], and the Stoneley and Rayleigh signals are examined for times after the application of loading that greatly exceed the thermoelastic characteristic time.

Joseph and Preziosi [1989] have surveyed models that include the phenomenon of thermal relaxation in heat conduction. Lord and Shulman [1967], Green and Lindsay [1972] and Chandrasekharia [1986] have included thermal relaxation in formulations for coupled thermoelasticity. Sharma and Sharma [2002] have applied such formulations to homogeneous plates. Based on all this work, and on an effort in (nontransient) dynamic steady-state analysis of two joined half-spaces governed by the Fourier model [Brock and Georgiadis 1999], this article considers two perfectly bonded, dissimilar elastic half-spaces

that are subject to thermal-mechanical line loads applied to the interface. Both half-spaces obey equations for coupled thermoelasticity that include the Fourier model [Chadwick 1960], and the single- and double-relaxation time models of Lord and Shulman [1967] and Green and Lindsay [1972], respectively, as special cases.

The study begins with construction of the exact solution in transform space for the general case of line loads applied in one of the half-spaces. The solution exhibits a Stoneley function that is more complicated in form than its isothermal counterpart [Cagniard 1962]. Conditions for the existence of Stoneley roots are determined, and found to be more restrictive than those for the isothermal case. Expressions for these roots, analytic to within a single integration, are developed, and found to give both real and imaginary values, again in contrast to the isothermal case. An exact formula for the time transform of the change in interface temperature when the line loads are applied to the interface is developed. Analytical expressions for the change itself, valid for either very long or very short times after loading is applied, are obtained for each of the three models. Consistent with previous observation [Brock 2004] the long-time results all have the character of the Fourier model, and describe a temperature change wave. The short-time results, on the other hand, are sensitive to the particular model but the Stoneley signals are again in the form of waves.

2. Statement of general problem and governing equations

In terms of Cartesian coordinates (x, y, z) two half-spaces of dissimilar isotropic, homogeneous, linear thermoelastic material are perfectly bonded along the plane $y = 0$. For time $t \leq 0$, both are at rest at the uniform ambient (absolute) temperature T_0 when, at $t = 0$, thermal-mechanical disturbances are introduced along the line $x = 0$, $y = L$. The disturbances may be time-dependent, but do not vary along the line, so that a state of plane strain is generated. For half-space $1(y > 0)$ the field equations for $t > 0$ are

$$\left(\nabla^2 - s_{r1}^2 \frac{\partial^2}{\partial t^2}\right)(u_{x1}, u_{y1}) + \left(\frac{\partial}{\partial x}, \frac{\partial}{\partial y}\right)(m_1 \Delta_1 - \alpha_{v1} D_1^{II} \theta_1) = \frac{1}{\mu_1}(F_x, F_y)\delta(x)\delta(y - L), \qquad (1a)$$

$$h_1 \nabla^2 \theta_1 - s_{r1} \frac{\partial}{\partial t}\left(\frac{\varepsilon_1}{\alpha_{v1}} D_1 \Delta_1 - D_1^I \theta_1\right) = F_T \delta(x)\delta(y - L), \qquad (1b)$$

$$\frac{1}{\mu_1}(\sigma_{x1}, \sigma_{y1}, \sigma_{z1}) = (m_1 - 1)\Delta_1 - \alpha_{v1} D_1^{II} \theta_1 + 2\left(\frac{\partial u_{x1}}{\partial x}, \frac{\partial u_{y1}}{\partial y}, 0\right), \qquad (1c)$$

$$\frac{1}{\mu_1}\sigma_{xy1} = \frac{\partial u_{x1}}{\partial y} + \frac{\partial u_{y1}}{\partial x}. \qquad (1d)$$

In (1) $(u_{x1}, u_{y1}, \Delta_1, \theta_1)$ are, respectively, displacement components, dilatation and change in temperature from T_0, and $(\sigma_{x1}, \sigma_{y1}, \sigma_{z1}, \sigma_{xy1})$ are stress components. These vary with (x, y, t). In (1a), (1b) (F_x, F_y, F_T) are the t-dependent line loads, and δ is the Dirac function. For the Fourier model F [Chadwick 1960] and single- and double-relaxation time model I [Lord and Shulman 1967] and II [Green

and Lindsay 1972], respectively,

$$F : (D_1, D_1^I, D_1^{II}) = 1 \tag{2a}$$

$$I : D_1^{II} = 1, \qquad (D_1, D_1^I) = 1 + \tau_1^I \frac{\partial}{\partial t} \tag{2b}$$

$$II : (D_1, D_1^{II}) = 1 + \tau_1^{II} \frac{\partial}{\partial t}, \qquad D_1^I = 1 + \tau_1^I \frac{\partial}{\partial t}. \tag{2c}$$

Constants $\tau_1^I > \tau_1^{II} \geq 0$ are thermal relaxation times, and it is noted that model II serves to introduce thermal relaxation explicitly in constitutive Equation (1c), (1d). In (1)

$$m_1 = \frac{1}{1 - 2\nu_1}, \qquad a_1 = 2\frac{1 - \nu_1}{1 - 2\nu_1}, \tag{3a}$$

$$\varepsilon_1 = \frac{\mu_1 T_0}{\rho_1 c_{v1}} \alpha_{1v}^2, \qquad h_1 = v_{r1} \tau_1^h, \qquad s_{r1} = \frac{1}{v_{r1}} \tag{3b}$$

$$\tau_1^h = \frac{k_1}{\mu_1 c_{v1}}, \qquad v_{r1} = \sqrt{\frac{\mu_1}{\rho_1}}. \tag{3c}$$

In (1) and (3) $(\nu_1, \mu_1, \rho_1, \alpha_{v1}, c_{v1}, k_1)$ are, respectively, Poisson's ratio, shear modulus, mass density, coefficient of volumetric thermal expansion, specific heat at constant volume and thermal conductivity. In turn $(\varepsilon_1, h_1, s_{r1}, v_{r1}, \tau_1^h)$ are, respectively, the thermal coupling constant, thermoelastic characteristic length, rotational wave slowness, rotational wave speed, and thermoelastic characteristic time. For half-space $2(y < 0)$ Equation (1)–(3) again hold, except that subscript 1 is replaced by 2 and (1a), (1b) are homogeneous. Data in a number of sources [Chadwick 1960; Achenbach 1973; Davis 1998; Sharma and Sharma 2002] suggests that in both half-spaces, that is, $n = (1, 2)$, we find

$$v_{rn} \approx O(10^3) \text{ m/s}, \qquad m_n \geq 2, \qquad \varepsilon_n \approx O(10^{-2}), \tag{4}$$
$$h_n \approx O(10^{-9}) \text{ m}, \qquad (\tau_n^I, \tau_n^{II}) \approx O(10^{-13}) \text{ s}.$$

These values indicate in turn that $\tau_n^h \gg \tau_n^I > \tau_n^{II}$.

For $y \neq 0$ the initial $(t \leq 0)$ conditions are

$$(u_{nx}, u_{ny}, \theta_n) \equiv 0, \quad n = (1, 2). \tag{5}$$

For $t > 0$ the interface $(y = 0)$ conditions are

$$u_{x1} - u_{x2} = 0, \qquad u_{y1} - u_{y2} = 0, \qquad \theta_1 - \theta_2 = 0$$
$$\sigma_{xy1} - \sigma_{xy2} = 0, \qquad \sigma_{y1} - \sigma_{y2} = 0, \qquad k_1 \frac{\partial \theta_1}{\partial y} - k_2 \frac{\partial \theta_2}{\partial y} = 0. \tag{6}$$

Equation (1a), (1b) imply for $(y = L, t > 0)$ that

$$[u_{x1}] = 0, \qquad [u_{y1}] = 0, \qquad [\theta_1] = 0$$
$$\mu_1 \left[\frac{\partial u_{x1}}{\partial y} \right] = F_x \delta(x), \qquad \mu_1 a_1 \left[\frac{\partial u_{y1}}{\partial y} \right] = F_y \delta(x), \qquad h_1 c_{v1} \left[\frac{\partial \theta_1}{\partial y} \right] = F_T \delta(x). \tag{7}$$

Here $[F]$ denotes the jump in function F for a given (x, t) as one moves from $y = L - 0$ to $y = L + 0$. For $t > 0 (u_{x1}, u_{y1}, \theta_1)$ and $(u_{x2}, u_{y2}, \theta_2)$ should vanish as $y \to \infty$ and $y \to -\infty$, respectively, and singular behavior may occur at $(x = 0, y = L)$. By explicitly imposing (7), homogeneous forms of (1a), (1b) can be addressed in both half-space 1 and 2. Decomposition of these in view of (5) gives for $n = (1, 2)$, $y \neq (0, L)$

$$\nabla^2 \left(a_n \Delta_n - \alpha_{vn} D_n^{II} \theta_n\right) - s_{rn}^2 \frac{\partial^2 \Delta_n}{\partial t^2} = 0, \qquad \left(\nabla^2 - s_{rn}^2 \frac{\partial^2}{\partial t^2}\right) r_{xyn} = 0 \qquad (t > 0) \tag{8a}$$

$$(\Delta_n, \theta_n, r_{xyn}) \equiv 0 \quad (t \leq 0). \tag{8b}$$

In (8), Equation (2) holds, and r_{xyn} is rotation in plane strain.

3. Transform solution for general problem

Unilateral and bilateral [Sneddon 1972] Laplace transforms over (t, x) are

$$\hat{F}(x) = \int_0^\infty F(x, t) \exp(-pt) dt, \qquad \tilde{F} = \int_{-\infty}^\infty \hat{F}(x) \exp(-pqx) dq. \tag{9}$$

Here p is positive and real, and q is imaginary. Application of (9) to (8) gives eigenfunctions and eigenvalues

$$\exp(\pm p A_n^+ y), \qquad \exp(\pm p A_n^- y), \qquad \exp(\pm p B_n y) \tag{10a}$$

$$A_n^+(q^2) = \sqrt{s_n^{+2} - q^2}, \qquad A_n^-(q^2) = \sqrt{s_n^{-2} - q^2}, \qquad B_n(q^2) = \sqrt{s_{rn}^2 - q^2}. \tag{10b}$$

In (10) the branch points are defined by (3) and for $n = (1, 2)$

$$s_n^\pm = k_n^\pm s_{dn}, \qquad s_{dn} = \frac{s_{rn}}{\sqrt{a_n}} \tag{11a}$$

$$2k_n^\pm = \sqrt{\left(1 + \sqrt{\frac{a_n d_n^I}{\tau_n^h p}}\right)^2 + \frac{\varepsilon_n d_n}{\tau_n^h p}} \pm \sqrt{\left(1 - \sqrt{\frac{a_n d_n^I}{\tau_n^h p}}\right)^2 + \frac{\varepsilon_n d_n}{\tau_n^h p}}. \tag{11b}$$

Here s_{dn} is the isothermal dilatational wave slowness, and from (2), (5) and (9)

$$\begin{aligned}
&\text{F} : (d_n, d_n^I) = 1, \\
&\text{I} : (d_n, d_n^I) = 1 + \tau_n^I p, \\
&\text{II} : (d_n, d_n^{II}) = 1 + \tau_n^{II} p, \qquad d_n^I = 1 + \tau_n^I p.
\end{aligned} \tag{12}$$

It can be shown in view of (4) for all three models that $k_n^+ > 1 > k_n^- > 0$ and thus $(s_n^+, s_{rn}) > s_n^-$ for positive real p. Inequality $s_n^+ > s_{rn}(k_n^+ > \sqrt{a_n})$ also holds when

$$
\begin{aligned}
\text{F} &: p < 1 + \frac{\varepsilon_n}{m_n}, \\[1ex]
\text{I} &: p < \frac{m_n + \varepsilon_n}{m_n \tau_n^h - (m_n + \varepsilon_n)\tau_n^I}, \\[1ex]
\text{II} &: p < \frac{m_n + \varepsilon_n}{m_n(\tau_n^h - \tau_n^I) - \varepsilon_n \tau_n^{II}}.
\end{aligned}
\tag{13}
$$

Application of (9) to the homogeneous versions of (1a), (1b) in light of (5) and using (10) and (12) gives transforms $(\tilde{u}_{1x}, \tilde{u}_{1y}, \tilde{\theta}_1)$ for $y > 0$, $y \neq L$ and $(\tilde{u}_{2x}, \tilde{u}_{2y}, \tilde{\theta}_2)$ for $y < 0$ as linear combinations of (10a). Operating on (1c), (1d), (6) and (7) with (9) then gives the equations required to find the coefficients of the linear combinations. For present purposes it is sufficient to display results for half-space 2:

$$
\begin{bmatrix} \tilde{u}_{2x} \\ \tilde{u}_{2y} \\ \tilde{\theta}_2 \end{bmatrix} =
\begin{bmatrix} q & q & 1 \\ A_2^+ & A_2^- & -q \\ \omega_2 \eta_2^+ & \omega_2 \eta_2^- & 0 \end{bmatrix}
\begin{bmatrix} C_+ \exp(pA_2^+ y) \\ C_- \exp(pA_2^- y) \\ C_B \exp(pB_2 y) \end{bmatrix}
\tag{14a}
$$

$$
\begin{bmatrix} C_+ \\ C_- \\ C_B \end{bmatrix} = \frac{1}{pS}
\begin{bmatrix} M_+^+ & M_-^+ & \omega_1 q M_B^+ \\ M_+^- & M_-^- & \omega_1 q M_B^- \\ q M_+ & q M_- & M_B \end{bmatrix}
\begin{bmatrix} F_+ \\ F_- \\ F_B \end{bmatrix}.
\tag{14b}
$$

For $n = (1, 2)$ in view of (11) and (12),

$$
\omega_n = \frac{s_{rn}^2 p}{\alpha_{vn} d_n}, \qquad \eta_n^\pm = 1 - k_n^{\pm 2}
\tag{15a}
$$

$$
\eta_n^+ \eta_n^- = -\frac{\varepsilon_n d_n}{\tau_n^h p},
$$

$$
\eta_n^- - \eta_n^+ = \eta_n = \sqrt{\left[1 + \frac{1}{\tau_n^h p}(a_n d_n^I + \varepsilon_n d_n) \right]^2 - 4\sqrt{\frac{a_n d_n^I}{\tau_n^h p}}}.
\tag{15b}
$$

For ω_n parameter d_n is defined by

$$
\text{I, F} : d_n = 1, \qquad \text{II} : (d_n, d_n^{II}) = 1 + \tau_n^{II} p.
\tag{16}
$$

In (15b), however, it is defined by (12). Introduction of branch cuts $\mathrm{Im}(q) = 0$, $|\mathrm{Re}(q)| > s_n^\pm$ and $\mathrm{Im}(q) = 0$, $|\mathrm{Re}(q)| > s_{rn}$ such that $\mathrm{Re}(A_n^\pm, B_n) \geq 0$ in the cut q-plane guarantees that (14a) is bounded

as $y \to -\infty$ for positive real p. In (14b)

$$F_+ = \left[\omega_1 \eta_1^- (q\hat{F}_x + A_1^- \hat{F}_y) - \frac{\hat{F}_T}{h_1 c_{v1}} \right] \exp(-pA_1^+ L) \tag{17a}$$

$$F_- = \left[\omega_1 \eta_1^+ (q\hat{F}_x + A_1^+ \hat{F}_y) - \frac{\hat{F}_T}{h_1 c_{v1}} \right] \exp(-pA_1^- L) \tag{17b}$$

$$F_B = (q\hat{F}_y - B_1 \hat{F}_x) \exp(-pB_1 L). \tag{17c}$$

The matrix coefficients in (14b) are given by

$$M_+^+ = \frac{\omega_1 \eta_1^+ k_1}{\rho_1} S_{1-}^{2-} - \omega_2 \eta_2^- Q_B (K_1^- + K_2^-), \qquad M_-^+ = \omega_2 \eta_2^- Q_B (K_1^+ + K_2^-) - \frac{\omega_1 \eta_1^- k_1}{\rho_1} S_{1+}^{2-}, \tag{18a}$$

$$M_B^+ = \omega_2 \eta_2^- \left[\eta_1^- Q_1^+ (K_1^- + K_2^-) - \eta_1^+ Q_1^- (K_1^+ + K_2^-) \right] + \frac{\omega_1 \varepsilon_1 d_1}{\tau_1^h \rho_1 p} (K_1^- - K_1^+)(T_2 T_{12} - \mu_{12} T_1 K_2^- B_2), \tag{18b}$$

$$M_-^- = \frac{\omega_1 \eta_1^- k_1}{\rho_1} S_{1+}^{2+} - \omega_2 \eta_2^+ Q_B (K_1^+ + K_2^+), \qquad M_+^- = \omega_2 \eta_2^+ Q_B (K_1^- + K_2^+) - \frac{\omega_1 \eta_1^+ k_1}{\rho_1} S_{1-}^{2+}, \tag{19a}$$

$$M_B^- = \omega_2 \eta_2^+ \left[\eta_1^+ Q_1^- (K_1^+ + K_2^+) - \eta_1^- Q_1^+ (K_1^- + K_2^+) \right] + \frac{\omega_1 \varepsilon_1 d_1}{\tau_1^h \rho_1 p} (K_1^+ - K_1^-)(T_2 T_{12} - \mu_{12} T_1 K_2^+ B_2), \tag{19b}$$

$$M_+ = \omega_2 \left[\eta_2^- Q_2^+ (K_1^- + K_2^-) - \eta_2^+ Q_2^- (K_1^- + K_2^+) \right] + \frac{\omega_1 \eta_1^+}{\rho_1} (K_2^+ - K_2^-)(T_1 T_{12} - \mu_{12} T_2 K_1^- B_1), \tag{20a}$$

$$M_- = \omega_2 \left[\eta_2^+ Q_2^- (K_1^- + K_2^+) - \eta_2^- Q_2^+ (K_1^- + K_2^-) \right] + \frac{\omega_1 \eta_1^-}{\rho_1} (K_2^+ - K_2^-)(T_1 T_{12} - \mu_{12} T_2 K_1^+ B_1), \tag{20b}$$

$$\begin{aligned}
M_B = {} & \omega_1 \omega_2 \left[\eta_1^+ \eta_2^+ (K_1^+ + K_2^+) Q_{1-}^{2-} + \eta_1^- \eta_2^- (K_1^- + K_2^-) Q_{1+}^{2+} \right] \\
& - \omega_1 \omega_2 \left[\eta_1^+ \eta_2^- (K_1^+ + K_2^-) Q_{1-}^{2+} + \eta_1^- \eta_2^+ (K_1^- + K_2^+) Q_{1+}^{2-} \right] \\
& - \left(\rho_1 \omega_2^2 \frac{k_2 \varepsilon_2 d_2}{\tau_2^h p} + \frac{\omega_1^2 k_1 \varepsilon_1 d_1}{\tau_1^h \rho_1 p} T_1 T_2 \right)(K_1^+ - K_1^-)(K_2^+ - K_2^-). \tag{20c}
\end{aligned}$$

Denominator term S is given by

$$\begin{aligned}
S = {} & -Q_B \left(\rho_2 \frac{k_1 \omega_1^2 \varepsilon_1 d_1}{\tau_1^h p} + \rho_1 \frac{k_2 \omega_2^2 \varepsilon_2 d_2}{\tau_2^h p} \right)(A_1^+ - A_1^-)(A_2^+ - A_2^-) \\
& + \omega_1 \omega_2 \left[\eta_1^+ \eta_2^+ (K_1^+ + K_2^+) S_{1-}^{2-} + \eta_1^- \eta_2^- (K_1^- + K_2^-) S_{1+}^{2+} \right] \\
& - \omega_1 \omega_2 \left[\eta_1^+ \eta_2^- (K_1^+ + K_2^-) S_{1-}^{2+} + \eta_1^- \eta_2^+ (K_1^- + K_2^+) S_{1+}^{2-} \right]. \tag{21}
\end{aligned}$$

Equation (12) defines d_n in (18)–(21) and in (18)–(20) functions

$$S_{1\pm}^{2\pm} = q^2 Q_1^\pm Q_2^\pm + Q_B Q_{1\pm}^{2\pm}, \qquad K_\eta^\pm = k_\eta A_\eta^\pm, \eta = (1, 2), \tag{22a}$$

$$Q_{1\pm}^{2\pm} = T_2 A_1^\pm + T_1 A_2^\pm, \qquad Q_B(q^2) = T_2 B_1 + T_1 B_2 \tag{22b}$$

$$Q_1^\pm(q^2) = T_{12} + \mu_{12} A_1^\pm B_2, \quad Q_2^\pm(q^2) = T_{12} + \mu_{12} A_2^\pm B_1, \tag{22c}$$

$$\mu_{12} = 2(\mu_2 - \mu_1) \tag{22d}$$

$$T_1 = \rho_1 + \mu_{12} q^2, \qquad T_2 = \rho_2 - \mu_{12} q^2, \tag{22e}$$

$$T_{12} = \rho_1 - \rho_2 + \mu_{12} q^2. \tag{22f}$$

If $s_n^\pm$ in $A_n^\pm$ is replaced by the isothermal dilatational wave slowness s_{dn}, then $(S_{1+}^{2+}, \ldots)$ all assume the form of the Stoneley function S_i for isothermal half-spaces [Cagniard 1962]. Thus S is the Stoneley function for the present case, and is now discussed.

4. Stoneley function

For positive real p, S has branch cuts $\text{Im}(q) = 0$, $|\text{Re}(q)| > s_*$, where in view of (13),

$$s_* = \min(s_1^-, s_2^-), \qquad s^* = \max(s_1^+, s_2^+, s_{r1}, s_{r2}). \tag{23}$$

Study of (21) shows that

$$S(q) \approx -2(\omega_1 \eta_1 s_{d1}^2)(\omega_2 n_2 s_{d2}^2) M q^2 \sqrt{0 - q^2}, \quad |q| \to \infty, \tag{24a}$$

$$S(0) = (\rho_2 s_{r1} + \rho_1 s_{r2})\left(M_{12}\omega_1\omega_2 - M_1\omega_1^2 - M_2\omega_2^2\right). \tag{24b}$$

In (24), (M, M_1, M_2, M_{12}) are defined by

$$M = (k_1 + k_2)(\mu_1 + m_2\mu_2)(\mu_2 + m_1\mu_1), \tag{25a}$$

$$(M_1, M_2) = \left(\rho_2 \frac{k_1\varepsilon_1 d_1}{\tau_1^h p}, \rho_1 \frac{k_2\varepsilon_2 d_2}{\tau_2^h p}\right)(s_1^+ - s_1^-)(s_2^+ - s_2^-), \tag{25b}$$

$$M_{12} = \eta_1^+ \eta_2^+ (k_1 s_1^+ + k_2 s_2^+)(\rho_2 s_1^- + \rho_1 s_2^-) + \eta_1^- \eta_2^- (k_1 s_1^- + k_2 s_2^-)(\rho_2 s_1^+ + \rho_1 s_2^+)$$
$$- \eta_1^+ \eta_2^- (k_1 s_1^+ + k_2 s_2^-)(\rho_2 s_1^- + \rho_1 s_2^+) - \eta_1^- \eta_2^+ (k_1 s_1^- + k_2 s_2^+)(\rho_2 s_1^+ + \rho_1 s_2^-). \tag{25c}$$

Equation (12) holds in (25b), and in view of (15) quantities $(M, M_1, M_2, M_{12}) > 0$ for positive real p. Study of (25a) shows for the isothermal case that $S_i(0) > 0$, and that this guarantees roots $q = \pm s_0^i$, $s_0^i > s_r^* = \max(s_{r1}, s_{r2})$ for S_i whenever $S_i(\pm s_r^*) < 0$. As noted in Appendix A, the sign of $S(0)$ depends on parameter P_- defined by (A3) and the dimensionless ratio ω_1/ω_2. In addition (22) and (25) show that S is real-valued at $q = \pm s_*$ but pure imaginary for $q = \pm s^*$ and $|q| \to \infty$, $\text{Im}(q) = \pm 0$, respectively. The signs of the imaginary values depend on the side of the branch cut. Study of (21), (24), (25), these

observations, and argument theory [Hille 1959] applied in the manner of [Brock 1997b] show that three cases arise.

$$\text{Case A}: \ S(0) > 0, \qquad \frac{S(s^* \pm i0)}{S(|q| \pm i0)}, \frac{S(-s^* \pm i0)}{S(-|q| \pm i0)} \longrightarrow -0, \quad |q| \to \infty, \tag{26a}$$

$$\text{Case B}: \ S(0) > 0, \qquad \frac{S(s^* \pm i0)}{S(|q| \pm i0)}, \frac{S(-s^* \pm i0)}{S(-|q| \pm i0)} \longrightarrow +0, \quad |q| \to \infty, \tag{26b}$$

$$\text{Case C}: \ S(0) < 0. \tag{26c}$$

For Case A, S exhibits roots $q = \pm s_0$, $s_0 > 0$. For Case B no roots arise in the cut q-plane. For Case C, S exhibits roots $q = \pm i\tau_0$, $\tau_0 > 0$.

Following [Norris and Achenbach 1984] and [Brock 1998] an expression for s_0 that is analytic to within a single integration is obtained. We introduce function

$$G(q) = \frac{S(q)}{C^* \omega_1 \omega_2 M(\eta_1 s_{d1}^2)(\eta_2 s_{d2}^2)} \frac{1}{s_0^2 - q^2}, \qquad C^* = \sqrt{s^{*2} - q^2}. \tag{27}$$

It has branch cuts $\text{Im}(q) = 0$, $s_* < |\text{Re}(q)| < s^*$, approaches unity as $|q| \to \infty$, and has no roots or zeros in the cut q-plane. After [Noble 1958], it factors as the product of functions $G_\pm$ that are analytic in the overlapping strips $\text{Re}(q) > -s_*$ and $\text{Re}(q) < s_*$, respectively. These are given by

$$\ln G_\pm(q) = \frac{1}{\pi} \int_{s_*}^{s^*} \tan^{-1} \frac{\text{Im } S(u + i0)}{\text{Re } S(u + i0)} \frac{du}{u \pm q}. \tag{28}$$

Setting $G = G_+ G_-$ in (27) and evaluating it at $q = 0$ gives the formula

$$s_0 = \frac{1}{G_\pm(0)} \sqrt{\frac{\rho_2 s_{r1} + \rho_1 s_{r2}}{s^* M(\eta_1 s_{d1}^2)(\eta_2 s_{d2}^2)}} \sqrt{M_{12} - M_1 \frac{\omega_1}{\omega_2} - M_2 \frac{\omega_2}{\omega_1}}. \tag{29}$$

Replacing s_0^2 by the term $-\tau_0^2$ in (27) gives (28) again, but (29) is replaced by

$$\tau_0 = \frac{1}{G_\pm(0)} \sqrt{\frac{\rho_2 s_{r1} + \rho_1 s_{r2}}{s^* M(\eta_1 s_{d1}^2)(\eta_2 s_{d2}^2)}} \sqrt{M_1 \frac{\omega_1}{\omega_2} + M_2 \frac{\omega_2}{\omega_1} - M_{12}}. \tag{30}$$

Formula (28) shows that both G_+ and G_- are analytic at $q = \pm(s_* - 0)$ and $q = \pm(s^* + 0)$. Thus setting $G = G_+ G_-$ in (27) and evaluating at these locations shows by way of a check that $S(0)$ and $S(\pm s_*)$ have the same sign, and that the limit in (26b) is achieved whenever $S(0) < 0$. Because Case A and B are analogous to the isothermal problem, the results obtained so far are used to study Stoneley effects in interface temperatures for these cases. For simplicity, the limit problem of interface line loads ($L = 0$) is considered.

5. Interface temperature change when $L = 0$

When (F_x, F_y, F_T) act on the interface $y = 0$ itself $(L = 0)$, (14) and (16) give the transform of the temperature change on the interface

$$(\tilde{\theta}_1, \tilde{\theta}_2) = \tilde{\theta}_{12} = \frac{\omega_1 \omega_2}{S} \left(q M_x \frac{\hat{F}_x}{p} + M_y \frac{\hat{F}_y}{p} + M_T \frac{\hat{F}_T}{\rho_1 p} \right). \tag{31}$$

In (49) the coefficients

$$M_x = \omega_2 \eta_1^+ \eta_1^- (K_1^+ - K_1^-) \left[\eta_2^- (Q_B - Q_2^+ B_2) - \eta_2^+ (Q_B - Q_2^- B_2) \right]$$
$$+ \omega_1 \eta_2^+ \eta_2^- (K_2^+ - K_2^-) \left[\eta_1^- (Q_B + Q_1^+ B_1) - \eta_1^+ (Q_B + Q_1^- B_1) \right] \tag{32a}$$

$$M_y = \omega_2 \eta_1^+ \eta_1^- (K_1^+ - K_1^-) \left[\eta_2^+ (q^2 Q_2^- + Q_B A_2^-) - \eta_2^- (q^2 Q_2^+ + Q_B A_2^+) \right]$$
$$+ \omega_1 \eta_2^+ \eta_2^- (K_2^+ - K_2^-) \left[\eta_1^+ (q^2 Q_1^- - Q_B A_1^-) - \eta_1^- (q^2 Q_1^+ - Q_B A_1^+) \right] \tag{32b}$$

$$M_T = \eta_1^+ \eta_2^- S_{1-}^{2+} + \eta_1^- \eta_2^+ S_{1+}^{2-} - \eta_1^+ \eta_2^+ S_{1-}^{2-} - \eta_1^- \eta_2^- S_{1+}^{2+}. \tag{32c}$$

The inverse of the bilateral Laplace transform [Sneddon 1972] in (9) can be written as

$$\hat{F}(x) = \frac{p}{2\pi i} \int \tilde{F} \exp(pqx) \, dq. \tag{33}$$

Integration is over a Bromwich contour which, for Case A, can be taken as the entire $\text{Im}(q)$-axis. However, (24a) and (32) show that

$$S \approx O(q^2 \sqrt{-q^2}), \quad M_x \approx O(1), \tag{34}$$

$$M_y \approx O(\sqrt{-q^2}), \qquad M_T \approx O(q^2), \quad |q| \to \infty. \tag{35}$$

Therefore, substitution of (31) in (33) gives integrands that vanish as $|q| \to \infty$ for all $x (M_x, M_y)$ and $x \neq 0(M_T)$. The (M_x, M_T)-contribution can then by Cauchy theory be obtained as principal value integrals about segment $\text{Im}(q) = 0, \text{Re}(q) < -s_*(x > 0)$ or $\text{Im}(q) = 0, \text{Re}(q) > s_*(x < 0)$. Similarly, the M_y-contribution becomes an integral about segment $\text{Im}(q) = 0, -s^* < \text{Re}(q) < -s_*(x > 0)$ or $\text{Im}(q) = 0, s_* < \text{Re}(q) < s^*(x < 0)$ and the pole residue

$$\hat{\theta}_{12}^S = \frac{\hat{F}_y}{2 s_0 p} \frac{v_{d1}^2 v_{d2}^2 N_y \exp(-p s_0 |x|)}{\eta_1 \eta_2 M G_0 \sqrt{s_0^2 - s^{*2}}} \tag{36a}$$

$$\ln G_0 = \frac{2}{\pi} \int\limits_{s_*}^{s^*} \tan^{-1} \frac{\text{Im} \, S(u + i0)}{\text{Re} \, S(u + i0)} \frac{u \, du}{u^2 - s_0^2} \tag{36b}$$

$$N_y = \frac{\varepsilon_1 d_1}{\tau_1^h}(\kappa_1^+ - \kappa_1^-)\omega_2\big[\eta_2^-(s_0^2 T_2^+ - \alpha_2^+ T_\beta) - \eta_2^+(s_0^2 T_2^- - \alpha_2^- T_\beta)\big]$$

$$+ \frac{\varepsilon_2 d_2}{\tau_2^h}(\kappa_2^+ - \kappa_2^-)\omega_1\big[\eta_1^-(s_0^2 T_1^+ + \alpha_1^+ T_\beta) - \eta_1^+(s_0^2 T_1^- + \alpha_1^- T_\beta)\big]. \quad (36c)$$

Equation (12) governs d_n in (36c), and

$$(T_1^\pm, T_2^\pm) = \rho_1 - \rho_2 + \mu_{12}s_0^2 - \mu_{12}(\alpha_1^\pm \beta_2, \alpha_2^\pm \beta_1) \tag{37a}$$

$$T_\beta = (\rho_2 - \mu_{12}s_0^2)\beta_1 + (\rho_1 + \mu_{12}s_0^2)\beta_2 \tag{37b}$$

$$\alpha_n^\pm = \sqrt{s_0^2 - s_n^{\pm 2}}, \qquad \kappa_n^\pm = k_n \alpha_n^\pm, \qquad \beta_n = \sqrt{s_0^2 - s_{rn}^2}, \quad n = (1, 2). \tag{37c}$$

Study of (36a) in view of (10a), (11), (12), (20)–(24) and (37) shows that $\hat{\theta}_{12}^S$ appropriately vanishes when the half-space materials are the same. For Case B a term such as (36a) does not arise. Inversion of (36a) is now sought for Case A for the three models. To allow more insight into behavior, analytical results are achieved with asymptotic versions of the transforms that are valid for very long or very short times after the line loads are applied.

6. Inversion for long times

A robust asymptotic result for long times, here defined for all three models as

$$t \gg \max(\tau_1^h, \tau_2^h) \tag{38}$$

is obtained by inverting an approximate transform valid for $\max(\tau_1^h p, \tau_2^h p) \ll 1$. It is noted that all D_n-operators (and thus corresponding d_n-factors) become unity, that is, all three models behave as Fourier model F. For $n = (1, 2)$ Equation (11)–(13) yield

$$k_n^+ \approx \sqrt{\frac{a_n^\varepsilon}{\tau_n^h p}}, \qquad \eta_n^+ \approx -\frac{a_n^\varepsilon}{\tau_n^h p}, \qquad k_n^- \approx \sqrt{\frac{a_n^\varepsilon}{a_n}}, \qquad \eta_n^- \approx \frac{\varepsilon_n}{a_n}, \qquad a_n^\varepsilon = a_n + \varepsilon_n \tag{39a}$$

$$s_n^+ \approx \frac{\lambda_n^\varepsilon}{\sqrt{p}}, \qquad s_n^- \approx \frac{s_{rn}}{\sqrt{a_n^\varepsilon}} = s_n^\varepsilon = \frac{1}{v_n^\varepsilon}, \qquad \omega_n \approx \frac{s_{rn}^2 p}{\alpha_{vn}}, \qquad \lambda_n^\varepsilon = \frac{a_n^\varepsilon s_{rn}}{a_n h_n}. \tag{39b}$$

In light of (11) and (39), $s_n^+ \gg s_{rn} > s_n^-$ and it is noted that $(v_n^\varepsilon, s_n^\varepsilon)$ are the thermoelastic dilatational wave speed and slowness [Brock and Georgiadis 1999]. For purposes of illustration we choose materials so that, in view of (39),

$$s_1^- < s_2^- < s_{r1} < s_{r2} \ll s_1^+ < s_2^+. \tag{40}$$

From Appendix A and (24) it can be shown that requirements for Case A are met if

$$s_{r2}^2(\rho_1 + \rho_2 - 2\mu_1 s_{r2}^2)^2 - \beta_1\big[(\rho_2 - 2\mu_1 s_{r2}^2)^2 \alpha_1 + \rho_1 \rho_2 \alpha_2\big] > 0 \tag{41a}$$

$$\alpha_n = \sqrt{s_{r2}^2 - s_n^{\varepsilon 2}}, \qquad n = (1, 2), \qquad \beta_1 = \sqrt{s_{r2}^2 - s_{r1}^2}. \tag{41b}$$

If (41b) does hold then (29), (36a) and a standard table [Sneddon 1972] give

$$s_0 \approx \sqrt{\rho_2 s_1^\varepsilon + \rho_1 s_2^\varepsilon} \sqrt{\rho_2 s_{r1} + \rho_1 s_{r2}} \frac{\sqrt{k_1 \lambda_1^\epsilon + k_2 \lambda_2^\epsilon}}{\sqrt{\lambda_1^\epsilon \lambda_2^\epsilon}} \frac{\exp(\Psi_F(0))}{s_2^\varepsilon \sqrt{M s_1^\varepsilon s_{r2}}} > s_{r2} \tag{42a}$$

$$\theta_{12}^S \approx \frac{N_F}{2M\sqrt{s_0^2 - s_{r2}^2}} \exp(-2\Psi_F(s_0)) F_y(t - s_0|x|) H(t - s_0|x|) \tag{42b}$$

$$N_F = \frac{k_1 \varepsilon_1 a_2 v_1^{\varepsilon 2}}{\tau_1^h \alpha_{v2}} \left(1 - \frac{\alpha_2^0}{s_0}\right)(s_0^2 T_1^0 + \alpha_1^0 T_\beta^0) + \frac{k_2 \varepsilon_2 a_1^\varepsilon v_2^{\varepsilon 2}}{\tau_2^h \alpha_{v1}} \left(1 - \frac{\alpha_1^0}{s_0}\right)(s_0^2 T_2^0 - \alpha_2^0 T_\beta^0). \tag{42c}$$

Here H is the Heaviside function, function Ψ_F is defined by (B1) in Appendix B and

$$(T_1^0, T_2^0) = \rho_1 - \rho_2 + \mu_{12} s_0^2 - \mu_{12}(\alpha_1^0 \beta_2^0, \alpha_2^0 \beta_1^0) \tag{43a}$$

$$T_\beta^0 = (\rho_2 - \mu_{12} s_0^2)\beta_1^0 + (\rho_1 + \mu_{12} s_0^2)\beta_2^0 \tag{43b}$$

$$\alpha_n^0 = \sqrt{s_0^2 - s_n^{\varepsilon 2}}, \qquad \beta_n^0 = \sqrt{s_0^2 - s_{rn}^2}, \quad n = (1, 2). \tag{43c}$$

7. Inversion for short times: model F

The short time range for Fourier model F is defined as

$$t \ll \min(\tau_1^h, \tau_2^h). \tag{44}$$

A robust asymptotic result can therefore be obtained from a transform approximation valid for

$$\min(\tau_1^h p, \tau_2^h p) \gg 1.$$

It can be shown that for $n = (1, 2)$

$$k_n^+ \approx 1, \qquad \eta_n^+ \approx \frac{-\varepsilon_n}{\tau_n^h p}, \qquad k_n^- \approx \sqrt{\frac{a_n}{\tau_n^h p}}, \qquad \eta_n^- \approx 1 \tag{45a}$$

$$s_n^+ \approx s_{dn}, \qquad s_n^- \approx \frac{\lambda_n}{\sqrt{p}}, \qquad \omega_n = \frac{s_{rn}^2 p}{\alpha_{vn}}, \qquad \lambda_n = \frac{s_{rn}}{h_n}. \tag{45b}$$

From (11) and (45) it follows that now $s_{rn} > s_n^+ \gg s_n^-$. For purposes of illustration the materials are chosen such that

$$s_1^- < s_2^- \ll s_1^+ < s_2^+ < s_{r1} < s_{r2}. \tag{46}$$

From Appendix A and (21) it can be shown that conditions for Case A are met if (38) is satisfied, but with (α_1, α_2) in (41b) replaced by

$$\alpha_n = \sqrt{s_{r2}^2 - s_{dn}^2}, \quad n = (1, 2). \tag{47}$$

If (41a) and (47) do hold then it can be shown that

$$s_0 \approx \sqrt{\rho_2 s_{d1} + \rho_1 s_{d2}} \sqrt{\rho_2 s_{r1} + \rho_1 s_{r2}} \frac{\sqrt{k_1 \lambda_1 + k_2 \lambda_2}}{\sqrt{k_1 k_2}} \frac{\exp(\Psi_F(0))}{s_{d2}\sqrt{s_{d1} s_{r2} M}} > s_{r2}, \tag{48a}$$

$$\theta_{12}^S \approx \frac{N_F}{2M\sqrt{s_0^2 - s_{r2}^2}} \exp(-2\Psi_F(s_0)) F_y(t - s_0|x|) H(t - s_0|x|), \tag{48b}$$

$$N_F = \frac{k_1 \varepsilon_1 a_2 v_{d1}^2}{\tau_1^h \alpha_{v2}} \left(1 - \frac{\alpha_2^0}{s_0}\right)(s_0^2 T_1^0 + \alpha_1^0 T_\beta^0) + \frac{k_2 \varepsilon_2 a_1 v_{d2}^2}{\tau_2^h \alpha_{v1}} \left(1 - \frac{\alpha_1^0}{s_0}\right)(s_0^2 T_2^0 - \alpha_2^0 T_\beta^0). \tag{48c}$$

Function Ψ_F is now given by (B3) in Appendix B.

8. Inversion for short times: model I

For the single-relaxation time model, valid results are obtained for

$$t \ll \min(\tau_1^I, \tau_2^I) \tag{49}$$

with approximate transforms valid for $\max(\tau_1^I p, \tau_2^I p) \gg 1$. Then for $n = (1, 2)$

$$2k_n^\pm \approx \sqrt{\left(1 + \sqrt{a_n l_n^I}\right)^2 + \varepsilon_n l_n^I} \pm \sqrt{\left(1 - \sqrt{a_n l_n^I}\right)^2 + \varepsilon_n l_n^I}, \qquad l_n^I = \frac{\tau_n^I}{\tau_n^h} \ll 1 \tag{50a}$$

$$\omega_n \approx \frac{s_{rn}^2 p}{\alpha_{nv}}, \qquad \eta_n^+ \eta_n^- \approx -\varepsilon_n l_n^I. \tag{50b}$$

It is noted that l_n^I is a dimensionless ratio of characteristic times. In light of (13) inequality $s_{rn} > s_n^+$ holds, and one can again consider the situation (46). However, each s-parameter is now a constant, that is, wave slowness, so that a difference of scale between s_n^+ and s_n^- would be due to material mismatch. Use of Appendix A, (24) and (50) shows that Case A arises only if

$$z_- < \frac{s_{r1}^2 \alpha_{v2}}{s_{r2}^2 \alpha_{v1}} < z_+, \qquad M_I < 0. \tag{51}$$

Parameters $z_\pm$ are given by (A6) in Appendix A, with (50) understood and

$$(M_1, M_2) \approx (k_1 \varepsilon_1 l_1^I \rho_2, k_2 \varepsilon_2 l_2^I \rho_1)(s_1^+ - s_1^-)(s_2^+ - s_2^-). \tag{52}$$

Parameter M_I is defined as

$$M_I = \eta_1^+ \eta_2^+ (\kappa_1^+ + \kappa_2^+) M_{1-}^{2-} + \eta_1^- \eta_2^- (\kappa_1^- + \kappa_2^-) M_{1+}^{2+}$$
$$- \eta_1^+ \eta_2^- (\kappa_1^+ + \kappa_2^-) M_{1-}^{2+} - \eta_1^- \eta_2^+ (\kappa_1^- + \kappa_2^+) M_{1+}^{2-}, \tag{53a}$$

$$M_{1\pm}^{2\pm} = s_{r2}^2 T_{12}^2 - (T_2^2 \alpha_1^\pm + \rho_1 \rho_2 \alpha_2^\pm), \tag{53b}$$

$$\alpha_n^\pm = \sqrt{s_{r2}^2 - s_n^{\pm 2}}, \quad \kappa_\eta^\pm = \kappa_\eta \alpha_{\eta_1}^\pm, \quad n = (1, 2), \quad \beta_1 = \sqrt{s_{r2}^2 - s_{r1}^2}. \tag{53c}$$

Here (10b) and (22e) govern with argument u^2. For Case A (29) is valid, with

$$s^* = s_{r2}, \qquad G_{\pm}(0) \approx \exp \Psi_I(0).$$ (54)

Inversion of (36a) then produces in light of (37)

$$\theta_{12}^S \approx \frac{1}{2s_0} \frac{N_I \exp(-2\Psi_I(s_0))}{M\eta_1\eta_2\sqrt{s_0^2 - s_{r2}^2}} \dot{F}_y(t - s_0|x|) H(t - s_0|x|),$$ (55a)

$$N_I = \varepsilon_1 l_1^I (\kappa_1^+ - \kappa_1^-) \frac{a_2 v_{d1}^2}{\alpha_{v2}} \left[\eta_2^- (s_0^2 T_2^+ - \alpha_2^+ T_\beta) - \eta_2^+ (s_0^2 T_2^- - \alpha_2^- T_\beta) \right]$$

$$+ \varepsilon_2 l_2^I (\kappa_2^+ - \kappa_2^-) \frac{a_1 v_{d2}^2}{\alpha_{v1}} \left[\eta_1^- (s_0^2 T_1^+ + \alpha_1^+ T_\beta) - \eta_1^+ (s_0^2 T_1^- + \alpha_1^- T_\beta) \right].$$ (55b)

The superposed dot signifies time differentiation; Ψ_I is defined by (C1) in Appendix C.

9. Inversion for short times: model II

For the double-relaxation time model, valid results for

$$t < \min(\tau_1^{II}, \tau_2^{II})$$ (56)

are obtained by examining approximate transforms valid for $\min(\tau_1^{II} p, \tau_2^{II} p) \gg 1$. For $n = (1, 2)$ asymptotic results are

$$2k_n^{\pm} \approx \sqrt{\left(1 + \sqrt{a_n l_n^I}\right)^2 + \varepsilon_n l_n^{II}} \pm \sqrt{\left(1 - \sqrt{a_n l_n^I}\right)^2 + \varepsilon_n l_n^{II}},$$ (57a)

$$l_n^{II} = \frac{\tau_n^{II}}{\tau_n^h} < l_n^I \ll 1,$$

$$\omega_n \approx \frac{s_{rn}^2}{\alpha_{vn}\tau_n^{II}}, \qquad \eta_n^+ \eta_n^- \approx -\varepsilon_n l_n^{II}.$$ (57b)

As with model I each s-parameter is wave slowness, and situation (46) can again be considered, with the understanding that any difference in scale is due to material mismatch. Use of Appendix A, (24) and (57) shows that Case A arises only when

$$z_- < \frac{s_{r1}^2 \alpha_{v2}\tau_2^{II}}{s_{r2}^2 \alpha_{v1}\tau_1^{II}} < z_+, \qquad M_{II} < 0.$$ (58)

Again (A6) in Appendix A holds, but now

$$(M_1, M_2) \approx \left(\kappa_1 \varepsilon_1 l_1^{II} \rho_2, \kappa_2 \varepsilon_2 l_2^{II} \rho_1 \right) (s_1^+ - s_1^-)(s_2^+ - s_2^-),$$ (59a)

$$M_{II} = M_I - (\rho_2 - \mu_{12} s_{r2}^2) \beta_1 (\kappa_1^+ - \kappa_1^-)(\kappa_2^+ - \kappa_2^-)\Omega_{II},$$ (59b)

$$\Omega_{II} = \kappa_1 \mu_1 \varepsilon_2 s_{r2}^2 l_2^{II} \frac{\alpha_{v1}}{\alpha_{v2}} + \kappa_2 \mu_2 \varepsilon_1 s_{r1}^2 l_1^{II} \frac{\alpha_{v2}}{\alpha_{v1}}.$$ (59c)

It is understood that (57) now holds for all quantities, including M_I. If (58) is satisfied then (29) holds, with

$$s^* = s_{r2}, \qquad G_0 \approx \exp \Psi_{II}(0). \tag{60}$$

Inversion of (36a) then gives

$$\theta_{12}^S \approx \frac{1}{2s_0} \frac{N_{II} \exp(-2\Psi_{II}(s_0))}{\eta_1 \eta_2 \sqrt{s_0^2 - s_{r2}^2}} F_y(t - s_0|x|) H(t - s_0|x|), \tag{61a}$$

$$N_{II} = \varepsilon_1 l_1^{II}(\kappa_1^+ - \kappa_1^-) \frac{s_{r2}^2}{\alpha_{v2} \tau_2^{II}} \left[\eta_2^-\left(s_0^2 T_2^+ - \alpha_2^+ T_\beta\right) - \eta_2^+\left(s_0^2 T_2^- - \alpha_2^- T_\beta\right) \right]$$

$$+ \varepsilon_2 l_2^{II}(\kappa_2^+ - \kappa_2^-) \frac{s_{r1}^2}{\alpha_{v1} \tau_1^{II}} \left[\eta_1^-\left(s_0^2 T_1^+ + \alpha_1^+ T_\beta\right) - \eta_1^+\left(s_0^2 T_1^- + \alpha_1^- T_\beta\right) \right]. \tag{61b}$$

Here (57) governs and function Ψ_{II} is defined in Appendix D.

10. Some observations

Equation (21) shows that a Stoneley function arises in transform space in a dynamic study of perfectly bonded thermoelastic half-spaces. The function includes a linear combination of four terms, each (22a) of which has the form of an isothermal Stoneley function. Condition (26) for existence of thermoelastic Stoneley roots is similar to those for the isothermal case, but more restrictive. Expressions (29) and (30) for the roots, analytic to within a single integration, may depend on the unilateral Laplace (time) transform variable p, that is, not correspond to, as in the isothermal case, a constant Stoneley wave slowness. Moreover, a root can for positive real p be real (29) or imaginary (30).

It is found that a line load force applied directly to the interface and acting normal to it produces, from the residue of the real root, contribution (36a) to the time transform of the interface temperature change. The contribution has an analytical form, and asymptotic versions of this, valid for long times or short times after the line load is applied, can be inverted analytically.

Inversion (42b) shows that the residue contribution behaves for long times as if the half-spaces obey classical Fourier theory [Chadwick 1960] even when thermal relaxation [Lord and Shulman 1967; Green and Lindsay 1972] is present. Conditions for existence of the Stoneley root (in asymptotic form) are always met, and the root (42a) is a constant. As a result, (42b) describes a temperature change wave.

For short times, a constant real root (48a), (29) and (54), and (29) and (60) arises for, respectively, the Fourier and single- and double-relaxation time models, and the contribution of the residue to the interface temperature change for each model again defines a wave. However, existence conditions (51) and (58) for the relaxation time models are more restrictive than condition (41a) and (47) for the Fourier model. Moreover, contribution (48b) and (61a) for the Fourier and double-relaxation time models are proportional to line load function F_y. Contribution (55a) for the single-relaxation time model is proportional to the time derivative of F_y.

The observation that $\tau_n^h \gg \tau_n^I > \tau_n^{II}$, $n = (1, 2)$ made in connection with (4) shows in view of (38), (44), (49) and (56) that asymptotic result (42a) and (42b) are the most robust. Nevertheless, work in fluids [Fan and Lu 2002] shows that behavior for very short times after a load is applied can be distinctive.

As noted just above, this is the case here. Specifically, if F_y is a step (Heaviside) function in time, the Stoneley contribution to interface temperature for long times is a propagating step function whose form is the same for all three models. For short times, the contribution for the Fourier (F) and double-relaxation (II) time models are propagating step functions that are not identical, while the single-relaxation (I) time model gives a propagating impulse.

In summary, the present analysis shows the sensitivity of Stoneley signals in perfectly bonded thermoelastic half-spaces to the nature of the heat conduction model that governs. It is hoped that the results given here may prove useful in the transient study of solids that consist of dissimilar thermoelastic materials.

Appendix A

The sign of $S(0)$ in (24b) is determined by the second factor on its right-hand side. Equation (15) indicates that (ω_1, ω_2) for positive real p is positive, so that this factor can be studied in terms of the quadratic

$$M_{12}z - M_1 z^2 - M_2, \qquad z = \frac{\omega_1}{\omega_2} > 0. \tag{A1}$$

Its discriminant and the location of its maximum value are

$$M_{12}^2 - 4M_1 M_2, \qquad z = \frac{M_{12}}{2M_1}, \qquad (M_1, M_2, M_{12}) > 0. \tag{A2}$$

The former can be factored as

$$(k_1^+ - k_1^-)^2 (k_2^+ - k_2^-)^2 P_+ P_-, \qquad P_\pm = C_1 \rho_1 s_{d2} + C_2 \rho_2 s_{d1} \pm 2C_3 \sqrt{\rho_1 s_{d2} \rho_2 s_{d1}}. \tag{A3}$$

Term $P_\pm$ is quadratic in $(\sqrt{\rho_1 s_{d2}}, \sqrt{\rho_2 s_{d1}})$ and (C_1, C_2, C_3) are quadratic in $(\sqrt{k_1 s_{d1}}, \sqrt{k_2 s_{d2}})$:

$$\begin{aligned} C_1 &= C_{11} k_1 s_{d1} + C_{12} k_2 s_{d2}, \\ C_2 &= C_{21} k_1 s_{d1} + C_{22} k_2 s_{d2}, \end{aligned} \tag{A4a}$$

$$\begin{aligned} C_{11} &= (k_1^{+2} + k_1^+ k_1^- + k_1^{-2})(1 + k_2^+ k_2^-), \\ C_{12} &= k_2^+ k_2^- (k_1^+ + k_1^-)(k_2^+ + k_2^-), \end{aligned} \tag{A4b}$$

$$\begin{aligned} C_{22} &= (k_2^{+2} + k_2^+ k_2^- + k_2^{-2})(1 + k_1^+ k_1^-), \\ C_{21} &= k_1^+ k_2^- (k_1^+ + k_1^-)(k_2^+ + k_2^-), \end{aligned} \tag{A4c}$$

$$C_3 = \frac{1}{p} \sqrt{d_1 \epsilon_1 d_2 \epsilon_2} \sqrt{\frac{k_1 \epsilon_1 s_{d1}}{\tau_1^h}} \sqrt{\frac{k_2 \epsilon_2 s_{d2}}{\tau_2^h}}. \tag{A4d}$$

Equation (12) holds in (A4d) and because $k_n^+ > 1 > k_n^- > 0, n = (1, 2)$, terms $(C_1, C_2, C_3, P_+) > 0$. Therefore if $P_- > 0$ the quadratic in (A2) has a positive maximum and two positive real roots. If $P_- < 0$ the quadratic in (A2) is itself negative for all $\omega_1/\omega_2 > 0$. It follows that

$$P_- > 0 : S(0) > 0 \Big(z_- < \frac{\omega_1}{\omega_2} < z_+ \Big), \qquad S(0) < 0 \Big(0 < \frac{\omega_1}{\omega_2} < z_-, \frac{\omega_1}{\omega_2} > z_+ \Big), \tag{A5a}$$

$$P_- < 0 : S(0) < 0\left(\frac{\omega_1}{\omega_2} > 0\right). \tag{A5b}$$

In (A5a) the terms $z_\pm$ are given by

$$z_\pm = \frac{1}{2M_1}\left(M_{12} \pm \sqrt{M_{12}^2 - 4M_1M_2}\right). \tag{A6}$$

Study of P_- is aided by several observations: its discriminant is

$$-C_{11}C_{21}k_1^2s_{d1}^2 - C_{22}C_{12}k_2^2s_{d2}^2 + \left[\frac{2}{p}\sqrt{\frac{\varepsilon_1d_1\varepsilon_2d_2}{\tau_1^h\tau_2^h}} - C_{11}C_{22} - C_{12}C_{21}\right]k_1s_{d1}k_2s_{d2}. \tag{A7}$$

This quadratic in turn has discriminant

$$D_+D_-, \quad D_\pm = \frac{\varepsilon_1d_1\varepsilon_2d_2}{\tau_1^h\tau_2^h p^2} - \frac{1}{2}\left(\sqrt{C_{11}C_{22}} \pm \sqrt{C_{12}C_{22}}\right)^2. \tag{A8}$$

The first term in $D_\pm$ can be written in light of (15) as

$$(1 - k_1^{+2})(1 - k_1^{-2})(1 - k_2^{+2})(1 - k_2^{-2}). \tag{A9}$$

Thus if $(k_1^\pm, k_2^\pm)$ have values for positive real p such that $D_+D_- < 0$, then (A7) is negative in (k_1s_{d1}, k_2s_{d2}), and $P_- > 0$ in $(\sqrt{\rho_1s_{d2}}, \sqrt{\rho_2s_{d1}})$. If $D_+D_- > 0$ however, (A7) exhibits $(k_1^\pm, k_2^\pm)$-dependent roots in on the s_{d1}/s_{d2}-axis and its sign depends on (k_1s_{d1}, k_2s_{d2}). Then, when it is positive the sign of P_- depends on $(\sqrt{\rho_1s_{d2}}, \sqrt{\rho_2s_{d1}})$.

Appendix B

Function Ψ_F that appears in (47) is defined as

$$\ln\Psi_F(q) = \frac{1}{\pi}\left(\int_{s_1^\varepsilon}^{s_2^\varepsilon} \frac{\psi_1 u\,du}{u^2 - q^2} + \int_{s_2^\varepsilon}^{s_{r1}} \frac{\psi_2 u\,du}{u^2 - q^2} + \int_{s_{r1}}^{s_{r2}} \frac{\psi_3 u\,du}{u^2 - q^2}\right), \tag{B1a}$$

$$\psi_1 = \tan^{-1}\frac{1}{\alpha_1}\frac{(\rho_1\rho_2 B_1 + T_1^2 B_2)A_2 + u^2 T_{12}^2}{\rho_1\rho_2 B_2 + (T_2^2 + \mu_{12}^2 A_2 B_2)B_1}, \tag{B1b}$$

$$\psi_2 = \tan^{-1} u^2 \frac{T_{12}^2 - \mu_{12}^2\alpha_1 B_1\alpha_2 B_2}{T_1^2\alpha_2 B_2 + T_2^2\alpha_1 B_1 + \rho_1\rho_2(\alpha_1 B_2 + \alpha_2 B_1)}, \tag{B1c}$$

$$\psi_3 = \tan^{-1}\frac{1}{B_2}\frac{u^2 T_{12}^2 - (T_2^2\alpha_1 + \rho_1\rho_2\alpha_2)\beta_1}{(T_1^2 - \mu_{12}^2 u^2\alpha_1\beta_1)\alpha_2 + \rho_1\rho_2\alpha_1}. \tag{B1d}$$

Here (10b), (22e) and (45) hold, with argument u^2, and

$$\alpha_n = \sqrt{u^2 - s_n^{\varepsilon 2}}, \quad n = (1, 2), \qquad \beta_1 = \sqrt{u^2 - s_{r1}^2}. \tag{B2}$$

In Equation (48a) and (48b) function Ψ_F is given by

$$\Psi_F(q) = \frac{1}{\pi} \left(\int_{s_{d1}}^{s_{d2}} \frac{\psi_1 u du}{u^2 - q^2} + \int_{s_{d2}}^{s_{r1}} \frac{\psi_2 u du}{u^2 - q^2} + \int_{s_{r1}}^{s_{r2}} \frac{\psi_3 u du}{u^2 - q^2} \right). \tag{B3}$$

Equation (B1) and (B2) again hold but with modification

$$\alpha_n = \sqrt{u^2 - s_{dn}^2}, \quad n = (1, 2). \tag{B4}$$

Appendix C

Function Ψ_I that appears in (55) is defined by

$$\Psi_I(q) = \frac{1}{\pi} \left(\int_{s_1^-}^{s_2^-} \frac{\psi_1 u du}{u^2 - q^2} + \int_{s_2^-}^{s_1^+} \frac{\psi_2 u du}{u^2 - q^2} + \int_{s_1^+}^{s_2^+} \frac{\psi_3 u du}{u^2 - q^2} + \int_{s_2^+}^{s_{r1}} \frac{\psi_4 u du}{u^2 - q^2} + \int_{s_{r1}}^{s_{r2}} \frac{\psi_5 u du}{u^2 - q^2} \right), \tag{C1a}$$

$$\psi_1 = \tan^{-1} \alpha_1^- \frac{N_1}{D_1}, \quad \psi_2 = \tan^{-1} \frac{1}{D_2} (\alpha_1^- N_{21} + \alpha_2^- N_{22}), \quad \psi_3 = \tan^{-1} \frac{N_3}{D_3}, \tag{C1b}$$

$$\psi_4 = \tan^{-1} u^2 \frac{N_4}{D_4}, \quad \psi_5 = \tan^{-1} \frac{N_5}{B_2 D_5}. \tag{C1c}$$

Equation (C1b) and (C1c) employ the quantities

$$N_1 = \eta_1^- \left(\eta_2^- S_{1+}^{2+} - \eta_2^+ S_{1+}^{2-} \right) + \eta_1^+ \left[\eta_2^+ (K_1^+ + K_2^+) U_{2-} - \eta_2^- (K_1^+ + K_2^-) U_{2+} \right], \tag{C2a}$$

$$D_1 = \eta_1^- \left(\eta_2^+ A_2^+ S_{1+}^{2-} - \eta_2^- A_2^- S_{1+}^{2+} \right) + \eta_1^+ \left[\eta_2^- (K_1^+ + K_2^-) V_{2+} - \eta_2^+ (K_1^+ + K_2^+) V_{2-} \right], \tag{C2b}$$

$$N_{21} = \eta_1^- \eta_2^- S_{1+}^{2+} + \eta_1^+ \eta_2^+ (K_1^+ + K_2^+)(\rho_1 \rho_2 B_2 + T_2^2 B_1) - k_1 \eta_1^+ \eta_2^- A_1^+ U_{2+} - k_1 \eta_1^- \eta_2^+ V_{1+}, \tag{C3a}$$

$$N_{22} = \eta_2^- \eta_1^- S_{1+}^{2+} + \eta_2^+ \eta_1^+ (K_1^+ + K_2^+)(\rho_1 \rho_2 B_1 + T_1^2 B_2) - k_2 \eta_2^+ \eta_1^- A_2^+ U_{1+} - k_2 \eta_2^- \eta_1^+ V_{2+}, \tag{C3b}$$

$$D_2 = \eta_1^+ \eta_2^- (A_1^+ V_{2+} - \alpha_1^- k_2^- U_{2+}) + \eta_1^- \eta_2^+ (A_2^+ V_{1+} - k_1^- \alpha_2^- U_{1+}), \tag{C3c}$$

$$N_3 = \eta_2^- \left[\eta_1^- (\kappa_1^- + \kappa_2^-) - \eta_1^+ (\kappa_1^+ + \kappa_2^-) \right]$$
$$+ \eta_2^+ \left[\eta_1^+ \left(u^2 \alpha_1^+ V_{1-}^{2-} + A_2^+ U_{1-}^{2-} \right) + \eta_1^- \left(u^2 k_1^- V_{1+}^{2-} - k_2^+ U_{1+}^{2-} \right) \right], \tag{C4a}$$

$$D_3 = \eta_2^- \left[\eta_1^- \alpha_1^+ (\eta_1^- + \kappa_2^+) + V_{2+} - \eta_1^+ \alpha_1^- (\eta_1^- \kappa_1^+ - \kappa_2^-) U_{2+} \right]$$
$$+ \eta_2^+ \left[\eta_1^- \left(u^2 K_2^+ V_{1+}^{2-} - \kappa_1^- U_{1+}^{2-} \right) - \eta_1^+ \left(u^2 K_2^+ V_{1-}^{2-} - \kappa_1^+ U_{1-}^{2-} \right) \right], \tag{C4b}$$

$$N_4 = \eta_1^+ \eta_2^- (\kappa_1^+ + \kappa_2^-) V_{1-}^{2+} + \eta_1^- \eta_2^+ (\kappa_1^- + \kappa_2^+) V_{1+}^{2-} - \eta_1^+ \eta_2^+ (\kappa_1^+ + \kappa_2^+) V_{1-}^{2-} - \eta_1^- \eta_2^- (\kappa_1^- + \kappa_2^-) V_{1+}^{2+}, \quad \text{(C5a)}$$

$$D_4 = \eta_1^+ \eta_2^+ (\kappa_1^+ + \kappa_2^+) U_{1-}^{2-} + \eta_1^- \eta_2^- (\kappa_1^- + \kappa_2^-) U_{1+}^{2+} + \eta_1^+ \eta_2^- (\kappa_1^+ + \kappa_2^-) U_{1-}^{2+} + \eta_1^- \eta_2^+ (\kappa_1^- + \kappa_2^+) U_{1+}^{2-}, \quad \text{(C5b)}$$

$$(N_5, D_5) = \eta_1^+ \eta_2^+ (\kappa_1^+ + \kappa_2^+)(X_{1-}^{2-}, Y_{1-}^{2-}) + \eta_1^- \eta_2^- (\kappa_1^- + \kappa_2^-)(X_{1+}^{2+}, Y_{1+}^{2+})$$
$$+ \eta_1^+ \eta_2^- (\kappa_1^+ + \kappa_2^-)(-X_{1-}^{2+}, Y_{1-}^{2+}) - \eta_1^- \eta_2^+ (\kappa_1^- + \kappa_2^+)(-X_{1+}^{2-}, Y_{1+}^{2-}). \quad \text{(C6)}$$

In (C2)–(C6) Equation (10b), (22a), (22e) and (49) hold, with argument u^2, and

$$U_{2\pm} = T_2^2 B_1 + (\rho_1 \rho_2 + \mu_{12}^2 u^2 A_2^\pm B_1) B_2,$$
$$V_{2\pm} = u^2 T_{12}^2 + (\rho_1 \rho_2 B_1 + T_1^2 B_2) A_2^\pm, \quad \text{(C7a)}$$

$$U_{1+} = T_1^2 B_2 + (\rho_1 \rho_2 + \mu_{12}^2 u^2 A_1^+ B_2) B_1,$$
$$V_{1+} = u^2 T_{12}^2 + (\rho_1 \rho_2 B_2 + T_2^2 B_1) A_1^+, \quad \text{(C7b)}$$

$$U_{1\pm}^{2\pm} = T_2^2 \alpha_1^\pm B_1 + T_1^2 \alpha_2^\pm B_2 + \rho_1 \rho_2 (\alpha_1^\pm B_2 + \alpha_2^\pm B_1),$$
$$V_{1\pm}^{2\pm} = T_{12}^2 - \mu_{12}^2 \alpha_1^\pm B_1 \alpha_2^\pm B_2, \quad \text{(C7c)}$$

$$X_{1\pm}^{2\pm} = u^2 T_{12}^2 - (T_2^2 \alpha_1^\pm + \rho_1 \rho_2 \alpha_2^\pm) \beta_1,$$
$$Y_{1\pm}^{2\pm} = T_1^2 \alpha_2^\pm + (\rho_1 \rho_2 - \mu_{12}^2 u^2 \alpha_2^\pm \beta_1) \alpha_1^\pm. \quad \text{(C7d)}$$

Appendix D

Function Ψ_{II} that appears in (61) has the same form as that given for Ψ_I by (C1a). However, (C1b) and (C1c) are modified:

$$\psi_1 = \tan^{-1} \alpha_1^- \frac{N_1 + \Omega_{12} Q_B (A_2^+ - A_2^-)}{D_1 + \Omega_{12} Q_B A_1^+ (A_2^+ - A_2^-)}, \quad \text{(D1a)}$$

$$\psi_2 = \tan^{-1} \frac{\alpha_1^- N_{21} + \alpha_2^- N_{22} + \Omega_{12} Q_B (\alpha_1^- A_2^+ + \alpha_2^- A_1^+)}{D_2 + \Omega_{12} Q_B (A_1^+ A_2^+ - \alpha_1^- \alpha_2^-)}, \quad \text{(D1b)}$$

$$\psi_3 = \tan^{-1} \frac{N_3 + \Omega_{12} Q_B \alpha_2^- (\alpha_1^+ - \alpha_1^-)}{D_3 - \Omega_{12} Q_B A_2^+ (\alpha_1^+ - \alpha_1^-)}, \quad \text{(D1c)}$$

$$\psi_4 = \tan^{-1} \frac{u^2 N_4}{D_4 + \Omega_{12} Q_B (\alpha_1^+ - \alpha_1^-)(\alpha_2^+ - \alpha_2^-)}, \quad \text{(D1d)}$$

$$\psi_5 = \tan^{-1} \frac{1}{B_2} \frac{N_5 - \Omega_{12} T_2 \beta_1 (\alpha_1^+ - \alpha_1^-)(\alpha_2^+ - \alpha_2^-)}{D_5 + \Omega_{12} T_1 (\alpha_1^+ - \alpha_1^-)(\alpha_2^+ - \alpha_2^-)}. \quad \text{(D1e)}$$

In Equation (C2)–(C6) in Appendix C, (D1), (10b), (22a), (22e), (C2), (56) and (58) now hold, with argument u^2.

References

[Achenbach 1973] J. D. Achenbach, *Wave propagation in elastic solids*, North-Holland, Amsterdam, 1973.

[Brock 1997a] L. M. Brock, "Some results for Rayleigh and Stoneley signals in thermoelastic solids", *Indian J. Pure Ap. Mat.* **28**:6 (1997), 835–850. MR 1461194 (98e:73014)

[Brock 1997b] L. M. Brock, "Transient three-dimensional rayleigh and stoneley signal effects in thermoelastic solids", *Int. J. Solids Struct.* **34**:12 (1997), 1463–1478. MR 1442859 (98b:73015)

[Brock 1998] L. M. Brock, "Analytic results for roots of two irrational functions in elastic wave propagation", *J. Aust. Math. Soc. B* **40**:1 (1998), 72–79. MR 1707766 (2000d:74037)

[Brock 2004] L. M. Brock, "Dynamic contact and fracture: some results for transversely isotropic solids", pp. 50–60 in *Proceedings of the 7th National Congress on Mechanics* (Chania, Crete), edited by A. Kounadis et al., Hellenic Society for Theoretical and Applied Mechanics, 2004.

[Brock and Georgiadis 1999] L. M. Brock and H. G. Georgiadis, "Response of welded thermoelastic solids to the rapid motion of thermomechanical sources parallel to the interface", *Int. J. Solids Struct.* **36**:10 (1999), 1503–1521.

[Cagniard 1962] L. Cagniard, *Reflection and refraction of progressive seismic waves*, McGraw-Hill, New York, 1962. (E. A. Flinn and C. H. Dix, translators).

[Carrier and Pearson 1988] G. F. Carrier and C. E. Pearson, *Partial differential equations: theory and technique*, Academic Press, Boston, 1988. MR 952148 (89j:35001)

[Chadwick 1960] P. Chadwick, "Thermoelasticity. The dynamical theory", pp. 263–328 in *Progress in solid mechanics*, vol. 1, edited by I. N. Sneddon and R. Hill, North-Holland Publishing, Amsterdam, 1960. MR 0113406 (22 #4244)

[Chandrasekharia 1986] D. S. Chandrasekharia, "Thermoelasticity with second sound", *Appl. Mech. Rev.* **39** (1986), 355–376.

[Davis 1998] J. R. Davis (editor), *Metals handbook: desk edition*, edited by J. R. Davis, ASM International, Metals Park, OH, 1998.

[Fan and Lu 2002] Q.-M. Fan and W.-Q. Lu, "A new numerical method to simulate the non-fourier heat conduction in a single-phase medium", *Int. J. Heat Mass Tran.* **45**:13 (2002), 2815–2821.

[Green and Lindsay 1972] A. E. Green and K. A. Lindsay, "Thermoelasticity", *J. Elasticity* **2**:1 (1972), 1–7.

[Hille 1959] E. Hille, *Analytic function theory*, vol. 1, Introduction to higher mathematics, Ginn, Boston, 1959. MR 0107692 (21 #6415)

[Jones 1999] R. M. Jones, *Mechanics of composite materials*, Taylor and Francis, New York, 1999.

[Joseph and Preziosi 1989] D. D. Joseph and L. Preziosi, "Heat waves", *Rev. Mod. Phys.* **61**:1 (1989), 41–73. MR 977943 (89k:80001)

[Lamb 1904] H. Lamb, "On the propagation of tremors over the surface of an elastic solid", *Philos. T. Roy. Soc. A* **203** (1904), 1–42.

[Lord and Shulman 1967] H. W. Lord and Y. Shulman, "A generalized dynamical theory of thermoelasticity", *J. Mech. Phys. Solids* **15**:5 (1967), 299–309.

[Noble 1958] B. Noble, *Methods based on the Wiener-Hopf technique for the solution of partial differential equations*, vol. 7, International series of monographs on pure and applied mathematics, Pergamon Press, New York, 1958. MR 0102719 (21 #1505)

[Norris and Achenbach 1984] A. N. Norris and J. D. Achenbach, "Elastic wave diffraction by a semi-infinite crack in a transversely isotropic material", *Q. J. Mech. Appl. Math.* **37**:4 (1984), 565–580. MR 774907 (86a:73014)

[Sharma and Sharma 2002] J. N. Sharma and P. K. Sharma, "Free vibration analysis of homogeneous transversely isotropic thermoelastic cylindrical panel", *J. Therm. Stresses* **25**:2 (2002), 169–182.

[Sneddon 1972] I. N. Sneddon, *The use of integral transforms*, McGraw-Hill, New York, 1972.

[Stoneley 1924] R. Stoneley, "Elastic waves at the surface of separation of two solids", *P. Roy. Soc. Lond. A Mat.* **106**:738 (1924), 416–428.

LOUIS MILTON BROCK: brock@engr.uky.edu
Mechanical Engineering, University of Kentucky, 265 RGAN, Lexington, KY 40506-0503, United States

MECHANICAL BEHAVIOR AND CONSTITUTIVE MODELING OF METAL CORES

ASHKAN VAZIRI AND ZHENYU XUE

Studying the mechanical behavior of metal cores provides insight into the overall performance of structures comprising metal sandwich plates, and can help immensely in designing metal sandwich plates for specific engineering applications. In this study, the response of folded (corrugated) plate and pyramidal truss cores are explored under both quasistatic and dynamic loadings. In particular, two important characteristics of metal cores, the nonuniform hardening/softening evolution due to stressing in different directions and the rate-dependence, are discussed for different core topologies, including the square honeycomb core. In addition, the role of core behavior on the overall performance of sandwich plates is studied by employing a constitutive model for the elastic-plastic behavior of plastically compressible orthotropic materials [Xue et al. 2005]. The constitutive model is capable of capturing both the anisotropy of the core, associated with stressing in different directions, and its rate-dependence. The approach, based on employing the core constitutive model, not only significantly reduces the computation time, but also permits exploration of the role of each fundamental rate-dependent response of the metal core on the overall response of the metal sandwich plates.

1. Introduction

Recent studies have indicated the advantage of well-designed metal sandwich plates over solid plates under high intensity dynamic loading, where combinations of high strength and energy absorption are vital for the structural performance [Qiu et al. 2003; Xue and Hutchinson 2004a; Fleck and Deshpande 2004; Rathbun et al. 2006; Vaziri and Hutchinson 2007; Vaziri et al. 2007]. Metal sandwich plates encompass further advantages when the high intensity loading is transmitted through water, which can make them an excellent choice for ship protection [Xue and Hutchinson 2003; Hutchinson and Xue 2005; Liang et al. 2007]. On the other hand, sandwich plates with foam-filled cores have been shown to perform as well, or nearly as well, as plates of the same weight with unfilled cores [Vaziri et al. 2006]. Therefore, it appears that the multifunctional advantages of foam-filled cores such as acoustic and thermal insulation can be exploited without jeopardizing the structural performance of metal sandwich plates.

The volume fraction of the core occupied by metal and the core topology are important design aspects of all-metal sandwich plates [Xue and Hutchinson 2004a]. Three core topologies that have been commonly considered in the design of high-performance structures are square honeycomb, folded plate (corrugated) and pyramidal truss cores. Full-scale metal sandwich plates designed to be effective against impulsive loads have cores with a low volume fraction of material, typically less than 0.08 [Hutchinson

and Xue 2005]. In this study, the volume fraction of the core material is 2%, which is lower than the optimum configuration suggested by Xue and Hutchinson [2004a] for sandwich plates with the overall geometry in the meter scale. The rationale for studying thinner cores is based on their potential advantage for water blast by accounting for fluid-structure interaction [Liang et al. 2007]. Studying the behavior of metal cores not only provides insight regarding the overall performance of metal sandwich plates but also is required for developing a continuum model for sandwich plates. While the structural behavior of square honeycomb sandwich cores has been documented in recent numerical and theoretical investigation [Xue et al. 2005; Xue and Hutchinson 2006], the behavior of folded plate and pyramidal truss cores has not been studied rigorously. Consequently one of the main objectives of this study is to explore the mechanical response of folded and pyramidal truss cores under quasistatic and dynamic loadings (Sections 3 and 4). In Section 5, insight into the structural role of metal cores on the overall performance of sandwich plates is gained by employing a constitutive model proposed for the elastic-plastic behavior of plastically compressible orthotropic materials with nonuniform hardening or softening evolution associated with stressing in different directions [Xue et al. 2005]. In particular two intrinsic characteristics of the metal core, Nonuniform hardening/softening, and rate-dependence, are considered and their influence on the overall response of a folded sandwich plate is examined. The inputs to this constitutive model are identified based on the numerical simulation of the folded plate core behavior discussed in Section 3. All the calculations in this study are performed by employing the commercially available software ABAQUS [Abaqus 2005].

2. Specification of sandwich plates and material properties

Figure 1 shows the schematic diagram of folded plate and pyramidal truss core sandwich plates considered in this study. Both types of sandwich plates have core height H and face sheet thickness h. The folded plate core has thickness t and an inclination angle between the core web and the face sheet α, while the width of its periodic section is $B = t/\sin\alpha + H/\tan\alpha$. All members of the pyramidal truss core are identical and have solid square cross-sections of width t. Each truss member has three neighbors coming into contact at their corners with an angle of inclination between the truss and the face sheet, α. The width of a periodic section of the pyramidal truss core sandwich plate is $B = (t + t/\sin\alpha + H/\tan\alpha)/\sqrt{2}$.

For the *folded plate core*, the volume fraction of the core occupied by the material can be expressed as,

$$\bar{\rho}_c = \frac{t/H}{t/H + \cos\alpha}. \tag{1}$$

Similarly for the *pyramidal truss core*,

$$\bar{\rho}_c = \frac{2\sin\alpha}{(1 + \sin\alpha + \cos\alpha \cdot H/t)^2}, \tag{2}$$

and the total mass/area of the sandwich plate, M, is given by

$$M = \rho_s(2h + \bar{\rho}_c H). \tag{3}$$

For both types of sandwich plate, with L, M, and ρ_s specified, the geometry of the plate is fully determined by the three independent dimensionless parameters $\bar{\rho}_c$, H/L, and α. The face sheet thickness, h/L, is then determined in terms of $\bar{\rho}_c$ and H/L by Equation (3). Note that the top and bottom faces are
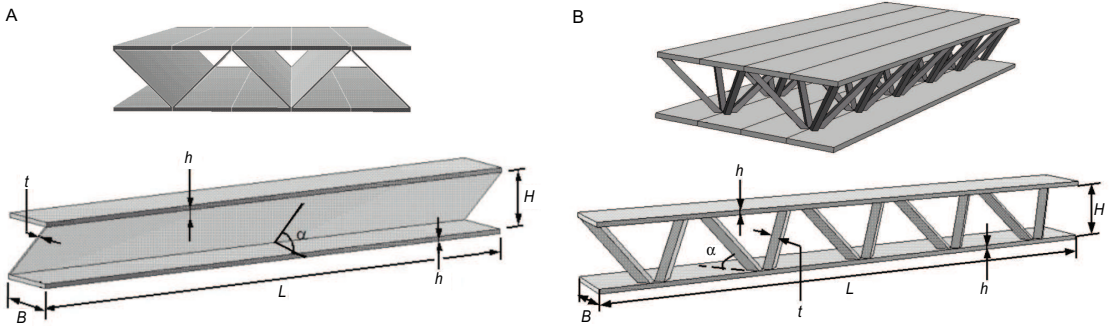
Figure 1. Schematic diagram of sandwich panels and corresponding computation model of sandwich panel: (a) folded sandwich plate; (b) pyramidal truss sandwich panel.

taken to have equal thickness in this study. In all the calculations presented in this paper, the following parameters are set to be constant: $M/\rho_s L = 0.02$, $H/L = 0.1$ and $L = 1$ m (width of the sandwich plates $= 2$ m).

The core and face sheets material of the sandwich plates are taken to be stainless steel (#304) with density of $\rho_s = 8000$ kg/m^3. A piecewise function has been fitted to the true stress-logarithmic strain tensile behavior of the material, giving

$$\sigma = \begin{cases} E\varepsilon, & \varepsilon \leq \sigma_Y/E, \\ \sigma_Y(E\varepsilon/\sigma_Y)^N, & \varepsilon > \sigma_Y/E, \end{cases} \tag{4}$$

with Young's modulus $E = 200$ GPa, Poisson ratio $\nu = 0.3$, tensile initial yield strength $\sigma_Y = 205$ MPa, and strain hardening exponent $N = 0.17$ [Boyer and Gall 1985]. The shear modulus and initial shear strength are $G = E/[2(1+\nu)] = 76.92$ GPa and $\tau_Y = \sigma_Y/\sqrt{3} = 118.35$ MPa. The material strain rate sensitivity of the steel is not taken into account. Classical flow theory of plasticity, based on the von Mises yield surface and isotropic hardening, is employed in the three-dimensional finite element simulations. The steel is assumed to be sufficiently ductile to sustain large strains without fracture.

3. Folded core unit cell response

The unit cell corresponding to the geometry of a folded plate core, along with the coordinate system used to define the anisotropy, are given in Figure 2a. Estimates of the overall elastic moduli associated with stressing in the directions of orthotropy, out-of-plane shearing, and in-plane shearing in two directions are obtained based on simple strength of materials formulas as described in [Xue and Hutchinson 2004b]:
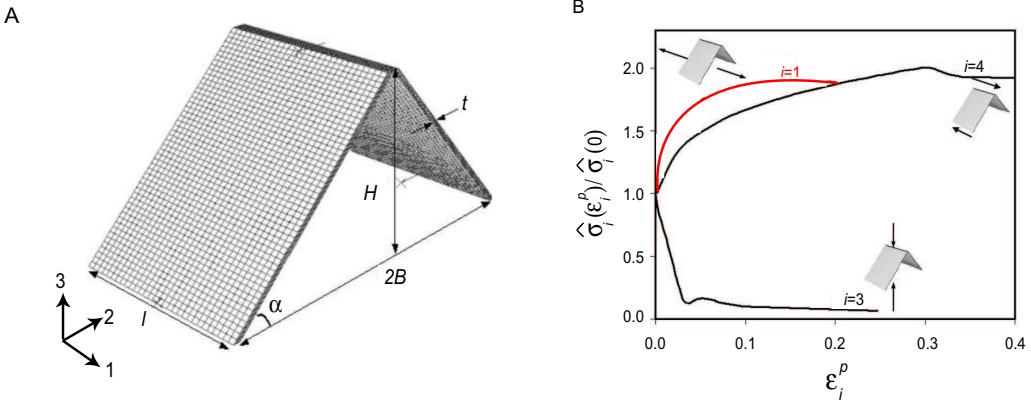
Figure 2. Mechanical behavior of folded plate cores: (a) finite element model of the folded core unit cell. (b) normalized true stress-true plastic strain relationships for three basic histories of the folded core with $\alpha = 45°$, $t/H = 0.0144$, corresponding to $B/H = 1.042$ and $\bar{\rho}_c = 0.02$. The true stresses are normalized by the theoretical values of the initial yield stress associated with each loading history under quasistatic loading, Equation (7). The horizontal axis is the plastic strain component ε_i^p associated with each stress history.

$$
\begin{aligned}
E_{11} &= \bar{\rho}_c E_s, \\
E_{33} &= \bar{\rho}_c E_s \sin^4 \alpha, \\
G_{13} &= \frac{1}{2} G_s \bar{\rho}_c \sin 2\alpha, \\
G_{23} &= \frac{1}{4} E_s \bar{\rho}_c \sin^2 2\alpha, \\
G_{12} &= \bar{\rho}_c G_s \sin^2 \alpha.
\end{aligned} \tag{5}
$$

Let the x_i axes be aligned with the orthotropic axes. Introduce stress, strain, and plastic strain vectors in the usual way with

$$
\begin{aligned}
\boldsymbol{\sigma} &= (\sigma_1, \sigma_2, \sigma_3, \sigma_4, \sigma_5, \sigma_6)^T \equiv (\sigma_{11}, \sigma_{22}, \sigma_{33}, \sigma_{13}, \sigma_{23}, \sigma_{12})^T, \\
\boldsymbol{\varepsilon} &= (\varepsilon_1, \varepsilon_2, \varepsilon_3, \varepsilon_4, \varepsilon_5, \varepsilon_6)^T \equiv (\varepsilon_{11}, \varepsilon_{22}, \varepsilon_{33}, 2\varepsilon_{13}, 2\varepsilon_{23}, 2\varepsilon_{12})^T, \\
\boldsymbol{\varepsilon}^P &= (\varepsilon_1^P, \varepsilon_2^P, \varepsilon_3^P, \varepsilon_4^P, \varepsilon_5^P, \varepsilon_6^P)^T \equiv (\varepsilon_{11}^P, \varepsilon_{22}^P, \varepsilon_{33}^P, 2\varepsilon_{13}^P, 2\varepsilon_{23}^P, 2\varepsilon_{12}^P)^T.
\end{aligned} \tag{6}
$$

Estimates for the initial quasistatic yield values in the directions of orthotropy, $\hat{\sigma}_i(0)$, are given by,

$$
\begin{aligned}
\hat{\sigma}_1(0) &= \bar{\rho}_c \sigma_Y, \\
\hat{\sigma}_3(0) &= \frac{2}{\sqrt{3}} \bar{\rho}_c \sigma_Y \sin^2 \alpha, \\
\hat{\sigma}_4(0) &= \hat{\sigma}_6(0) = \bar{\rho}_c \tau_Y \sin \alpha, \\
\hat{\sigma}_5(0) &= \frac{1}{2} \bar{\rho}_c \sigma_Y \sin 2\alpha.
\end{aligned} \tag{7}
$$

As in the case of overall elastic stiffness, these estimates are based on elementary estimates from the strength of materials, and it was assumed that under crushing, yielding precedes the buckling of the core plate. The factor $(2/\sqrt{3})$ (for web materials having a von Mises yield surface) reflects the constraint of the faces such that the webs undergo plane strain tension (compression). It is noteworthy that E_{22} and $\hat{\sigma}_2(0)$ are exceedingly low and essentially irrelevant to the overall performance of sandwich plates as the faces supply essentially all the tensile strength and stiffness. In the calculations, they are taken as $\hat{\sigma}_2(0) = \bar{\rho}_c \sigma_Y / 200$, and $E_{22} = \bar{\rho}_c E_s / 200$.

The core responses under both quasistatic and dynamic loadings are calculated for a folded plate core having $\alpha = 45°$ and $t/H = 0.0144$, (corresponding to $\bar{\rho}_c = 0.02$).

3.1. *Numerical results for unit cell response under quasistatic loading.* Periodic boundary conditions consistent with each loading history are imposed on the unit cell of the folded plate core. Under compression and shear loadings, rigid plates are bonded to top and bottom surfaces of the unit cell to simulate the behavior of the core attached to the face sheets. The bottom rigid plate is fixed and the top face is displaced. Figure 2b depicts the strain-stress curves of the folded plate core computed for three basic loading histories: in-plane stretching, out-of-plane shearing, and core crushing in the vertical direction. The dimensions of the folded core under study are such that under crushing, elastic buckling precedes yielding and the compression curve, $\hat{\sigma}_3(\varepsilon_3^P)$, falls sharply with buckling and yielding. Under out-of-plane shear, the response subsequent to buckling depends on the length of the segment as discussed in [Xue and Hutchinson 2004b]. In the results shown in Figure 2b, the length of the unit cell is taken to be equal to B, where yielding occurs prior to elastic buckling, and plastic buckling is the source of nonlinear deformation. Similar calculations were performed in [Xue and Hutchinson 2004b] and [Vaziri et al. 2006] for a higher relative density of the core, where yielding of the steel core precedes its elastic buckling under crushing. At early stages of deformation under out-of-plane shear ($\varepsilon_4^p < 0.2$), the shear-induced compaction of the core is almost zero, which corresponds to associated flow with respect to the ellipsoidal yield surface [Mohr et al. 2006].

In order to gain insight into the interaction among the stresses under multiaxial stressing, the initial yield surface of the folded core, defined as the onset of significant nonlinearity for the present purpose, is attained using the three-dimensional unit cell for two combinations of loading: (i) in-plane tension and core crushing (σ_1, σ_3), and (ii) core crushing and out-of-plane shear (σ_3, σ_4). The calculations are performed to simulate the response of the core unit cell under displacement control loading. Various ratios of displacements associated with each combined loading are imposed to specify the initial yield surface. The boundary conditions for the core under combined core crushing and out-of-plane shear are akin to the boundary conditions employed for calculating the strain-stress behavior under out-of-plane shear. For combined loading of core compression and in-plane tension, the edges of the web aligned with the direction of loading are displaced relative to one another uniformly, while a uniform crushing displacement is imposed. The calculated initial yield surfaces for the aforementioned combinations of loading, along with the prediction from the ellipsoidal yield surface invoked in the proposed constitutive model when all the plastic Poisson ratios are zero, are presented in Figure 3. Note that in the proposed constitutive model, an ellipsoidal yield surface is invoked that generalizes Hill's surface for orthotropic plastically incompressible materials. This ellipsoidal yield surface can be written in the form of
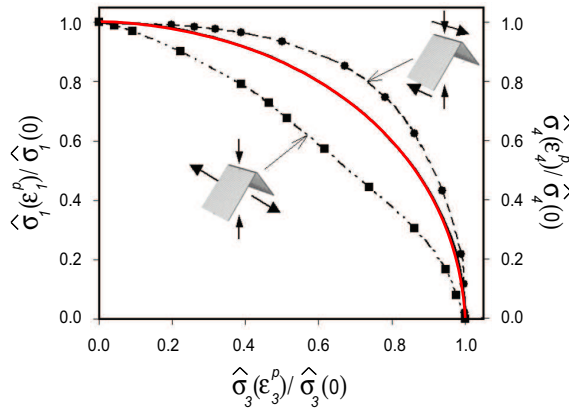
$$f \equiv \sigma_{\text{eff}} - \sigma_0 = 0$$

Figure 3. Initial yield surface of the folded plate core subject to two different combined loadings. The true stresses are normalized by the initial yield stress associated with each simple loading history under quasistatic loading. The solid line corresponds to the ellipsoidal yield surface invoked in the constitutive model when all the plastic Poisson ratios are taken to be zero. The folded core has the same geometrical parameter as that in Figure 2.

where the effective stress σ_{eff} is defined by

$$(\sigma_{\text{eff}}/\sigma_0)^2 = \sum_{i=1}^{6} (\sigma_i/\hat{\sigma}_i)^2$$

for the case that plastic Poisson ratios are zero. The stress quantity σ_0 is a fixed reference stress that can be chosen arbitrarily. $\hat{\sigma}_i(\varepsilon_i^P)$ denotes the hardening (or softening) function specifying the dependence of σ_i on the associated plastic strain component. See [Xue et al. 2005] for details. Figure 3 shows that the unit cell results for combination of crushing and out-of-plane shear indicate that the proposed constitutive model overestimates the interaction among the stresses under this loading condition at early stages of deformation. For combined core crushing and in-plane tension, the folded plate core has an initial yield surface which nearly mimics the generalized Hill's surface for orthotropic plastic incompressible materials, as the plastic incompressibility of the steel core contributes remarkably to its overall behavior at the onset of plastic deformation. As the deformation proceeds under combined core crushing and in-plane tension, the apparent plastic Poisson ratio abruptly decreases and then approaches zero, and the calculated yield surface approaches the prediction from the proposed constitutive model. This happens for an effective plastic strain smaller than 5%. (The numerical results are not shown for the sake of brevity).

Similar computations are performed for the folded plate core with higher core volume fraction $\bar{\rho}_c = 0.04$ ($\alpha = 45°$, $t/H = 0.0295$), for which the material yielding precedes the buckling of the core under core crushing. The computed initial yield surfaces associated with each loading combination are very close to the yield surface invoked in the proposed constitutive model. Similar conclusions are made for the response of the square honeycomb cores [Xue et al. 2005], hexagonal aluminum honeycomb with volume fraction of 0.02 [Doyoyo and Mohr 2003; Mohr and Doyoyo 2004] and pyramidal truss cores

(results not shown). The initial yield surface and failure surface of metal sandwich cores, specifically honeycomb cores under an in-plane state of stress, have been reported by several groups [Gibson et al. 1989; Papka and Kyriakides 1999; Okumura et al. 2002]. Wang and McDowell [2005] studied the initial yield surface of several periodic metal honeycomb cores with high relative density under in-plane biaxial and triaxial stress states. For all the cases studied, the relative density of the core is sufficiently high that the initial nonlinearity of the response is mainly due to plastic yielding of the core material. The developed analytical model revealed a strong interaction between stresses for combined loading of crushing and in-plane stretching.

3.2. *Numerical results for unit cell response under dynamic loading.* In this section, we study the rate-dependent behavior of the folded plate core under crushing and out-of-plane shear. The boundary conditions associated with each loading history are similar to those described in Section 3.1. Rigid plates are bonded to the top and bottom surfaces of the unit cell to simulate the behavior of the core attached to the face sheets. Equal and opposite constant velocities, V_3 and V_4, are applied to the top and bottom rigid faces to invoke a constant strain rate for core crushing and for shearing, respectively. The center of mass of the core is stationary during each loading. The associated overall strain rates of the core are defined as $\dot{\bar{\varepsilon}}_3 = 2V_3/H$ for dynamic core crushing and $\dot{\bar{\varepsilon}}_4 = 2V_4/H$ for dynamic core shearing.

The dependence of the overall crushing response of the folded core on the overall strain rate is presented in Figure 4a. The overall compressive stress, $\hat{\sigma}_3$, is normalized by its theoretical quasistatic initial yield value, $\hat{\sigma}_3(0)$ (from Equation (7)). The range of crushing strain rates selected in Figure 4a is widely representative of shock-loaded metal sandwich plates. The deformed configurations of the folded core subject to various crushing strain rates are depicted in Figure 4b at the overall crushing strain of 0.5, that is, the relative displacement of top and bottom faces is equal to half of the original core height. The strain rate dependence of core response is related to three effects: (i) inertia resistance in the vertical direction, (ii) inertial stabilization of the core plates against buckling, and (iii) contact between the core plates and top and bottom faces. Note that the material strain rate-dependence is not taken into account in these calculations. The inertia resistance elevates the level of stress at early stages of deformation. It is informative to compare these results with those of the square honeycomb core with the same steel core density presented in [Xue et al. 2005]. The influence of inertia resistance at early stages of deformation appears to be similar for both core topologies. However, while the core resistance can be maintained up to large deformations for the square honeycomb core, it falls steadily with deformation for the folded core as seen in Figure 4b. In general, the webs of the square honeycomb do not come in contact with the bottom and top faces except at very large core compressions, while the webs of the folded plate core make contact with the faces at relatively early stages of crushing. Increasing the strain rate alters the underlying mechanism of crushing deformation of the folded plate core; higher strain rates lead to a more localized deformation of the folded plate at the junctions with the face sheets resulting in earlier contact of the folded plate with the face sheets. The contacts elevate the overall crushing strength of the folded core at relatively early stages of deformation (for example, for $\dot{\bar{\varepsilon}}_3 = 2000\,\mathrm{s}^{-1}$ at the effective plastic strain ∼0.12). This phenomenon is to some extent analogous to the densification effect of the foam materials at high levels of deformation. As the deformation proceeds, a secondary elevation of stress is observed due to additional contacts, occurring at much larger deformations (for example, for $\dot{\bar{\varepsilon}}_3 = 2000\,\mathrm{s}^{-1}$ at the effective plastic strain ∼0.85, see inset of Figure 4a). Larger deformations result in the full densification
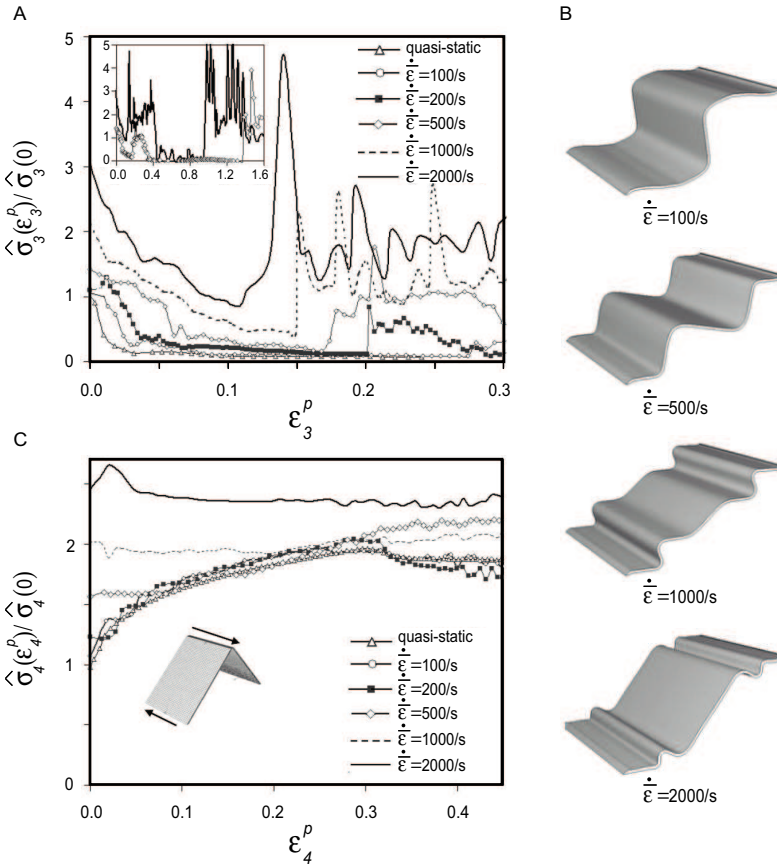
Figure 4. Rate dependence behavior of folded plate cores: (a) effect of crushing rate on the normalized true stress-true plastic strain relation of the folded core under core crushing. Inset: additional contacts occur at large deformations which lead to sudden elevation of stress; (b) deformed configurations of the folded plate core unit cell subject to various crushing rates at average crushing strain of 0.5; (c) dynamic response of the folded plate core under out-of-plane shear. The true stresses are normalized by the theoretical values of the initial yield stress associated with each loading history under quasistatic loading, Equation (7). The folded core has the same geometrical parameter as that in Figure 2.

of the core. It is noteworthy that at high strain rates, square honeycomb cores are more effective than folded plate cores for energy dissipation, mainly due to stabilization of the webs against buckling, an effect that promotes the axial compression of the webs. We will discuss this further when assessing the response of folded sandwich plates under high intensity loading in Section 5.2.

Figure 4c presents the overall out-of-plane shear response of the folded core (normalized by its theoretical quasistatic initial yield values, $\hat{\sigma}_4(0)$) subjected to various engineering strain rates. The strain rate-dependence of the dynamic core shearing is mainly attributed to the microinertia effects and stabilization

of the core plate against shear buckling. The contact between the core plate and face sheets is not evident in the range of deformation considered in Figure 4c.

4. Pyramidal truss core unit cell response

The geometry of the pyramidal truss core along with the coordinate system used to define the anisotropy are depicted in Figure 5a. In the computational model, the ends of the truss members are constrained, assuming that the ends are welded to the rigid face sheets. The overall elastic moduli associated with crushing and out-of-plane shear responses of the pyramidal truss core are estimated based on simple strength-of-materials formulas as follows:

$$E_{22} = \bar{\rho}_c E \sin^4 \alpha,$$
$$G_{12} = G_{23} = \frac{1}{8} \bar{\rho}_c E \sin^2 2\alpha. \tag{8}$$

Estimates for the initial quasistatic yield values, $\hat{\sigma}_i(0)$, are given by,

$$\hat{\sigma}_3(0) = \sigma_Y \bar{\rho}_c \sin^2 \alpha,$$
$$\hat{\sigma}_4(0) = \hat{\sigma}_5(0) = \frac{1}{2\sqrt{2}} \sigma_Y \bar{\rho}_c \sin 2\alpha. \tag{9}$$

The pyramidal truss core responses under quasistatic and dynamic loadings are calculated for the following geometrical parameters: $\alpha = 45°$, $t/H = 0.1055$, which corresponds to $\bar{\rho}_c = 0.02$.

4.1. *Numerical results for unit cell response under quasistatic loading.* In this section are described simulations that have been performed to ascertain the basic stress histories of the pyramidal truss core under crushing and out-of-plane shear, Figure 5b. The imposed boundary conditions associated with each loading history are similar to those employed in Section 3.1 for the folded plate core. Under crushing, yielding of the truss members is followed by their plastic buckling, which results in a significant reduction in the load carrying capacity of the core under crushing. As in the case of folded plate cores, at large deformation the truss members make contact with the rigid face sheets. This contact leads to a significant elevation in the load carrying capacity of the pyramidal truss core, analogous to the effect of densification on the crushing response of foam materials. The displaced configurations of the pyramidal truss core at different overall crushing strains are depicted in Figure 5c. The overall response of the pyramidal truss core under out-of-plane shear is associated with utterly dissimilar deformations of the truss members: two of the truss members of the core unit cell shown in Figure 5a undergo stretching, while the other two truss members experience compression. As the deformation proceeds, the plastic yielding of the truss cores is followed by the buckling of the members under compression, which leads to a considerable reduction in the load carrying capacity of the pyramidal truss core, Figure 5b. The softening exhibited by the core under out-of-plane shear is contrary to the behavior of folded plate and square honeycomb cores where the webs undergo plastic buckling but with no significant softening. For sandwich plates with the overall geometry on the meter scale under quasistatic loading, the first occurrence of nonlinearity in most applications is related to buckling of core members due to out-of-plane shear as discussed for rigid punch indentation of folded sandwich plates in Section 5.1. The softening of the pyramidal truss core under out-of-plane shear could jeopardize the structural performance of pyramidal truss core sandwich
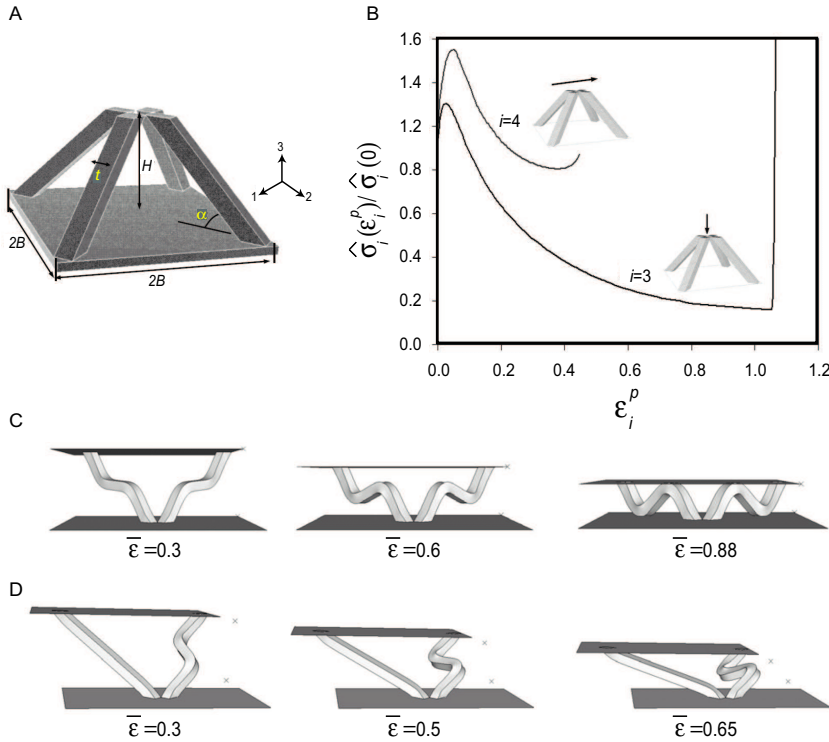
Figure 5. Mechanical behavior of pyramidal truss cores: (a) schematic diagram of a pyramidal truss core unit cell; (b) normalized true stress-true plastic strain response of the pyramidal truss cores with $\alpha = 45°$, $t/H = 0.1055$, corresponding to $\bar{\rho}_c = 0.02$ under two basic loading histories. The true stresses are normalized by the theoretical values of the initial yield stress associated with each loading history under quasistatic loading; see Equation (9) (c) and (d); deformed configurations of the pyramidal truss core unit cell at different levels of average engineering strain, $\bar{\varepsilon}$, subject to core crushing (c) and out-of-plane shear (d).

plates [Xue and Hutchinson 2004a]. Figure 5d depicts the displaced configurations of the pyramidal truss core at different overall shear strains. It is also noteworthy that the strength and stiffness associated with in-plane stretching and shearing are exceptionally low for pyramidal truss cores but of little consequence to the structural performance of the sandwich plates in most applications.

4.2. *Numerical results for unit cell response under dynamic loading.* Finite element simulations have been carried out to study the effect of deformation rate on the dynamic behavior of the pyramidal truss core under crushing and out-of-plane shear following the same procedure discussed in Section 3.2. The overall responses of the pyramidal truss core subject to different crushing strain rates are depicted in Figure 6a. Firstly, inertia resistance in the vertical direction, which manifests as plastic wave propagation, elevates the initial level of stress [Vaughn et al. 2005]. Secondly, the core starts to soften at very early stages of deformation due to the buckling of each truss member triggered by its tilt. Thirdly, the contact between the truss members and the faces generally does not occur until relatively large
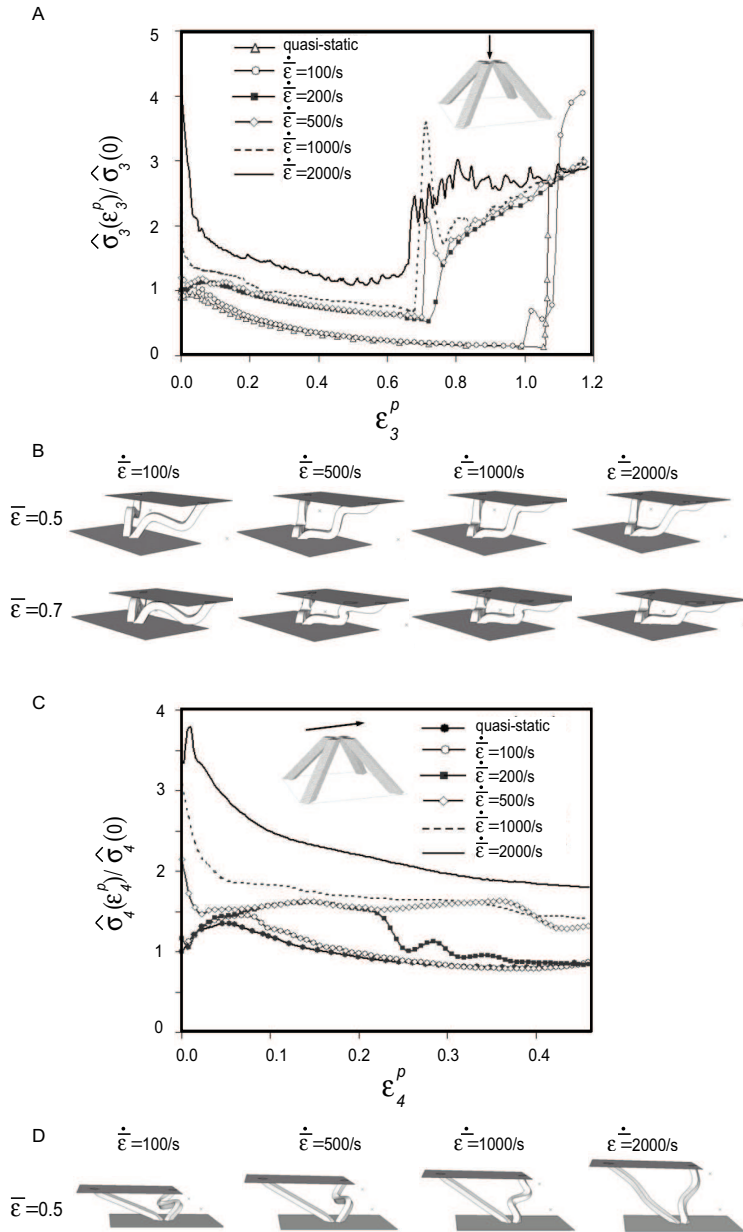
Figure 6. Rate dependence behavior of pyramidal truss cores. Dynamic response of a pyramidal truss core with $\alpha = 45°$, $t/H = 0.1055$, corresponding to $\bar{\rho}_c = 0.02$ under crushing and out-of-plane shear at different deformation rates is quantified in (a) and (c), respectively. Deformed configurations of the pyramidal truss core under crushing at different crushing rates are depicted in (b) at two different stages of deformation corresponding to average crushing strain of 0.5 and 0.7. Similarly, the deformed configurations of the core subject to out-of-plane shear at different strain rates are shown in (d) at the average crushing strain of 0.5. The pyramidal truss core has the same geometrical parameter as that in Figure 5.

deformations, which results in a sudden increase in the load carrying capacity of the core under crushing. It is noteworthy that there is little difference between deformed configurations of the truss cores subject to crushing strains in the range of 200–2000 s^{-1}, leading to low sensitivity for the onset of densification on the crushing strain rate (the contact between the truss cores and the face sheets occurs at the plastic strain of $\varepsilon_3^p \sim 0.7$ for overall strain rates equal to or higher than 200 s^{-1}). This is in sharp contrast to the response exhibited by the folded plate cores in Figure 4a and 4b, where the crushing rate significantly alters the deformation of the core.

The dynamic shear response of the pyramidal truss core is quantified in Figure 6c. The deformed configurations of the pyramidal truss core, subject to various strain rates under out-of-plane shear, are depicted in Figure 6d at an average crushing strain of 0.5. At high deformation rates, the inertia resistance enhances the overall dynamic strength of the pyramidal truss core by elevating the level of stress of the truss members under stretching, and also by stabilizing the members, which undergo shear-induced compaction. This leads to an utterly different overall behavior compared to folded plate cores (see Section 3.2) and square honeycomb cores [Xue et al. 2005].

5. Folded sandwich plate response

Computational tools are indispensable for augmenting experimental techniques for assessing the structural performance of metal sandwich plates. This, in general, entails full three-dimensional models of sandwich plates subject to quasistatic and dynamic loading, and consideration of the geometrical details of the core [Xue and Hutchinson 2004a]. These calculations are extremely expensive and even unrealistic for complex structures. Such computation limitations motivate an alternative approach based on continuum representation of the metal cores. Recently, we have developed a constitutive model for the elastic-plastic behavior of plastically compressible orthotropic materials with nonuniform hardening or softening evolution in different stressing directions. This constitutive model invokes an ellipsoidal yield surface with evolving ellipticity to accommodate the nonuniform stress-strain responses under the six fundamental stress histories in the orthotropic axes. Furthermore, the model is able to incorporate rate-dependence arising from material rate-dependence, inertial effects, as well as geometrical constraints (for example, contact). The general formulation of the constitutive model for plastically compressible orthotropic materials is able to incorporate nonconstant plastic Poisson ratios in the axes of anisotropy (for example, the plastic Poisson ratios can be a function of plastic strain). However, for the sandwich plates under study, the plastic deformation of the core is well approximated by taking all plastic Poisson ratios as zero. The readers are referred to [Xue et al. 2005] for details of the constitutive model. The proposed model is employed in this paper to investigate the structural role of sandwich cores on the overall response of folded sandwich plates, and complements our previous work on the structural performance of square honeycomb sandwich plates [Xue et al. 2005]. Specifically, infinite folded plates of width 2m that are clamped along their edges (Figure 1) and subject to (i) quasistatic punch load and (ii) dynamic impulsive pressure load, are considered to illustrate the applicability of the proposed constitutive model for simulating and predicting the overall response of sandwich plates. To assess the accuracy of the approach based on the constitutive model, a set of calculations is performed using three-dimensional finite element models of the folded core with full meshing of the core geometrical details. Three-dimensional finite element models employ the geometrical unit of the plate, exploiting the

periodicity of the plate in its long direction. The faces are modeled by the classical plasticity with the von Mises yield criterion and isotropic hardening, with material properties given in Section 2. On the other hand, finite element models of the sandwich plate with continuum core models satisfy plane strain conditions for the loadings under study in this section, rendering the problem two dimensional. In all the calculations, which employ the proposed core continuum model, the core is modeled using one element through thickness. It is noteworthy that the proposed core continuum model, as a macroscopic modeling approach, cannot predict the details of structural localization. This is discussed further in [Mohr et al. 2006].

5.1. *Numerical results for quasistatic loading of folded sandwich plate.* Like the plate, the rigid punch in Figure 7a is infinite in the direction perpendicular to the cross-section shown, and has the half-width and edge radius of $a_{\text{punch}}/L = 0.3$ and $R_{\text{punch}}/a_{\text{punch}} = 0.334$, respectively. The sandwich plate has the normalized mass per unit area, $M/(\rho_s L) = 0.02$. For clamped sandwich plates subject to transverse loads, the important basic stressing histories of the core are: crushing normal to the sandwich faces; out-of-plane shear; and in-plane stretching. Here, the flexibility offered by the core constitutive model is employed to highlight the role of individual basic stressing histories of the core on the overall performance of sandwich plates. Calculations for three sets of inputs have been carried out:

(A) All six input functions, $\hat{\sigma}_i$. The stress-strain response under each basic stressing history is transferred directly from the numerical simulations presented in Section 3.1 into the code.

(B) Uniform hardening with all components specified by the crushing response, $\hat{\sigma}_i = \hat{\sigma}_3$

(C) Uniform hardening with all components specified by the shear response, $\hat{\sigma}_i = \hat{\sigma}_4$.

For each set of calculations, the elastic constants and the initial yields are predicted based on simple strength-of-material relations, Equations (5), and (7). The constitutive model provides two hardening formulations for representing the core behavior as outlined in [Xue et al. 2005]. In this paper, all the calculations are performed using the Coupled Hardening Formulations.

Figure 7b displays the variation of normalized reacting force/length of the punch, P/P_c versus the normalized displacement of the punch, δ_{Punch}/L based on the full three-dimensional simulation and also the continuum models with the abovementioned inputs (A–C). P_c is the limit load/length for a perfectly plastic empty sandwich plate having limited bending moment/length, (based only on contributions from the faces), for example,

$$P_c = 4\sigma_Y hH/L. \tag{10}$$

The variation of the average compressive strain of the folded plate core at its middle section,

$$\bar{\varepsilon}_c = \Delta H/H$$

(where ΔH is the reduction in core height), with the normalized punch displacement, δ_{Punch}/L, for the same set of simulations is depicted in Figure 7c. The dimensions of the sandwich plate and its material properties are such that the core yielding in shear is the first occurrence of nonlinear behavior followed by core crushing due to elastic buckling of the core plate beneath the punch. The same mechanism of response is observed for square honeycomb and pyramidal truss sandwich plates with the same steel core density. However, the elastic buckling of the square honeycomb cores occurs at significantly larger punch displacement. The results from the three-dimensional finite element simulation indicate that the
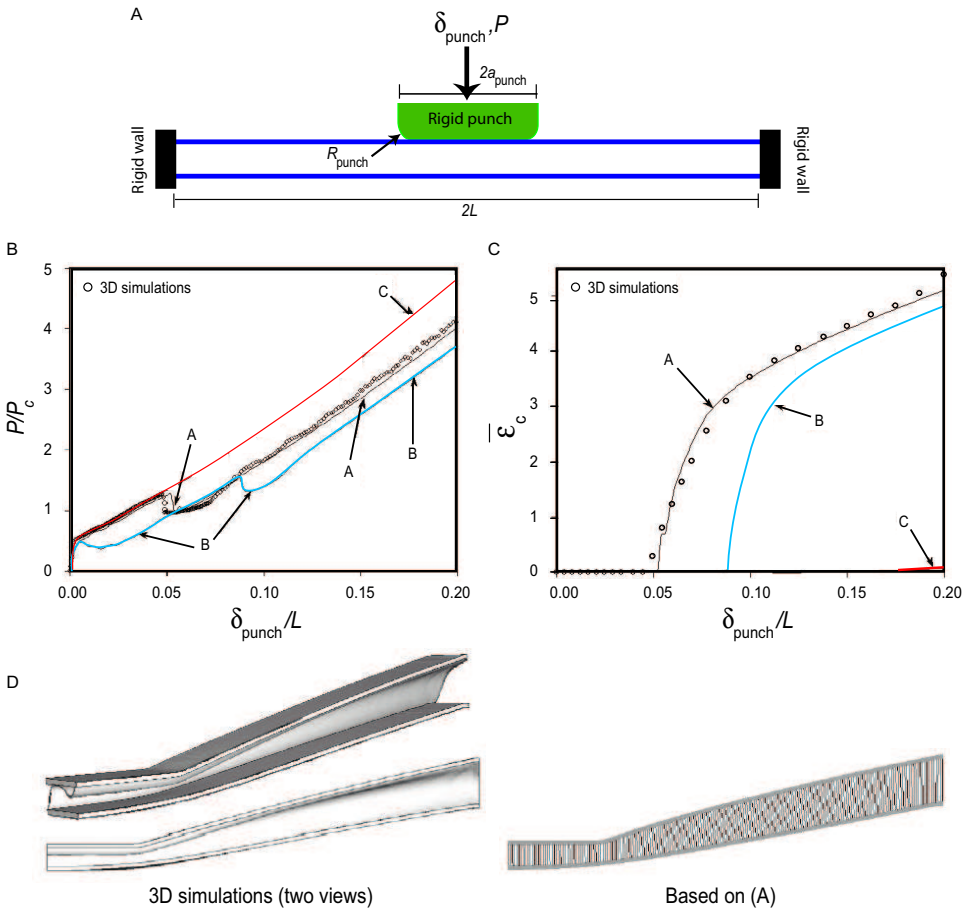
Figure 7. Folded sandwich plates subject to quasistatic rigid punch indentation: (a) schematic diagram of the folded core sandwich plate subject to punch loading; the rigid punch is infinite in the direction perpendicular to the cross-section shown and has normalized half width of $a_{\text{punch}}/L = 0.3$ and normalized edge radius of $R_{\text{punch}}/a_{\text{punch}} = 0.334$. The folded core has the same geometrical parameter as that in Figure 2. The sandwich plate has the total mass per unit area, $M/(\rho_s L) = 0.02$; (b) normalized reaction force applied to the rigid punch, P/P_c verses normalized punch displacement, δ_{Punch}/L, obtained based on both the three-dimensional finite element model of the sandwich plate and the proposed continuum core model; (c) dependence of the average compressive strain of the core at its center, $\bar{\varepsilon}_c$, on the normalized punch displacement, δ_{Punch}/L; (d) deformed configuration at $\delta_{\text{Punch}}/L = 0.2$ predicted from the three-dimensional finite element model and by employing input set A in the proposed continuum core model.

elastic buckling of the core occurs at $\delta_{\text{Punch}}/L \approx 0.05$. By employing the input set (C), the initial nonlinear response of the sandwich plate can be predicted accurately. However, the unrealistic hardening behavior in crushing represented by (C), as opposed to softening, suppresses nearly all core crushing, as is evident in Figures 7c and 7d. On the other hand, uniform *hardening* based on inputting the crushing
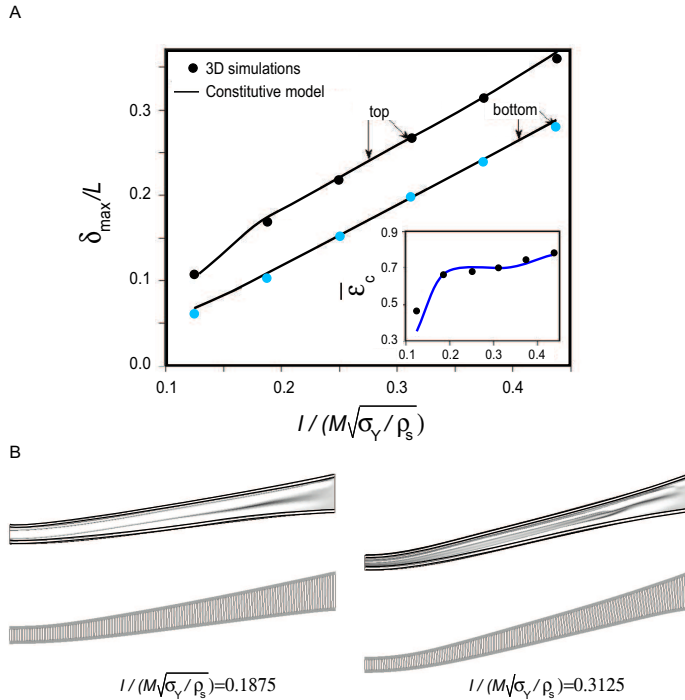
Figure 8. Folded sandwich plates subject to uniform shock loading: (a) normalized maximum deflection of the top and bottom faces of the folded sandwich plate versus normalized momentum imparted to the sandwich plate, $I/(M\sqrt{\sigma_Y/\rho_s})$. Inset: Residual average compressive strain of the core at its middle, $\bar{\varepsilon}_c$, versus $I/(M\sqrt{\sigma_Y/\rho_s})$. The results are obtained based on both three-dimensional finite element model of the sandwich plate and the proposed continuum core model. The sandwich plate has the same geometrical parameter as that in Figure 7. (b) Finalized deformed configurations of the folded core sandwich plates subject to two different impulse levels predicted using the three-dimensional finite element model (left) and the proposed continuum core model (right).

stress-strain curve (B) severely underestimates the early strength of the sandwich plate because of the unrealistic representation of the shear behavior. The inputs using all six basic stress-strain curves (A) rather accurately reproduce the entire load-deflection curve, as well as the crushing strain. The displaced configuration of the folded sandwich plates corresponding to $\delta_{\text{Punch}}/L = 0.2$ under the rigid indentation load applied at the center of the sandwich plate for the three dimensional finite element model and also the model based on the continuum representation of the core based on (A) are depicted in Figure 7d.

5.2. *Numerical results for dynamic loading of folded sandwich plate.* For $t \geq 0$, a pressure $p = p_0 e^{-t/t_0}$ is applied uniformly over the upper face sheet of the sandwich plate to simulate a shock transmitted through air to the metal sandwich plates [Taylor 1963; Smith and Hetherington 1994]. The decay time of the pressure pulse is set at $t_0 = 10^{-4}$ s, which is a typical decay period for a high intensity pulse

generated in air. Without accounting for fluid-structure interaction, the transmitted momentum/area is $I_0 = \int_0^\infty p\,dt = p_0 t_0$.

Computations are carried out at different levels of dynamic loading as measured by the normalized impulse $I/(M\sqrt{\sigma_Y/\rho_s})$. The inputs to the constitutive model are identified using the numerical simulations presented in Section 3. Figure 8a presents the normalized maximum deflection of the top and bottom faces, $\delta_{\max}/L$, and the crushing strain in the center of the plate at the final deformed state as a function of the dimensionless impulse. For the folded sandwich plate under study, the excessive crushing of the steel core clearly compromises the performance of the sandwich plate such that the crushing strain is almost 75%. Figure 8b compares the final deformed state predicted by the three-dimensional finite element simulations with that based on the constitutive model for two different levels of impulse. It is clear from Figure 8 that the continuum constitutive model captures the overall deflection of the sandwich plate, as well as the average crushing strain of the folded plate core with remarkable fidelity.

An additional set of calculations is carried out to highlight the effect of rate-dependent behavior of the core under crushing on the overall response of the folded sandwich plate. The calculations are performed by employing the constitutive model without accounting for the strain rate influence when representing the core behavior under crushing (for example, a quasistatic response is used to represent the core response under crushing). Although there are some differences in the details of the response, such as the history of energy dissipation in the sandwich plate constituent, the finalized configurations and the overall performance of the folded sandwich plate can be predicted accurately using this model. The behavior of folded sandwich plates is different from that of the square honeycomb sandwich plates in which case ignoring the dependence of the crushing response on the deformation rate significantly underestimates their structural performance under a high intensity pulse [Xue et al. 2005]. As discussed in Section 3.2, the plastic energy dissipation associated with core crushing is not significantly altered by varying the strain rates for folded plate cores. It is also noteworthy that in most applications, the core shearing strain rate in metal sandwich plates is considerably lower than $1000\,\mathrm{s}^{-1}$. In this range, the rate-dependent behavior of a metal core subject to out-of-plane shear is not significant and can be neglected in analyzing the structural performance of sandwich plates.

6. Concluding remarks

Metal sandwich plates have been considered recently for designing high-performance structures, specifically for enhancing the resistance of structures under shock loading. The structural performance of metal sandwich plates under dynamic loading, which involves both material and geometric nonlinearity, is governed by complex localized phenomena, including dynamic buckling and microinertial resistance associated with core crushing. In the present study, mechanical behavior of folded plate and pyramidal truss metal cores under both quasistatic and dynamic loadings are discussed. This study complements previous studies on the mechanical behavior of square honeycomb cores [Xue et al. 2005; Xue and Hutchinson 2006], pyramidal truss cores [Lee et al. 2006] and polymeric foam-filled cores [Vaziri et al. 2006], and has direct implications in designing high-performance metal sandwich plates. This study also further emphasizes the importance of 'core topology' as one of the major design criteria for metal sandwich plates, as also illustrated in studies on failure of metal sandwich plates [Vaziri et al. 2007]. In the second part of this study, a recently-developed constitutive model for the elastic-plastic behavior

of orthotropic materials with nonuniform hardening or softening under stressing in different directions [Xue et al. 2005] is employed to study the structural response of large scale folded metal sandwich plates under both quasistatic and dynamic loadings. Insights into the structural performance of these structures, specifically the role of core material behavior, are gained by using the capabilities of the proposed constitutive model such as selecting the input curves which represent the rate-dependent behavior of the core material under each basic stressing history.

Acknowledgment

References

[Abaqus 2005] Abaqus, *Abaqus version 6.5 reference manuals*, Abaqus Inc., Providence, R.I., 2005.

[Boyer and Gall 1985] H. E. Boyer and T. L. Gall, *Metals handbook desk edition*, American Society for Metals, 1985.

[Doyoyo and Mohr 2003] M. Doyoyo and D. Mohr, "Microstructural response of aluminum honeycomb to combined out of plan loading", *Mech. Mater.* **35** (2003), 865–876.

[Fleck and Deshpande 2004] N. A. Fleck and V. S. Deshpande, "The resistance of clamped sandwich beams to shock loading", *J. Appl. Mech. (Trans. ASME)* **71** (2004), 386–401.

[Gibson et al. 1989] L. J. Gibson, M. F. Ashby, J. Zhang, and T. C. Triantafillou, "Failure surfaces for cellular materials under multiaxial loads I. Modeling", *Int. J. Mech. Sci.* **31** (1989), 635–663.

[Hutchinson and Xue 2005] J. W. Hutchinson and Z. Xue, "Metal sandwich plates optimized for pressure impulses", *Int. J. Mech. Sci.* **47** (2005), 545–569.

[Lee et al. 2006] S. Lee, F. Barthelat, J. W. Hutchinson, and H. D. Espinosa, "Dynamic failure of metallic pyramidal truss core materials - Experiments and modeling", *Int. J. Plasticity* **22** (2006), 2118–2145.

[Liang et al. 2007] Y. Liang, A. V. Spuskanyuk, S. E. Flores, D. R. Hayhurst, J. W. Hutchinson, R. M. McMeeking, and A. G. Evans, "The response of metallic sandwich panels to water blast", *J. Appl. Mech. (Trans. ASME)* **74** (2007), 81–99.

[Mohr and Doyoyo 2004] D. Mohr and M. Doyoyo, "Experimental investigation on the plasticity of hexagonal aluminum honeycomb under multiaxial loading", *J. Appl. Mech. (Trans. ASME)* **71** (2004), 375–385.

[Mohr et al. 2006] D. Mohr, X. Z., and A. Vaziri, "Quasi-static punch indentation of a honeycomb sandwich plate: Experiments and modeling", *J. Mech. Mater. Struct.* **1**:3 (2006), 581–604.

[Okumura et al. 2002] D. Okumura, N. Ohno, and H. Noguchi, "Post-buckling analysis of elastic honeycombs subject to in-plane biaxial compression", *Internat. J. Solids Structures* **39** (2002), 3487–3503.

[Papka and Kyriakides 1999] S. D. Papka and S. Kyriakides, "Biaxial crushing of honeycombs-Part 1: Experiments", *Internat. J. Solids Structures* **36** (1999), 4367–4396.

[Qiu et al. 2003] X. Qiu, V. S. Deshpande, and N. A. Fleck, "Finite element analysis of the dynamic response of clamped sandwich beams subject to shock loading", *Eur. J. Mech. A: Solids* **22** (2003), 801.

[Rathbun et al. 2006] H. J. Rathbun, D. D. Radford, Z. Xue, M. Y. He, J. Yang, V. Deshpande, N. A. Fleck, J. W. Hutchinson, F. W. Zok, and A. G. Evans, "Performance of metallic honeycomb-core sandwich beams under shock loading", *Internat. J. Solids Structures* **43** (2006), 1746–1763.

[Smith and Hetherington 1994] P. D. Smith and J. G. Hetherington, *Blast and ballistic loading of structures*, Butterworth-Heinemann, Oxford, 1994.

[Taylor 1963] G. I. Taylor, "The pressure and impulse of submarine explosion waves on plates", pp. 287–303 in *The scientific papers of sir Geoffrey Ingram Taylor, volume III: Aerodynamics and the mechanics of projectiles and explosions*, edited by G. K. Batchelor, Cambridge University Press, 1963.

[Vaughn et al. 2005] D. Vaughn, M. Canning, and J. W. Hutchinson, "Coupled plastic wave propagation and column buckling", *J. Appl. Mech. (Trans. ASME)* **72** (2005), 1–8.

[Vaziri and Hutchinson 2007] A. Vaziri and J. W. Hutchinson, "Metal sandwich plates subject to intense air shocks", *Internat. J. Solids Structures* **44** (2007), 2021–2035.

[Vaziri et al. 2006] A. Vaziri, Z. Xue, and J. W. Hutchinson, "Metal sandwich plates with polymeric foam-filled cores", *J. Mech. Mater. Struct.* **1** (2006), 95–128.

[Vaziri et al. 2007] A. Vaziri, Z. Xue, and J. W. Hutchinson, "Performance and failure of metal sandwich plates subject to shock loading", *J. Mech. Mater. Struct.* (2007). in press.

[Wang and McDowell 2005] A. J. Wang and D. L. McDowell, "Yield surfaces of various periodic metal honeycombs at intermediate relative density", *Int. J. Plasticity* **21** (2005), 285–320.

[Xue and Hutchinson 2003] Z. Xue and J. W. Hutchinson, "Preliminary assessment of sandwich plates subject to blast loads", *Int. J. Mech. Sci.* **45** (2003), 687–705.

[Xue and Hutchinson 2004a] Z. Xue and J. W. Hutchinson, "A comparative study of impulse-resistant metallic sandwich plates", *Int. J. Impact Engineering* **30** (2004a), 1283–1305.

[Xue and Hutchinson 2004b] Z. Xue and J. W. Hutchinson, "Constitutive model for quasi-static deformation of metallic sandwich cores", *Internat. J. Numer. Methods Engrg.* **61** (2004b), 2205–2238.

[Xue and Hutchinson 2006] Z. Xue and J. W. Hutchinson, "Crush dynamics of square honeycomb sandwich cores", *Internat. J. Numer. Methods Engrg.* **65** (2006), 2221–2245.

[Xue et al. 2005] Z. Xue, A. Vaziri, and J. W. Hutchinson, "Non-uniform constitutive model for compressible orthotropic materials with application to sandwich plate cores", *Computer Modeling in Engineering and Applied Sciences* **10** (2005), 79–95.

ASHKAN VAZIRI: avaziri@seas.harvard.edu
School of Engineering and Applied Sciences, Harvard University, Cambridge, MA 02138, United States
www.seas.harvard.edu/~avaziri

ZHENYU XUE: xue@seas.harvard.edu
School of Engineering and Applied Sciences, Harvard University, Cambridge, MA 02138, United States

NEW APPROACH TO INVESTIGATION OF RESONANT VIBRATIONS OF NONCIRCULAR SHELLS BASED ON THE THEORY OF COUPLED WAVEGUIDES

VICTOR V. KRYLOV AND VASIL B. GEORGIEV

In the present paper a new simple method of analytical description of resonant vibrations of finite noncircular cylindrical shells is developed. The method is based on the theory of coupled waveguides formed by quasiflat areas of the same noncircular shells having an infinite length (depth). The physical reason for guided wave propagation along quasiflat areas of such shells is the difference between flexural wave velocities in their quasiflat and curved areas, respectively. Using asymptotic expressions for flexural wave velocities in circular shells with different radii of curvature, approximate dispersion equations are derived for waves propagating in such waveguides and their corresponding coupling coefficients. After that, considering shells of finite length, the transition is made from the coupled guided modes to the coupled resonant vibrations of the shell. The obtained resonant frequencies and spatial distributions of the resulting vibration modes are in good agreement with the results of finite element calculations.

1. Introduction

Noncircular cylindrical shells are relatively simple structures that are widely used for their own sake as well as for describing physical processes in more complex structures, especially in aeronautical and oceanic engineering applications; see [Armenakas and Koumousis 1983; Kumar and Singh 1993; Suzuki et al. 1996; Ganapathi and Haboussi 2003]. Some recent applications of elliptical or oval-type noncircular shells include modeling structure-borne vehicle interior noise in simplified reduced-scale vehicle models, where they form flexible parts of the model structures [Krylov et al. 2003; 2004]. Finite element calculations of resonant vibrations of such noncircular cylindrical shells, as seen in Figure 1, show that normal vibration modes of such structures can be represented as symmetric and antisymmetric combinations of vibrations of their quasiflat parts taken separately [Georgiev et al. 2004]. The same conclusions follow also from analytical or semianalytical solutions currently available for noncircular shells; see, for example, [Kumar and Singh 1993].

Note that obtaining analytical solutions for noncircular cylindrical shells is a very complex task that normally involves solving a system of governing differential equations with variable coefficients that describe the effects of variable curvature. This can be done, for example, using power series expansion of the solution [Suzuki et al. 1996] or by means of its representation in terms of special functions, such as Bezier polynomials [Kumar and Singh 1993].

In the present paper we propose to describe resonant vibrations of noncircular cylindrical shells analytically in a simpler way using the so-called coupled-wave theory approach utilizing the concept of coupled-waveguide propagation in shells of the same noncircular shape, but having an infinite length

---

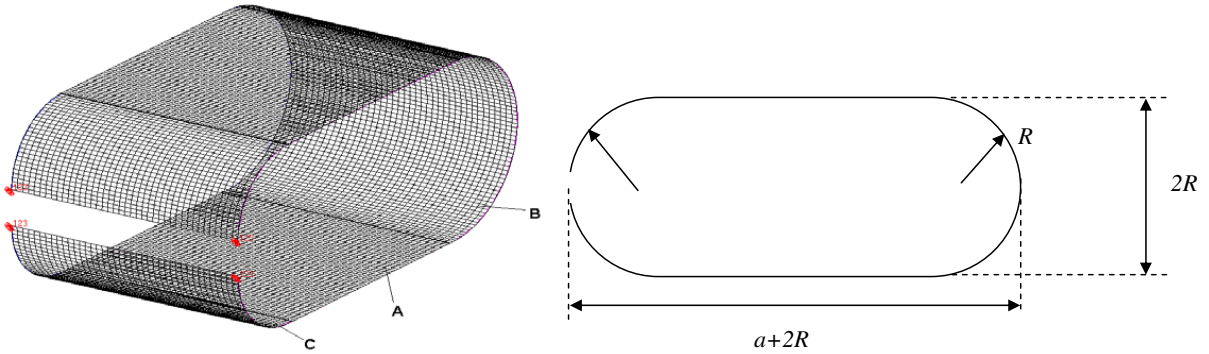*Keywords:* resonant vibrations, noncircular cylindrical shells, coupled waveguides.

Figure 1. Three-dimensional view (left) and profile (right) of noncircular cylindrical shell used for experimental modeling of structure-borne vehicle interior noise [Krylov et al. 2003; 2004].

(depth). Note that the concept of coupled waveguides has been previously applied to studying Rayleigh wave propagation on the surfaces of elastic bodies having complex cross-sectional shapes [Krylov 1987]. This method simplifies the analysis of noncircular shells by the fact that the effects of variable curvature can be taken into account indirectly, via the local curvature-dependent velocity of flexural waves freely propagating at arbitrary angle in the circular shell of the same radius of curvature. The problem is then reduced to the wave propagation problem in an inhomogeneous medium that contains two or more coupled waveguides for flexural waves formed by quasiflat areas of the shell.

The physical reason for waveguide propagation along quasiflat areas of noncircular cylindrical shells is the difference between flexural wave velocities in their quasiflat and curved parts. In particular, for waveguide propagation to be possible it is necessary that the velocity of flexural waves in the quasiflat area is lower than their velocity in the adjacent curved areas. This is always the case for flexural wave propagation in near-axial directions of circular cylindrical shells.

In the following sections we first employ the approximate expressions for flexural wave velocities (wavenumbers) in circular shells with different radii of curvature to derive the dispersion equations for flexural waves propagating in the waveguides composed of infinitely long flat plates (strips) bounded by fragments of two circular shells. We then discuss the coupling between two neighboring waveguides and the coupled waveguide modes. After that we will consider shells of finite length making the transition from coupled guided modes to coupled resonant vibrations of quasiflat parts of the shells. It will be demonstrated that resonant frequencies and spatial distributions of the normal vibration modes are in good agreement with the results of finite element calculations [Georgiev et al. 2004].

The proposed coupled-wave theory approach can be useful for a quick prediction of resonant vibration modes in oval-type shells containing two coupled waveguides and in more complex shell structures that can be associated with combinations of several coupled waveguides. The advantage of this approach lies in the fact that it is much easier to estimate resonant frequencies and modal shapes of complex noncircular shells on the basis of understanding the behavior of a single quasiflat waveguide considered as their basic structural component.
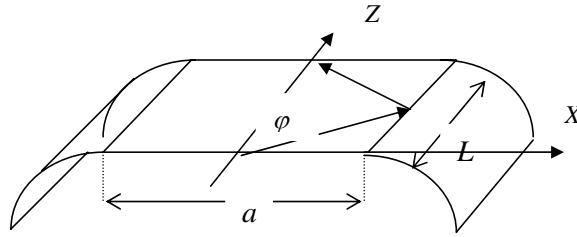
Figure 2. Waveguide propagation of flexural waves in an infinitely long flat plate (strip) bounded by two circular cylindrical shells.

2. Waveguide propagation in a plate bounded by two circular cylindrical shells

Let us consider waveguide propagation of flexural waves in an infinitely long flat plate (strip) of thickness h and width a bounded by fragments of two cylindrical shells having equal radii R as shown in Figure 2. We assume that the shells are of the same thickness as the flat plate. Such a structure can be considered as a three-layered anisotropic medium for flexural waves, the middle layer (a flat isotropic strip) being characterised by a lower phase velocity of flexural waves in comparison with flexural wave velocities in the near-axial direction in the adjacent cylindrical shells. It is well known that the layers formed by adjacent cylindrical shells are anisotropic in respect of flexural wave propagation. We remind the reader that we assume initially that the aforementioned structure is infinite in the z-direction, that is, $L = \infty$.

Waveguide propagation in such a three-layered medium can be described by the general dispersion equation well-known from acoustics and optics [Brekhovskikh and Godin 1990] that is slightly modified for the case of shell-induced anisotropic side layers [Schmidt and Coldren 1975; Krylov 1987]:

$$\frac{a}{2}\left[k_{pl}^2 - \gamma^2\right]^{1/2} = m\frac{\pi}{2} + \tan^{-1}\left[\frac{\gamma^2 - k_{sh}^2(\varphi)}{k_{pl}^2 - \gamma^2}\right]^{1/2}. \tag{1}$$

Here γ is as of yet unknown wavenumber of a guided flexural wave propagating in our three-layered system, $k_{pl} = (\omega^2 \rho_s h/D)^{1/4}$ is the wavenumber of flexural waves in a flat plate, where ρ_s is the mass density of the plate material and D is plate flexural rigidity, $k_{sh}(\varphi)$ is the angle-dependent wavenumber of flexural waves in a circular cylindrical shell, and $m = 0, 1, 2, \ldots$ Note that

$$\gamma = k_{pl} \cos\varphi, \tag{2}$$

where φ is the angle of propagation of two plane waves comprising a guided mode; see Figure 2. The guided wave fields propagating in the flat plate area and penetrating into the adjacent shells are described by, respectively,

$$w_{pl} = \cos\left[(k_{pl}^2 - \gamma^2)^{1/2} x\right] \exp(i\gamma z - i\omega t), \quad w_{sh} = C \exp\left[-\left(\gamma^2 - k_{sh}^2(\varphi(\gamma))\right)^{1/2} |x_{sh}|\right] \exp(i\gamma z - i\omega t). \tag{3}$$

Here x_{sh} is the surface curvilinear coordinate that extends the coordinate x from the plate to the shell area, and C is the constant determined from the continuity condition at the plate-shell boundary.

To find γ from the dispersion equation (1) one has to use appropriate analytical expressions for the wavenumber of flexural waves in the shell $k_{sh}(\varphi)$ propagating at arbitrary angle φ with respect to the axial direction of the shell. It is well known that propagation of flexural waves in shells is governed by

bending and membrane effects, which makes the expressions for flexural wavenumbers rather complex [Junger and Feit 1972; Fahy 1985; Leissa 1973]. Their functional appearance depends on the characteristic parameters of the shell, in particular on its ring frequency $\omega_r = c_l'/R$, where c_l' is the velocity of a quasilongitudinal wave in a thin flat plate (plate wave velocity), and R is the mean radius of the shell's curvature [Germogenova 1973; Tyutekin 2004]. In what follows we will use the relationships following from Kirchhoff–Love theory of thin elastic shells made of isotropic materials; see, for example, [Fahy 1985; Leissa 1973; Tyutekin 2004].

Let us first consider the case of wave propagation in a circular shell at frequencies ω that are essentially higher than the ring frequency ω_r, that is, consider the nondimensional parameter $\Omega = \omega/\omega_r \gg 1$.

Our starting point in this derivation is the simplified dispersion equation for flexural type wave propagation in a circular cylindrical shell; see [Fahy 1985, Equation (4.167)]. We can rewrite it in a more compact form using a slightly different notation as

$$\cos^4 \varphi + R^4 k_{sh}^{\,4} \beta^2 = \Omega^2. \tag{4}$$

Here $k_{sh} = k_{sh}(\varphi)$ is the wavenumber of flexural waves in the shell propagating at arbitrary angle φ with respect to the axial direction of the shell, R is the mean radius of the shell, and $\beta = h/\sqrt{12}R$, where h is the shell thickness. The first term on the left hand side of Equation (4) is associated with membrane strain energy, while the second term is associated with strain energy of bending. Equation (4) is accurate for thin shells ($\beta \ll 10^{-1}$) with $k_{sh} R \sin \varphi > 2$.

Using the condition $\Omega \gg 1$ one easily derives the approximate expression for the wavenumber of a flexural wave propagating in such a shell

$$k_{sh}(\varphi) = k_{pl}\left[1 - \frac{1}{4\Omega^2} \cos^4 \varphi\right], \tag{5}$$

where $k_{pl} = (\Omega^{1/2}/R\beta^{1/2}) = 12^{1/4}\omega^{1/2}/(c_l')^{1/2}h^{1/2} = (\omega^2 \rho_s h/D)^{1/4}$ is the wavenumber of flexural waves in a flat plate of the same thickness h (see also above).

Keeping in mind that $\cos \varphi = 1 - \varphi^2/2$ for small φ and substituting Equations (2) and (5) into Equation (1), one can derive the following simplified equation for φ:

$$\frac{a}{2}k_{pl}\varphi = m\frac{\pi}{2} + \tan^{-1}\left[\frac{1}{2\Omega^2\varphi^2} - 1\right]^{1/2}.$$

Considering for simplicity the propagation of only the lowest order mode $m = 0$, this equation can be reduced to a biquadratic one. Assuming that $ak_{pl} \gg \Omega$, the approximate solution of this equation is $\varphi^2 = 2^{1/2}/\Omega k_{pl}a$, which describes a weak waveguide effect. Using Equation (2) and this solution, one can obtain the following expression for γ

$$\gamma = k_{pl}\left[1 - \frac{1}{2^{1/2}\Omega k_{pl}a}\right]. \tag{6}$$

As it could be expected for waveguide propagation in a three-layered system, the velocity of guided wave $c = \omega/\gamma$ in the case under consideration is higher than the velocity in the *slow region* (flat plate), but lower than the velocity in the adjacent *fast regions* (fragments of circular shell).

Let us now turn to waveguide propagation at frequencies lower than the ring frequency. In this case the expressions for $k_{sh}(\varphi)$ are generally too complex to be described analytically [Junger and Feit 1972;

Fahy 1985]. For illustration purposes we limit ourselves, as above, to the case of small wave propagation angles φ, for which $k_{sh}(\varphi)$ is known to be extremely small. To simplify things even further, we assume that $k_{sh}(\varphi) = 0$ for all φ in the range of interest. In this case the dispersion equation (1) becomes

$$\frac{a}{2}\left[k_{pl}^2 - \gamma^2\right]^{1/2} = m\frac{\pi}{2} + \tan^{-1}\left[\frac{\gamma^2}{k_{pl}^2 - \gamma^2}\right]^{1/2}. \tag{7}$$

Again using the fact that $\cos\varphi = 1 - \varphi^2/2$ for small φ and substituting Equation (2) into Equation (7), one can derive the following simplified equation for φ

$$\frac{a}{2}k_{pl}\varphi = m\frac{\pi}{2} + \tan^{-1}\left[\frac{1-\varphi^2}{\varphi^2}\right]^{1/2}.$$

For small φ the last term in the right hand side of this equation is approximately equal to $\pi/2$, allowing us to reduce it to

$$\frac{a}{2}k_{pl}\varphi = (m+1)\frac{\pi}{2},$$

from which it follows that $\varphi = (m+1)\pi/ak_{pl}$. Substituting this solution into Equation (2), one can derive the following approximate expression for the wavenumbers of guided flexural waves propagating in the above system at frequencies below the ring frequency

$$\gamma = k_{pl}\left[1 - \frac{(m+1)^2\pi^2}{2a^2k_{pl}^2}\right]. \tag{8}$$

In this case the waveguide effect is rather strong, and the energy of a guided wave is almost entirely concentrated in the flat plate area.

3. Resonant vibrations of a flat plate bounded by two circular shells

In this section we consider the plate/shell system of finite length L and assume for simplicity that at $z = 0, L$ the system is subject to simply supported boundary conditions. Then the distribution of the resulting elastic field along the z-axis formed by incident and reflected guided waves can be expressed in the form $\sin(\gamma z)$. Using the condition $\sin(\gamma L) = 0$, we see that $\gamma L = \pi n$, where $n \in \mathbb{N}$.

Let us first analyze resonant vibrations for the case of frequencies higher than the ring frequency ω_r. Then using Equation (6) subject to the condition $\gamma L = \pi n$ and expressing $k_{pl} = \omega/c_{pl}$, with $c_{pl} = \omega^{1/2}(D/\rho_s h)^{1/4}$, one can derive a simple equation for resonant frequencies ω_{0n}. Solving this equation by the perturbation method, one obtains the following expression for the resonant frequencies ω_{0n}, where we consider only modes with $m = 0$,

$$\omega_{0n} = \frac{\pi^2 n^2}{L^2}\left(\frac{D}{\rho_s h}\right)^{1/2}\left[1 + \frac{2^{1/2}c_l'\rho_s^{1/2}h^{1/2}L^3}{\pi^3 n^3 D^{1/2}Ra}\right].$$

Note that this equation describes the increase in resonant frequencies of the plate with waveguiding properties in comparison with the case of one-dimensional wave propagation in a flat plate of the same length L but with infinitely large value of the width a. We recall that the distribution of the guided wave field in the transverse direction is described by Equation (3).

Similarly for the case of frequencies lower than the ring one, one can obtain the equation for the system's resonant frequencies

$$\omega_{mn} = \left(\frac{D}{\rho_s h}\right)^{1/2}\left[\frac{\pi^2(m+1)^2}{a^2} + \frac{\pi^2 n^2}{L^2}\right]. \tag{9}$$

It is remarkable that Equation (9) coincides with the well-known expression for resonant frequencies of simply supported plates having the dimensions L and a (note that in the present paper we assume that $m = 0, 1, 2, 3, \ldots$, whereas in the plate theory usually $m = 1, 2, 3, \ldots$). This coincidence reflects the fact that at frequencies lower than the ring frequency the waveguide effect provided by two adjacent circular shells is very strong and almost the entirety of vibration energy is concentrated in the flat plate area. One should keep in mind, however, that Equation (9) is valid for $n \gg m$, which corresponds to low values of the propagation angle φ.

Note that, although in the above derivations we have used simply supported boundary conditions at $z = 0, L$, the approach we have developed remains valid for any other types of boundary conditions at the edges, such as, for example, free or clamped boundary conditions. In these cases, however, one has to take into account the presence of nonpropagating field components in the z-direction, which are important only near the edges, and the corresponding phase changes for the reflection coefficients of propagating waves.

4. Effect of coupling between the neighboring strip/shell waveguides

Let us now return to the full cylindrical noncircular shell shown in Figure 1 and consider it as a system of two coupled identical parallel strip/shell waveguides separated by the distance $d = a + \pi R$ between their central lines measured along the surface. If we assume that $u_n = u_n(z)$ is a slowly varying amplitude factor which characterises the field in the n-th waveguide, where $n = 1, 2$ in the case considered, then for a shell with a gap on one side, as shown in Figure 1, the coupling takes place on the opposite side only. In such a case the amplitude factors u_n should satisfy the system of two simultaneous coupled equations [Louisell 1960; Schmidt and Coldren 1975; Krylov 1987]:

$$\frac{\partial u_1}{\partial z} - i\gamma u_1 + i\kappa u_2 = 0, \qquad \frac{\partial u_2}{\partial z} - i\gamma u_2 + i\kappa u_1 = 0. \tag{10}$$

Here γ represents the wavenumber of any chosen guided mode in each waveguide taken separately (uncoupled waveguides), and κ is the wave coupling coefficient for this particular mode, which depends on the strength of mutual penetration of the vibration fields from the neighboring waveguides. In this case κ can be written as [Schmidt and Coldren 1975; Krylov 1987]

$$\kappa = \frac{\left(k_{pl}^2 - \gamma^2\right)\left(\gamma^2 - k_{sh}^2(\gamma)\right)}{\gamma\left[1 + \left(\gamma^2 - k_{sh}^2(\gamma)\right)^{1/2}a/2\right)\right]\left(k_{pl}^2 - k_{sh}^2(\gamma)\right)} \exp\left[-\left(\gamma^2 - k_{sh}^2(\gamma)\right)^{1/2}(d - a)\right]. \tag{11}$$

It is seen from Equation (11) that the coupling coefficient κ is determined primarily by the exponential factor that describes the decay of the field outside the waveguides.

Making an ansatz $u_n = A_n \exp(ikz)$ with $A_n = \text{const}$, for the solution of the simultaneous coupled equations (10), one obtains two types of relationships between A_1 and A_2 that correspond to the wavenumber

mismatch $\Delta\gamma = k - \gamma$. $\Delta\gamma = \kappa$ corresponds to the antisymmetric mode of the coupled system $A_1 = -A_2$, while $\Delta\gamma = -\kappa$ corresponds to the symmetric mode of the coupled system $A_1 = A_2$.

If the gap on the left hand side of the shell shown in Figure 1 is bridged, then both waveguides interact with each other on two sides and the resulting coupling coefficient increases by a factor of two. The values of the mismatch $\Delta\gamma$ here can be obtained from the above expressions replacing κ by 2κ.

Considering propagation of antisymmetric and symmetric modes in the coupled system of finite length L, one can easily derive the expressions for resonant frequencies of our finite noncircular shell. Obviously, the coupling is stronger at frequencies higher than the ring frequency and weaker at frequencies below it, where there is a little energy escape from the flat plate area; see also Equation (11).

For the case of higher frequencies one can use Equation (6) for γ and derive the following expression for resonant frequencies of symmetric and antisymmetric modes, denoted by $+$ and $-$, respectively

$$\omega_{0n} = \left(\frac{\pi n}{L} \pm \kappa\right)^2 \left(\frac{D}{\rho_s h}\right)^{1/2} \left[1 + \frac{2^{1/2} c_l' \rho_s^{1/2} h^{1/2} L^3}{\pi^3 n^3 D^{1/2} Ra}\right].$$

For the case of frequencies lower than the ring frequency, Equation (8) must be used, giving the expression for resonant frequencies of symmetric and antisymmetric modes, denoted by $+$ and $-$, respectively,

$$\omega_{mn} = \left(\frac{D}{\rho_s h}\right)^{1/2} \left[\frac{\pi^2 (m+1)^2}{a^2} + \left(\frac{\pi n}{L} \pm \kappa\right)^2\right]. \tag{12}$$

Note that in the latter case the values of κ are extremely small and can be ignored in Equation (12), since the energy of vibrations is almost entirely confined in the flat plate area. Nevertheless, the symmetric and antisymmetric coupled modes do exist even at negligibly small coupling, though their resonant frequencies are almost indistinguishable. This agrees well with the results of recent experiments [Krylov et al. 2003; 2004] and with the corresponding finite element calculations [Georgiev et al. 2004].

In particular, according to the finite element calculations, the resonant frequencies of symmetric and antisymmetric modes of the noncircular shells under consideration are practically the same. Moreover, they are close to the resonant frequencies of the simply-supported plates with same geometrical dimensions as the flat areas of the shells (Table 1), which agrees with the above theory, Equations (9) and (12), for the case of weak coupling. Furthermore, the numerical routine clearly identifies the lowest-order symmetric and antisymmetric modes in the calculated distributions of vibrations over the shell cross-section; see Figure 3. In the case of higher-order vibration modes, one can also clearly see the similarity of the modal patterns of higher-order modes with the corresponding modes of the simply supported plates; see Figure 4.

Although in the present paper we analyzed a noncircular shell composed of only two coupled plate areas, the results of the analysis can be easily extended to an arbitrary number of coupled components, in particular to structures with 3, 4 or more quasiflat surfaces. For example, in the case of a noncircular cylindrical shell shaped like a rounded rectangle as shown in Figure 5, one should consider the same quasiflat single waveguides that have been analyzed in the previous sections and then take into account wave coupling in the system of four equal waveguides. Moreover, one can analyze the case of coupled shell systems characterised by spatially changing signs of shell curvature, for example, periodically corrugated thin-walled structures. In this case the waveguide propagation will take place in the quasiflat shell areas around zero curvature, and all other calculations will be the same as above. The obvious
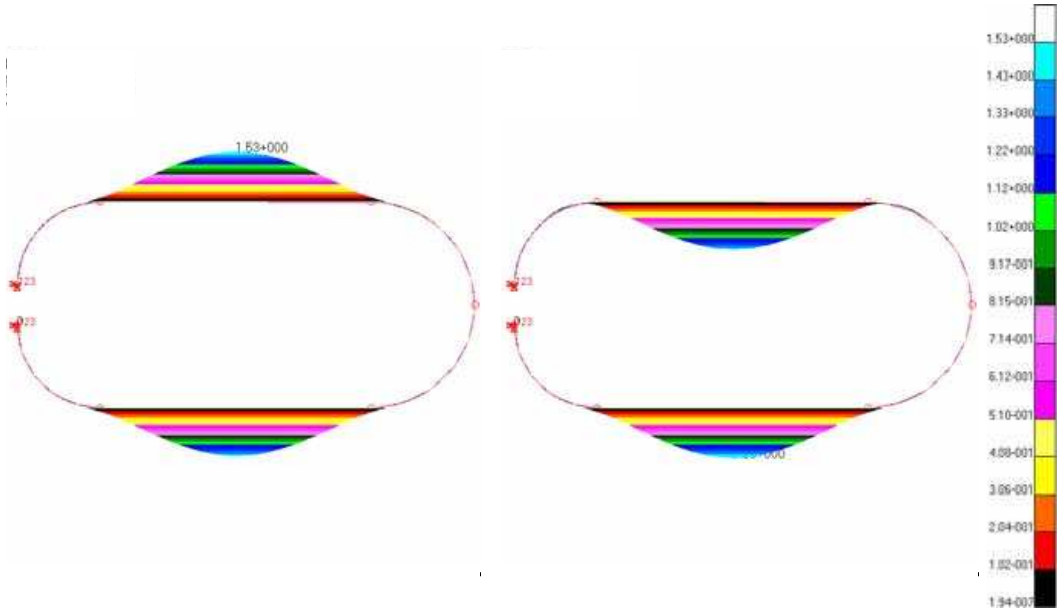
Figure 3. Numerically calculated distributions of the vibration fields for lowest order symmetric (left) and antisymmetric (right) modes of the noncircular cylindrical shell made of steel and having two quasiflat surfaces; see also Figure 1. Shell dimensions: radius $R = 125$ mm, total length $a + 2R = 550$ mm, width $L = 300$ mm, and shell thickness $h = 1.2$ mm; natural frequency is 67.039 Hz.

Simply supported plate			Noncircular shell
Plate mode	Analytical	FE	FE
(1,1)	59.04	59.18	67.04
(1,2)	140.54	140.89	146.22
(2,1)	154.68	155.10	157.67
(2,2)	236.18	236.62	239.15
(1,3)	276.36	277.12	264.51
(3,1)	314.08	314.99	315.33
(2,3)	372.00	372.62	364.40
(3,2)	395.58	396.29	394.69

Table 1. The first eight numerically calculated natural frequencies of noncircular cylindrical shell and of simply-supported rectangular plates of same dimensions as the shell's flat areas. Shell dimensions are as in Figures 3 and 4. Frequencies in Hz.
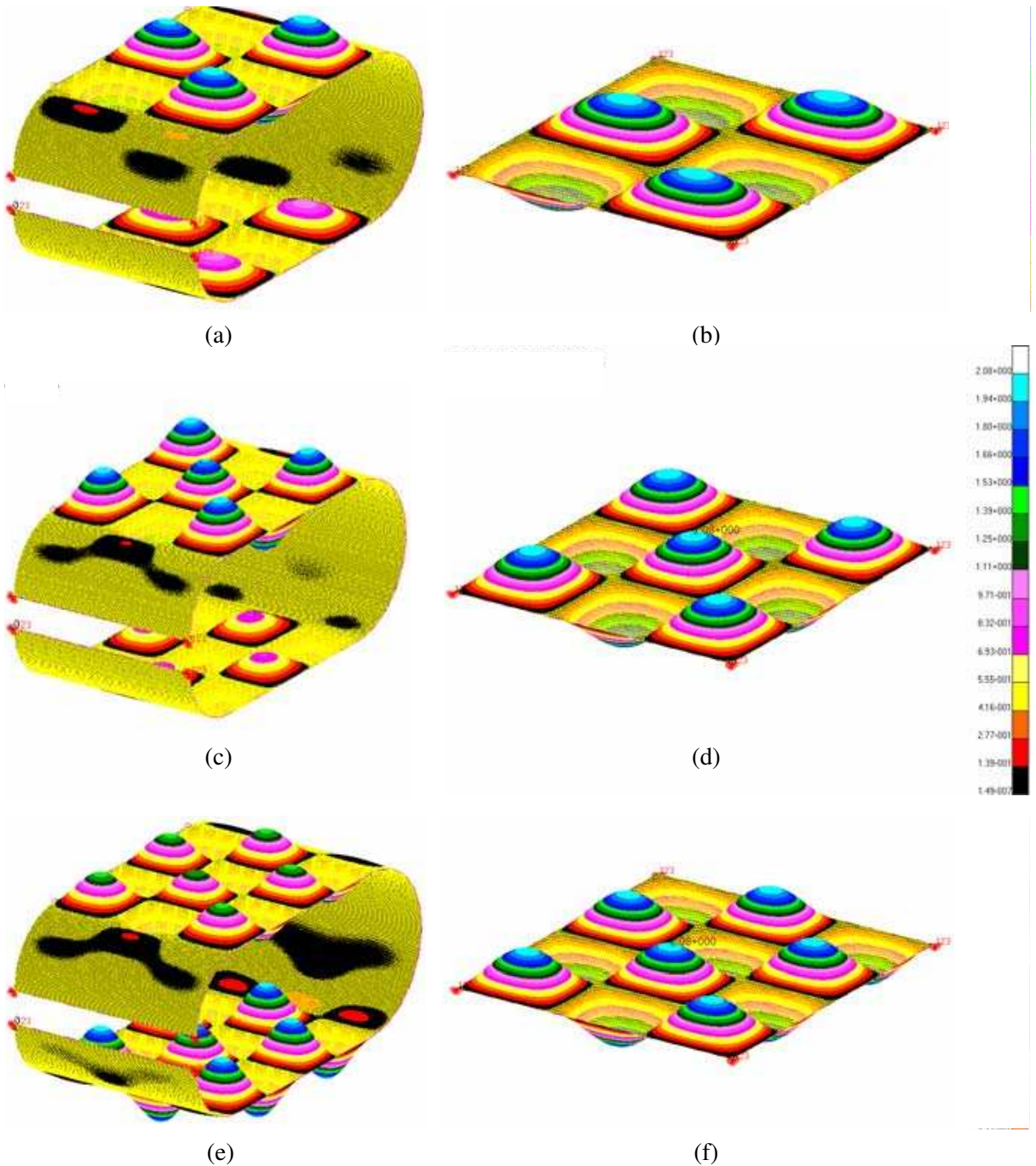
Figure 4. Numerically calculated higher-order structural modes of noncircular cylindrical shell (left) and of corresponding simply-supported rectangular plates (right); dimensions are as in Figure 3. (a) antisymmetric mode at 364.4 Hz, (b) 372.2 Hz, (c) symmetric mode at 521.45 Hz, (d) 531.95 Hz, (e) antisymmetric mode at 691.68 Hz, (f) 721.99 Hz.
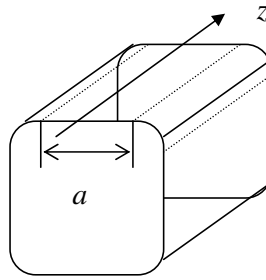
Figure 5. Noncircular cylindrical shell with shape of rounded rectangle that can be considered as a system of four coupled strip/shell waveguides.

advantage of the developed coupled-wave theory approach lies in the fact that it is much easier to estimate resonant frequencies and modal shapes of complex noncircular shells on the basis of understanding the behavior of a single quasiflat waveguide considered as their basic structural component.

5. Conclusions

In the present paper we have demonstrated that resonant vibrations of cylindrical noncircular shells can be easily described analytically using the coupled-wave theory approach utilizing the concept of coupled-waveguide propagation in shells of the same noncircular shape, but having an infinite length. The physical reason for waveguide propagation along quasiflat parts of such shells is the difference between flexural wave velocities in their flat and curved areas.

Using simple approximations for wavenumbers of flexural waves propagating in circular shells with different radii of curvature, the approximate expressions for resonant frequencies have been derived for both uncoupled and coupled finite shell systems. In the case of very weak coupling, which is typical for vibrations at frequencies lower than the ring frequencies of adjacent circular shells, the values of the resultant resonant frequencies are almost entirely determined by resonant properties of the flat plate areas. This agrees well with the experiments and with the results of finite element calculations.

The developed coupled-wave theory approach to the description of resonant flexural vibrations of finite noncircular cylindrical shells can be used for quick estimations of resonant frequencies and normal modes in such shells. It also can be applied to analyzing resonant vibrations in more complex noncircular shells containing arbitrary numbers of quasiflat surfaces.

References

[Armenakas and Koumousis 1983] A. E. Armenakas and V. K. Koumousis, "Free vibrations of simply supported cylindrical shells of oval crosssection", *AIAA J.* **21**:7 (1983), 1017–1027.

[Brekhovskikh and Godin 1990] L. M. Brekhovskikh and O. A. Godin, *Acoustics of layered media: plane and quasi-plane waves*, vol. 1, Springer series on wave phenomena, Springer, Berlin, 1990.

[Fahy 1985] F. Fahy, *Sound and structural vibration: radiation, transmission and response*, Academic Press, London, 1985.

[Ganapathi and Haboussi 2003] M. Ganapathi and M. Haboussi, "Free vibrations of thick laminated anisotropic non-circular cylindrical shells", *Compos. Struct.* **60**:2 (2003), 125–133.

[Georgiev et al. 2004] V. B. Georgiev, V. V. Krylov, and R. E. T. B. Winward, "Finite element calculations of structural-acoustic modes of vehicle interior for simplified models of motorcars", in *Proceedings of the 33rd international congress and exposition on noise control engineering inter-noise 2004* (Prague, Czech Republic), 22–25 August 2004. on CD.

[Germogenova 1973] O. A. Germogenova, "Geometrical theory of flexural waves in shells", *J. Acoust. Soc. Am.* **53**:2 (1973), 535–540.

[Junger and Feit 1972] M. C. Junger and D. Feit, *Sound, structures and their interaction*, MIT Press, Cambridge, Mass., 1972.

[Krylov 1987] V. V. Krylov, "Distinctive characteristics of guided surface-wave propagation in complex topographic structures", *Sov. Phys. Acoust.* **33**:4 (1987), 407–411.

[Krylov et al. 2003] V. V. Krylov, S. J. Walsh, and R. E. T. B. Winward, "Modelling of vehicle interior noise at reduced scale", in *Proceedings of the EuroNoise 2003* (Naples, Italy), 19–21 May 2003. on CD.

[Krylov et al. 2004] V. V. Krylov, S. J. Walsh, and R. E. T. B. Winward, "Investigation of structural-acoustic coupling in a thin-walled reduced-scale model of a car", pp. 95–102 in *Thin-walled structures: advances in research, design and manufacturing technology and proceedings of the 4th international conference on thin-walled structures*, edited by J. Loughlan, Institute of Physics Publishing, Loughborough, UK and Bristol and Philadelphia, 22–24 June 2004.

[Kumar and Singh 1993] V. Kumar and A. V. Singh, "Vibration analysis of non-circular cylindrical shells using bezier functions", *J. Sound Vib.* **161**:2 (1993), 333–354.

[Leissa 1973] A. W. Leissa, *Vibration of shells*, Scientific and Technical Information Office, National Aeronautics and Space Administration, Washington, 1973.

[Louisell 1960] W. H. Louisell, *Coupled mode and parametric electronics*, Wiley, New York, 1960.

[Schmidt and Coldren 1975] R. V. Schmidt and L. A. Coldren, "Thin film acoustic surface waveguides on anisotropic media", *IEEE T. Son. Ultrason.* **22**:2 (1975), 115–122.

[Suzuki et al. 1996] K. Suzuki, G. Shikanai, and A. W. Leissa, "Free vibrations of laminated composite non-circular thick cylindrical shells", *Int. J. Solids Struct.* **33**:27 (1996), 4079–4100.

[Tyutekin 2004] V. V. Tyutekin, "Helical waves of an elastic cylindrical shell", *Acoust. Phys.* **50**:3 (2004), 273–277.

VICTOR V. KRYLOV: V.V.Krylov@lboro.ac.uk
Department of Aeronautical and Automotive Engineering, Loughborough University, Loughborough, Leicestershire LE11 3TU, United Kingdom

VASIL B. GEORGIEV: V.Georgiev@lboro.ac.uk
Department of Aeronautical and Automotive Engineering, Loughborough University, Loughborough, Leicestershire LE11 3TU, United Kingdom

SERRATION EFFECTS ON INTERFACIAL CRACKS

ASSIMINA A. PELEGRI AND BAOXIANG X. SHAN

To investigate the effect of serrations in an interfacial crack between dissimilar materials, we introduce into the Finite Element (FE) framework a unit cell (UC) at microscale. By assigning material-specific properties to these unit cells, we can model various serration profiles and distributions and calculate their effect on the mixed-mode stress intensity factor (SIF), including its magnitude and phase angle. The simulation demonstrates that serration profoundly changes the local behavior of an interfacial crack. The serrations decrease the SIF in mode I, increase it in mode II, and, when the serration's height-to-width ratio increases, the mode mixity SIF increases as well. We find that sparse serration confines variation in the SIFs to the local peaks and that dense serrations cause widespread undulations in the SIF's magnitude and phase angle.

1. Introduction

Materials scientists are increasingly interested in fractures at the interface between two dissimilar materials, because they are fundamental for understanding thin-film coatings [Hutchinson and Suo 1992; Diao and Kato 1994; Mishnaevsky and Gross 2005], electronic packaging, adhesion [Straffelini 2001; Packham 2003], and composites and biomaterials [Wang and Agrawal 2000; Lucksanasombool et al. 2003]. Experiments cumulatively show that the waviness at the interface profoundly effects interfacial crack propagation. Liechti [2007] has made atomic force microscope (AFM) images of cracks at a glass/epoxy interface. Shown in Figure 1, they clearly demonstrate that the interfacial crack is not smooth and flat, but rather features dense sharp hackles and serrations. Hackles and serrations appear also in fractographic images of composites, such as Carbon/Fibredux-97 [Partridge and Singh 1995] and T300H/914C [Gilchrist and Svensson 1995; Gilchrist et al. 1996], especially in the mode II dominant conditions.

Previously, serrations and hackles were modeled by first identifying a scalar material parameter with the interfacial roughness and then investigating its effect on interfacial fracture and strength [Cao and Evans 1989; Ramulu et al. 2001; Lucksanasombool et al. 2003; Packham 2003]. Because the method is simple, it fails to capture micromechanical and microgeometric details at the interface and around the crack's tip. The FEM [Larson and Miles 1998; Schuller et al. 1999; Diao and Kandori 2006] and BEM [Young 2001] models adopt a more detailed view of the micromechanics. They represent the interfacial roughness by a discrete triangular arrangement of surface integral elements with specific period and amplitude. However, these models can accommodate only limited serration profiles and distributions.

Therefore, in the FEM framework, we introduce a specific unit cell (UC) so that we can more flexibly adjust the serration profile and distribution and hence investigate their effect on the magnitude and phase angle of the stress intensity factor.
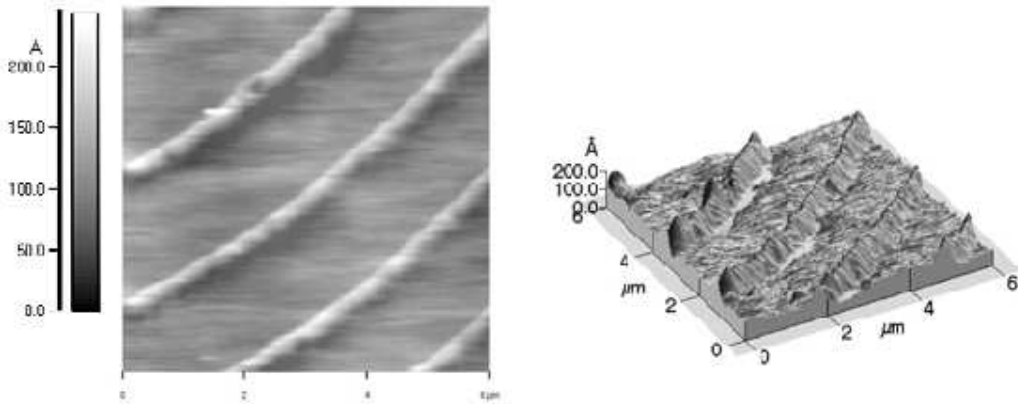

Figure 1. AFM images of a glass/epoxy interface crack.

2. Modeling

2.1. *DCB sandwich specimen.* In experiments, Lee and Qu [2003] investigated the effect of serration on interfacial adhesion using a double cantilever beam (DCB). We will use a similar setup to test the performance of our UC-based FE model. The specimen is shown in Figure 2, borrowed from [Lee and Qu 2003]: a leadframe sandwiches an epoxy molding component (EMC). Ours differs by setting the leadframe thickness to 1.7 mm, because we want to increase the initial phase angle shift. The global loads are opposite 200 N forces applied to the circle centers so as to open the crack further. To simulate the experimental setup, we set the structural boundary conditions as follows: the circle centers are free to move vertically, but are horizontally fixed. All edges are stress-free.
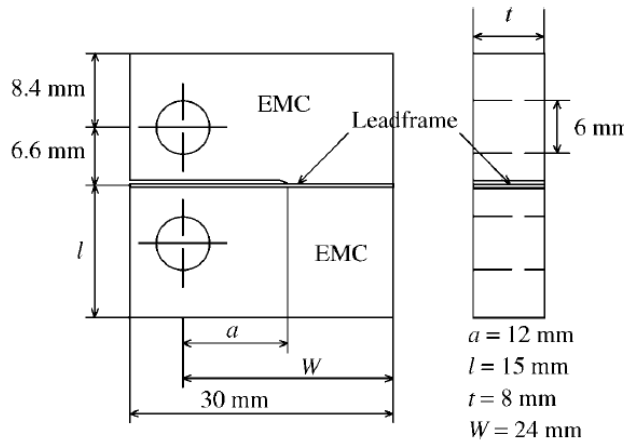
Figure 2. Geometry of DCB sandwich specimen.
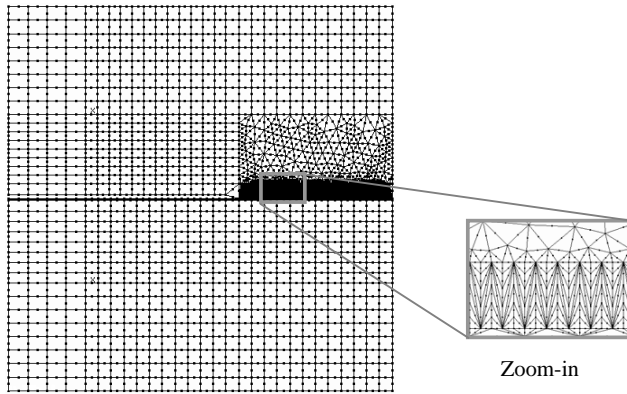
Figure 3. FEM elements of specimen.

The leadframe is a copper alloy, with Young's modulus $E = 127$ GPa and Poisson ratio $\nu = 0.34$. The EMC has Young's modulus $E = 3$ GPa and Poisson ratio $\nu = 0.3$.

2.2. *FE model and unit cell.* After we specify the DCB dimensions, we input them into CASCA, a 2-D mesh generator in the FE software package FRANC2DL [Swenson and James 1997]. We divided the specimen into several subregions to guarantee a fine mesh around the interface, especially at the crack tip and the potential crack trajectory. We allow the software to initially mesh the subregions, but, in the interface ahead of the crack tip, we fix the mesh manually, using our proposed unit cells. In addition to the surface boundary conditions, the interface is initially set to be perfectly binding before it cracks. After separation, the delaminated surfaces are free from any stress. The initial FE model of the sandwich specimen is shown in Figure 3, and the zoomed-in insert illustrates the meshing elements with specialized unit cells.

The FEM model was designed to explore the effect of serration on phase angle shift and specifically how different shapes and distributions affect the shift. We propose a general unit cell (UC) to avoid constructing a different FEM model each case. The unit cell, shown in Figure 4, has circular points numbered from 1–5 counterclockwise. For a unit cell whose height is six times its width, we list the slope angle for each marked point in Table 1.

Point	Height	Angle
1	$h/6$	45.0°
2	$h/3$	63.4°
3	$2h/3$	76.0°
4	h	80.5°
5	h	90.0°

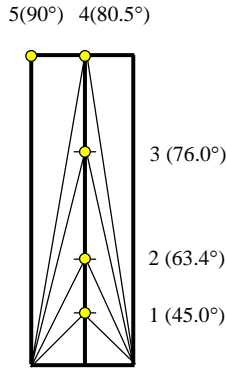**Table 1.** The height and angle of each point in UC.

Figure 4. Unit cell for interfacial serration in FEM simulation.

Using the proposed unit cell, a number of serration patterns can be easily drawn and implemented in FEM. Each can be evolved from an initial FEM model by changing the expected cell from material 1 (EMC here) from material 2 (copper alloy here). Figure 5 demonstrates how the initial smooth and flat interface evolves into one with a pattern of small, sparse serrations.

After setting the profiles at the interface, we start the FE analysis for the crack tip at its initial position. Then, step by step, we simulate the progress of a growing crack by intentionally controlling the crack propagation direction and length in FRANC2DL. To ensure continued accuracy as the crack grows, finer analysis elements near the crack tip are generated automatically both inside and outside of the serration, as shown as Figure 6. We constrain the element size near the crack tip to be less than one quarter of the thin leadframe thickness, as this strikes a balance between good resolution and reasonable computation time [La Saponara et al. 2002].

2.3. *Computation of stress intensity factors and mode mixity.* In our FEM, we calculate the mode I and II stress intensity factors using the modified crack closure integral (MCCI) method [Rybicki and Kanninen 1977; Narayana and Dattaguru 1996; Sethuraman and Maiti 1988]. The method, first proposed by Rybicki and Kanninen [1977], was based on Irwin's virtual crack closure method. The principle of MCCI is that the energy to create a new crack surface is equal to the work required to close the crack
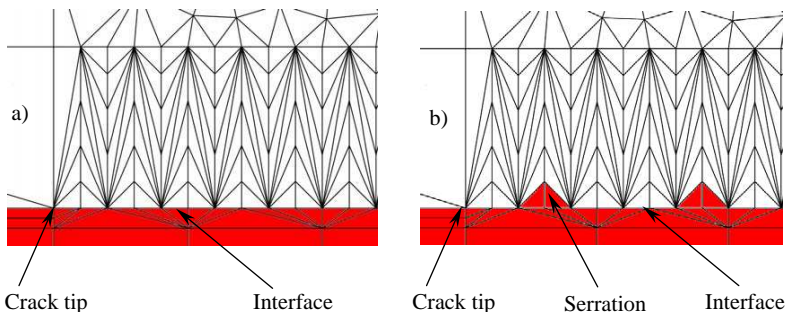

Figure 5. Evolution of FEM model: (a) initial FEM model without serration; (b) FEM model with sparse, small peaks.
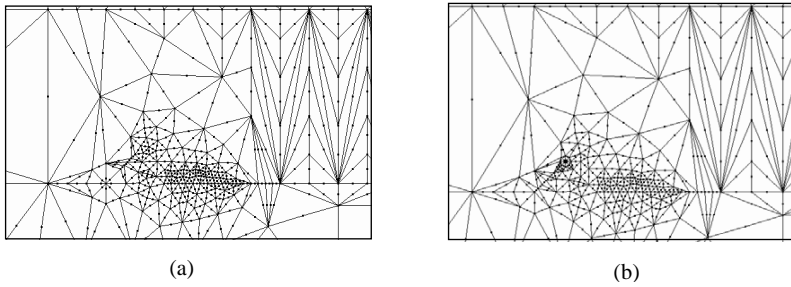
Figure 6. Element refinement at the crack tip for the SIF computation: (a) finer elements around the crack tip at the serration's bottom corner; (b) finer elements around the crack tip at the serration's peak.

to its original length. The MCCI can calculate the strain energy release rates and stress intensity factors without assuming isotropy or homogeneity around a crack, and it calculates both the mode I and II stress intensity values in a single analysis. Hence this method is ideally suited for modeling interfacial cracks in bimaterials.

In MCCI, the strain energy release rates of modes I and II are [Kim and Paulino 2002]

$$G_I = \lim_{\delta a \to 0} \frac{2}{\delta a} \int\limits_{x_1=0}^{x_1=\delta a} \frac{1}{2} \sigma_{22}(r = x_1, \theta = 0, a) \cdot u_2(r = \delta a - x_1, \theta = \pi, a + \delta a) dx_1,$$

$$G_{II} = \lim_{\delta a \to 0} \frac{2}{\delta a} \int\limits_{x_1=0}^{x_1=\delta a} \frac{1}{2} \sigma_{12}(r = x_1, \theta = 0, a) \cdot u_1(r = \delta a - x_1, \theta = \pi, a + \delta a) dx_1,$$

where σ_{22} and σ_{12} are normal and shear stresses ahead of the crack tip, u_1 and u_2 are the relative displacements with respect to the crack tip, a is the length of initial crack, and δa is a virtual crack extension.

Raju [1987] expressed the two strain energy release rates in terms of the nodal forces and displacements by using six-node quarter-point triangular elements around the crack tip (see Figure 6), finding

$$
\begin{aligned}
G_I = \frac{1}{2\Delta a} \big[& F_{2,i}\big(t_{11}u_{2,i-2} + t_{12}u_{2,i-1}\big) + F_{2,i+1}\big(t_{21}u_{2,i-2} + t_{22}u_{2,i-1}\big) \\
& + F_{2,i+2}^T\big(t_{31}\bar{u}_{2,i-2} + t_{32}\bar{u}_{2,i-1}\big) + F_{2,i+2}^B\big(t_{31}\hat{u}_{2,i-2} + t_{32}\hat{u}_{2,i-1}\big)\big],
\end{aligned}
$$

$$
\begin{aligned}
G_{II} = \frac{1}{2\Delta a} \big[& F_{1,i}\big(t_{11}u_{1,i-2} + t_{12}u_{1,i-1}\big) + F_{1,i+1}\big(t_{21}u_{1,i-2} + t_{22}u_{1,i-1}\big) \\
& + F_{1,i+2}^T\big(t_{31}\bar{u}_{1,i-2} + t_{32}\bar{u}_{1,i-1}\big) + F_{1,i+2}^B\big(t_{31}\hat{u}_{1,i-2} + t_{32}\hat{u}_{1,i-1}\big)\big],
\end{aligned}
$$

where the first subscript in the nodal force F and displacement u refer to the Cartesian coordinate and the second subscript refers to the nodal point. The parameters t_{kl} ($k = 1, 2, 3; l = 1, 2$) are given in [Kim and Paulino 2002]. Δa is the characteristic length of an element. The superscripts T and B indicate the regions above and below the x_1 axis, and F^T and F^B indicate the forces at top and bottom surfaces. The displacements $\bar{u}$ and $\hat{u}$ represent the relative displacement of the top and bottom parts from the crack tip.

The stress intensity factors can then be computed from the relations [Kim and Paulino 2002]:

$$K_I = \sqrt{G_I \bar{E}} \qquad \text{and} \qquad K_{II} = \sqrt{G_{II} \bar{E}},$$

where the effective Young's modulus $\bar{E}$ for an interfacial crack is defined [Suo and Hutchinson 1989] as

$$\bar{E} = 2\cosh^2(\pi\varepsilon) \Big/ \left(\frac{1}{E_1} + \frac{1}{E_2} \right), \quad \text{for plane stress,}$$

$$\bar{E} = 2\cosh^2(\pi\varepsilon) \Big/ \left(\frac{1 - v_1^2}{E_1} + \frac{1 - v_2^2}{E_2} \right), \quad \text{for plane strain,}$$

and the material mismatch index ε is related to the second Dundurs' material parameter β by

$$\varepsilon = \frac{1}{2\pi} \ln\left(\frac{1 - \beta}{1 + \beta} \right).$$

Another important parameter is mode mixity ψ, defined as [Wang and Suo 1990]

$$\psi = \tan^{-1}\left(\frac{K_{II}}{K_I} \right).$$

2.4. *Serration profile and distribution.* We selected a series of serration patterns to investigate the effect of shape and distribution on stress intensity factors and mode-mixity. We classify serrations by the peak density, that is, sparse or dense, and by peak shape, that is, small, sharp, or rectangular (see Figure 7). By controlling for density or shape, we can, through our simulations, see the effect of varying the other characteristic.
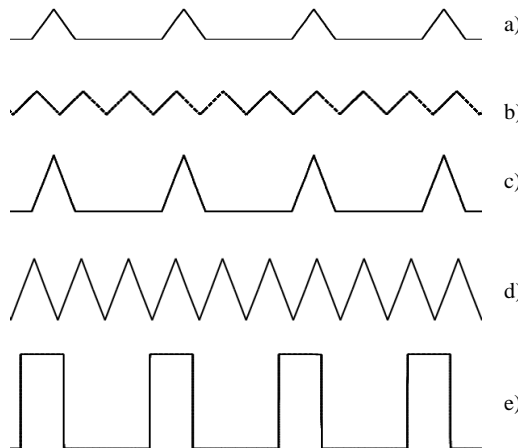
Figure 7. Serration patterns: (a) sparse small peaks; (b) dense small peaks; (c) sparse sharp peaks; (d) dense sharp peaks; (e) sparse rectangular peaks.

3. Results and discussion

For each pattern, we use FEM to find the stress intensity factor (SIF) and mode mixity. We calculated the SIF's using the virtual crack extension method [Matos et al. 1989] and summarize the results in Figures 8 through 14. We focus on how SIF magnitudes and phase angle vary along the crack, and how this variation depends on the type of serration.

Figure 8 illustrates how stress intensity factors K and mode mixity ψ vary in the presence of small sparse peaks (peak angle 45.0°) and, for comparison, in the absence of any serration. Between peaks, introducing the serrated edge slightly modifies K and ψ. However, directly above the peaks, they change substantially due to local effects. A sparse small serration evidently has only a localized effect on K and ψ.

Figure 9 illustrates the same, but with denser peaks (peak angle still 45.0°). Introducing this serration causes a dramatic undulation of K_1 and ψ. However, K_2 substantially decreases, meaning that sliding is restrained at the interface.

In Figure 10, we consider sparse, but somewhat sharper peaks (peak angle 63.4°). This causes slight change of K and ψ between the peaks, but, directly at the peaks, K and ψ change more than they did for smaller peaks.

In Figure 11, we make the previous peaks more dense. In comparison with Figure 9, we see an even greater undulation of K and ψ.

Next, in Figure 12 and Figure 13, we consider sharp, sparse peaks with peak angles 76.0° and 80.5°. As expected, sharpening the peaks continues to magnify the change in K and ψ in their vicinity, while the values elsewhere remain relatively fixed.

Table 2 summarizes the effects of sparse serration as the peaks vary from small to sharp, that is, as the angle increases from 45.0°–80.5°. Although sparse serration has only a local effect near the peaks, the effect increases as the angle increases.

Figure 14 illustrates the effect of sparse rectangular peaks. The rectangular peaks effect substantially the nearby interfacial fracture, and there is also a transition from global mode I to local mode II.
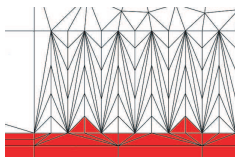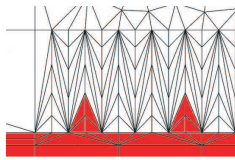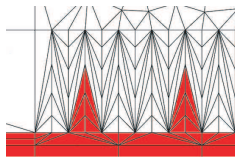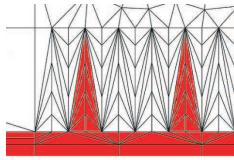

Angle (°)	45.0	63.4	76.0	80.5
Norm K_1	1.63	1.66	1.42	1.31
Norm K_2	0.01	-1.00	-1.22	-1.33
ψ (°)	0.2	-18.7	-25.8	29.4

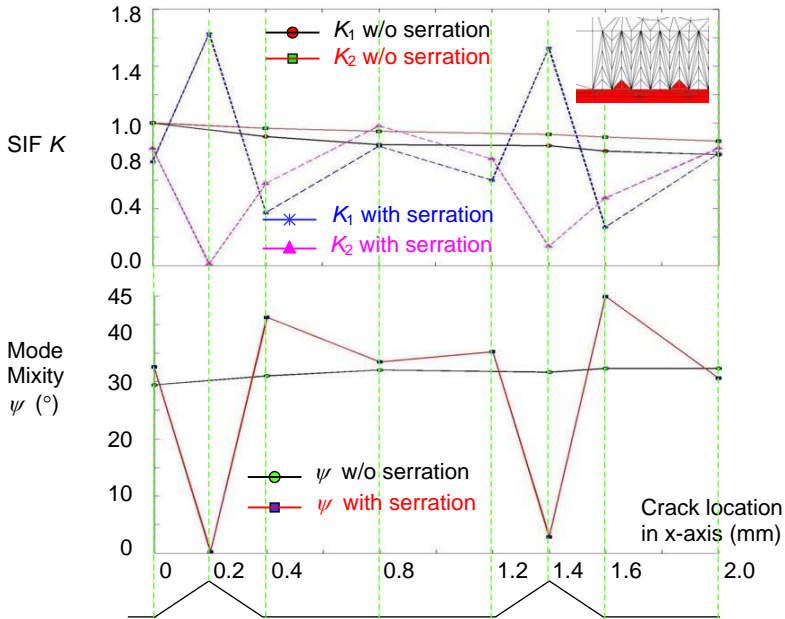**Table 2.** Comparison of sparse serration from small to sharp.

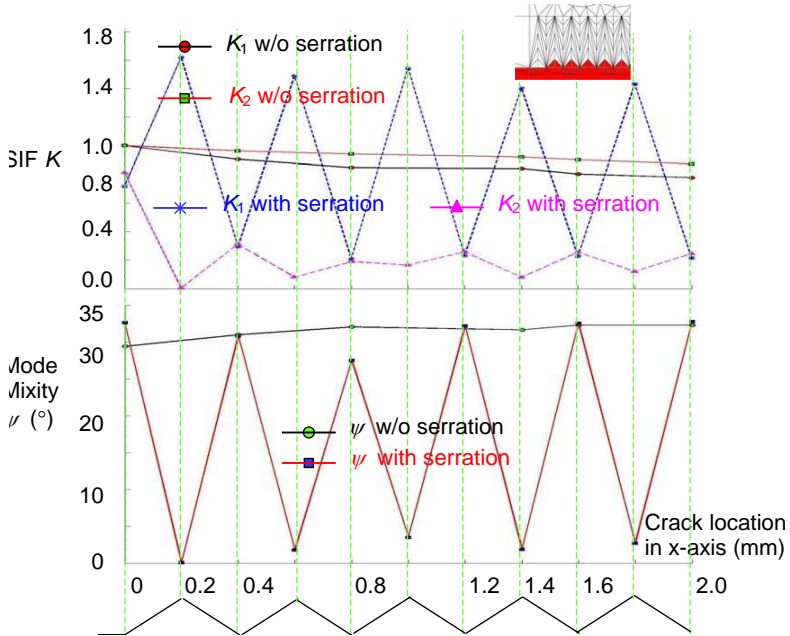**Figure 8.** K and ψ versus crack location for sparse small serrations (45.0°).

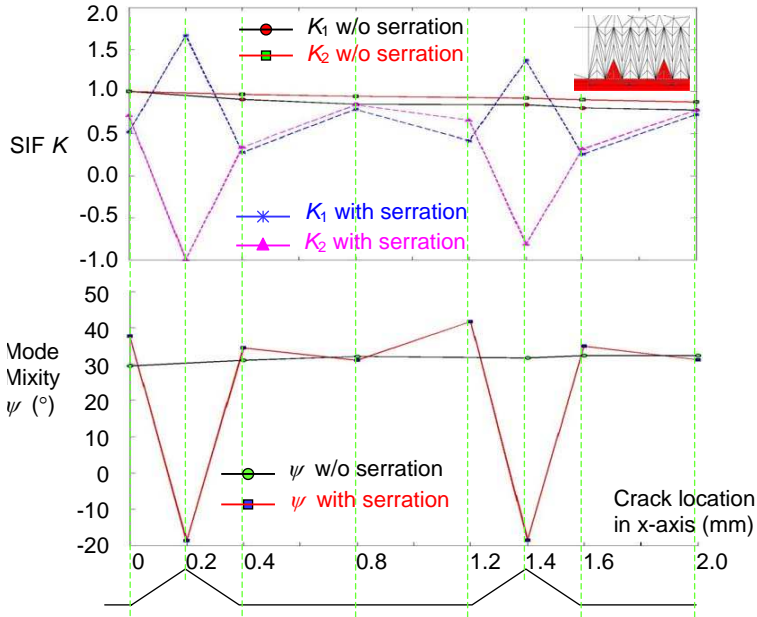**Figure 9.** K and ψ versus crack location for dense small serrations (45.0°).

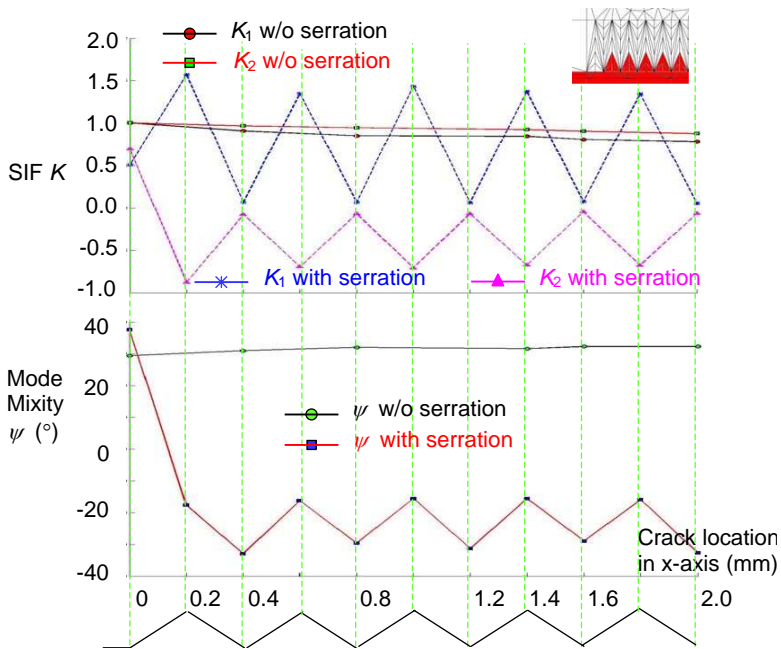**Figure 10.** K and ψ vs crack location for sparse medium serrations (63.4°).

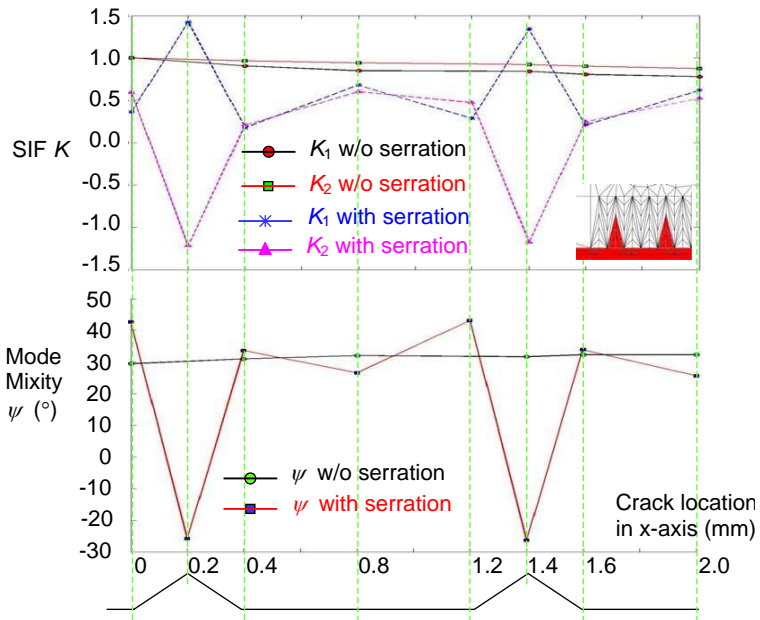**Figure 11.** K and ψ vs crack location for dense medium serrations (63.4°).

Figure 12. K and ψ vs crack location for sparse sharp serrations (76.0°).
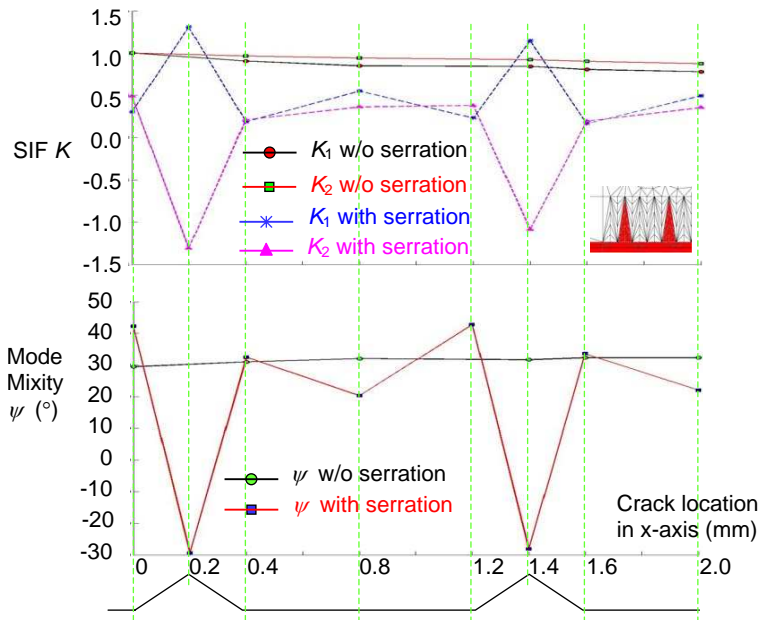

Figure 13. K and ψ vs crack location for sparse sharp serrations (80.5°).
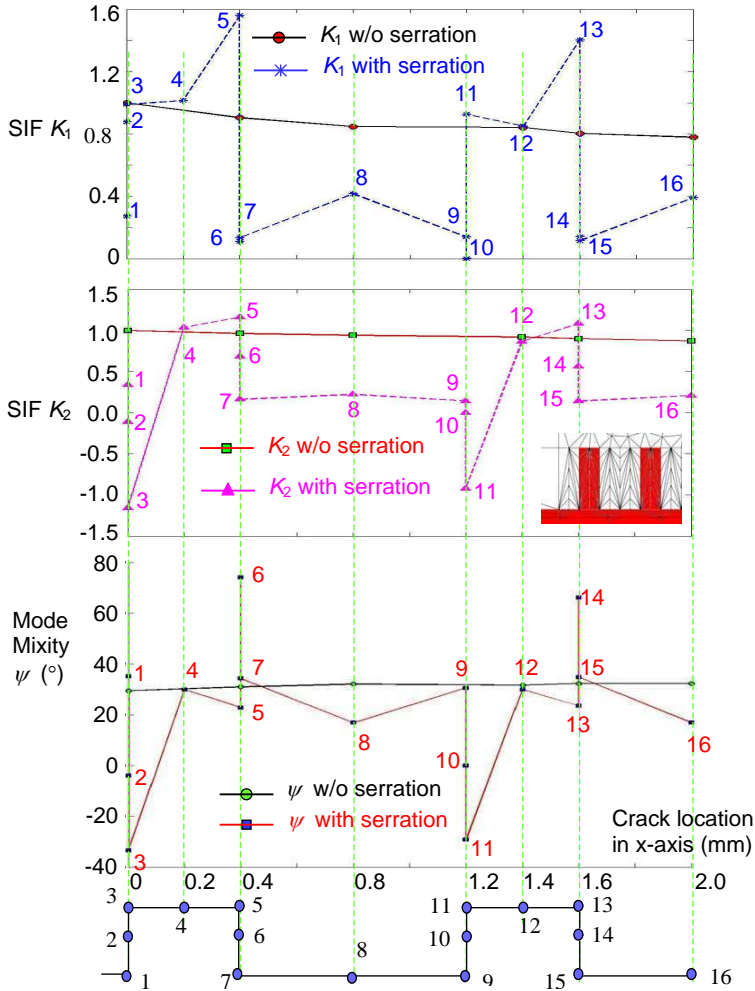
Figure 14. K and ψ vs crack location for sparse rectangular serrations (90.0°).

4. Conclusions

From our simulation and analysis, we conclude the following. (i) Sparse serration affects interfacial fracture only locally, near the serration's peaks. By sharpening the peaks, we demonstrate the effect of geometry: the disruption increases with peak sharpness. (ii) By making the peaks more dense, we study the effect of distribution: dense serration causes an undulation of the stress intensity factor and mode mixity along the interface. (iii) Altogether different geometry, namely rectangular peaks, can cause a transition from a global opening load (mode I) to a local shearing load (mode II).

Acknowledgements

References

[Cao and Evans 1989] H. C. Cao and A. G. Evans, "An experimental study of the fracture resistance of bimaterial interfaces", *Mech. Mater.* **7**:4 (1989), 295–304.

[Diao and Kandori 2006] D. Diao and A. Kandori, "Finite element analysis of the effect of interfacial roughness and adhesion strength on the local delamination of hard coating under sliding contact", *Tribol. Int.* **39**:9 (2006), 849–855.

[Diao and Kato 1994] D. Diao and K. Kato, "Interface yield map of a hard coating under sliding contact", *Thin Solid Films* **245** (1994), 115–121.

[Gilchrist and Svensson 1995] M. D. Gilchrist and N. Svensson, "A fractographic analysis of delamination within multidirectional carbon/epoxy laminates", *Compos. Sci. Technol.* **55**:2 (1995), 195–207.

[Gilchrist et al. 1996] M. D. Gilchrist, A. J. Kinloch, and F. L. Matthews, "Mechanical performance of carbon-fibre and glass-fibre-reinforced epoxy I-beams: II. fractographic failure observation", *Compos. Sci. Technol.* **56**:9 (1996), 1031–1045.

[Hutchinson and Suo 1992] J. W. Hutchinson and Z. Suo, "Mixed mode cracking in layered materials", *Adv. Appl. Mech.* **29** (1992), 63–187.

[Kim and Paulino 2002] J.-H. Kim and G. H. Paulino, "Finite element evaluation of mixed mode stress intensity factors in functionally graded materials", *Int. J. Numer. Meth. Eng.* **53**:8 (2002), 1903–1935.

[La Saponara et al. 2002] V. La Saponara, H. Muliana, R. Haj-Ali, and G. A. Kardomateas, "Experimental and numerical analysis of delamination growth in double cantilever laminated beams", *Eng. Fract. Mech.* **69**:6 (2002), 687–699.

[Larson and Miles 1998] M. C. Larson and H. F. Miles, "On the effects of friction, roughness and toughness on interfacial sliding in brittle composites", *Mech. Mater.* **27**:2 (1998), 77–89.

[Lee and Qu 2003] H.-Y. Lee and J. Qu, "Microstructure, adhesion strength and failure path at a polymer/roughened metal interface", *J. Adhes. Sci. Technol.* **17**:2 (2003), 195–215.

[Liechti 2007] K. M. Liechti, *Interfacial crack growth at glass epoxy interfaces*, 2007. Research described at author's website www.ae.utexas.edu/research/mssm/KML_BIO.htm.

[Lucksanasombool et al. 2003] P. Lucksanasombool, W. A. Higgs, R. J. Higgs, and M. Swain, "Interfacial fracture toughness between bovine cortical bone and cements", *Biomaterials* **24**:7 (2003), 1159–1166.

[Matos et al. 1989] P. P. L. Matos, R. M. McMeeking, P. G. Charalambides, and M. D. Drory, "A method for calculating stress intensities in bimaterial fracture", *Int. J. Fracture* **40**:4 (1989), 235–254.

[Mishnaevsky and Gross 2005] L. L. Mishnaevsky and D. Gross, "Deformation and failure in thin films/substrate systems: methods of theoretical analysis", *Appl. Mech. Rev.* (*Trans.ASME*) **58**:5 (2005), 338–353.

[Narayana and Dattaguru 1996] K. B. Narayana and B. Dattaguru, "Certain aspects related to computation by modified crack closure integral (MCCI)", *Eng. Fract. Mech.* **55**:2 (1996), 335–339.

[Packham 2003] D. E. Packham, "Surface energy, surface topography and adhesion", *Int. J. Adhes. Adhes.* **23**:6 (2003), 437–448.

[Partridge and Singh 1995] I. K. Partridge and S. Singh, "Mixed-mode fracture in an interleaved carbon-fibre/epoxy composite", *Compos. Sci. Technol.* **55**:4 (1995), 319–327.

[Raju 1987] I. S. Raju, "Calculation of strain-energy release rates with higher order and singular finite elements", *Eng. Fract. Mech.* **28**:3 (1987), 251–274.

[Ramulu et al. 2001] M. Ramulu, G. Paul, and J. Patel, "EDM surface effects on the fatigue strength of a 15 vol% SiCp/Al metal matric composite material", *Compos. Struct.* **54**:1 (2001), 79–86.

[Rybicki and Kanninen 1977] E. F. Rybicki and M. F. Kanninen, "A finite element calculation of stress intensity factors by a modified crack closure integral", *Eng. Fract. Mech.* **9**:4 (1977), 931–938.

[Schuller et al. 1999] T. Schuller, W. Beckert, and B. Lauke, "A finite element model to include interfacial roughness into simulations of micromechanical tests", *Comp. Mater. Sci.* **15**:3 (1999), 357–366.

[Sethuraman and Maiti 1988] R. Sethuraman and S. K. Maiti, "Finite element based computation of strain energy release rate by modified crack closure integral", *Eng. Fract. Mech.* **30**:2 (1988), 227–231.

[Straffelini 2001] G. Straffelini, "A simplified approach to the adhesive theory of friction", *Wear* **249**:1-2 (2001), 78–84.

[Suo and Hutchinson 1989] Z. Suo and J. W. Hutchinson, "Sandwich test specimens for measuring interface crack toughness", *Mater. Sci. Eng.* **107** (1989), 135–143.

[Swenson and James 1997] D. Swenson and M. James, "FRANC2D/L: a crack propagation simulator for plane layered structures", 1997, Available at http://www.fim.utp.ac.pa/FTP/Linux/CASCA/Short.pdf. Short user's guide. Version 1.4.

[Wang and Agrawal 2000] X. Wang and C. M. Agrawal, "A mixed mode fracture toughness test of bone-biomaterial interface", *J. Biomed. Mater. Res.* **53**:6 (2000), 664–672.

[Wang and Suo 1990] J.-S. Wang and Z. Suo, "Experimental determination of interfacial toughness curves using Brazil-nut-sandwiches", *Acta Metall. Mater.* **38**:7 (1990), 1279–1290.

[Young 2001] L.-J. Young, "A further investigation of mixed mode loading center crack problem", *Int. J. Solids Struct.* **38**:42-43 (2001), 7461–7471.

ASSIMINA A. PELEGRI: pelegri@jove.rutgers.edu
Mechanical and Aerospace Engineering, School of Engineering, Rutgers, The State University of New Jersey, 98 Brett Road, Piscataway, NJ 08854-8058, United States

BAOXIANG X. SHAN: bxshan@eden.rutgers.edu
Mechanical and Aerospace Engineering, School of Engineering, Rutgers, The State University of New Jersey, 98 Brett Road, Piscataway, NJ 08854-8058, United States

A MODEL FOR CHEMICALLY-INDUCED MECHANICAL LOADING ON MEMS

FABIEN AMIOT

The development of full displacement field measurements as an alternative to the optical lever technique to measure the mechanical response for microelectro-mechanical systems components in their environment calls for a modeling of chemically-induced mechanical fields (stress, strain, and displacements). As these phenomena usually arise from species adsorption, adsorbate modification or surface reconstruction, they are surface-related by nature and thus require some dedicated mechanical modeling. The accompanying mechanical modeling proposed herein is intended to represent the chemical part of the system free energy and its dependence on the surface amount. It is solved in the cantilever case thanks to an asymptotic analysis, and an approached closed-form solution is obtained for the interfacial stress field. Finally, some conclusions regarding the transducer efficiency of cantilevers are drawn from the energy balance in the accompanying model, highlighting the role of surface functionalization parameters in micromechanical sensors engineering.

1. Introduction

The increasing interest in microelectro-mechanical systems (MEMS) has raised the issue of several specific mechanical phenomena. Decreasing the size of mechanical objects down to the 1–100 micrometer range significantly enhances the surface-driven aspect of the mechanical behavior, so that these objects are used in a wide range of sensing applications [Lavrik et al. 2004]. In particular, the use of functionalized microcantilevers as environmental sensors has become very popular during the last decade. However, the basic understanding of the involved phenomena remains controversial because of numerous experimental parameters to control, and because of the lack of reliable spatially resolved mechanical information. For example, the basic understanding of the mechanisms involved in the mechanical effect induced by DNA hybridization at a cantilever surface remains an open issue [Fritz et al. 2000; Wu et al. 2001; Hansen et al. 2001; McKendry et al. 2002; Hagan et al. 2002], as well as the modeling of coupled phenomena such as electrocapillarity [Marichev 2005]. To overcome the latter difficulty, several authors [Amiot et al. 2003; 2006; Helm et al. 2005; Mertens et al. 2005; Amiot and Roger 2006] have proposed using full displacement field measurements instead of the optical lever technique to measure the microcantilever deformation. This has several advantages, depending on the way the displacement field is used; namely, averaging the displacement field across the cantilever allows one to increase the signal-to-noise ratio, if one is interested in a uniformly coated cantilever, and to achieve the selective readout of cantilevers functionalized in a heterogeneous manner. Moreover, the use of full-field measurements leads to a significantly increased amount of information, which has to be compared to suitable mechanical models of surface phenomena. In particular, the widely used Stoney's equation [Stoney 1909] (which is

obtained by assuming that the cantilever is subjected to a uniform mechanical effect) has to be enriched to describe the experimentally obtained displacement fields.

The goal of this paper is to propose such a modeling, taking into account the finite size of the functionalized area to obtain a full displacement field instead of a mean curvature. The first section is devoted to deriving such a mechanical modeling using thermodynamics arguments. Focusing on cantilever sensors, the chemical environment effect is represented by a mechanical layer, referred to as "the membrane" (bonded to the cantilever surface), whose thickness tends to zero. In Section 2, the solution for the interfacial shear-stress field is obtained by using the asymptotic expansion method [Lions 1973; Klarbring 1991; Geymonat and Krasucki 1997]. A general closed form is proposed for the derived shear-stress field, which depends on only three physical parameters. Last, a parametric study is carried out to provide some trends and perspectives to improve the efficiency of environmental sensors.

2. Mechanical modeling for chemically-actuated cantilevers

The accompanying mechanical modeling intended to represent the chemical part of the system free energy and its dependence on the surface amount is described in the first section.

2.1. *Definition of the accompanying mechanical modeling.* Let us consider a representative interface element whose size is:

- small enough to satisfy the definiteness of partial derivatives involved in continuum mechanics;
- large enough to provide a representative description of the surface mechanical behavior.

These requirements are referred to as scale separation conditions in the following. For polycrystalline thin films, a representative element should then include at least 100 grains. Three phases are classically distinguished inside this interfacial element:

- a liquid phase, whose volume is V at pressure p. Several other state variables, denoted by the set $\{n_L^\alpha\}$, represent the amount of species α in the liquid phase, and thus describe its composition;
- the interphase, whose surface is S_i and composition is described by the set $\{n_S^\alpha\}$;
- the solid phase, whose surface is S_i, described by its stress field σ.

This system is assumed to be closed, in equilibrium with an external thermostat. The system is described by its Gibbs' free enthalpy $\mathcal{G}$. If the scale separation conditions are met, then the state variables set $\{T, p, \{n_L^\alpha/V\}, \{n_S^\alpha/S_i\}, \sigma\}$ describes the local interfacial state. In particular, the initial state corresponds to the sets

$$\{n_{L,0}^\alpha\} \qquad \text{and} \qquad \{n_{S,0}^\alpha\}.$$

As one deals with a closed system, the conservation conditions lead to

$$dn_L^\alpha = -\beta^\alpha, \qquad dn_S^\alpha = \beta^\alpha,$$

where β^α is the processed quantity for species α by the reaction
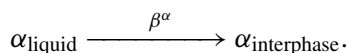
$$\alpha_{\text{liquid}} \xrightarrow{\quad \beta^\alpha \quad} \alpha_{\text{interphase}}.$$

The system free enthalpy $\mathcal{G}$ reads

$$\mathcal{G} = \mathcal{G}_L + \mathcal{G}_S + \mathcal{G}_m = \mathcal{G}_c + \mathcal{G}_m. \tag{1}$$

where $\mathcal{G}_L$ is the liquid phase contribution, $\mathcal{G}_S$ is the interphase one, and $\mathcal{G}_m$ arises from the solid substrate. Both of the first two terms are formally merged into $\mathcal{G}_c$, which represents the chemical part in $\mathcal{G}$. Each free enthalpy contribution is expressed as a function of the state variables:

- The liquid phase is assumed to be an ideal solution, so that, considering a unit volume, $\mathcal{G}_L$ reads

$$\mathcal{G}_L \left(p, T, \left\{ \frac{n_L^\alpha}{V} \right\} \right) = \sum_\alpha \frac{n_L^\alpha}{V} \left[\mu_{L,0}^\alpha(p, T) + RT \log \left(\frac{n_L^\alpha}{V} \right) \right], \tag{2}$$

  where $\mu_{L,0}^\alpha(p, T)$ is the reference chemical potential at temperature T and pressure p for species α, R the molar gas constant.

- For the sake of generality, a general form for an elementary interphase portion is considered:

$$\mathcal{G}_S \left(p, T, \left\{ \frac{n_S^\alpha}{S_i} \right\} \right) = g \left(T, \left\{ \frac{n_S^\alpha}{S_i} \right\} \right) + \sum_\alpha \left[\frac{n_S^\alpha}{S_i} \mu_{S,0}^\alpha(p, T) \right],$$

  where the function $g \left(T, \{ n_S^\alpha / S_i \} \right)$ has to be chosen to represent the evolution of the adsorbate's free enthalpy as a function of the surface concentration. For instance, a noninteracting adsorbate would lead to choosing an expression g_{ni} for g similar to the one used in Equation (2):

$$g_{ni} \left(T, \left\{ \frac{n_S^\alpha}{S_i} \right\} \right) = RT \sum_\alpha \frac{n_S^\alpha}{S_i} \log \left(\frac{n_S^\alpha}{S_i} \right). \tag{3}$$

Setting $S_i = S_0 + dS$, the chemical part of the overall free enthalpy reads

$$\mathcal{G}_c(S_i) = \sum_\alpha \left[\frac{n_{L,0}^\alpha - \beta^\alpha}{V} \left[\mu_{L,0}^\alpha(p, T) + RT \log \left(\frac{n_{L,0}^\alpha - \beta^\alpha}{V} \right) \right] \right.$$
$$\left. + \frac{n_{S,0}^\alpha + \beta^\alpha}{S_0 + dS} \mu_{S,0}^\alpha(p, T) \right] + g \left(T, \left\{ \frac{n_{S,0}^\alpha + \beta^\alpha}{S_0 + dS} \right\} \right).$$

The chemical contribution to the free enthalpy depends on the available surface amount. Considering small area variations,

$$\mathcal{G}_c(S_i) \simeq \mathcal{G}_c(S_0) + \frac{1}{S_0} \sum_\alpha \left[- \left((n_{S,0}^\alpha + \beta^\alpha) \mu_{S,0}^\alpha(p, T) + \frac{\partial g}{\partial \left(\frac{n_S^\alpha}{S_i} \right)} \right) \frac{dS}{S_0} \right.$$
$$\left. + \left((n_{S,0}^\alpha + \beta^\alpha) \mu_{S,0}^\alpha(p, T) + \frac{\partial g}{\partial \frac{n_S^\alpha}{S_i}} + \frac{1}{2S_0} \frac{\partial^2 g}{\partial \left(\frac{n_S^\alpha}{S_i} \right)^2} \right) \left(\frac{dS}{S_0} \right)^2 \right] + o \left(\frac{dS}{S_0} \right)^3. \tag{4}$$

Finally, both $\mathcal{G}_c$ and $\mathcal{G}_m$ depend on the available surface area. To include this shared dependence in the mechanical modeling of cantilevers, it is assumed that there is a virtual layer bonded to the surface under scrutiny, so that this surface and the virtual layer are constrained to deform together.

Moreover, it is considered that the virtual layer is subjected to a free strain ϵ_L. This local free strain value is identified by minimizing the free enthalpy, assuming that no mechanical constraint acts on the virtual layer, that is by minimizing the chemical term $\mathcal{G}_c$ with respect to the surface variation dS. Assuming that expansion (4) holds, ϵ_L satisfies

$$2 \times \epsilon_L \times \sum_{\alpha} \left[(n_{S,0}^{\alpha} + \beta^{\alpha}) \mu_{S,0}^{\alpha}(p, T) + \frac{\partial g}{\partial \left(\frac{n_S^{\alpha}}{S_i} \right)} + \frac{1}{2S_0} \frac{\partial^2 g}{\partial \left(\frac{n_S^{\alpha}}{S_i} \right)^2} \right]$$
$$- \sum_{\alpha} \left[(n_{S,0}^{\alpha} + \beta^{\alpha}) \mu_{S,0}^{\alpha}(p, T) + \frac{\partial g}{\partial \left(\frac{n_S^{\alpha}}{S_i} \right)} \right] = 0. \quad (5)$$

If one prescribes, by any external means, the virtual layer strain to be $\epsilon_L + \delta\epsilon$, its free enthalpy variation reads

$$\Delta \mathcal{G}_c = \left((n_{S,0}^{\alpha} + \beta^{\alpha}) \mu_{S,0}^{\alpha}(p, T) + \frac{\partial g}{\partial \left(\frac{n_S^{\alpha}}{S_i} \right)} + \frac{1}{2S_0} \frac{\partial^2 g}{\partial \left(\frac{n_S^{\alpha}}{S_i} \right)^2} \right) (\delta\epsilon)^2. \quad (6)$$

By analogy with the strain energy of a membrane, one is able to represent chemical effects by a bonded virtual membrane, whose thickness is e_v, whose Young's modulus E_v reads

$$E_v = \frac{2}{e_v S_0} \left((n_{S,0}^{\alpha} + \beta^{\alpha}) \mu_{S,0}^{\alpha}(p, T) + \frac{\partial g}{\partial \left(\frac{n_S^{\alpha}}{S_i} \right)} + \frac{1}{2S_0} \frac{\partial^2 g}{\partial \left(\frac{n_S^{\alpha}}{S_i} \right)^2} \right), \quad (7)$$

and whose free-strain satisfies (5). Equations (5) and (7) thus define, for a given membrane thickness e_v, an energetically equivalent mechanical modeling for the chemical effects. In addition to this energy equivalence, to account for the two-dimensional nature of the phenomena under scrutiny, it is assumed that the virtual membrane thickness is small compared with that of the considered substrate. Consequently, the chemical effects are described by a virtual membrane whose thickness is small compared with the others, and which is constrained to deform together with the substrate surface, thus defining an accompanying mechanical modeling.

2.2. Initial problem. The system is modeled as described in Figure 1. The parameters related to the beam are denoted with the subscript 1, whereas those related to the thin layer (the membrane) are denoted with the subscript 2. The behavior of both the phases is assumed to be linear elastic. The beam obeys an Euler–Bernoulli kinematics and has Young's modulus E_1, width b, length L, and thickness e_1. This beam is then subjected to an axial free strain $\epsilon_{L1}(x)$. A thin membrane (having Young's modulus E_2, width b, length $l < L$, and thickness e_2) is constrained to deform together with beam 1 along the interface Γ when subjected to a free strain field $\epsilon_{L2}(x)$ with $-\frac{l}{2} < x < \frac{l}{2}$ (one sets $x = 0$ at the center of the membrane area). Denoting by σ_1 the Cauchy stress tensor in cantilever 1, the interactions between the two beams are then represented by the scalar field $\tau(x)$ (shear-stress)

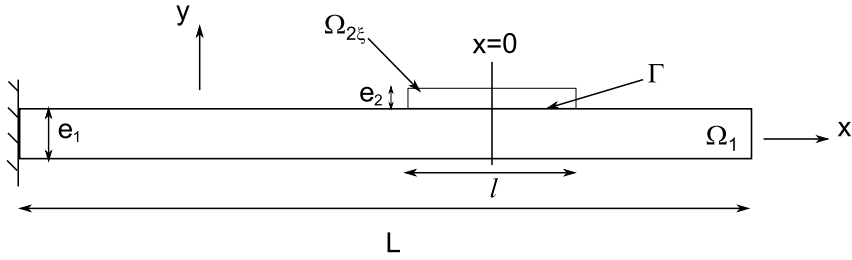$$\sigma_1 \mathbf{y} = \tau(x) \mathbf{x},$$

Figure 1. Schematic view of the accompanying mechanical model.

where **x** denotes the unit vector in the cantilever's direction and **y** the outgoing normal to its upper surface. The equilibrium conditions read

$$\frac{dN_1}{dx} + \tau b = 0,$$
$$\frac{dM_1}{dx} - \tau b \frac{e_1}{2} = 0,$$

(8)

for cantilever 1 and

$$\frac{dN_2}{dx} - \tau b = 0,$$

for membrane 2, where N_i is the normal force in phase i and M_i the bending moment. It should be noted that the proposed modeling is expected to somehow fail to represent the mechanical effect induced by adsorbates subjected to strong in-plane interactions such as electrostatic interactions, since this would require to take the adsorbate's bending stiffness into account. The tension and bending problems are assumed to be decoupled for the cantilever 1, so that the constitutive law reads

$$M_1 = E_1 I_1 \frac{d^2 w}{dx^2},$$

(9)

where $E_1 I_1$ is the bending stiffness for cantilever 1 in the middle of the cross-section (homogeneous cantilever), and $w(x)$ is the out-of-plane displacement field of the assembly. At this point, it should be underlined that using a beam or membrane theory corresponds to specific forms for the Cauchy stress tensor and displacement (strain) fields inside the phases. According to Saint-Venant's principle, the computed fields will then be correctly predicted "far enough" from the loading application points, that is, in the described case, "far enough" from the interface. As a consequence, to describe the displacement at the interface, it is required to take into account the "local" contribution of the displacement field (that is, close to the interface) in addition to the long-range displacement field provided by beam or membrane theories. A closed-form solution to this local contribution is obtained using Kolossov–Muskhelishvili potentials [Muskhelishvili 1953] and expanding the shear-stress field in a Legendre polynomial basis

$$\tau(x) = \sum_{k=0}^{\infty} \tau_k P_k \left(\frac{2x}{l} \right),$$

where $P_k(x)$ is Legendre polynomial of order k, and $\{\tau_k\}$ the projection of $\tau(x)$ onto the Legendre basis. The calculation of the in-plane displacement field $v(x)$ as the sum of the contributions $v_k(x)$ induced by

the elementary shear-stress field $P_k(2x/l)$ is detailed in Appendix A, assuming the cantilever's material behavior to be isotropic. For the sake of simplicity, let us consider uniform free strain fields

$$\epsilon_{Li}(x) = \epsilon_{Li}, \qquad i \in \{1, 2\}.$$

The plane displacement on the interface for both the cantilever 1 and the membrane 2 reads

$$u_1(x) - u_1\left(-\frac{l}{2}\right) = \epsilon_{L1} \times \left(x + \frac{l}{2}\right) + \int_{-\frac{l}{2}}^{x} \frac{N_1(\zeta)}{be_1 E_1} d\zeta - \frac{e_1}{2} \int_{-\frac{l}{2}}^{x} \frac{d^2 w}{d\zeta^2}(\zeta) d\zeta + \sum_{k=0}^{\infty} \tau_k v_k(x),$$

$$u_2(x) - u_2\left(-\frac{l}{2}\right) = \epsilon_{L2} \times \left(x + \frac{l}{2}\right) + \int_{-\frac{l}{2}}^{x} \frac{N_2(\zeta)}{be_2 E_2} d\zeta + \frac{e_2}{2} \int_{-\frac{l}{2}}^{x} \frac{d^2 w}{d\zeta^2}(\zeta) d\zeta.$$

The kinematic compatibility condition at the interface reads

$$u_1(x) - u_1\left(-\frac{l}{2}\right) = u_2(x) - u_2\left(-\frac{l}{2}\right), \tag{10}$$

and has to be satisfied for all x such that $-\frac{l}{2} < x < \frac{l}{2}$. Differentiating Equation (10) three times yields

$$-\left(\frac{1}{e_1 E_1} + \frac{1}{e_2 E_2} + \frac{be_1(e_1 + e_2)}{4I_1 E_1}\right) \tau'(x) + \sum_{k=0}^{\infty} \tau_k v_k'''(x) = 0, \tag{11}$$

so that, from Equation (11), it is proved that neglecting the local contribution to the interface plane displacement leads one to prescribe $\tau'(x) = 0$. Consequently, the equilibrium of the membrane is satisfied if and only if the shear stress field vanishes. This result underlines the fact that it is necessary to describe the mechanical fields close to the interface in a much more detailed manner than classical phenomenological methods (see for instance [Cammarata 1994]).

3. Variational formulation and asymptotic analysis

The aim of this section is to provide a suitable formulation of the problem to be solved to get the shear-stress field representing the environmental effect on the cantilever.

3.1. *Complementary energy calculation for the initial problem.* The shear-stress field is found as the minimizer of the complementary energy of the overall structure. By assuming that there is no mechanical action on the membrane except the interaction with the beam, the set $\mathcal{V}$ of statically admissible shear-stress fields reads

$$\mathcal{V} = \left\{\phi \in L^2\left(\left[-\frac{l}{2}, \frac{l}{2}\right]\right), \int_{-\frac{l}{2}}^{\frac{l}{2}} \phi(\zeta) d\zeta = 0\right\}.$$

Denoting by ξ the ratio between the thicknesses of the membrane and the beam,

$$\xi = \frac{e_2}{e_1},$$

one defines the family of initial problems P_ξ as finding the shear-stress field $\tau_s(x)$ minimizing the complementary energy I_ξ:

$$P_\xi : \begin{cases} \tau_s(x) \in \mathcal{V}, \\ I_\xi(\tau_s) \leq I_\xi(\phi), \qquad \text{for all } \phi \in \mathcal{V}, \end{cases} \tag{12}$$

with

$$I_\xi(\phi) = \Delta\sigma_1(\phi) + \Delta\sigma_{2,\xi}(\phi),$$

where $\Delta\sigma_1(\phi)$ and $\Delta\sigma_{2,\xi}(\phi)$ are the complementary energies for the cantilever and membrane. These are given by

$$\Delta\sigma_1(\phi) = \frac{1}{2}\int_{\Omega_1} \sigma_{1,xx}(\phi)\varepsilon_{1,xx}(\phi)dV - \int_\Gamma \phi(\zeta)\left(u_2(\zeta,z) - u_2\left(-\frac{l}{2},z\right)\right)dS + E_{d\tau}(\phi),$$

$$\Delta\sigma_{2,\xi}(\phi) = \frac{1}{2}\int_{\Omega_{2,\xi}} \sigma_{2,xx}(\phi)\varepsilon_{2,xx}(\phi)dV - \int_\Gamma \phi(\zeta)\left(u_1(\zeta,z) - u_1\left(-\frac{l}{2},z\right)\right)dS,$$

where $\varepsilon_{i,xx}$ is the linearized xx strain component in phase i and $E_{d\tau}(\phi)$ is the strain energy in the localized deformation mode. It should be underlined that $I_\xi(\phi)$ (through the $\Delta\sigma_{2,\xi}$ term) is defined over a domain that depends on ξ. $I_\xi(\phi)$ is rewritten as

$$I_\xi(\phi) = a_\xi(\phi,\phi) - L(\phi),$$

where the quadratic and linear forms a_ξ and L read

$$a_\xi(\phi,\phi) = 3E_{d\tau}(\phi) + \left(\xi^{-1}\frac{1}{2E_2be_1} + \frac{1}{2E_1be_1} + \frac{2}{E_1be_1}\right)\int_{-\frac{l}{2}}^{\frac{l}{2}} N_1^2(\phi)dx$$

$$+ \left(\xi^{-1}\frac{1}{e_1E_2} + \frac{1}{e_1E_1} + \frac{be_1^2(1+\xi)}{E_1I_1}\right)\int_{-\frac{l}{2}}^{\frac{l}{2}} \phi\int_{-\frac{l}{2}}^{x} N_1(\phi)d\zeta\,dx,$$

$$L(\phi) = b(\epsilon_{L2} - \epsilon_{L1})\int_{-\frac{l}{2}}^{\frac{l}{2}} \phi\left(x + \frac{l}{2}\right)dx.$$

The coercivity condition on the quadratic form a_ξ is lost when $\xi \to 0$. Consequently,

- from a practical point of view, the initial problem cannot be accurately solved by standard (that is, three-dimensional) finite element formulations;
- from a theoretical point of view, formulation (12) falls out of the framework of the Lax–Milgram theorem, meaning that existence and uniqueness of its solution cannot be directly ensured.

Formulation (12) thus needs to be modified to get a reliable solution for the shear-stress field.

3.2. Scaled problem. To transform P_ξ into a new problem defined on a fixed domain [Klarbring 1991; Geymonat and Krasucki 1997] (that is, on independent of ξ), one maps the domain

$$\Omega_{2,\xi} = \{\mathbf{x}_\Gamma + \xi y\mathbf{y},\ y \in [0, e_1],\ \mathbf{x}_\Gamma \in \Gamma\}$$

onto

$$\Omega_2 = \{\mathbf{x}_\Gamma + \tilde{y}\mathbf{y},\ \tilde{y} \in [0, e_1],\ \mathbf{x}_\Gamma \in \Gamma\}.$$

The displacement fields in both phases, as well as the interfacial shear-stress field, remain unscaled. It is then straightforward to check that if τ_s is a solution for Equation (12), then $\tau_{s,\xi}$ is a solution for problem $\widehat{P}$:

$$\widehat{P} : \begin{cases} \tau_{s,\xi}(x) \in \mathcal{V} \\ \widehat{I}_\xi(\tau_{s,\xi}) \leq \widehat{I}_\xi(\phi), & \text{for all } \phi \in \mathcal{V}, \end{cases} \tag{13}$$

where $\widehat{I}_\xi$ reads

$$\widehat{I}_\xi(\phi) = \widehat{a}_\xi(\phi, \phi) - L(\phi),$$

with the new quadratic form

$$\widehat{a}_\xi(\phi, \phi) = \left(\xi \frac{1}{E_2 b e_1} + \frac{1}{E_1 b e_1} + \frac{4e_1^2}{E_1 I_1} \right) \frac{1}{2} a_N(\phi, \phi)$$

$$+ \left(\frac{\xi^{-1}}{e_1 E_2} + \frac{1}{e_1 E_1} + \frac{(1+\xi)be_1^2}{E_1 I_1} \right) \frac{1}{2} a_d(\phi, \phi) + \frac{3b}{2} \times \frac{1}{2} a_\tau(\phi, \phi),$$

where

$$a_N(\tau, \phi) = \int_{-\frac{l}{2}}^{\frac{l}{2}} N_1(\tau) N_1(\phi) dx,$$

$$\frac{1}{2} a_d(\tau, \phi) = \frac{1}{2} \left\{ \int_{-\frac{l}{2}}^{\frac{l}{2}} \tau \int_{-\frac{l}{2}}^{x} N_1(\phi) d\zeta dx + \int_{-\frac{l}{2}}^{\frac{l}{2}} \phi \int_{-\frac{l}{2}}^{x} N_1(\tau) d\zeta dx \right\},$$

$$\frac{1}{2} a_\tau(\tau, \phi) = \frac{1}{2} \left\{ \int_{-\frac{l}{2}}^{\frac{l}{2}} \phi(x) v(\tau)(x) dx + \int_{-\frac{l}{2}}^{\frac{l}{2}} \tau(x) v(\phi)(x) dx \right\}.$$

According to Equation (7), it is assumed that the product ξE_2 tends to a finite value K_2 when ξ tends to zero:

$$E_2 = K_2 \xi^{-1},$$

so that this new quadratic form $\widehat{a}_\xi$ satisfies the Lax–Milgram conditions, and solving problem $\widehat{P}$ consists in finding the solution $\tau_{s,\xi}(x) \in \mathcal{V}$ for the linear system

$$\left(\xi^2 \frac{1}{K_2 b e_1} + \frac{1}{E_1 b e_1} + \frac{4e_1^2}{E_1 I_1} \right) a_N(\tau_{s,\xi}, \phi + \left(\frac{1}{e_1 K_2} + \frac{1}{e_1 E_1} + \frac{(1+\xi)be_1^2}{E_1 I_1} \right) a_d(\tau_{s,\xi}, \phi)$$

$$+ \frac{3b}{2} a_\tau(\tau_{s,\xi}, \phi) - L(\phi) = 0, \qquad \text{for all } \phi \in \mathcal{V}. \tag{14}$$

The solution $\tau_{s,\xi}$ is then sought as a formal asymptotic expansion [Lions 1973]

$$\tau_{s,\xi} = {}^0\tau + \xi \times {}^1\tau + \xi^2 \times {}^2\tau + \dots. \tag{15}$$

Putting (15) into the stationarity conditions of (14) leads to a separate linear system for each ξ order. The leading term ${}^0\tau \in \mathcal{V}$ is found to satisfy

$$a_0({}^0\tau, \phi) - L(\phi) = 0, \qquad \text{for all } \phi \in \mathcal{V}, \tag{16}$$
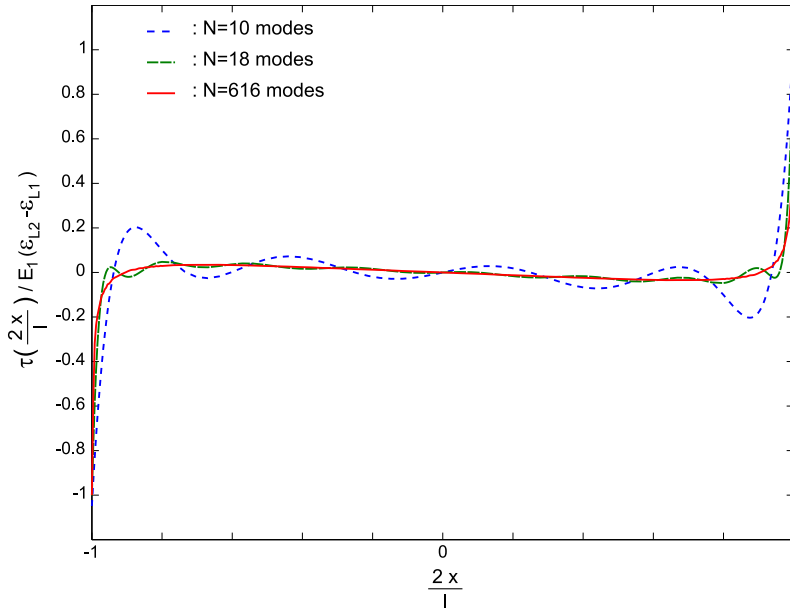
Figure 2. Convergence of the computed shear-stress field with the space dimension N.

with

$$a_0(\tau, \phi) = \left(\frac{1}{E_1 b e_1} + \frac{4e_1^2}{E_1 I_1} \right) a_N(\tau, \phi) + \left(\frac{1}{e_1 K_2} + \frac{1}{e_1 E_1} + \frac{b e_1^2}{E_1 I_1} \right) a_d(\tau, \phi) + \frac{3b}{2} a_\tau(\tau, \phi)$$

A finite dimension space $\mathcal{V}$ is chosen, described by the orthogonal basis of Legendre polynomials

$$P_n, \ n \in \{1, \ldots N\},$$

so that,

$$^0\tau(x) = \sum_{k=1}^{N} {}^0\tau_k P_k \left(\frac{2x}{l} \right). \tag{17}$$

System (16) then yields a square linear system, which is solved to provide the shear-stress field $^0\tau(x)$ along the interface Γ as its expansion (17).

4. Data reduction and parametric study

Even though describing the shear stress field by its expansion in Legendre polynomials is natural from the mathematical point of view (see Appendix A), this is of little practical interest. After demonstrating the convergence of the computed shear-stress field with the space dimension N, a closed-form solution for the interfacial stress field is provided, and from the above results some practical conclusions concerning the transducer efficiency are derived.

4.1. *Convergence and data reduction.* By using the variational formulation obtained above, the (normalized) shear-stress field is calculated as a function of three physical parameters, namely, the geometrical

parameter $s = l/e_1$; the modulus ratio $r = E_1/K_2$; and the Poisson's ratio ν. Figure 2 shows the shear-stress field computed under plane strain conditions when $N = \{10, 18, 616\}$ and the parameters $s = 0.1$, $r = 1$ and $\nu = 0.3$ are chosen. The reference solution is obtained with about 400–500 terms. All the even terms (that is, Legendre polynomials of even orders) vanish, since the solution is an odd function of the position. The shear-stress field is linear with the position at the center of the interval and drastically increases (in norm) close to the edges, but remains bounded. This reference shear-stress field, expressed as a series of Legendre's polynomials, is denoted τ_{ref} in the following.

To make these results useful, the shear stress field is modeled by using a closed-form solution $\tau(2x/l)$:

$$\frac{1}{E_1(\epsilon_{L2} - \epsilon_{L1})} \tau\left(\frac{2x}{l}\right) = T_t \tan\left(C\frac{\pi x}{l}\right) + T_l \frac{2x}{l}, \tag{18}$$

where the constants C, T_t and T_l have to be identified from the computed shear-stress fields $\tau_{ref}(2x/l)$. The reference shear-stress field has thus been computed in the following parameter ranges: $0.1 \leq \nu \leq 0.5$, $10^{-3} \leq r \leq 10^3$, and $0 \leq s \leq 1$. The local displacement contributions v_k have been obtained assuming the membrane's length to be small compared to the cantilever's thickness (see Appendix A). As the "local" contribution is significant over a depth which scales as l under the interphase, the upper bound for the s range is chosen to comply with the validity domain for the in-plane displacement field calculation, that is, $s \leq 1$. The range for ν and r is supposed to cover most practical cases. An approached closed-form solution $\tau(2x/l)$ for the shear-stress field is obtained by minimizing

$$\chi^2 = \frac{\int (\tau(\frac{2x}{l}) - \tau_{ref}(\frac{2x}{l}))^2 dx}{\int \tau_{ref}(\frac{2x}{l})^2 dx}$$

over the set $\{C, T_t, T_l\}$. The identified values are recast as

$$C = (-1.47 \times 10^{-2}\nu^2 - 3.71 \times 10^{-3}\nu + 0.9957) + 10^{-4} \times (29.4\nu^2 + 3.87\nu + 4.92)t^{0.3217 - 6.23 \times 10^{-2}\nu},$$

$$T_t = (1.72 \times 10^{-1}\nu^2 - 4.73 \times 10^{-3}\nu + 5.5 \times 10^{-2})$$
$$+ 10^{-3} \times (-45.3\nu^2 + 4.09\nu - 7.01)t^{0.313 - 5.47 \times 10^{-2}\nu - 6.38 \times 10^{-2}\nu^2},$$

$$T_l = (-8.93 \times 10^{-1}\nu^2 - 3.36 \times 10^{-2}\nu - 3.61 \times 10^{-1})$$
$$+ 10^{-2} \times (11.9\nu^2 + 0.182\nu + 1.41)t^{(4.52 - 1.71\nu) \times 10^{-1}},$$

with

$$t = s(75 + 2r).$$

The maximum relative deviation $|\chi|$ between the reference solution τ_{ref} and the proposed closed form solution τ is found to be less than 7% over the entire parameter range, thereby proving the close agreement between the reference and closed-form solutions. For practical stress estimations, it is worth noting that all stresses, including the interfacial shear-stress, scale as the longitudinal stress for the 1D inclusion problem $|\epsilon_{L2} - \epsilon_{L1}|E_1$. From closed-form solution (18), the curvature field is obtained by using the

second of Equation (8) and (9):

$$\frac{1}{E_1(\epsilon_{L2} - \epsilon_{L1})} \frac{d^2 w}{dx^2} = -\frac{e_1 b}{2E_1 I_1} \left\{ \frac{T_t l}{C\pi} \ln \left| \frac{\cos\left(\frac{C\pi x}{l}\right)}{\cos\left(\frac{C\pi}{2}\right)} \right| + T_l \left(\frac{l}{4} - \frac{x^2}{l} \right) \right\}, \tag{19}$$

which is integrated using polylogarithm functions to provide the out-of plane displacement field. Considering a single functionalized area, this integration obviously yields the fact that the longer the distance between the membrane and the cantilever's edge, the greater the end-point displacement. It is worth noting that, similarly to the well-known shear-lag problem [Volkersen 1938; Cox 1952; Lemaitre et al. 1992], the above described stress-field doesn't vanish near the membrane edges, since the whole interface is subjected to shear-stress. On the other hand, this stress field exhibits a rather different form than the one obtained with the shear-lag problem: the former diverges as $\tan(x)$ while the latter behaves as $\exp(x)$. This is thought to be the consequence of rather different interface conditions:

- the kinematic compatibility is ensured through a thin adhesion layer (typically a glue layer between two plies of a composite material) for the shear-lag problems;

- no adhesion layer is considered here, but the kinematic compatibility at the interface is ensured considering the local elastic displacement field to enrich the beam kinematic description.

4.2. *Transducer efficiency.* Moving back to the thermodynamic grounds of the modeling, and focusing on the sensing applications, the total energy in the accompanying model $\mathscr{E}_{tot}$ is decomposed as the following:

$$\mathscr{E}_{tot} = \mathscr{E}_{1,flex} + \mathscr{E}_{1,tens} + \mathscr{E}_{1,surf} + \mathscr{E}_2, \tag{20}$$

where

- $\mathscr{E}_{1,flex}$ is the strain energy located in the bending mode of the cantilever, so that it represents the useful part of the energy when the detection scheme relies on the cantilever bending;

- $\mathscr{E}_{1,tens}$ is the strain energy located in the tension mode of the cantilever;

- $\mathscr{E}_{1,surf}$ is the strain energy transferred to the "local" (surface) deformation mode of the cantilever;

- $\mathscr{E}_2$ is the strain energy of the membrane, and thus represents, according to the equivalence principle which lead to the Equations (5), (6) and (7), the chemical energy stored in the system.

The sensing problem can then be expressed as converting the stored chemical energy $\mathscr{E}_2$ into some bending strain energy $\mathscr{E}_{1,flex}$. The transducer efficiency η is thus defined as

$$\eta = \frac{\mathscr{E}_{1,flex}}{\mathscr{E}_{tot}}. \tag{21}$$

η is then the ratio of the energy used to produce the signal in most sensing applications [Lavrik et al. 2004] to the available energy. The ratio η is virtually independent of ν, and its change with the parameters r and s is shown in Figure 3 when $\nu = 0.3$. Let us first consider that any typical length for the functionalized area is attainable for any considered cantilever's material using suitable functionalization techniques. This statement implies that any point in the (r, s) plane described in Figure 3 is achievable. The change of η with the parameter r is intuitive, namely, for a given K_2, decreasing $r = E_1/K_2$ is a way of improving the sensor efficiency, as was utilized with the development of polymeric cantilevers [Johansson et al. 2005].
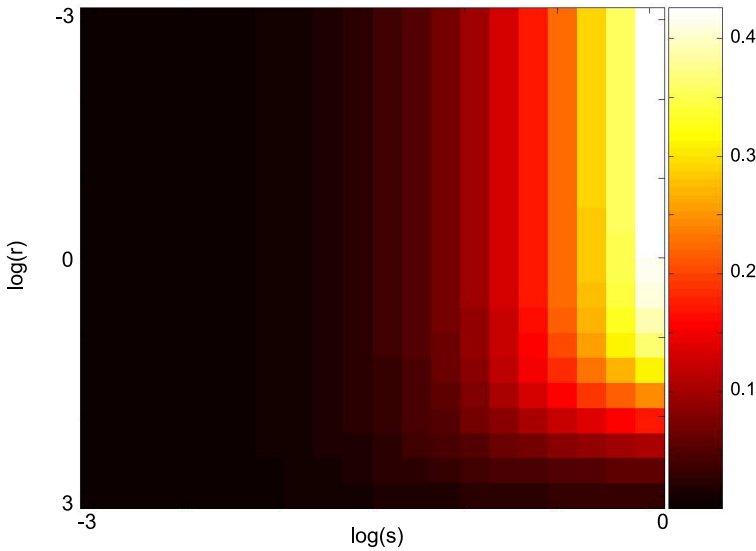
Figure 3. Overall transducer efficiency η as a function of the parameters r and s (log scales) when $\nu = 0.3$.

It should be underlined that if this trend is verified, the transducer efficiency does not vary significantly with r when $r \leq 1$, thus setting a limit to the transducer efficiency improvement one could achieve by reducing the cantilever's material stiffness. This optimal efficiency is then about 0.4, obtained when $r \to 0$ and $s \to 1$. The drastic efficiency loss when $r \gg 1$ is the result of the large amount of chemically "stored" (or blocked) energy in this range. The latter is monitored through the ratio ϱ, defined as

$$\varrho = \frac{\mathscr{E}_2}{\mathscr{E}_{\text{tot}}}. \tag{22}$$

Figure 4 shows the ratio ϱ of the stored chemical energy (that is, the final strain energy in the membrane $\mathscr{E}_2$) over the total system energy as a function of the parameters r and s when $\nu = 0.3$. For instance, this ratio is found to be around 0.85 for $r = 10^3$ and $s = 1$, meaning that only 15% of the available chemical energy is used to produce a mechanical effect, and only part of this "mechanical" energy is used to bend the cantilever, the rest being mainly spent in the local deformation mode. This argument should be used carefully, especially if one is interested in noninvasive sensing applications. If the monitored chemical system is supposed to interact with some low concentration reagents, there is a balance between the transducer efficiency and the amount of energy taken from the chemical system to bend the cantilever to ensure the measurement's noninvasiveness, that is to ensure the energy used to bend the cantilever is small enough compared to the stored chemical energy.

The change of η with the size parameter s, described in Figure 3, is less intuitive. It should be noted that the cantilever's length (or the ratio of the membrane's length to the cantilever's) is not involved at this stage. The possibility of converting more chemical energy into a mechanical one by extending the
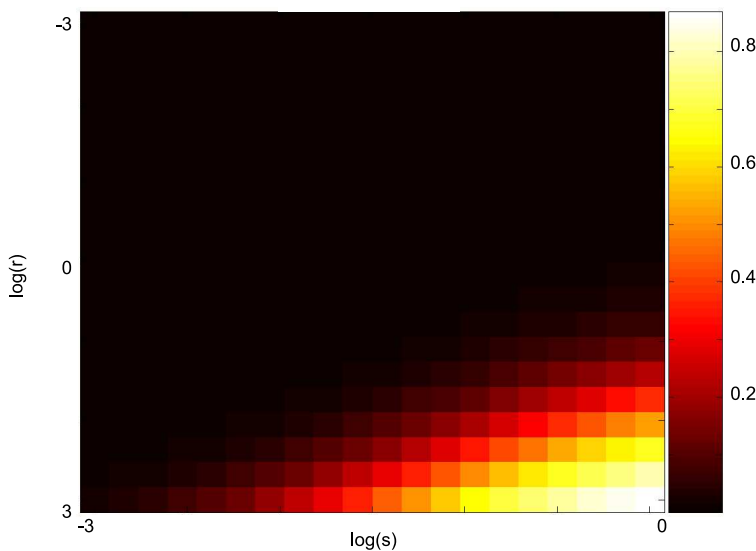
Figure 4. Ratio ϱ of the blocked chemical energy over the total system energy as a function of the parameters r and s (log scales) for $\nu = 0.3$.

functionalized area is thus not considered here. For a given value of the membrane's size l, decreasing the cantilever's thickness e_1 increases the transducer efficiency. This results from the fact the surface deformation mode extends over a depth l under the surface (see Appendix A). The described coupling efficiency change is only related to the fact that the thinner the cantilever (that is, . the higher the s parameter), the more efficiently the strain energy located in the "local" (that is, surface) deformation mode (which is not monitored so far) is converted into strain energy located into the cantilever bending mode (which is usually monitored using optical or piezoresistive read-out). This scaling effect is thus distinct from the lowering of the bending stiffness obtained by decreasing the cantilever's thickness. This raises comments regarding both the engineering and the basic understanding of the involved phenomena:

- In the previous discussion it was assumed that it is possible to move independently along both the axis of Figure 3 and Figure 4. From a practical point of view, this is false since chemical patterning techniques are substrate-dependent. Moreover, there is no experimental evidence that the K_2 value is not substrate dependent. Consequently, all the regions in those figures are not attainable, and tailoring a cantilever based sensor requires balancing transducer efficiency and sensor invasiveness in the available parameters.

- The widely used alkanethiols adsorption on gold is known to follow a two-step adsorption process, namely a random adsorption process followed by a reorganization step [Damos et al. 2005]. The typical length describing the thiol-modified surface is then supposed to grow during the adsorption process. The transducer efficiency η dependence on the membrane's size may then play a key role in the inception of the observed mechanical effects, and the observed gap between the kinetics of the optical and the mechanical effects induced by this adsorption process [Godin et al. 2003].

Finally, both of these comments raise the need for the simultaneous experimental description of the functionalization pattern and the observed mechanical effect.

5. Conclusion

A thermodynamics-based modeling of chemically-induced mechanical loadings was described. The effect of the environment is described by an accompanying mechanical modeling representing the chemical part of the system free energy and its dependence on the surface amount. A dedicated variational formulation was proposed to solve this model for the surface stress, which is finally described by an approached closed-form expression depending on three parameters. The curvature field is also expressed as a closed-form solution, allowing for future comparisons with experimentally obtained fields. Finally, a parametric study was carried out, highlighting the need for both the engineering and basic understanding point of view to control the functionalization pattern.

Appendix A: Inplane displacement field calculation

The aim of this appendix is to compute the in-plane displacement field of the surface induced by a heterogeneous shear-stress field applied to the surface of a homogeneous half-space. To comply with the cantilever case (that is, a one-dimensional model), the calculation is restricted to the $(\mathbf{x}, \mathbf{y})$ plane, by considering the elastic half-plane $y < 0$. For the sake of simplicity, its behavior is described by its Young's modulus E and its Poisson's ratio v. This half-plane is loaded along the line $y = 0$, $-1 < x < 1$ by an elementary shear-stress field

$$\sigma_{xy}(x, 0) = \begin{cases} P_k(x), & \text{if } -1 \leq x \leq 1, \\ 0, & \text{if } 1 < |x|, \end{cases}$$

where P_k is Legendre polynomial of order k. Moving to the complex plane and setting $z = x + iy$, the derivatives Φ and Y of the Kolossov–Muskhelishvili potentials [Muskhelishvili 1953] φ and Ψ read

$$\Phi_k(z) = \frac{1}{2\pi} \int_{-1}^{1} \frac{P_k(r)}{r - z} dr, \qquad Y_k(z) = -\frac{1}{\pi} \left\{ \int_{-1}^{1} \frac{P_k(r)}{r - z} dr + \frac{z}{2} \int_{-1}^{1} \frac{P_k(r)}{(r - z)^2} dr \right\}.$$

Using the properties of Legendre functions of first $P_k(z)$ and second kinds $Q_k(z)$ (see for instance [Gradstein and Ryzhik 1980]), and extending the definition of $Q_k(z)$ to the $y = 0$, $-1 < x < 1$ segment by continuity from the $y < 0$ side, one gets

$$\Phi_k(z) = -\frac{1}{\pi} Q_k(z),$$

$$Y_k(z) = -\frac{1}{\pi} \left\{ -2Q_k(z) + \frac{z}{2} \left(-\frac{1}{1 - z} - \frac{(-1)^k}{1 + z} - 2 \sum_{l=0}^{k-2l-1 \geq 0} (2k - 4l - 1) Q_{k-2l-1}(z) \right) \right\}.$$

From [Muskhelishvili 1953], the complex displacement field reads

$$2\mu U = \kappa \varphi - z \overline{\varphi'} - \overline{\Psi},$$

with

$$\mu = E/(2 + 2v),$$

and κ is defined by

$$\kappa = \begin{cases} 3 - 4\nu, & \text{for plane strain,} \\ \frac{3-\nu}{1+\nu}, & \text{for plane stress.} \end{cases}$$

The plane component of the strain fields is obtained using

$$2\mu v'_k(z) = \Re\left[2\mu\frac{dU}{dz}\right] = \Re\left[(\kappa - 1)\Phi_k(z) - z\overline{\Phi'_k(z)} - \overline{Y_k(z)}\right].$$

The strain field is found to extend to a depth of the order of l, so that this local solution should be used for systems where l is less than the substrate thickness ($l \le e_1$). The in-plane displacement field of the interface v_k is then obtained by setting $z \in [-1, 1]$ and assuming $v_k(-1) = 0$:

$$2\pi\mu v_1 = -(1+\kappa)\left\{\frac{Q_2 - Q_0}{3} - \frac{P_0}{2}\right\},$$

$$2\pi\mu v_2 = -(1+\kappa)\left\{\frac{Q_3 - Q_1}{5} + \frac{P_0}{6}\right\},$$

$$2\pi\mu v_3 = -(1+\kappa)\left\{\frac{Q_4 - Q_2}{7}\right\} + P_1 + (13+\kappa)\frac{P_0}{12},$$

$$2\pi\mu v_4 = -(1+\kappa)\left\{\frac{Q_5 - Q_3}{9} + \frac{P_0}{20}\right\},$$

$$2\pi\mu v_{2p+1} = -(1+\kappa)\left\{\frac{Q_{2p+2} - Q_{2p}}{4p+3}\right\} - \frac{Q_2 - Q_0}{3} + \sum_{k=1}^{p}\theta_{k,p}P_{2(p-k)+1} + \tilde{\theta}_p P_0, \quad \text{if } p > 1,$$

$$2\pi\mu v_{2p} = -(1+\kappa)\left\{\frac{Q_{2p+1} - Q_{2p-1}}{4p+1}\right\} + \sum_{k=1}^{p}\lambda_{k,p}P_{2(p-k)}, \quad \text{if } p > 2,$$

where

$$\theta_{1,p} = \frac{d_{1,p}}{4p-3},$$

$$\theta_{p,p} = -\frac{d_{p-1,p}}{5} + \frac{1}{p+1} + b_{p,p} - \sum_{l=0}^{p-1}\frac{4(p-l)+1}{2(p-l)(2(p-l)+1)},$$

$$\theta_{k,p} = \frac{d_{k,p}}{4(p-k)+1} - \frac{d_{k-1,p}}{4(p-k)+5}, \quad \text{if } 1 < k < p,$$

$$\tilde{\theta}_p = \frac{1+\kappa}{(2p+1)(2p+2)} + \frac{1}{2} + \frac{1}{p+1} + b_{p,p} - \sum_{l=0}^{p-1}\frac{4(p-l)+1}{2(p-l)(2(p-l)+1)},$$

$$\lambda_{1,p} = \frac{c_{1,p}}{4p-5},$$

$$\lambda_{p,p} = -\frac{1+\kappa}{2p(2p+1)} - \frac{c_{p-1,p}}{3},$$

$$\lambda_{k,p} = \frac{c_{k,p}}{4(p-k)-1} - \frac{c_{k-1,p}}{4(p-k)+3}, \quad \text{if } 1 < k < p,$$

with the constants

$$a_{r,p} = \sum_{k=0}^{r-1} \left\{ \frac{(4(p-k)-3)\,(4(p-r)-1)}{(2(r-k)-1)\,(2p-r-k-1)} - \frac{(4(p-k)-1)\,(4(p-r)-1)}{(2k+1)(2p-k)} \right\},$$

$$b_{r,p} = \sum_{k=0}^{r-1} \left\{ \frac{(4(p-k)-1)\,(4(p-r)+1)}{(2(r-k)-1)\,(2p-r-k)} - \frac{(4(p-k)+1)\,(4(p-r)+1)}{(2k+1)(2p+1-k)} \right\},$$

$$c_{r,p} = \frac{4(p-r)+1}{2p-r} + a_{r,p} - \frac{4(p-r)-1}{2(p-r)} - \sum_{k=1}^{r} \frac{(4(p-k)+3)\,(4(p-r)-1)}{2\,(2(p-k)+1)\,(p-k+1)},$$

$$d_{r,p} = \frac{4(p-r)+1}{2p+1-r} + b_{r,p} - \frac{4(p-r)+1}{2(p-r)+1} - \sum_{k=0}^{r-1} \frac{(4(p-k)+1)\,(4(p-r)+1)}{2\,(2(p-k)+1)\,(p-k)}.$$

Acknowledgement

References

[Amiot and Roger 2006] F. Amiot and J. P. Roger, "Nomarski imaging interferometry to measure the displacement field of micro-electro-mechanical systems", *Appl. Optics* **45** (2006), 7800–7810.

[Amiot et al. 2003] F. Amiot, J. P. Roger, and A. C. Boccara, "Advanced biomedical and clinical diagnostic systems", pp. 183–188 in *Progress in biomedical optics and imaging* (San Jose, California), vol. 4, 2003, Available at http://link.spie.org/PSISDG/4958/1.

[Amiot et al. 2006] F. Amiot, F. Hild, and J. P. Roger, "Identification of elastic property and loading fields from full-field measurements", *Int. J. Solids Struct.* **44** (2006), 2863–2887.

[Cammarata 1994] R. C. Cammarata, "Surface and interface stress effects in thin films", *Prog. Surf. Sci.* **46** (1994), 1–38.

[Cox 1952] H. L. Cox, "The elasticity and the strength of paper and other fibrous materials", *Br. J. Appl. Phys.* **3** (1952), 72–79.

[Damos et al. 2005] F. S. Damos, R. C. S. Luz, and L. T. Kubota, "Determination of thickness, dielectric constant of thiol films, and kinetics of adsorption using surface plasmon resonance", *Langmuir* **21** (2005), 602–609.

[Fritz et al. 2000] J. Fritz, M. K. Baller, H. P. Lang, H. Rothuizen, P. Vettiger, E. Meyer, H. Güntherodt, C. Gerber, and J. K. Gimzewski, "Translating biomolecular recognition into nanomechanics", *Science* **288** (2000), 316–318.

[Geymonat and Krasucki 1997] G. Geymonat and F. Krasucki, "Analyse asymptotique du comportement en flexion de deux plaques collés", *C. R. Acad Sci. Paris* **325** (1997), 307–314.

[Godin et al. 2003] M. Godin, O. Laroche, V. Tabard-Cossa, L. Y. Beaulieu, P. Grütter, and P. J. Williams, "Combined in-situ micromechanical cantilever-based sensing and ellipsometry", *Rev. Sci. Instrum.* **74** (2003), 4902–4907.

[Gradstein and Ryzhik 1980] I. S. Gradstein and I. M. Ryzhik, *Tables of integrals, sums, series and products*, Academic Press, New York, 1980.

[Hagan et al. 2002] F. H. Hagan, A. Majumdar, and A. K. Chakraborty, "Nanomechanical forces generated by surface grafted DNA", *J. Phys. Chem. B* **106** (2002), 10163–10173.

[Hansen et al. 2001] K. M. Hansen, H. F. Ji, G. Wu, R. Datar, R. Cote, A. Majumdar, and T. Thundat, "Cantilever-based optical deflection assay for discrimination of DNA single-nucleotide mismatches", *Anal. Chem.* **73** (2001), 1567–1571.

[Helm et al. 2005] M. Helm, J. J. Servant, F. Saurenbach, and R. Berger, "Read-out of micromechanical cantilever sensors by phase shifting interferometry", *Appl. Phys. Lett.* **87** (2005), 064101.

[Johansson et al. 2005] A. Johansson, M. Calleja, P. A. Rasmussen, and A. Boisen, "SU-8 cantilever sensor system with integrated readout", *Sens. Actuators A: Phys.* **123-124** (2005), 111–115.

[Klarbring 1991] A. Klarbring, "Derivation of a model of adhesively bonded joints by the asymptotic expansion method", *Int. J. Eng. Sci.* **29** (1991), 493–512.

[Lavrik et al. 2004] N. V. Lavrik, M. J. Sepaniak, and P. G. Datskos, "Cantilever transducers as a platform for chemical and biological sensors", *Rev. Sci. Instrum.* **75** (2004), 2229–2253.

[Lemaitre et al. 1992] J. Lemaitre, D. Sherman, and F. A. Leckie, "Crazing of laminates", *Eur. J. Mech. A:Solids* **11** (1992), 289–304.

[Lions 1973] J.-L. Lions, *Perturbations singulières dans les problèmes aux limites et en contrôle optimal*, Springer, Berlin, 1973.

[Marichev 2005] V. A. Marichev, "Partial charge transfer during anion adsorption methodological aspects", *Surf. Sci. Rep.* **56** (2005), 277–324.

[McKendry et al. 2002] R. McKendry, J. Zhang, Y. Arntz, T. Strunz, M. Hegner, H. P. Lang, M. K. Baller, U. Certa, E. Meyer, H. Güntherodt, and C. Gerber, "Multiple label-free biodetection and quantitative DNA-binding assays on a nanomechanical cantilever array", *PNAS* **99** (2002), 9783–9788.

[Mertens et al. 2005] J. Mertens, M. Álavarez, and J. Tamayo, "Real-time profile of microcantilevers for sensing applications", *Appl. Phys. Lett.* **87** (2005), 234102.

[Muskhelishvili 1953] N. I. Muskhelishvili, *Some basic problems of the mathematical theory of elasticity*, P. Noordholl Ltd, Grönigen (Holland), 1953.

[Stoney 1909] G. Stoney, "The tension of metallic films deposited by electrolysis", *Proc. Roy. Soc. London Ser A* **82** (1909), 172.

[Volkersen 1938] O. Volkersen, "Die Nietkraftverteilung in zugbeanspruchten Nietverbindungen mit konstanten Laschenquerschnitten", *Luftfahrtforschung* **15** (1938), 41–47.

[Wu et al. 2001] G. Wu, H. Ji, K. Hansen, T. Thundat, R. Datar, R. Cote, M. F. Hagan, A. K. Chakraborty, and A. Majumdar, "Origin of nanomechanical cantilever motion generated from biomolecular interactions", *PNAS* **98** (2001), 1560–1564.

FABIEN AMIOT: fabien.amiot@mic.dtu.dk

MIC — Department of Micro and Nanotechnology NanoDTU, Technical University of Denmark, Ørsteds Plads, Bygning, 345 east DK-2800 Kgs., DK-2800 Lyngby, Denmark

INVARIANTS OF $C^{1/2}$ IN TERMS OF THE INVARIANTS OF C

ANDREW N. NORRIS

The three invariants of $C^{1/2}$ are key to expressing this tensor and its inverse as a polynomial in C. Simple and symmetric expressions are presented connecting the two sets of invariants $\{I_1, I_2, I_3\}$ and $\{i_1, i_2, i_3\}$ of C and $C^{1/2}$, respectively. The first result is a bivariate function relating I_1, I_2 to i_1, i_2. The functional form of i_1 is the same as that of i_2 when the roles of the C-invariants are reversed. The second result expresses the invariants using a single function call. The two sets of expressions emphasize symmetries in the relations among these four invariants.

1. Introduction

We consider relations among the basic tensors of three dimensional continuum mechanics, all defined by the deformation F,

$$F = RU = VR, \qquad C = F^t F, \qquad B = FF^t.$$

U and V are symmetric and positive definite, and therefore

$$U = C^{1/2}, \qquad V = B^{1/2}.$$

Here we will only consider properties of U and C, but the results apply to V and B.

Although the square root of a second order positive definite symmetric tensor is unique and unambiguous it is not, however, a simple algebraic construct. One way to circumvent this problem is to express U as a polynomial in C using the Cayley–Hamilton equation,

$$U^3 - i_1 U^2 + i_2 U - i_3 I = 0. \tag{1}$$

Here i_1, i_2, i_3 are the invariants of U,

$$i_1 = \operatorname{tr} U, \qquad i_2 = \frac{1}{2}(\operatorname{tr} U)^2 - \frac{1}{2}\operatorname{tr} U^2, \qquad i_3 = \det U,$$

Multiply Equation (1) by $(U + i_1 I)$, and note that the result contains terms proportional to I, U, U^2, and U^4. Replacing the latter two by C and C^2 gives [Ting 1985]

$$U = (i_1 i_2 - i_3)^{-1}(i_1 i_3 I + (i_1^2 - i_2)C - C^2). \tag{2}$$

Note that $i_1 i_2 - i_3 = \det(i_1 I - U) > 0$ [Carroll 2004]. The inverse U^{-1} may be obtained by multiplying each side of Equation (2) with C^{-1} and using the Cayley–Hamilton equation for C to eliminate the single remaining C^{-1} term. The orthogonal rotation tensor follows as $R = FU^{-1}$, from which one can determine kinematic quantities such as the rotation angle and the axis of rotation [Guan-Suo 1998].

Equation (2) for U in terms of C avoids the tensor square root difficulty but introduces another: how to express $\{i_1, i_2, i_3\}$ in terms of C, or more specifically, in terms of its invariants

$$I_1 = \operatorname{tr} C, \qquad I_2 = \frac{1}{2}(\operatorname{tr} C)^2 - \frac{1}{2}\operatorname{tr} C^2, \qquad I_3 = \det C.$$

While the relation $i_3 = \sqrt{I_3}$ is simple, formulas for i_1 and i_2 are not. But as Equation (2) and related identities illustrate, the functional relations between the two sets of invariants are important for obtaining semiexplicit expressions for stretch and rotation tensors, and for their derivatives [Hoger and Carlson 1984b; Steigmann 2002; Carroll 2004].

The first such relations are due to Hoger and Carlson [1984a], who derived expressions for $\{i_1, i_2\}$ by solving a quartic equation. Sawyers [1986] subsequently showed that one can obtain alternative relations using the standard solutions [Goddard and Ledniczky 1997] for the cubic equation of the eigenvalue of C. Let $\lambda_1, \lambda_2, \lambda_3$ be the (necessarily positive) eigenvalues of U, then the eigenvalues of C are $\lambda_1^2, \lambda_2^2, \lambda_3^2$, and

$$i_1 = \lambda_1 + \lambda_2 + \lambda_3, \qquad i_2 = \lambda_1\lambda_2 + \lambda_2\lambda_3 + \lambda_3\lambda_1, \qquad i_3 = \lambda_1\lambda_2\lambda_3, \tag{3a}$$

$$I_1 = \lambda_1^2 + \lambda_2^2 + \lambda_3^2, \qquad I_2 = \lambda_1^2\lambda_2^2 + \lambda_2^2\lambda_3^2 + \lambda_3^2\lambda_1^2, \qquad I_3 = \lambda_1^2\lambda_2^2\lambda_3^2. \tag{3b}$$

Sawyers' approach is to essentially compute the eigenvalues of C, take their square roots and from these determine the invariants of U by Equation (3a). Jog [2006] generalized this scheme to tensors of order $n > 3$. This method does not provide direct relations between the invariants. Although the formulas of Hoger and Carlson [1984a] and of Sawyers [1986] are explicit, they are not totally satisfactory. In each case the functional forms are complicated. As we will see, there is no way to avoid this complexity since we are dealing with roots of cubic and quartic equations. But that is not the basic issue, rather it is a lack of any underlying symmetry or balance in the solutions of Hoger and Carlson [1984a] and of Sawyers [1986]. This makes it difficult to comprehend the formulas, and to place them in context. It is all the more unsettling by virtue of the fact that the formulas are associated with algebraic systems of deformation tensors, systems that are elegant and generally quite transparent.

The object of this paper is to express $\{i_1, i_2, i_3\}$ in terms of $\{I_1, I_2, I_3\}$ in two forms that each display the underlying symmetry of the relations. Both forms employ a single function, but have slightly different properties. We begin in section Section 2 with a summary of the principal results, followed by a review of the previously known solutions in Section 3. The new formulas for the invariants of $C^{1/2}$ are derived in Section 4, with some closing comments in Section 5.

2. Principal results

Theorem 1. The invariants of $C^{1/2}$ are

$$i_1 = I_3^{1/6} f\left(\frac{I_1}{I_3^{1/3}}, \frac{I_2}{I_3^{2/3}}\right), \qquad i_2 = I_3^{1/3} f\left(\frac{I_2}{I_3^{2/3}}, \frac{I_1}{I_3^{1/3}}\right), \qquad i_3 = I_3^{1/2}, \tag{4}$$

where f is a function of two variables,

$$f(x, y) = g(x, y) + \sqrt{x - g^2(x, y) + 2/g(x, y)}, \tag{5a}$$

$$g(x, y) = \left(\frac{1}{3}\left(x + \sqrt{x^2 - 3y}\left[(\zeta + \sqrt{\zeta^2 - 1})^{1/3} + (\zeta - \sqrt{\zeta^2 - 1})^{1/3}\right]\right)\right)^{1/2}, \tag{5b}$$

$$\zeta = \frac{27 + 2x^3 - 9xy}{2(x^2 - 3y)^{3/2}}. \tag{5c}$$

The function g can be expressed in the alternate form

$$g(x, y) = \sqrt{\frac{1}{3}\left(x + 2\sqrt{x^2 - 3y} \, \cos\left(\frac{1}{3} \arccos \zeta(x, y)\right)\right)}.$$

It is clear from Theorem 1 that the following reduced quantities are the important variables:

$$j_1 = \frac{i_1}{i_3^{1/3}}, \qquad j_2 = \frac{i_2}{i_3^{2/3}}, \tag{6a}$$

$$J_1 = \frac{I_1}{I_3^{1/3}}, \qquad J_2 = \frac{I_2}{I_3^{2/3}}, \tag{6b}$$

in terms of which the theorem states

$$j_1 = f(J_1, J_2), \qquad j_2 = f(J_2, J_1).$$

Alternatively, the sum and difference of reduced invariants may be considered as the key parameters, which is evident from:

Lemma 1. The following relation holds between the invariants of C and $C^{1/2}$:

$$\frac{J_1 - J_2}{j_1 - j_2} = j_1 + j_2 + 2.$$

An immediate consequence is that we need only determine $j_1 + j_2$ or $j_1 - j_2$ since the other follows directly from Lemma 1. For instance, we could calculate $j_1 + j_2 = f(J_1, J_2) + f(J_2, J_1)$, but this requires evaluation of f twice, and it does not reveal the underlying symmetry of the arguments. The second result is a simpler relation between the invariants, one that uses a single call to the function f:

Theorem 2. The reduced invariants of $C^{1/2}$ and C are connected by

$$j_1 = \frac{s}{2} + \frac{J_1 - J_2}{2s + 4}, \tag{7a}$$

$$j_2 = \frac{s}{2} - \frac{J_1 - J_2}{2s + 4}, \tag{7b}$$

where $s = s(J_1, J_2)$ is

$$s = (2 + J_1 + J_2)^{1/3} f\left(\frac{6 + J_1 + J_2}{(2 + J_1 + J_2)^{2/3}}, \frac{9 + 5J_1 + 5J_2 + J_1 J_2}{(2 + J_1 + J_2)^{4/3}}\right). \tag{7c}$$

Thus $j_1 + j_2 = s(J_1, J_2)$, and s is a symmetric function of its arguments $s(x, y) = s(y, x)$. Also, s provides an alternative expression for the function f:

$$f(x, y) = \frac{1}{2}s(x, y) + \frac{x - y}{2s(x, y) + 4}.$$

This form for f employs the function itself, but evaluated at different arguments. This is a property of the nonlinear nature of the function.

3. The methods of Hoger and Carlson and of Sawyers

Starting from the identities Equation (3) it may be easily verified that [Hoger and Carlson 1984a]

$$i_1^2 - 2i_2 = I_1, \tag{8a}$$

$$i_2^2 - 2i_1 i_3 = I_2, \tag{8b}$$

$$i_3^2 = I_3. \tag{8c}$$

Equation (8c) implies $i_3 = I_3^{1/2}$. It remains to find i_1 and i_2.

Hoger and Carlson [1984a] eliminated i_2 between Equation (8a) and (8b) to obtain a quartic equation in i_i which they then solved. The same solution for i_i is obtained more directly by starting with the *ansatz*

$$i_i = \lambda + \rho, \tag{9}$$

where λ is any one of the triplet $\{\lambda_1, \lambda_2, \lambda_3\}$. For instance, if $\lambda = \lambda_1$ then $\rho = \lambda_2 + \lambda_3$ and $i_2 = \lambda_1(\lambda_2 + \lambda_3) + \lambda_2\lambda_3$ is

$$i_2 = \rho\lambda + i_3/\lambda. \tag{10}$$

This holds no matter which value λ takes. Substituting from Equation (9) into Equation (8a) implies

$$\rho^2 = I_1 - \lambda^2 + 2i_3/\lambda. \tag{11}$$

The right member is necessarily positive, and using $i_3 = I_3^{1/2}$ we can therefore express $\rho > 0$ in terms of I_1, I_3 and λ.

In summary,

$$i_1 = \lambda + \sqrt{I_1 - \lambda^2 + 2\sqrt{I_3}/\lambda}, \tag{12a}$$

$$i_2 = \sqrt{I_3}/\lambda + \sqrt{I_1\lambda^2 - \lambda^4 + 2\sqrt{I_3}\lambda}, \tag{12b}$$

$$i_3 = \sqrt{I_3}, \tag{12c}$$

where λ is any positive root of the characteristic equation of C,

$$\lambda^6 - I_1\lambda^4 + I_2\lambda^2 - I_3 = 0. \tag{13}$$

For instance,

$$\lambda = \left(\frac{1}{3} \left(I_1 + \left[\xi + \sqrt{\xi^2 - (I_1^2 - 3I_2)^3} \right]^{1/3} + \left[\xi - \sqrt{\xi^2 - (I_1^2 - 3I_2)^3} \right]^{1/3} \right) \right)^{1/2},$$

and

$$\xi = \frac{1}{2}(2I_1^3 - 9I_1I_2 + 27I_3).$$

Note that we assumed that λ in Equations (9) and (10) is a root of (13), but this is actually a requirement, as can be seen from Equations (8) using (9)–(11). Equations (9) and (10) represent a standard method of reducing a quartic to a cubic equation.

Equation (12a) is essentially the same as the first relation of Hoger and Carlson [1984a, Equation (5.5)], although they did not identify the root of the cubic explicitly. It should be noted that the second relation in their Equation (5.5) never applies, because it can be shown that the equality cannot occur. Hoger and Carlson [1984a] recommended using Equation (8b) to obtain i_2. The relation (12b) is quite different and is suggestive of the symmetry underlying the solutions for i_1 and i_2 that is evident in Theorem 1. We discuss this further in the next section from a different perspective.

It is interesting to compare this with the explicit positive solution of Equation (13) provided by Guan-Suo [1998], based on [Sawyers 1986]. Starting with the characteristic equation for U,

$$\lambda^3 - i_1\lambda^2 + i_2\lambda - i_3 = 0, \tag{14}$$

combined with Equation (8b) and Equation (8c), this becomes a quadratic equation for i_2. The solution is [Guan-Suo 1998, p. 199]

$$i_2 = \lambda^{-1}\left(\sqrt{I_3} + \sqrt{2\sqrt{I_3}\lambda^3 + I_2\lambda^2 - I_3}\right).$$

This appears to be different than Equation (12b), but they are equivalent when one takes into account that λ satisfies (13).

In short, Hoger and Carlson [1984a] and Sawyers [1986] derived Equation (12a) and (12b), respectively. They did not however note the symmetry between the formulas, which is one of the central themes in this paper: that a single function determines both i_1 and i_2. In the next section we complete the proof of Theorem 1.

4. An alternative approach

The three conditions in Equation (8) can be combined into a single polynomial identity,

$$(1 - i_2z^2)^2 + (i_1z - i_3z^3)^2 = 1 + I_1z^2 + I_2z^4 + I_3z^6, \quad \text{for all } z \in \mathbb{C}.$$

Using the reduced variables of Equation (6), this becomes

$$(1 - j_2z^2)^2 + (j_1z - z^3)^2 = 1 + J_1z^2 + J_2z^4 + z^6, \quad \text{for all } z \in \mathbb{C}.$$

Comparing coefficients implies the pair of coupled equations

$$j_1^2 - 2j_2 = J_1, \tag{15a}$$

$$j_2^2 - 2j_1 = J_2. \tag{15b}$$

Thus, solutions must be of the form

$$j_1 = f(J_1, J_2), \qquad j_2 = f(J_2, J_1),$$

for some function $f(x, y)$ which satisfies

$$f^2(x, y) - 2f(y, x) - x = 0. \tag{16}$$

This is the fundamental equation for $f(x, y)$. It implies the dual relation

$$f^2(y, x) - 2f(x, y) - y = 0. \tag{17}$$

Eliminating $f(y, x)$ leads to a quartic in $f = f(x, y)$:

$$(f^2 - x)^2 - 8f - 4y = 0. \tag{18}$$

This is equivalent to the quartic of [Hoger and Carlson 1984a] but expressed in the reduced variables. We have already derived a solution of the quartic in the previous section by using the ansatz of Equation (9) based on a root of the cubic (13). (12a) therefore *defines* the function f, which can be read off by converting to the reduced variables j_1, j_2, J_1, J_2. It may be easily verified that the function of (5) results.

But what about the relation (12b) for i_2? It does not seem to convert into the expression claimed in Theorem 1, that is, $j_2 = f(J_2, J_1)$. Rather, using (12b) and $j_2 = f(J_2, J_1)$ to define f we obtain a different expression for f:

$$f(y, x) = \frac{1}{g(x, y)} + \sqrt{x - g^2(x, y) + 2/g(x, y)}\, g(x, y). \tag{19}$$

This is, in fact, consistent with the definition of f in Theorem 1 because $g(x, y)$ satisfies the normalized version of (14),

$$g^3(x, y) - f(x, y)g^2(x, y) + f(y, x)g(x, y) - 1 = 0. \tag{20}$$

Using this and the expression for $f(x, y)$ in Equation (5), gives (19). This completes the proof of Theorem 1.

It is interesting to note from Equation (20) that $1/g(y, x)$ satisfies the same equations as $g(x, y)$, that is,

$$g^{-3}(y, x) - f(x, y)g^{-2}(y, x) + f(y, x)g^{-1}(y, x) - 1 = 0.$$

But this does not mean that $g(y, x)$ equals $1/g(x, y)$, since they can (and do) correspond to different roots of the cubic.

The identity in Lemma 1 follows from the coupled equations (15), and the details of the proof of Theorem 2 are in the Appendix.

5. Conclusion

Although the expressions for i_1 and i_2 involve the roots of the characteristic cubic equation of C, it seems that the governing quartic Equation (18) is more fundamental. This is the equation that defines the functions f and s of Theorems 1 and 2. In fact s is defined by f, which is in some ways the central function involved. It is interesting that the quartic equation first considered by Hoger and Carlson [1984a] reappears in this manner.

Which of the expressions for i_1 and i_2 are actually best in practice? While the expressions in Equation (7) are perhaps the most aesthetically pleasing in form, (4) is probably simpler to implement. The final choice is of course left to the reader.

Appendix A. Proof of Theorem 2

For simplicity of notation, let f and f' denote $f(x, y)$ and $f(y, x)$, respectively. Then the coupled Equation (16) and (17) are

$$f^2 - 2f' = x,$$
$$f'^2 - 2f = y.$$

Adding and subtracting yields, respectively,

$$(f + f' - 1)^2 = 1 + x + y + 2ff',$$
$$(f - f')(f + f' + 2) = x - y,$$

which in turn imply

$$f + f' = s,$$
$$f - f' = \frac{x - y}{s + 2},$$

where $s = 1 + \sqrt{1 + x + y + 2ff'}$. The function $s = s(x, y)$ is clearly a symmetric function of x and y, that is, it is unchanged if the arguments are switched.

Solving the linear equations for f and f' gives

$$f = \frac{s}{2} + \frac{x - y}{2s + 4},$$
$$f' = \frac{s}{2} - \frac{x - y}{2s + 4}.$$

Although these formulas clearly split f into parts that are symmetric and asymmetric in the two arguments, they are not explicit since the function s involves the product ff'. Taking the product of the two expressions leads to an equation for ff'. It is simpler to consider the equation for s, which after some manipulation may be reduced to the quartic:

$$[s^2 - (6 + x + y)]^2 - 8(2 + x + y)s - 4[(5 + x)(5 + y) - 16] = 0.$$

Let $s = (2 + x + y)^{1/3} u$; then u satisfies $(u^2 - X)^2 - 8u - 4Y = 0$, where

$$X = \frac{6 + x + y}{(2 + x + y)^{2/3}}, \qquad Y = \frac{9 + 5x + 5y + xy}{(2 + x + y)^{4/3}}.$$

The quartic equation for u is the same as the quartic Equation (18) satisfied by f, but with X and Y instead of x and y. Thus,

$$u = f(X, Y),$$

which completes the proof of Theorem 2.

References

[Carroll 2004] M. M. Carroll, "Derivatives of the rotation and stretch tensors", *Math. Mech. Solids* **9** (2004), 543–553.

[Goddard and Ledniczky 1997] J. D. Goddard and K. Ledniczky, "On the spectral representation of stretch and rotation", *J. Elasticity* **47** (1997), 255–259.

[Guan-Suo 1998] D. Guan-Suo, "Determination of the rotation tensor in the polar decomposition", *J. Elasticity* **50** (1998), 197–207.

[Hoger and Carlson 1984a] A. Hoger and D. E. Carlson, "Determination of the stretch and rotation in the polar decomposition of the deformation gradient", *Q. Appl. Math.* **42** (1984), 113–117.

[Hoger and Carlson 1984b] A. Hoger and D. E. Carlson, "On the derivative of the square root of a tensor and Guo's rate theorems", *J. Elasticity* **14** (1984), 329–336.

[Jog 2006] C. S. Jog, "Concise proof of the representation theorem for fourth-order isotropic tensors", *J. Elasticity* **85** (2006), 119–124.

[Sawyers 1986] K. Sawyers, "Comments on the paper "Determination of the stretch and rotation in the polar decomposition of the deformation gradient" by A. Hoger and D. E. Carlson", *Q. Appl. Math.* **44** (1986), 309–311.

[Steigmann 2002] D. J. Steigmann, "Invariants of the stretch tensors and their application to finite elasticity theory", *Math. Mech. Solids* **7** (2002), 393–403.

[Ting 1985] T. C. T. Ting, "Determination of $C^{1/2}$, $C^{-1/2}$ and more general isotropic tensor functions of C", *J. Elasticity* **15** (1985), 319–323.

ANDREW N. NORRIS: norris@rutgers.edu
Rutgers University, Mechanical and Aerospace Engineering, 98 Brett Road, Piscataway, NJ 08854-8058, United States
http://mechanical.rutgers.edu/norris

A VARIATIONAL ASYMPTOTIC MICROMECHANICS MODEL FOR PREDICTING CONDUCTIVITIES OF COMPOSITE MATERIALS

TIAN TANG AND WENBIN YU

The focus of this paper is to extend the variational asymptotic method for unit cell homogenization (VA-MUCH) to predict the effective thermal conductivity and local temperature field distribution of heterogeneous materials. Starting from a variational statement of the conduction problem of the heterogeneous continuum, we formulate the micromechanics model as a constrained minimization problem using the variational asymptotic method. To handle realistic microstructures in applications, we implement this new model using the finite element method. For validation, a few examples are used to demonstrate the application and accuracy of this theory and companion code. Since heat conduction is mathematically analogous to electrostatics, magnetostatics, and diffusion, the present model can also be used to predict effective dielectric, magnetic, and diffusion properties of heterogeneous materials.

1. Introduction

Along with increased knowledge and manufacturing techniques for materials, more and more materials are made with engineered microstructures to achieve better performance. To successfully design and fabricate these materials, we need efficient high-fidelity analysis tools to predict their effective properties. Many composites are applied in temperature sensitive environments such as electronic packaging and thermal protection systems. Accurate prediction of thermal properties such as the specific heat, coefficients of thermal expansion, and thermal conductivity becomes important for such applications. In this paper, we focus on developing a model to predict effective thermal conductivity and associated local temperature and heat flux distribution within the heterogeneous materials.

The effective thermal conductivity of composites is strongly affected by many parameters including the properties, volume fractions, distributions, and orientations of constituents. Numerous models have been proposed to predict the effective thermal conductivity [Progelhof et al. 1976]. These models include simple rules of mixtures, self consistent scheme [Hashin 1968], generalized self consistent scheme [Lee et al. 2006], finite element method [Ramani and Vaidyanathan 1995; Islam and Pramila 1999; Xu and Yagi 2004; Kumlutas and Tavman 2006], effective unit cell approach [Ganapathy et al. 2005] and variational bounds [Hashin and Shtrikman 1962]. Very recently, a new framework for micromechanics modeling, namely variational asymptotic method for unit cell homogenization (VAMUCH) [Yu and Tang 2007a], has been introduced using two essential assumptions in the context of micromechanics for composites with an identifiable unit cell.

Assumption 1. The exact field variable has volume average over the unit cell. For example, if ϕ is the exact temperature within the unit cell, there exist ψ such that

$$\psi = \frac{1}{\Omega} \int_{\Omega} \phi \, d\Omega \equiv \langle \phi \rangle, \tag{1}$$

where Ω denotes the domain occupied by the unit cell and its volume, and symbol $\equiv$ denotes a definition.

Assumption 2. The effective material properties obtained from the micromechanical analysis of the unit cell are independent of the geometry, boundary conditions, and loading conditions of the macroscopic structure, which means that effective properties are assumed to be the intrinsic properties of the material when viewed macroscopically.

Note that these assumptions are not restrictive. The mathematical meaning of the first assumption is that the exact solutions of the field are integrable over the domain of the unit cell, which is true almost all the time. The second assumption implies that we will neglect the size effects of the material properties in the macroscopic analysis, which is an assumption often made in the conventional continuum mechanics. Of course, the micromechanical analysis of the unit cell is only needed and appropriate if $\eta = h/l \ll 1$, with h as the characteristic size of the unit cell and l as the macroscopic size of the macroscopic material.

This new approach to micromechanical modeling has been successfully applied to predict thermomechanical properties including elastic properties, coefficients of thermal expansion, and specific heats [Yu and Tang 2007a; 2007b]. In this work, we will use this approach to construct micromechanics models for effective thermal conductivity and the corresponding local fields such as temperature and heat flux within a unit cell.

2. Theoretical formulation

VAMUCH formulation uses three coordinates systems: two Cartesian coordinates $\mathbf{x} = (x_1, x_2, x_3)$ and $\mathbf{y} = (y_1, y_2, y_3)$, and an integer-valued coordinate $\mathbf{n} = (n_1, n_2, n_3)$ (see Figure 1). We use x_i as the global coordinates to describe the macroscopic structure and y_i parallel to x_i as the local coordinates to describe the unit cell (Here and throughout the paper, Latin indices assume 1, 2, and 3 and repeated indices are summed over their range except where explicitly indicated). We choose the origin of the local coordinates y_i to be the geometric center of unit cell. For example, if the unit cell is a cube with edge lengths d_i, then $y_i \in [-\frac{d_i}{2}, \frac{d_i}{2}]$. To uniquely locate a unit cell in the heterogeneous material we also introduce integer coordinates n_i. The integer coordinates are related to the global coordinates in such a way that $n_i = x_i/d_i$ (no summation over i). It is emphasized that although only a square array is sketched in Figure 1, the present theory has not such limitations.

As implied by Assumption 2, we can obtain the same effective properties from an imaginary, unbounded, and unloaded heterogeneous material with the same microstrucutre as the real, loaded, and bounded one. Hence we could derive the micromechanics model from an imaginary, unloaded, heterogeneous material which completely occupies the three-dimensional space $\mathcal{R}$ and composes infinitely many repeating unit cells. The solution to the steady-state conduction problem, which is sufficient for us to find the effective thermal conductivity, can be obtained by the stationary value problem of summation of
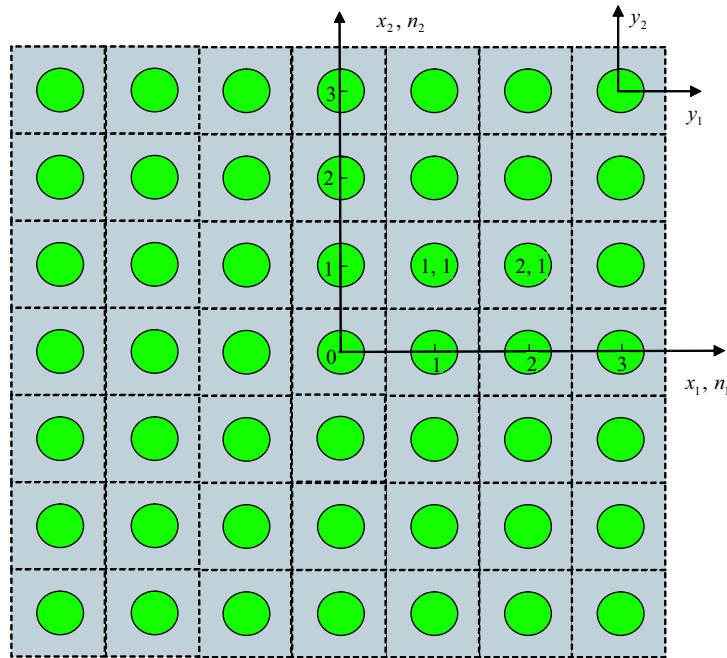
Figure 1. Coordinate systems for heterogenous materials (only a two-dimensional square array unit cell is drawn for clarity).

the "energy" integral over all the unit cells [Hashin 1968; Berdichevsky 1977], which is:

$$\Pi = \sum_{n=-\infty}^{\infty} \tfrac{1}{2} \int_{\Omega} K_{ij}\, \phi_{,i}\, \phi_{,j} \mathrm{d}\Omega, \tag{2}$$

where K_{ij} are components of the second-order thermal conductivity tensor, and

$$\phi_{,i}(\mathbf{n}; \mathbf{y}) = \frac{\partial \phi(\mathbf{n}; \mathbf{y})}{\partial y_i}, \tag{3}$$

with $()_{,i} \equiv \frac{\partial ()}{\partial y_i}$. Here ϕ is a function of the integer coordinates and the local coordinates for each unit cell. In view of the fact that the infinitely many unit cells form a continuous heterogeneous material, we need to enforce the continuity of the temperature field ϕ on the interface between adjacent unit cells, which is (n_1, n_2, n_3):

$$\phi(n_1, n_2, n_3; d_1/2, y_2, y_3) = \phi(n_1 + 1, n_2, n_3; -d_1/2, y_2, y_3),$$
$$\phi(n_1, n_2, n_3; y_1, d_2/2, y_3) = \phi(n_1, n_2 + 1, n_3; y_1, -d_2/2, y_3),$$
$$\phi(n_1, n_2, n_3; y_1, y_2, d_3/2) = \phi(n_1, n_2, n_3 + 1; y_1, y_2, -d_3/2). \tag{4}$$

The exact solution of the steady heat conduction problem will minimize the summation of the "energy" integral in Equation (2) under the constraints in Equations (1), and (4). To avoid the difficulty associated with discrete integer arguments, we can reformulate the problem, including Equations (2), (3), and (4),

in terms of continuous functions using the idea of the quasicontinuum [Kunin 1982]. The corresponding formulas are:

$$\Pi = \tfrac{1}{2} \int_{\mathcal{R}} \langle K_{ij}\, \phi_{,i}\, \phi_{,j}\rangle \mathrm{d}\mathcal{R}, \qquad \phi_{,i}(\mathbf{x}; \mathbf{y}) = \frac{\partial \phi(\mathbf{x}; \mathbf{y})}{\partial y_i}, \tag{5}$$

and

$$\phi(x_1, x_2, x_3; d_1/2, y_2, y_3) = \phi(x_1 + d_1, x_2, x_3; -d_1/2, y_2, y_3),$$
$$\phi(x_1, x_2, x_3; y_1, d_2/2, y_3) = \phi(x_1, x_2 + d_2, x_3; y_1, -d_2/2, y_3),$$
$$\phi(x_1, x_2, x_3; y_1, y_2, d_3/2) = \phi(x_1, x_2, x_3 + d_3; y_1, y_2, -d_3/2). \tag{6}$$

Using the technique of Lagrange multipliers, we can pose the thermal conduction problem as a stationary value problem for the following functional:

$$J = \int_{\mathcal{R}} \left\{ \langle \tfrac{1}{2} K_{ij}\, \phi_{,i}\, \phi_{,j}\rangle + \lambda(\langle \phi \rangle - \psi) \right.$$
$$+ \int_{S_1} \gamma_1 \left[\phi(x_1, x_2, x_3; d_1/2, y_2, y_3) - \phi(x_1 + d_1, x_2, x_3; -d_1/2, y_2, y_3)\right] \mathrm{d}S_1$$
$$+ \int_{S_2} \gamma_2 \left[\phi(x_1, x_2, x_3; y_1, d_2/2, y_3) - \phi(x_1, x_2 + d_2, x_3; y_1, -d_2/2, y_3)\right] \mathrm{d}S_2$$
$$\left. + \int_{S_3} \gamma_3 \left[\phi(x_1, x_2, x_3; y_1, y_2, d_3/2) - \phi(x_1, x_2, x_3 + d_3; y_1, y_2, -d_3/2)\right] \mathrm{d}S_3 \right\} \mathrm{d}\mathcal{R}, \tag{7}$$

where λ and γ_i are Lagrange multipliers introduced to enforce the constraints in Equations (1) and (6), respectively, and S_i are the surfaces with $n_i = 1$. The main objective of micromechanics is to find the real temperature field ϕ in terms of ψ, which is a very difficult problem because we have to solve this stationary problem for each point in the global system x_i as in Equation (7). It will be desirable if we can formulate the variational statement posed over a single unit cell only. In view of Equation (1), it is natural to express the exact solution ϕ as a sum of the volume average ψ plus the difference, such that

$$\phi(\mathbf{x}; \mathbf{y}) = \psi(\mathbf{x}) + w(\mathbf{x}; \mathbf{y}), \tag{8}$$

where $\langle w \rangle = 0$ according to Equation (1). The very reason that the heterogenous material can be homogenized leads us to believe that w should be asymptotically smaller than ψ, that is, $w \sim \eta\, \psi$. Substituting Equation (8) into Equation (7) and making use of Equation (5), we can obtain the leading terms of the functional according to the variational asymptotic method [Berdichevsky 1977] as:

$$J_1 = \int_{\mathcal{R}} \left\{ \langle \tfrac{1}{2} K_{ij}\, w_{,i}\, w_{,j}\rangle + \lambda\langle w \rangle + \int_{S_1} \gamma_1 \left[w(\mathbf{x}; d_1/2, y_2, y_3) - w(\mathbf{x}; -d_1/2, y_2, y_3) - \psi_{;1} d_1\right] \mathrm{d}S_1 \right.$$
$$+ \int_{S_2} \gamma_2 \left[w(\mathbf{x}; y_1, d_2/2, y_3) - w(\mathbf{x}; y_1, -d_2/2, y_3) - \psi_{;2} d_2\right] \mathrm{d}S_2$$
$$\left. + \int_{S_3} \gamma_3 \left[w(\mathbf{x}; y_1, y_2, d_3/2) - w(\mathbf{x}; y_1, y_2, -d_3/2) - \psi_{;3} d_3\right] \mathrm{d}S_3 \right\} \mathrm{d}\mathcal{R}, \tag{9}$$

where $()_{;i} \equiv \frac{\partial ()}{\partial x_i}$. Although it is possible to carry out the variation of J_1 and find the Euler–Lagrange equations and associated boundary conditions for w, which results in inhomogeneous boundary conditions, it is more convenient to use a change of variables to reformulate the same problem so that the boundary conditions are homogeneous. Considering the last three terms in Equation (9), we use the following change of variables to express w as:

$$w(\mathbf{x}; \mathbf{y}) = y_i \psi_{;i} + \zeta(\mathbf{x}; \mathbf{y}), \tag{10}$$

with ζ normally termed as fluctuation functions. We are free to choose the origin of the local coordinate system to be the center of the unit cell, which implies the following constraints on ζ:

$$\langle \zeta \rangle = 0. \tag{11}$$

Substituting Equation (10) into Equation (9), we obtain a stationary value problem defined on the unit cell for ζ, such that

$$J_\Omega = \tfrac{1}{2} \langle K_{ij} \left(\psi_{;i} + \zeta_{,i} \right) \left(\psi_{;j} + \zeta_{,j} \right) \rangle + \lambda \langle \zeta \rangle + \int_{S_1} \gamma_1 (\zeta^{+1} - \zeta^{-1}) dS_1 + \int_{S_2} \gamma_2 (\zeta^{+2} - \zeta^{-2}) dS_2$$
$$+ \int_{S_3} \gamma_3 (\zeta^{+3} - \zeta^{-3}) dS_3, \quad (12)$$

with $\zeta^{+i} = \zeta|_{y_i = d_i/2}$, and $\zeta^{-i} = \zeta|_{y_i = -d_i/2}$, for $i = 1, 2, 3$ where $\psi_{;i}$ will be shown later to be the components of the global temperature gradient vector for the effective material with homogenized material properties. The functional J_Ω in Equation (12) forms the backbone of the present theory. This stationary problem can be solved analytically for very simple cases such as binary composites, however, for general cases we need to use numerical techniques such as the finite element method to seek numerical solutions.

3. An illustrative example

To illustrate the solution procedure of the stationary problem of the functional in Equation (12), we will consider a periodic binary composite made of anisotropic layers with material axes that are the same as the global coordinates x_i, so that the material is uniform in the $x_1 - x_2$ plane and periodic along the x_3 direction. A typical unit cell can be identified as shown in Figure 2, with the dimension along y_3 given by h and dimensions along y_1 and y_2 arbitrary. Let ϕ_1 and ϕ_2 denote the volume fraction of the first and second layer, respectively, and we have $\phi_1 + \phi_2 = 1$.

Because of the uniformity of the structure in the $x_1 - x_2$ plane, we know that the solution to ζ will be independent of y_1 and y_2, and is a function of y_3 only. Taking advantage of the this fact, we can specialize the functional in Equation (12) for this particular case in a matrix form as:

$$J_\Omega^* = \int_{S_3} \left\{ \int_{-\frac{h}{2}}^{(\phi_1 - \frac{1}{2})h} \left[\frac{1}{2} \Psi^{(1)T} K^{(1)} \Psi^{(1)} + \lambda \zeta^{(1)} \right] dy_3 + \int_{(\phi_1 - \frac{1}{2})h}^{\frac{h}{2}} \left[\frac{1}{2} \Psi^{(2)T} K^{(2)} \Psi^{(2)} + \lambda \zeta^{(2)} \right] dy_3 \right.$$
$$\left. + \gamma_3 \left[\zeta^{(2)}(\frac{h}{2}) - \zeta^{(1)}(-\frac{h}{2}) \right] \right\} dS, \quad (13)$$
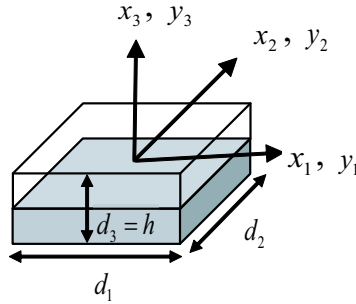
Figure 2. Sketch of a binary composite.

with $\Psi^{(\alpha)} = \lfloor \psi_{;1} \ \psi_{;2} \ \psi_{;3} + \zeta_{,3}^{(\alpha)} \rfloor^T$ for $\alpha = 1, 2$, and $\zeta^{(\alpha)}$ as the fluctuation functions of the temperature for each layer. The thermal conductivity matrix $K^{(\alpha)}$ is a fully populated symmetric matrix for a general anisotropic material, such that

$$K^{(\alpha)} = \begin{bmatrix} K_{11}^{(\alpha)} & K_{12}^{(\alpha)} & K_{13}^{(\alpha)} \\ K_{12}^{(\alpha)} & K_{22}^{(\alpha)} & K_{23}^{(\alpha)} \\ K_{13}^{(\alpha)} & K_{23}^{(\alpha)} & K_{33}^{(\alpha)} \end{bmatrix}.$$

The corresponding differential statement of the variational statement in Equation (13) can be obtained following normal procedures of the calculus of variations, as follows:

$$K_{33}^{(\alpha)} \zeta_{,33}^{(\alpha)} = \lambda, \tag{14}$$

$$\int_{-\frac{h}{2}}^{(\phi_1 - \frac{1}{2})h} \zeta^{(1)} \, dy_3 + \int_{(\frac{1}{2} - \phi_2)h}^{\frac{h}{2}} \zeta^{(2)} \, dy_3 = 0,$$

$$\zeta^{(1)}(-\frac{h}{2}) = \zeta^{(2)}(\frac{h}{2}),$$

$$\zeta^{(1)}(\phi_1 h - h/2) = \zeta^{(2)}(\phi_1 h - h/2),$$

$$K_{13}^{(1)} \psi_{;1} + K_{23}^{(1)} \psi_{;2} + K_{33}^{(1)} \left[\psi_{;3} + \zeta_{,3}^{(1)} \right] |_{y_3 = -\frac{h}{2}} = K_{13}^{(2)} \psi_{;1} + K_{23}^{(2)} \psi_{;2} + K_{33}^{(2)} \left[\psi_{;3} + \zeta_{,3}^{(2)} \right] |_{y_3 = \frac{h}{2}},$$

$$K_{13}^{(1)} \psi_{;1} + K_{23}^{(1)} \psi_{;2} + K_{33}^{(1)} \left[\psi_{;3} + \zeta_{,3}^{(1)} \right] |_{y_3 = (\phi_1 - \frac{1}{2})h} = K_{13}^{(2)} \psi_{;1} + K_{23}^{(2)} \psi_{;2} + K_{33}^{(2)} \left[\psi_{;3} + \zeta_{,3}^{(2)} \right] |_{y_3 = (\phi_1 - \frac{1}{2})h}.$$

Clearly this differential statement contains two second-order ordinary differential equations in Equation (14) and five constraints for solving $\zeta^{(\alpha)}$ and λ. The solution to λ is found to be zero and $\zeta^{(\alpha)}$ are linear functions of y_3. Having solved the fluctuation functions, $\zeta^{(\alpha)}$, the density of the "energy" integral of this effective material can be trivially obtained as:

$$\Pi_\Omega = \frac{1}{2} \begin{Bmatrix} \psi_{;1} \\ \psi_{;2} \\ \psi_{;3} \end{Bmatrix}^T \begin{bmatrix} K_{11}^* & K_{12}^* & K_{13}^* \\ K_{12}^* & K_{22}^* & K_{23}^* \\ K_{13}^* & K_{23}^* & K_{33}^* \end{bmatrix} \begin{Bmatrix} \psi_{;1} \\ \psi_{;2} \\ \psi_{;3} \end{Bmatrix},$$

with the effective thermal conductivity coefficients K_{ij}^* as

$$K_{11}^* = \langle K_{11} \rangle - \frac{(K_{13}^{(1)} - K_{13}^{(2)})^2 \phi_1 \phi_2}{K_{33}^{(2)} \phi_1 + K_{33}^{(1)} \phi_2},$$

$$K_{22}^* = \langle K_{22} \rangle - \frac{(K_{23}^{(1)} - K_{23}^{(2)})^2 \phi_1 \phi_2}{K_{33}^{(2)} \phi_1 + K_{33}^{(1)} \phi_2},$$

$$K_{33}^* = \frac{K_{33}^{(1)} K_{33}^{(2)}}{\phi_2 K_{33}^{(1)} + \phi_1 K_{33}^{(2)}},$$

$$K_{12}^* = \langle K_{12} \rangle - \frac{(K_{13}^{(1)} - K_{13}^{(2)})(K_{23}^{(1)} - K_{23}^{(2)}) \phi_1 \phi_2}{\phi_2 K_{33}^{(1)} + \phi_1 K_{33}^{(2)}},$$

$$K_{13}^* = \frac{K_{13}^{(1)} K_{33}^{(2)} \phi_1 + K_{13}^{(2)} K_{33}^{(1)} \phi_2}{\phi_2 K_{33}^{(1)} + \phi_1 K_{33}^{(2)}},$$

$$K_{23}^* = \frac{K_{23}^{(1)} K_{33}^{(2)} \phi_1 + K_{23}^{(2)} K_{33}^{(1)} \phi_2}{\phi_2 K_{33}^{(1)} + \phi_1 K_{33}^{(2)}}.$$

It is interesting to note that K_{33}^* is the same as the rule of mixtures based on Reuss' hypothesis for this special case. If $K_{13}^{(1)} = K_{13}^{(2)}$ and $K_{23}^{(1)} = K_{23}^{(2)}$, then K_{11}^*, K_{22}^*, and K_{12}^* are the same as the rule of mixtures based on Voigt's hypothesis, and K_{13}^* and K_{23}^* are the same as the constituent properties.

4. Finite element implementation

For more general cases, we need to rely on numerical solutions. Here, we will implement the variational statement in Equation (12) using the well-established finite element method. It is possible to formulate the finite element method solution based on Equation (12), however, it is not the most convenient and efficient way because Lagrange multipliers will increase the number of unknowns. To this end, we can reformulate the variational statement in Equation (12) as the stationary value of the following functional

$$\Pi_\Omega = \frac{1}{2\Omega} \int_\Omega K_{ij} \left(\psi_{;i} + \zeta_{,i} \right) \left(\psi_{;j} + \zeta_{,j} \right) d\Omega, \tag{15}$$

under the following three constraints

$$\zeta^{+i} = \zeta^{-i}, \qquad \text{for } i = 1, 2, 3. \tag{16}$$

The constraint in Equation (11) does not affect the minimum value of Π_Ω but helps uniquely determine ζ. In practice, we can constrain the fluctuation function at an arbitrary node to be zero and later use this constraint to recover the unique fluctuation function. It is fine to use the penalty function method to introduce the constraints in Equation (16). However, this method introduces additional approximation and the robustness of the solution depends on the choice of large penalty numbers. Here, we choose to make the nodes on the positive boundary surface, $y_i = d_i/2$, slave to the nodes on the opposite negative

boundary surface, $y_i = -d_i/2$. By assembling all the independent active degrees of freedom, we can implicitly and exactly incorporate the constraints in Equation (16). In this way, we also reduce the total number of unknowns in the linear system which will be formulated as follows.

Introduce the following matrix notations

$$\Phi = \lfloor \psi_{;1} \ \psi_{;2} \ \psi_{;3} \rfloor^T, \tag{17}$$

$$\Phi_1 = \left\{ \begin{matrix} \frac{\partial \zeta}{\partial y_1} \\ \frac{\partial \zeta}{\partial y_2} \\ \frac{\partial \zeta}{\partial y_3} \end{matrix} \right\} = \left\{ \begin{matrix} \frac{\partial}{\partial y_1} \\ \frac{\partial}{\partial y_2} \\ \frac{\partial}{\partial y_3} \end{matrix} \right\} \zeta \equiv \Gamma_h \zeta, \tag{18}$$

where Γ_h is an operator matrix. If we discretize ζ using the finite elements as

$$\zeta(x_i; y_i) = G(y_i)\xi(x_i), \tag{19}$$

where G representing the shape functions and ξ a column matrix of the nodal values of the fluctuation function. Substituting Equations (17), (18), and (19) into Equation (15), we obtain a discretized version of the functional,

$$\Pi_\Omega = \frac{1}{2\Omega}(\xi^T F \xi + 2\xi^T K_{h\Phi} \Phi + \Phi^T K_{\Phi\Phi} \Phi), \tag{20}$$

where

$$F = \int_\Omega (\Gamma_h G)^T K (\Gamma_h G) \mathrm{d}\Omega, \qquad K_{h\Phi} = \int_\Omega (\Gamma_h G)^T K \mathrm{d}\Omega, \qquad K_{\Phi\Phi} = \int_\Omega K \mathrm{d}\Omega,$$

with K as the 3×3 matrix of K_{ij}. Minimizing Π_Ω in Equation (20), we obtain the following linear system

$$F\xi = -K_{h\Phi} \Phi. \tag{21}$$

It is clear from Equation (21) that the fluctuation function, ξ, is linearly proportional to Φ, which means the solution can be written symbolically as

$$\xi = \xi_0 \Phi \tag{22}$$

Substituting Equation (22) into (20), we can calculate the density of the "energy" integral of the unit cell as

$$\Pi_\Omega = \frac{1}{2\Omega} \Phi^T \left(\xi_0^T K_{h\Phi} + K_{\Phi\Phi} \right) \Phi \equiv \frac{1}{2} \Phi^T K^* \Phi. \tag{23}$$

It can be seen that K^* in Equation (23) is the effective thermal conductivity matrix, and Φ is the global temperature gradient.

If the local fields within the unit cell are of interest, we can recover those fields, including local temperature and heat flux, in terms of the macroscopic behavior, including the global temperature ψ and the corresponding gradient $\psi_{;i}$, and the fluctuation function ζ. First, we need to uniquely determine the fluctuation function. Otherwise, we could not uniquely determine the local temperature field. Because we have fixed an arbitrary node and made nodes on the positive boundary surfaces, $y_i = +d_i/2$, slave to the corresponding negative boundary surfaces, $y_i = -d_i/2$, in forming the linear system in Equation (21), we need to construct a new array $\tilde{\xi}_0$ from ξ_0 by assigning the values for slave nodes according

to the corresponding active nodes, and assigning zero to the fixed node. Clearly, $\tilde{\bar{\xi}}_0$ corresponds to the stationary value of Π_Ω in Equation (15) under constraints in (16). However, $\tilde{\bar{\xi}}_0$ may not satisfy (11). The real solution, denoted as $\bar{\xi}_0$, can be found trivially by adding a constant to each node so that Equation (11) is satisfied.

After having determined the fluctuation functions uniquely, we can recover the local temperature using Equations (8) and (10) as $\phi = \psi + y_i \psi_{;i} + \bar{G} \bar{\xi}_0 \Phi$, where $\bar{G}$ is different from G due to the recovery of slave nodes and the constrained node. The local temperature gradient field can be recovered using Equations (3) and (18):

$$\lfloor \phi_{,1} \ \phi_{,2} \ \phi_{,3} \rfloor^T = \Phi + \Gamma_h \bar{G} \bar{\xi}_0 \Phi.$$

Finally, the local heat flux field can be recovered straightforwardly using the three-dimensional Fourier law for the constituent materials, $q_i = -K_{ij}\phi_{,j}$. We have implemented this formulation in the computer program VAMUCH. In the next section, we will use a few numerical examples to demonstrate the application and accuracy of this theory and code.

5. Numerical examples

VAMUCH provides a unified analysis for general one-, two-, or three-dimensional unit cells. First, the same code VAMUCH can be used to homogenize binary composites (modeled using one-dimensional unit cells), fiber reinforced composites (modeled using two-dimensional unit cells), and particle reinforced composites (modeled using three-dimensional unit cells). Second, VAMUCH can reproduce the results for lower-dimensional unit cells using higher-dimensional unit cells. That is, VAMUCH predicts the same results for binary composites using one-, two-, or three-dimensional unit cells, and for fiber reinforced composites using two- or three-dimensional unit cells.

In this section, several examples will be used to demonstrate the accuracy of VAMUCH for predicting the effective thermal conductivity and calculating the local heat flux field within a unit cell due to temperature gradients. To facilitate comparison with existing models in the literature, we only consider composites with isotropic constituents although the present method and code can handle general anisotropic constituents.

5.1. *Effective thermal conductivity of fiber reinforced composites.* The first example is a carbon fiber reinforced aluminum matrix composite. Both constituents are isotropic with thermal conductivity $K = 129$ W/(m · K) for the carbon fiber, and $K = 237$ W/(m · K) for aluminum matrix. The fiber is of circular shape and arranged in a square array. The prediction of VAMUCH for the effective thermal conductivity along the fiber direction exactly obeys the rule of mixtures, which has been generally accepted as the exact solution for the longitudinal thermal conductivity for fiber reinforced composites with isotropic constituents [Hashin 1968].

However, the effective thermal conductivity coefficients in the transverse directions (K_{22}^* and K_{33}^*) do not in general obey the rule of mixtures. To validate the present theory, we compare the VAMUCH prediction with other models in the literature [Springer and Tsai 1967; Behrens 1968; Donea 1972; Hashin 1983; Hatta and Taya 1986]. As shown in Figure 3, VAMUCH results are perfectly located between the variational bounds of [Donea 1972], while the Springer–Tsai model [Springer and Tsai 1967] and the lower bound of [Hashin 1983] underpredict the results. We have also found out that
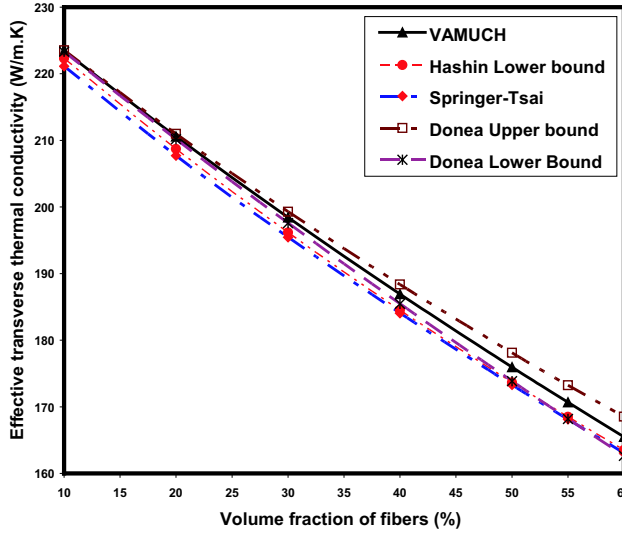
Figure 3. Effective transverse thermal conductivity of the carbon/Al composite.

VAMUCH results are the same as those obtained by Behrens [1968], Hatta and Taya [1986], and the upper bound of [Hashin 1983], and these results are not shown in the plot for clarity.

The second example is a boron fiber reinforced aluminum composite with isotropic constituents and thermal conductivity $K = 27.4$ W/(m $\cdot$ K) for the boron fiber, and $K = 237$ W/(m $\cdot$ K) for the aluminum matrix. The fiber is also circular and arranged in a square array. The effective thermal conductivities computed by different models are plotted in Figure 4. We found out that the results of the Hashin upper
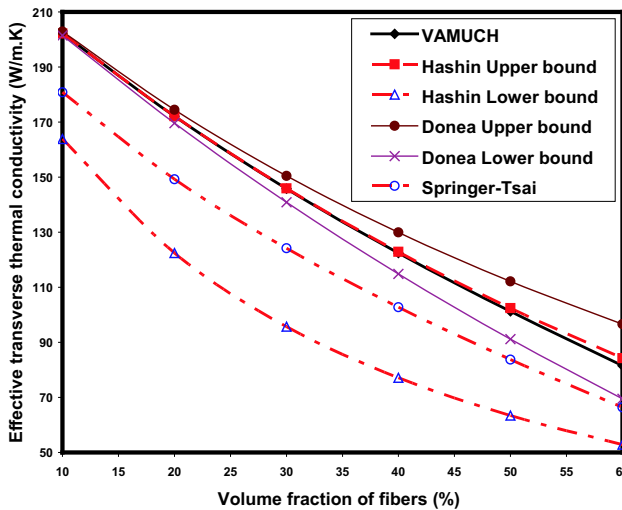
Figure 4. Effective transverse thermal conductivity of the boron/Al composite.

bound [Hashin 1983] are the same as those of [Behrens 1968] and [Hatta and Taya 1986]. Hence only the Hashin upper bound is plotted in the figure. It can be observed that the predictions of the Hashin upper bound are slightly higher than those of VAMUCH when the fiber volume fraction is higher than 40%. We also observe that the difference between the Hashin upper and lower bounds [Hashin 1983] is significant for this case which means they are not very useful for composites with constituents having relatively high contrast ratio in thermal conductivity properties. VAMUCH results are also nicely located in the much narrower bounds of [Donea 1972], while the prediction of Springer and Tsai [1967] is not accurate for this case because it is significantly lower than the lower bound of [Donea 1972].

In the two examples just described, the thermal conductivity of the matrix is higher than that of the fiber. Now, let us consider a glass/polypropylene composite with thermal conductivity $K = 1.05$ W/(m·K) for the glass fiber, and $K = 0.2$ W/(m · K) for the polypropylene matrix. We plot the change of effective transverse thermal conductivity of composites with respect to volume fraction of fibers in Figure 5. Again, we find out that VAMUCH results lie between the variational bounds of [Donea 1972]. And the results of the Hashin lower bound [Behrens 1968; Hashin 1983; Hatta and Taya 1986] are identical but slightly lower than VAMUCH results when the volume fraction of fibers is higher than 40%. Similarly, as in the previous case, we can observe that Donea [1972] provides much narrower bounds than Hashin [1983] for this case.

We also use ANSYS, a commercial finite element method package, to calculate the effective thermal conductivities of these three fiber reinforced composites. According to Islam and Pramila [1999], given the direction along which we would like to evaluate the thermal conductivity, we apply isothermal conditions to the edges perpendicular to the direction we want to evaluate the thermal conductivity and apply adiabatic conditions to the edges parallel to this direction. The effective thermal conductivity is obtained as the ratio between the average heat flux and average temperature gradient. We found out that VAMUCH results are almost the same as the ANSYS results for similar discretization schemes.
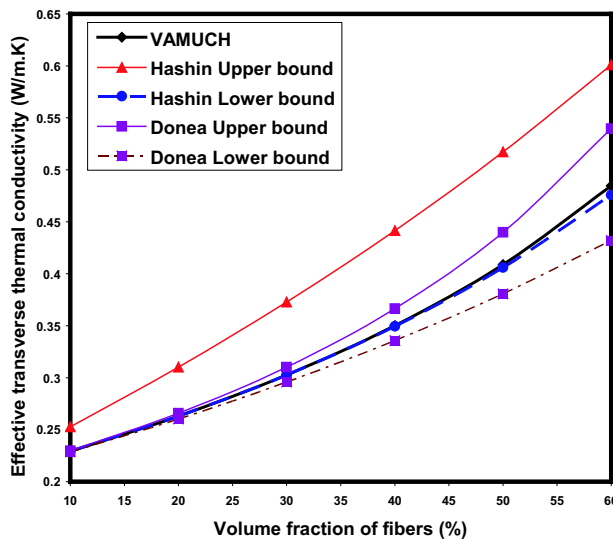
Figure 5. Effective transverse thermal conductivity of the glass/polypropylene composite.
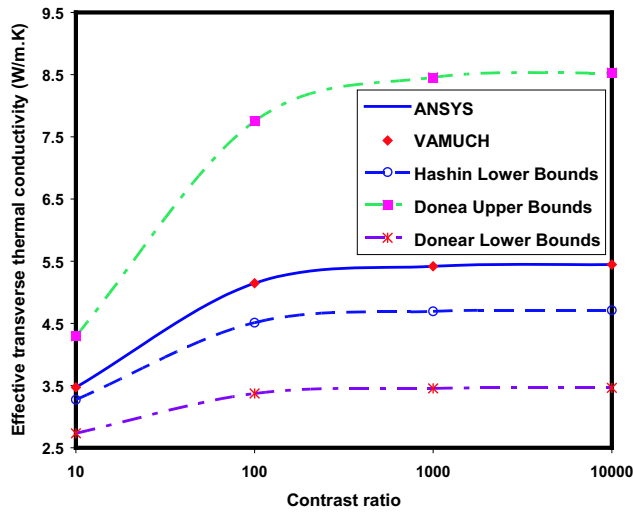
Figure 6. Effective transverse thermal conductivity with respect to varying contrast ratios.

To verify whether VAMUCH can be applied to composites with very high contrast ratio and high volume fraction, we choose a composite formed by circular fibers arranged in a square array. The volume fraction of fibers is 65%. We fix the thermal conductivity of the matrix at 1 W/(m · K), while the thermal conductivity of the fiber varies from 10 to 10^4. We plot the effective thermal conductivity computed using different approaches with different contrast ratios in Figure 6. It can be seen that VAMUCH results fall right on the curve of the ANSYS results and lie between the Donea variational bounds. The results of the Hashin lower bound [Hashin 1983] are identical to those obtained from Behrens [1968], Progelhof et al. [1976], and Hatta and Taya [1986]. It is obvious that these approaches underpredict the results. For these contrast ratios, the Hashin upper bounds are too large to be nicely plotted in the same figure.

5.2. *Effective thermal conductivity of particle reinforced composites.* Due to the special arrangements of the constituents of particle reinforced composites, three-dimensional unit cells are required to accurately model the microstructures. In this section, we will use VAMUCH to analyze two typical particle reinforced composites to validate the three-dimensional predictive capability of VAMUCH.

The first example is a SiC particle reinforced aluminum composite. The spherical SiC particles are embedded in a triply periodic cubic array. Both constituents are isotropic with thermal conductivities $K = 120$ W/(m · K) for the SiC particles, and $K = 237$ W/(m · K) for the aluminum matrix. The change in effective thermal conductivity of composites with respect to volume fraction of particles are plotted in Figure 7. VAMUCH results have an excellent agreement with the Hashin upper bound [Budiansky 1970; Cheng and Vachon 1970; Hashin 1983], although Budiansky [1970] and Cheng and Vachon [1970] slightly underpredict the results when the volume fraction of particles are higher than 20%. It was also found that the VAMUCH results are very close to those calculated by McPhedran and Mckenzie [1978]. All these predictions fall within the variational bounds of [Donea 1972]. It can be observed that the results
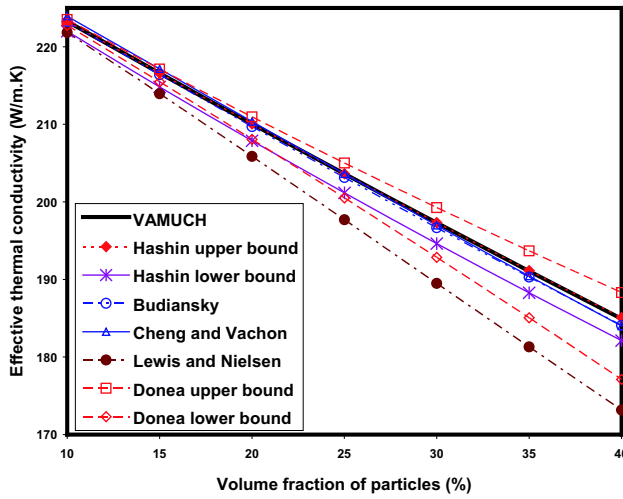
Figure 7. Effective thermal conductivity of the SiC/Al composite.

of Lewis and Nielsen [2003] significantly underpredict the effective thermal conductivity in comparison to other approaches.

Another example is an alumina (Al_2O_3) particle reinforced polyethylene composite. This composite has the same microstructure as the previous example. Both components are also isotropic with thermal conductivities $K = 31$ W/(m·K) for alumina particles, and $K = 0.545$ W/(m·K) for the polyethylene matrix. The contrast ratio of the thermal conductivity of the two components is as high as 56.88. The predictions of different approaches are shown in Figure 8. VAMUCH results agree with McPhedran and
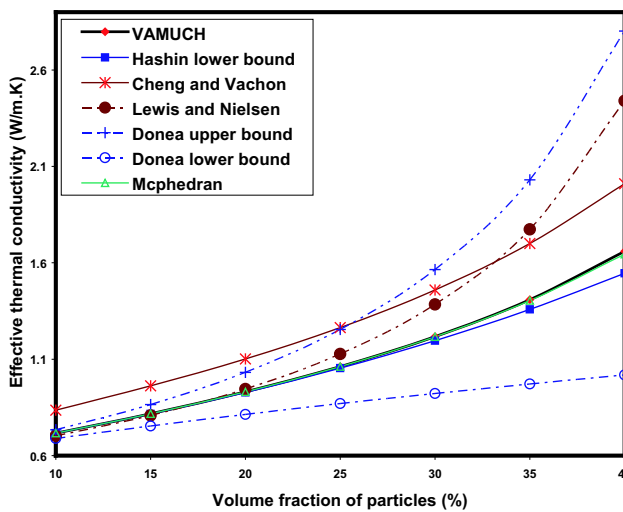
Figure 8. Effective thermal conductivity of the Al_2O_3/polyethylene composite.

Mckenzie [1978] at different volume fractions and with the lower bound of Hashin [1983] very well if the volume fraction of the particles is smaller than 25%. The prediction of Lewis and Nielsen [2003] is also very close to that of VAMUCH if the volume fraction of particles is very small. The difference between the variational bounds of [Donea 1972] becomes too large to be useful for high volume fraction of particles. The prediction of Cheng and Vachon [1970] for this case cannot be considered as accurate because it is not located between the lower and upper bounds of [Donea 1972]. We also need to point out that for this case, the results of the Hashin upper bound are too different from the lower bound and cannot be nicely plotted in the same figure.

We also analyzed these two examples of particle reinforced composites using ANSYS following the approach of Kumlutas and Tavman [2006]. Again, we found out VAMUCH results are identical to ANSYS results if similar meshes are used for both approaches.

It is noted that the Hashin bounds are known to be the best possible bounds for statistically isotropic or transversely isotropic composites, when the only available geometrical information is the phase volume fractions [Hashin and Shtrikman 1962]. However, such bounds can be improved if additional information, such as shape of inclusions and geometry of microstructure are added into the formulation [Hashin 1983]. It has been shown that the Hashin lower bound or upper bound is the exact solution for composite spheres assemblage (CSA) [Hashin 1968], which explains why one of the Hashin bounds agrees with VAMUCH very well if the inclusion volume fraction is not very large. Donea bounds [Donea 1972] are not rigorous variational bounds. Rather the material is considered as a composition of CSA within the largest possible circle/sphere and matrix. The Voigt rule of mixtures is used to obtain the Donea upper bound and the Ruess rule of mixtures is used to obtain the Donea lower bound. The effective properties of a CSA are calculated using the theory of Hashin [1968], which is also one of the Hashin bounds. Therefore, Donea bounds will fall outside at least one of the Hashin bounds, as is consistently shown in these examples. The gap between the Donea bounds could be smaller than that of the Hashin bounds because more information has been used in obtaining the Donea bounds.

5.3. *Recovery of local heat flux.* VAMUCH can accurately recover the local heat flux distribution within the unit cell due to temperature gradients. We will use the ANSYS results as benchmarks to verify the prediction of VAMUCH. First, we consider the glass/polypropylene fiber reinforced composite with a fiber volume fraction of 0.2. Due to the difference in thermal conductivities of the two components, the local heat flux distribution resulting from 100 K/m in the y_2 direction is not uniform within a unit cell. The distribution contours of q_2 and q_3 are plotted in Figure 9 (left and right, respectively). The sudden changes of local heat flux at the interface between the fibers and the matrix are well captured by VAMUCH. For a quantitative comparison, we also plot the local heat flux distribution q_2 along $y_2 = 0$ predicted by VAMUCH and ANSYS in Figure 10. It can be seen that there is excellent agreement between these two sets of results.

Second, we choose a special example that is a composite having an X-shape microstructure. The local heat flux distribution predicted by VAMUCH is shown in Figure 11. There are narrow necks at the corner contacts between the reinforcements that exhibit significant fluctuation in the local heat flux. The local heat flux distributions along the diagonal line predicted by VAMUCH and ANSYS are plotted in Figure 12. Excellent match between these two approaches is clear from this plot.
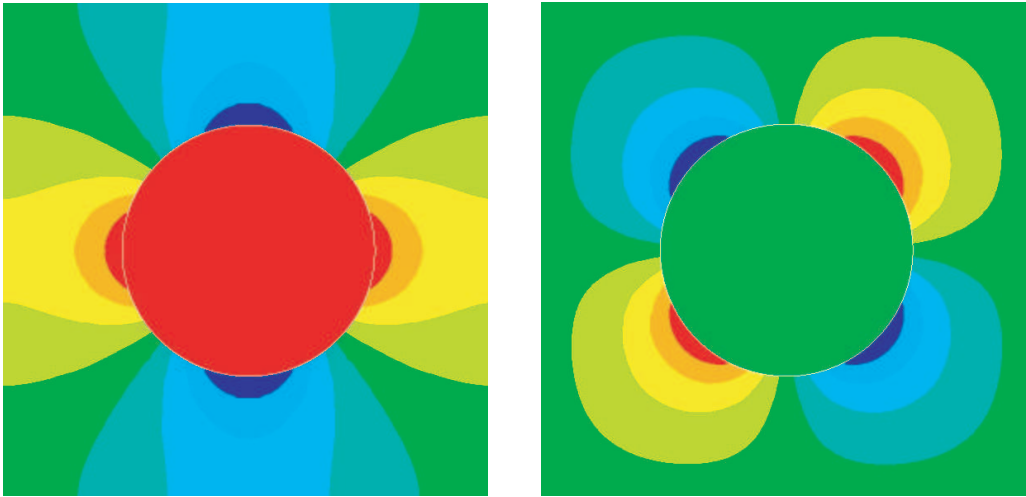
Figure 9. Left: Contour plot of heat flux q_2 in the glass/polypropylene composite. Right: Contour plot of heat flux q_3 in the glass/polypropylene composite.

6. Conclusion

The variational asymptotic method for unit cell homogenization (VAMUCH) has been extended to predict the effective thermal conductivity coefficients of composites. In comparison to existing models, the present theory has the following unique features:
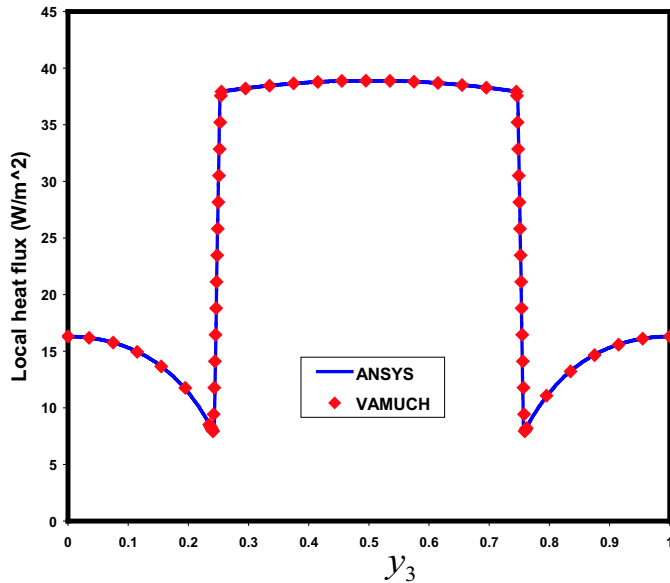

Figure 10. Heat flux q_2 distribution along $y_2 = 0$ in the glass/polypropylene composite.
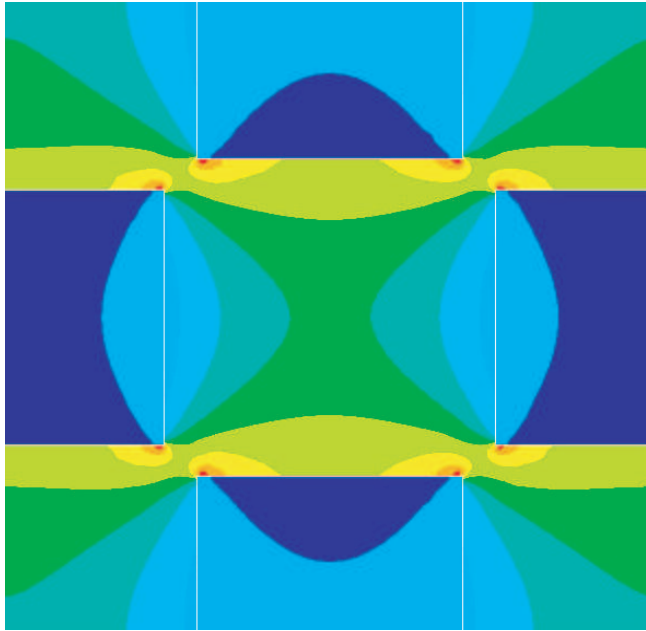
Figure 11. Contour plot of the heat flux of an X-shape composite.
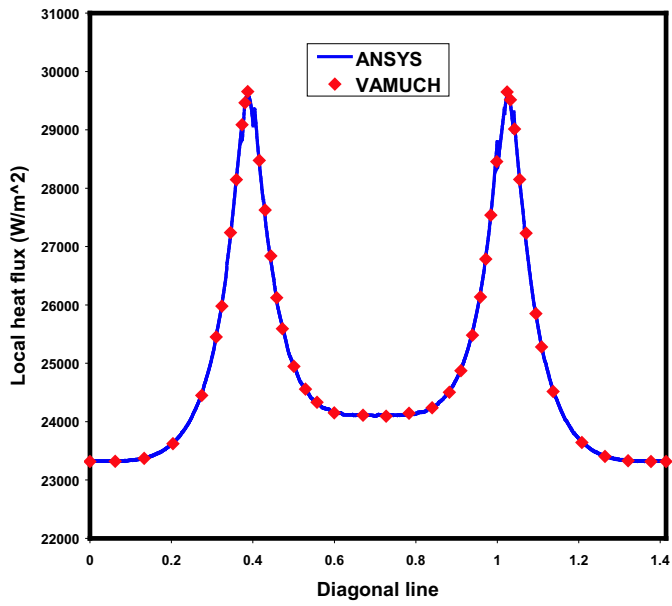
Figure 12. Heat flux of the X-shape composite along the diagonal line.

(i) It adopts the variational asymptotic method as its mathematical foundation. It invokes only essential assumptions inherent to the concept of micromechanics.

(ii) It has an inherent variational nature and its numerical implementation is shown to be straightforward.

(iii) It handles one-, two-, and three-dimensional unit cells uniformly. The dimensionality of the problem is determined by the periodicity of the unit cell.

The present theory is implemented in the computer program, VAMUCH. Numerous examples have clearly demonstrated its application and accuracy as a general-purpose micromechanical analysis tool. For the examples we have studied, although VAMUCH results are almost identical to ANSYS results, VAMUCH has the following advantages over ANSYS for micromechanical analysis:

(i) VAMUCH can obtain different material properties in different directions simultaneously, which is more efficient than those approaches requiring multiple runs under different temperature conditions.

(ii) VAMUCH can model general anisotropic heterogeneous materials with constituents having full anisotropy (with six material constants for thermal conductivity), while ANSYS and other finite element method packages can only handle constituents up to orthotropic material (with three material constants for thermal conductivity). The current finite element method approaches for predicting thermal conductivity [Islam and Pramila 1999; Kumlutas and Tavman 2006] are restricted to be at most macroscopically orthotropic, which is an unnecessary restriction.

(iii) VAMUCH calculates effective properties and local fields directly with the same accuracy as the fluctuation functions. No postprocessing calculations which introduces more approximations, such as averaging temperature gradient and heat flux, are needed.

As a byproduct of validating VAMUCH, we also provided a brief assessment of existing models for predicting effective thermal conductivity.

Due to the mathematical analogy of heat conduction, electrostatics, magnetostatics, and diffusion, the present theory and the companion code can also be used to predict effective dielectric, magnetic, and diffusion properties of heterogeneous materials.

References

[Behrens 1968] E. Behrens, "Thermal Conductivities of Composite Materials", *Journal of Composite Materials* **2** (1968), 2–17.

[Berdichevsky 1977] V. L. Berdichevsky, "On Averaging of Periodic Systems", *PMM* **41**:6 (1977), 993 – 1006.

[Budiansky 1970] B. Budiansky, "Thermal and Thermoelastic Properties of Isotropic Composites", *Journal of Composite Materials* **4** (1970), 286–295.

[Cheng and Vachon 1970] S. Cheng and R. Vachon, "A Technique for Predicting the Thermal Conductivity of Suspensions, Emulsions and Porous Materials", *International Journal of Heat and Mass Transfer* **13** (1970), 537–546.

[Donea 1972] J. Donea, "Thermal Conductivities Based on Variational Principles", *Journal of Composite Materials* **6** (1972), 262–266.

[Ganapathy et al. 2005] D. Ganapathy, K. Singh, P. Phelan, and R. Prasher, "An effective unit cell approach to compute the thermal conductivity of composites with cylindrical particles", *Journal of Heat Transfer* **127** (2005), 553–559.

[Hashin 1968] Z. Hashin, "Assessment of the self consistent scheme approximation: conductivity of particulate composites", *Journal of Composite Materials* **2** (1968), 284–300.

[Hashin 1983] Z. Hashin, "Analysis of Composite Materials-A Survey", *Applied Mechanics Review* **50** (1983), 481–505.

[Hashin and Shtrikman 1962] Z. Hashin and S. Shtrikman, "A variational approach to the theory of the effective magnetic permeability of multiphase materials", *Journal of Applied Physics* **33** (1962), 3125–3131.

[Hatta and Taya 1986] H. Hatta and M. Taya, "Thermal conductivity of coated filler composites", *Journal of Applied Physics* **59** (1986), 1851–1860.

[Islam and Pramila 1999] M. R. Islam and A. Pramila, "Thermal conductivity of fiber reinforced composites by the FEM", *Journal of Composite Materials* **33** (1999), 1699–1715.

[Kumlutas and Tavman 2006] D. Kumlutas and I. Tavman, "A Numerical and Experimental Study on Thermal Conductivity of Particle Filled Polymer Composites", *Journal of Thermoplastic Composite Materials* **19** (2006), 441–455.

[Kunin 1982] I. Kunin, *Theory of Elastic Media with Microstructure*, vol. 1 and 2, Springer Verlag, 1982.

[Lee et al. 2006] Y.-M. Lee, R.-B. Yang, and S.-S. Gau, "A generalized self consistent method for calculation of effective thermal conductivity of composites with interfacial contact conductance", *International Communications in Heat and Mass Transfer* **33** (2006), 142–150.

[Lewis and Nielsen 2003] T. Lewis and L. Nielsen, "Dynamic Mechanical Properties of Particulate-Filled Composites", *Journal of Applied Polymer Science* **14** (2003), 1449–1471.

[McPhedran and Mckenzie 1978] R. C. McPhedran and D. R. Mckenzie, "The conductivity of lattices of spheres I. the simple cubic lattice", *Proc. R. Soc. Lond. A* **359** (1978), 45–63.

[Progelhof et al. 1976] R. Progelhof, J. Throne, and R. Ruetsch, "Methods for predicting the thermal conductivity of composite systems: a review", *Polymer Engineering and Science* **16** (1976), 615–625.

[Ramani and Vaidyanathan 1995] K. Ramani and A. Vaidyanathan, "Finite element analysis of effective thermal conductivity of filled polymeric composites", *Journal of Composite Materials* **29** (1995), 1725–1740.

[Springer and Tsai 1967] G. Springer and S. Tsai, "Thermal conductivities of unidirectional materials", *Journal of Composite Materials* **1** (1967), 167–173.

[Xu and Yagi 2004] Y. Xu and K. Yagi, "Calculation of the thermal conductivity of randomly dispersed composites using a finite element modeling method", *Materials Transactions* **45** (2004), 2602–2605.

[Yu and Tang 2007a] W. Yu and T. Tang, "Variational asymptotic method for unit cell homogenization of periodically heterogeneous materials", *International Journal of Solids and Structures* **44**:11-12 (2007), 3738–3755.

[Yu and Tang 2007b] W. Yu and T. Tang, "A variational asymptotic micromechanics model for predicting thermoelastic properties of heterogeneous materials", *International Journal of Solids and Structures* **44**:22-23 (2007), 7510–7525.

TIAN TANG: tiantang@cc.usu.edu
Department of Mechanical and Aerospace Engineering, Utah State University, Logan, Utah 80322-4130, United States

WENBIN YU: wenbin.yu@usu.edu
Department of Mechanical and Aerospace Engineering, Utah State University, Logan, Utah 80322-4130, United States

FRACTURE MECHANICS ANALYSIS OF THREE-DIMENSIONAL ION CUT TECHNOLOGY

Xi-Qiao Feng, Mei Xu, Xuyue Wang and Bin Gu

The recently established ion cut technology enables accurate fabrication of silicon-on-insulator (SOI) wafers and has found some other significant applications. We study fracture mechanics of the technology when directly cutting a wafer into a desired surface morphology. First, we describe integral transform-based methods for calculating the stress intensity factors of subsurface cracks embedded in a semiinfinite solid. Because the crack and the free surface interact, the crack tip fields are generally of I-II mixed mode. We derive solutions for plane-strain or axisymmetrical configurations. We then analyze the suggested three-dimensional ion cut method using the fracture criterion for kinking propagation of a mixed-mode crack. To illustrate the approach, we consider circular hole and straight groove surface patterns.

1. Introduction

Silicon-on-insulator (SOI) wafers have been used extensively as the starting materials for ultralarge-scale integration (ULSI) device structures. A typical SOI system consists of a thin layer of single-crystal silicon supported by an underlying insulator (for example, SiO_2 and sapphire). SOI wafer structures have important advantages over bulk or epitaxial starting wafers for a wide range of ULSI applications [Colinge 1991; Haisma and Spierings 2002]. SOI wafers potentially offer fast circuit performance and packing density, immunity from latch-up, low power consumption, high resistance to ionizing radiation, and simplified processing compared to bulk or epitaxial silicon. Hence, they appear ideal for making leading edge integrated circuits with high speed and transistor count but also low voltage and power operation, leading to better performance in battery operated systems, such as portable logic or micro-processor ICs. Two conventional and commercially-available methods for making SOI wavers are the separation-by-implanted oxygen (SIMOX) method and the bonded silicon-on-insulator (BSOI) method [Colinge 1991]. However, neither is suited to industrial-scale production.

In 1995, Bruel [1995; 1996], Aspar et al. [1996], and Aspar et al. [1999] at LETI developed a novel technique, Smart-Cut™, a registered trademark of SOITEC, for fabricating high-quality SOI systems. This process skillfully combines hydrogen implantation and wafer bonding, and involves four main steps: (1) Through hydrogen ion implantation, a wafer A capped with a dielectric layer (for example, SiO_2) is imparted a thin layer of sufficiently dense hydrogen ions. (2) The wafer A is then bonded with a handle wafer B. (3) The bonded wafer is then split and annealed through two stages of heating, first at medium-temperature (400–600° C), and then at high-temperature (about 1100° C). In the first heating

stage, numerous microcracks appear at the depth of the maximum hydrogen ion concentration. The wafer A then splits into two parts, yielding an SOI structure and the remainder of wafer *A*. (4) The SOI layer is polished using a chemical-mechanical method to produce a high-quality surface.

The basic principle behind the Smart-Cut technology applies for fabricating single-crystal silicon or semiconductor films transferred onto different types of substrates (for example, glass and metals) [Bruel 1995; Bruel 1996; Aspar et al. 1996; Aspar et al. 1999; Tong and Bower 1998]. This technique has several significant advantages over traditional SOI synthesis methods such as SIMOX and BSOI. First, the Smart-Cut process helps ensure the wafers are accurate in thickness to less than 4 nm, compared to (20–30 nm) for conventional methods. Second, the SOI systems have high crystalline quality from using medium implantation doses of the smallest ion (H^+) and the final fine polishing. Third, ULSI devices based on the Smart-Cut wafers exhibit electrical characteristics comparable to or better than those made on bulk silicon wafers. Fourth, the Smart-Cut process can be performed using the standard equipment of microelectronics facilities, an important consideration for large-scale industrial production.

Since it was first published by Bruel [1995], the Smart-Cut technology has attracted considerable attention and found various applications. Using the technique, Tong and Bower [1998] transformed Si, Ge, and SiC films on substrates of a high melting temperature glass. Aspar et al. [1999] and Jalaguier et al. [1998] obtained some new structures with thin films of Si, GaAs or InP on silicon substrates by combining the Smart-Cut process with metal bonding. Di Cioccio et al. [1997] used the Smart-Cut technology to make *silicon carbide-on-insulator* structures. By implanting erbium into the top layer of a Smart-Cut SOI wafer, Gad et al. [2003] fabricated single-mode SOI waveguides with good optical quality. Recently, Feng and Huang [2004] studied the fundamental physics and mechanics of the Smart-Cut technology.

The previous Smart-Cut process synthesizes smooth SOI wafers that are highly uniform in thickness. Some wafer patterns, such as grooves and holes, still need to be prepared using more complicated manufacturing procedures. In this paper, we suggest extending the Smart-Cut technique to produce three-dimensional patterns. Hydrogen ions are not implanted into the whole wafer, but instead directed to localized regions by a specialized metal mask. In the heating stages, microcracks will still form to remove the unwanted material, leaving the designed surface pattern.

In the present paper, we analyze theoretically the three-dimensional ion cut method using linear elastic fracture mechanics. In Section 2, we present integral transform methods for finding the stress intensity factors (SIFs) for subsurface cracks in a semiinfinite space. We discuss two typical classes of crack configurations, plane strain and axisymmetrical problems. In Section 3, we apply the above integral transform methods to generate the feasibility conditions for pattern cutting by hydrogen ion implantation.

2. Integral transform methods for subsurface cracks

Engineers are generally interested in near-surface or subsurface cracks because they appear in a variety of engineered structures [Spence and Sharp 1985; Hutchinson and Suo 1992]. Subsurface cracks may form for various reasons, for example, thermal or residual stresses due to welding or other processes, contact fatigue stresses, preexisting defects beneath subsurfaces, or relatively weak interfaces in layered or laminated structures. Srivastava and Singh [1969] analyzed the effect of a penny-shaped crack on the stress field in a semiinfinite solid. Other researchers have studied the fracture mechanisms of subsurface cracks under different loading conditions, for example, contact, wear, and indentation [Komvopoulos

1996; Ma and Hwang 1996; Goshima and Soda 1997; Dyskin et al. 2000; Zhang et al. 2002; 2005; Feng and Xu 2006]. Fleming and Suh [1977] studied how surface traction helped propagate a horizontal subsurface crack. Cao [2002] presented a finite element model to determine subsurface median cracking in a trilayer sandwich subjected to contact loading. Bunger and Detournay [2005] and Zhang et al. [2002; 2005] studied the asymptotic behaviors of penny-shaped hydraulic cracks. Dyskin et al. [2000] employed the beam and dipole asymptotic approaches to analyze the interaction of a crack with parallel free boundaries. Despite the extensive interest, however, the community has not produced efficient methods for deriving the SIFs of subsurface cracks due to the crack-free surface interaction [Ma et al. 2005]. Therefore, with the aim of extending the ion cut method to surface pattern formation, we present in this section a method for calculating the SIFs of subsurface cracks using singular integral equation methods based on integral transforms. For illustration, we consider several typical subsurface crack configurations, although the presented methods may work for other configurations as well.

2.1. *Axisymmetrical problems.* Consider a circular crack beneath and parallel to the free surface of a semiinfinite body and subjected to an internal pressure p, as shown in Figure 1. Denote the crack radius as c, and its distance from the free surface as h. Refer to a cylindrical coordinate system (r, θ, z). For axisymmetrical problems, the stress equilibrium equations read

$$\frac{\partial \sigma_{rr}}{\partial r} + \frac{\partial \sigma_{rz}}{\partial z} + \frac{\sigma_{rr} - \sigma_{\theta\theta}}{r} = 0, \qquad \frac{\partial \sigma_{rz}}{\partial r} + \frac{\partial \sigma_{zz}}{\partial z} + \frac{\sigma_{rz}}{r} = 0, \tag{2-1}$$

and the strain-displacement relations are

$$\varepsilon_{rr} = \frac{\partial u}{\partial r}, \qquad \varepsilon_{\theta\theta} = \frac{u}{r}, \qquad \varepsilon_{rz} = \frac{1}{2}\left(\frac{\partial u}{\partial z} + \frac{\partial w}{\partial r}\right), \qquad \varepsilon_{zz} = \frac{\partial w}{\partial z}, \tag{2-2}$$

where σ_{ij} denote the stresses, ε_{ij} denote the strains, $u = u_r$ and $w = u_z$ are the nonzero displacements. Since the constitutive relation of single crystalline silicon is of weak anisotropy, the material is assumed throughout the paper to be linearly elastic and isotropic, with Young's modulus E and Poisson's ratio ν. Using Equation (2–2) and Hooke's law, the equilibrium equations in Equation (2–1) can be reexpressed
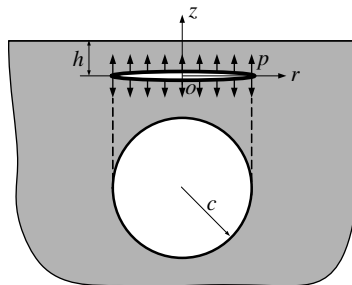

Figure 1. A circular subsurface crack beneath the free surface of a semiinfinite body.

in terms of the displacement components u and w as

$$(\kappa + 1)\left(\frac{\partial^2 u}{\partial r^2} + \frac{1}{r}\frac{\partial u}{\partial r} - \frac{u}{r^2} + \frac{\partial^2 w}{\partial r\partial z}\right) + (\kappa - 1)\left(\frac{\partial^2 u}{\partial z^2} - \frac{\partial^2 w}{\partial r\partial z}\right) = 0,$$

$$(\kappa + 1)\left(\frac{\partial^2 u}{\partial r\partial z} + \frac{1}{r}\frac{\partial u}{\partial z} + \frac{\partial^2 w}{\partial z^2}\right) - (\kappa - 1)\left(\frac{\partial^2 u}{\partial r\partial z} - \frac{\partial^2 w}{\partial r^2}\right) - \frac{\kappa - 1}{r}\left(\frac{\partial u}{\partial z} - \frac{\partial w}{\partial r}\right) = 0,$$

$$(2\text{–}3)$$

where $\kappa = 3 - 4\nu$.

To solve Equation (2–3), introduce in the radial variable the Hankel transforms $\tilde{u}$ and $\tilde{w}$ of the displacements u and w by

$$u(r, z) = \int_0^\infty \tilde{u}(z, \rho)\rho J_1(r\rho)d\rho, \qquad w(r, z) = \int_0^\infty \tilde{w}(z, \rho)\rho J_0(r\rho)d\rho, \qquad (2\text{–}4)$$

where J_0 and J_1 are Bessel functions.

Substituting Equation (2–4) into the partial differential equations in Equation (2–3) yields the ordinary differential equations

$$(\kappa + 1)\tilde{u}\rho^2 - 2\frac{\partial \tilde{w}}{\partial z}\rho + (\kappa - 1)\frac{\partial^2 \tilde{u}}{\partial z^2} = 0,$$

$$(\kappa - 1)\tilde{w}\rho^2 - 2\frac{\partial \tilde{u}}{\partial z}\rho - (\kappa + 1)\frac{\partial^2 \tilde{w}}{\partial z^2} = 0.$$

$$(2\text{–}5)$$

The general solution of Equation (2–5) can be written as

$$\begin{cases} \tilde{u}_1(z, \rho) = (A_1 + zA_2)e^{-\rho z} + (A_3 + zA_4)e^{\rho z}, & (z \geq 0), \\[2mm] \tilde{w}_1(z, \rho) = \left[A_1 + \left(\frac{\kappa}{\rho} + z\right)A_2\right]e^{-\rho z} + \left[-A_3 + \left(\frac{\kappa}{\rho} - z\right)A_4\right]e^{\rho z}, & (z \geq 0), \end{cases}$$

$$\begin{cases} \tilde{u}_2(z, \rho) = (A_5 + zA_6)e^{\rho z}, & (z \leq 0), \\[2mm] \tilde{w}_2(z, \rho) = \left[-A_5 + \left(\frac{\kappa}{\rho} - z\right)A_6\right]e^{\rho z}, & (z \leq 0), \end{cases}$$

$$(2\text{–}6)$$

where the subscripts 1 and 2 of $\tilde{u}$ and $\tilde{w}$ label the regions $z \geq 0$ and $z < 0$, respectively, and A_α ($\alpha = 1, \ldots, 6$) are integral constants to be determined from the specific boundary conditions and the continuity conditions. We could obtain expressions for the stress and strain fields by substituting the above solutions into Equation (2–2) and using Hooke's law. We omit these for short. However, the stresses on the crack

surfaces are

$$\sigma_{rz}(r, 0^-) = \mu \int_0^\infty \left[2\rho^2 J_1(r\rho)A_5 + \rho J_1(r\rho)(1-\kappa)A_6\right]d\rho,$$

$$\sigma_{zz}(r, 0^-) = -\int_0^\infty \rho J_0(r\rho)\left[2\mu\rho A_5 + (\lambda+2\mu)(1-\kappa)A_6\right]d\rho,$$

(2–7)

where λ and μ are the Lame's constants of elasticity.

Now, define two dislocation density functions $g_1(r)$ and $g_2(r)$ associated with the crack opening displacements by

$$g_1(r) = \frac{\partial}{\partial r}(w_1 - w_2)\big|_{z=0}, \qquad g_2(r) = \frac{1}{r}\frac{\partial}{\partial r}(ru_1 - ru_2)\big|_{z=0}.$$

(2–8)

We noted that the displacement w has its maximum at the center of the crack, and u is continuous at the crack tip. Therefore, g_1 and g_2 must satisfy the following auxiliary conditions:

$$g_1(r)\big|_{r=0} = 0, \qquad \int_0^c rg_2(r)dr = 0.$$

(2–9)

For the crack configuration in Figure 1, the free surface of the semiinfinite body is traction-free and the crack is subjected to an internal pressure p. Thus, the boundary conditions are

$$\sigma_{rz}(r, h) = 0, \qquad\qquad \sigma_{zz}(r, h) = 0, \quad (0 < r < \infty)$$

$$\sigma_{rz}(r, 0^+) = \sigma_{rz}(r, 0^-) = 0, \qquad \sigma_{zz}(r, 0^+) = \sigma_{zz}(r, 0^-) = -p, \quad (r < c).$$

(2–10)

In addition, the continuity conditions of stresses and displacements at $z = 0$ require that

$$\sigma_{rz}(r, 0^+) = \sigma_{rz}(r, 0^-),$$
$$\sigma_{zz}(r, 0^+) = \sigma_{zz}(r, 0^-),$$
$$u(r, 0^+) = u(r, 0^-),$$
$$w(r, 0^+) = w(r, 0^-),$$

(2–11)

for $r \geq c$. Using Equations (2–6)–(2–11), the parameters A_5 and A_6 become

$$A_5 = \frac{\Delta_{11}X + \Delta_{12}Y}{\Delta}, \qquad A_6 = \frac{\Delta_{21}X + \Delta_{22}Y}{\Delta},$$

(2–12)

where

$$\Delta = 8\rho^3(\kappa - 1)(1 - \kappa^2)(\lambda + \mu)(\lambda + 2\mu)e^{2\rho h},$$

$$\Delta_{11} = 4\rho^2(\kappa - 1)(\lambda + 2\mu)\Big[(e^{2\rho h} - 1)(\kappa - 1)^2(\lambda + \mu) + 4\mu\rho h(1 - \kappa) + 8\mu\rho^2 h^2\Big],$$

$$\Delta_{12} = 4\rho^2(1 + \kappa)\Big[(e^{2\rho h} - 1)(\kappa - 1)^2(\lambda + \mu)(\lambda + 2\mu) - 4\lambda\mu\rho h(1 - \kappa) - 8\mu^2\rho h(1 - \kappa) - 8\mu^2\rho^2 h^2\Big],$$

$$\Delta_{21} = 8\rho^3(\kappa - 1)(\lambda + 2\mu)\Big[(e^{2\rho h} - 1)(\kappa - 1)(\lambda + \mu) - 4\mu\rho h\Big],$$

$$\Delta_{22} = 8\rho^3\mu(1 + \kappa)\Big[(e^{2\rho h} - 1)(\kappa - 1)(\lambda + \mu) + 4\mu\rho h\Big],$$

and

$$X = \int_0^\infty r g_1(r) J_1(\rho r) dr, \qquad Y = \int_0^\infty r g_2(r) J_0(\rho r) dr. \tag{2–13}$$

Substituting Equation (2–12) into (2–7) and using the following relation of Bessel functions

$$\int_0^\infty \rho J_0(\rho r) J_1(\rho s) d\rho = -\frac{1}{\pi}\left[\frac{1}{s - r} + \frac{1}{s + r} + \frac{2M(s, r) - 2s}{s^2 - r^2}\right], \tag{2–14}$$

we obtain the singular integral equations

$$\frac{\mu}{2\pi(1 - \nu)}\int_0^c \left[\frac{1}{s - r} + \frac{1}{s + r} + \frac{M_1(s, r) - 1}{s - r} + \frac{M_1(s, r) - 1}{s + r}\right]g_1(s)ds$$

$$+ \int_0^c D_{11}(s, r)g_1(s)ds + \int_0^c D_{12}(s, r)g_2(s)ds$$

$$= \sigma_{zz}(r, 0^-) = -p, \text{ for } 0 < r < c,$$

$$\frac{\mu}{2\pi(1 - \nu)}\int_0^c \left[\frac{1}{s - r} - \frac{1}{s + r} + \frac{M_2(s, r) - 1}{s - r} - \frac{M_2(s, r) - 1}{s + r}\right]g_2(s)ds$$

$$+ \int_0^c D_{21}(s, r)g_1(s)ds + \int_0^c D_{22}(s, r)g_2(s)ds$$

$$= \sigma_{rz}(r, 0^-) = 0, \text{ for } 0 < r < c, \tag{2–15}$$

where

$$M(s, r) = \begin{cases} \dfrac{r}{s}E(r/s), & \text{for } r < s, \\[2mm] \dfrac{r^2}{s^2}E(r/s) - \dfrac{r^2 - s^2}{s^2}K(r/s), & \text{for } r > s, \end{cases} \tag{2–16}$$

$$D_{11}(r,s) = -s \int_0^\infty \left(\frac{-2\mu\rho\Delta_{11} + (\lambda+2\mu)(\kappa-1)\Delta_{21}}{\Delta} + \frac{\mu}{2(1-\nu)} \right) \rho J_0(\rho r) J_1(\rho s) d\rho,$$

$$D_{12}(r,s) = -s \int_0^\infty \frac{-2\mu\rho\Delta_{12} + (\lambda+2\mu)(\kappa-1)\Delta_{22}}{\Delta} \rho J_0(\rho r) J_1(\rho s) d\rho,$$

$$D_{21}(r,s) = -\mu s \int_0^\infty \frac{2\rho\Delta_{11} + (1-\kappa)\Delta_{21}}{\Delta} \rho J_1(\rho r) J_1(\rho s) d\rho,$$ (2–17)

$$D_{22}(r,s) = s \int_0^\infty \left[\mu \frac{2\rho\Delta_{12} + (1-\kappa)\Delta_{22}}{\Delta} + \frac{\mu}{2(1-\nu)} \right] \rho J_1(\rho r) J_0(\rho s) d\rho,$$

with $K(x)$ and $E(x)$ being the elliptical integrals of the first and the second kind.

We next adopt dimensionless variables $t = (2s-c)/c$ and $x = (2r-c)/c$, and Equation (2–15) becomes

$$\frac{\mu}{2\pi(1-\nu)} \int_{-1}^1 \left[\frac{1}{t-x} + \frac{1}{t+x+2} + \frac{M_1(t,x)-1}{t-x} + \frac{M_1(t,x)-1}{t+x+2} \right] g_1(t) dt$$

$$+ \int_{-1}^1 D_{11}(t,x) g_1(t) \frac{c}{2} dt + \int_{-1}^1 D_{12}(t,x) g_2(t) \frac{c}{2} dt = -p, \quad \text{for } -1 < t < 1,$$

$$\frac{\mu}{2\pi(1-\nu)} \int_{-1}^1 \left[\frac{1}{t-x} - \frac{1}{t+x+2} + \frac{M_2(t,x)-1}{t-x} - \frac{M_2(t,x)-1}{t+x+2} \right] g_2(t) dt$$

$$+ \int_{-1}^1 D_{21}(t,x) g_1(t) \frac{c}{2} dt + \int_{-1}^1 D_{22}(t,x) g_2(t) \frac{c}{2} dt = 0, \quad \text{for } -1 < t < 1. \quad (2\text{–}18)$$

Let us assume

$$H_1(t) = g_1(t)\sqrt{1-t^2}, \qquad H_2(t) = g_2(t)\sqrt{1-t^2}. \tag{2–19}$$

To solve the singular integral equations in Equation (2–9), expand the functions $H_1(t)$ and $H_2(t)$ in series

$$H_1(t) = \sum_{n=0}^\infty A_n T_n(t), \qquad H_2(t) = \sum_{n=0}^\infty B_n T_n(t), \tag{2–20}$$

where $T_n(t)$ is the Chebyshev polynomial of the first kind. Then, after truncating the series after N terms, Equations (2–18) and (2–9) become

$$\frac{\mu}{2(1-v)} \sum_{\alpha=1}^{N} \left[\frac{1}{t_\alpha - x_m} + \frac{1}{t_\alpha + x_m + 2} + \frac{M_1(t_\alpha, x_m) - 1}{t_\alpha - x_m} \right.$$

$$\left. + \frac{M_1(t_\beta, x_m) - 1}{t_\beta + x_m + 2} + \frac{\pi c}{2} D_{11}(t_\beta, x_m) \right] \frac{H_1(t_l)}{N} + \sum_{\beta=1}^{N} \frac{\pi c}{2} D_{12}(t_\beta, x_j) H_2(t_\beta) = -p,$$

$$\frac{\mu}{2(1-v)} \sum_{\alpha=1}^{N} \left[\frac{1}{t_\alpha - x_j} - \frac{1}{t_\alpha + x_j + 2} + \frac{M_2(t_\alpha, x_j) - 1}{t_\alpha - x_j} \right.$$

$$\left. - \frac{M_2(t_\alpha, x_j) - 1}{t_\alpha + x_j + 2} + \frac{\pi c}{2} D_{22}(t_\alpha, x_j) \right] \frac{H_2(t_\alpha)}{N} + \sum_{\beta=1}^{N} \frac{\pi c}{2} D_{21}(t_\beta, x_m) \frac{H_1(t_\beta)}{N} = 0,$$

$$H_1(t_N) = 0,$$

$$\sum_{\beta=1}^{N} \frac{1 + t_\beta}{2} H_1(t_\beta) = 0, \tag{2–21}$$

where t_α and x_m are defined by

$$t_\alpha = \cos \frac{2\alpha - 1}{2N} \qquad (l = 1, \ldots, N),$$

$$x_m = \cos \frac{m\pi}{N} \qquad (m = 1, \ldots, N-1). \tag{2–22}$$

The system (2–21) comprises $2N$ linear algebraic equations in $2N$ unknowns $H_1(t_\alpha)$ and $H_2(t_\alpha)$. They can be solved numerically. By increasing N, the result tends to the exact solution; in our experience, some 50 terms yield a highly accurate solution. In this way, the stresses, strains, and displacements in the crack system can all be determined.

Finally, using the definitions of the mode-I and mode-II SIFs, we find

$$K_{\mathrm{I}} = \lim_{r \to c^+} \sqrt{2\pi(r-c)} \sigma_{zz}(r, 0) = -\frac{\mu c \sqrt{\pi}}{2\sqrt{2}(1-v)} H_1(1),$$

$$K_{\mathrm{II}} = \lim_{r \to c^+} \sqrt{2\pi(r-c)} \sigma_{rz}(r, 0) = -\frac{\mu c \sqrt{\pi}}{2\sqrt{2}(1-v)} H_2(1). \tag{2–23}$$

In Figure 2, we illustrate. For the circular subsurface crack subjected to an internal pressure p (Figure 1), we plot both the mode-I and mode-II SIFs K_{I} and K_{II} as a function of c/h, the ratio between the crack radius and its distance from the upper surface. The reference value $K_0 = 2p\sqrt{c/\pi}$ is the mode-I SIF of a circular crack embedded in an infinite body (that is, $c/h \to 0$) and subjected to internal pressure p. For a fixed crack size c, both the absolute values of K_{I} and K_{II} vary against increasing relative depth, h/c. For a crack near the free surface of a semiinfinite body, K_{II} is relatively high because the crack interacts with the surface. For a deeply embedded crack (that is, $c/h \to 0$), K_{I} tends to K_0, and K_{II} is
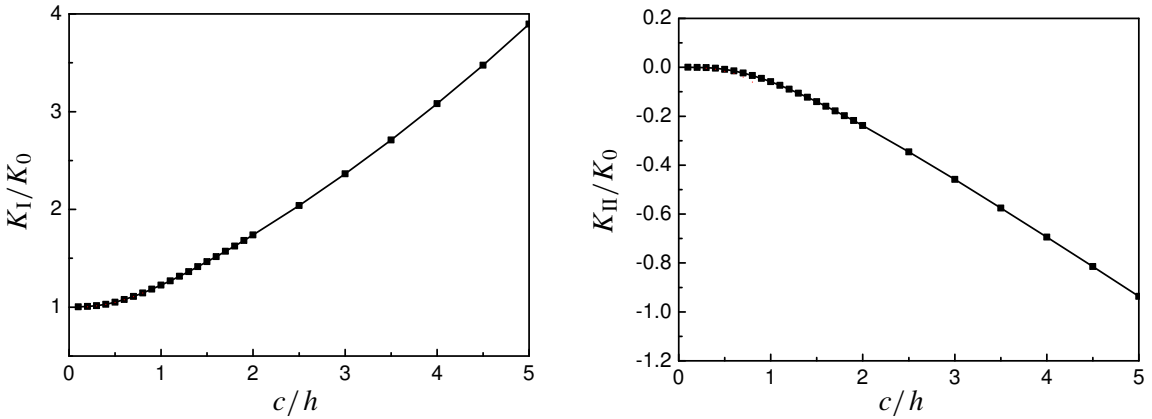
Figure 2. SIFs of a circular subsurface crack under internal pressure.

negligible. Also, for a very large ratio c/h, the aperture's square root tip behavior is confined to a very small region. For more detailed discussion of the asymptote's changing nature, the reader may refer to [Dyskin et al. 2000]. Additionally, we note that the values of K_{II} in Figure 2 differ by a factor of about 2 from those of [Bunger and Detournay 2005], while the respective values of K_{I} agree, approximately. We attribute the discrepancy to Bunger and Detournay [2005]'s assumption of a linear distribution of radial stress, which is not exact near the crack front at the plate boundary.

2.2. *Plane strain problems.* To illustrate plane strain problems, we consider a semiinfinite body containing a straight planar crack in parallel with the upper surface and subjected to an internal pressure p. Establish a Cartesian coordinate system $(o - xyz)$, as shown in Figure 3. The crack has length $2c$ in the x-direction and is infinite in the z-direction. The stress equilibrium equations are satisfied automatically when the stress components are expressed from the Airy stress function F as

$$\sigma_{xx} = \frac{\partial^2 F}{\partial y^2}, \qquad \sigma_{yy} = \frac{\partial^2 F}{\partial x^2}, \qquad \sigma_{xy} = -\frac{\partial^2 F}{\partial x \partial y}. \tag{2–24}$$

Substituting Equation (2–24) into the isotropic elastic constitutive relations and the result into the strain compatibility condition, we find that F must satisfy the biharmonic equation

$$\nabla^2 \nabla^2 F(x, y) = 0. \tag{2–25}$$
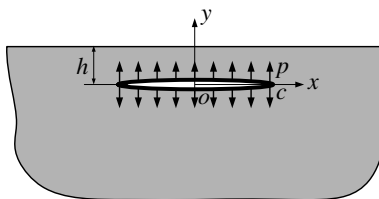
Figure 3. A subsurface Griffith crack beneath the free surface of a semiinfinite body.

For Section 2.1's axisymmetrical case, we used the Hankel transform. For plane strain problems, we use the Fourier transform instead. After Fourier transforming in x, Equation (2–25) becomes an ordinary differential equation

$$\frac{d^4}{dy^4}\widetilde{F} - 2\xi^2\frac{d^2}{dy^2}\widetilde{F} + \xi^4\widetilde{F} = 0. \tag{2-26}$$

It has the general solution

$$\widetilde{F_1} = A_1 e^{|\xi|y} + A_2 y e^{|\xi|y} + A_3 e^{-|\xi|y} + A_4 y e^{-|\xi|y}, \text{ for } y \geq 0, \tag{2-27}$$

$$\widetilde{F_2} = A_5 e^{|\xi|y} + A_6 y e^{|\xi|y}, \qquad\qquad\qquad \text{for } y < 0, \tag{2-28}$$

where A_α ($\alpha = 1, \ldots, 6$) are integral constants as before.

Analogously to Equation (2–8), we define two dislocation density functions $g_{i=1,2}(x)$,

$$g_i(x) = \frac{\partial}{\partial x}\left[u_i(x, 0^+) - u_i(x, 0^-)\right], \tag{2-29}$$

where $u_i(x, y)$, $i = 1, 2$ denote the displacement components in the x- and y-directions, respectively. The $g_i(x)$ satisfy the auxiliary conditions

$$\int_{-c}^{c} g_i(x)dx = 0. \tag{2-30}$$

As we did in Equation (2–18), we then derive the following singular integral equations for the crack configuration in Figure 3:

$$\frac{\mu}{2\pi(1-\nu)}\left[-c\int_{-1}^{+1} D_{11}(t, r)g_1(t)dt + \int_{-1}^{+1}\frac{g_1(t)}{t-r}dt - 2c\int_{-1}^{+1} D_{12}(t, r)g_2(t)dt\right] = -p,$$

$$\frac{\mu}{2\pi(1-\nu)}\left[-c\int_{-1}^{+1} D_{22}(t, r)g_2(t)dt + \int_{-1}^{+1}\frac{g_2(t)}{t-r}dt + 2c\int_{-1}^{+1} D_{21}(t, r)g_1(t)dt\right] = 0, \tag{2-31}$$

where $t = x/c$ is the dimensionless coordinate in the x-direction, and

$$D_{11}(t, r) = \int_{0}^{+\infty} (1 + 2\xi h + 2\xi^2 h^2)e^{-2\xi h}\sin\xi[(t-r)c]d\xi,$$

$$D_{12}(t, r) = D_{21}(t, r) = \int_{0}^{+\infty} \xi^2 h^2 e^{-2\xi h}\cos\xi[(t-r)c]d\xi, \tag{2-32}$$

$$D_{22}(t, r) = \int_{0}^{+\infty} (1 - 2\xi h + 2\xi^2 h^2)e^{-2\xi h}\sin\xi[(t-r)c]d\xi.$$

Now define $H_{i=1,2}$ by $H_i(t) = g_i(t)\sqrt{1-t^2}$. By expanding $H_i(t)$ as a truncated series of first kind Chebyshev polynomials, as in Equation (2–20), we obtain the system of linear equations

$$\frac{\mu}{2(1-\nu)}\left[-c\sum_{l=1}^{N}D_{11}(t_l,x_m)\frac{H_1(t_l)}{N}+\sum_{l=1}^{N}\frac{H_1(t_l)}{N(t_i,x_j)}-2c\sum_{i=1}^{N}D_{12}(t_i,x_j)\frac{H_2(t_i)}{N}\right]=-p,$$

$$\frac{\mu}{2(1-\nu)}\left[-c\sum_{i=1}^{N}D_{22}(t_i,x_j)\frac{H_2(t_i)}{N}+\sum_{i=1}^{N}\frac{H_2(t_i)}{N(t_i-x_j)}+2c\sum_{l=1}^{N}D_{21}(t_l,x_m)\frac{H_1(t_l)}{N}\right]=0,$$

$$\sum_{l=1}^{N}H_i(t_l)=0, \tag{2–33}$$

These we solve easily using numerical matrix methods, and hence determine the fields of stresses, strains and displacements.

Finally, the SIFs are

$$K_{\mathrm{I}}=\lim_{x\to c^+}\sqrt{2\pi(x-c)}\,\sigma_y(x,0)=\lim_{r\to1^+}\sqrt{\pi c(r-1)}\int_{-1}^{+1}\frac{g(s)}{s-r}\,ds=\alpha\sqrt{\pi c}\,H_1(1) \tag{2–34}$$

$$K_{\mathrm{II}}=\lim_{x\to c^+}\sqrt{2\pi(x-c)}\,\tau_{xy}(x,0)=\lim_{r\to1^+}\sqrt{\pi c(r-1)}\int_{-1}^{+1}\frac{f(s)}{s-r}\,ds=\alpha\sqrt{\pi c}\,H_2(1). \tag{2–35}$$

We plot the calculated K_{I} and K_{II} in Figure 4, where $K_0 = p\sqrt{\pi c}$ is the SIF of a Griffith crack in an infinite solid and subjected to an internal pressure p. Both the absolute values of K_{I} and K_{II} increase with c/h. For a deeply embedded crack (that is, $c/h \to 0$), K_{I} and K_{II} tend to K_0 and zero.

Another important plane strain problem consists of a semiinfinite body containing a periodic array of interacting Griffith cracks in parallel with the upper surface and subjected to a uniform internal pressure
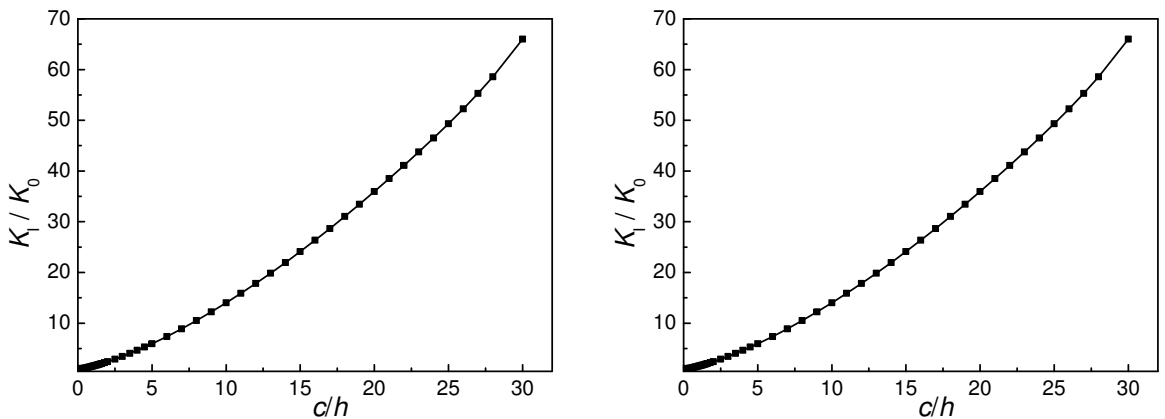
Figure 4. SIFs of a subsurface Griffith crack, (a) K_{I} and (b) K_{II}.
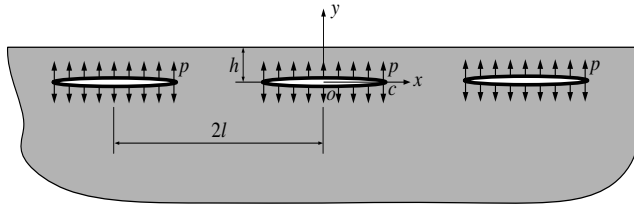
Figure 5. A periodic array of plane-strain subsurface Griffith cracks.

p, as shown in Figure 5. All cracks have length $2c$, and the spacing between neighboring cracks is $2l$. The singular integral transform method described above extends readily to this problem. Omitting the detailed derivation, this problem reduces to solving the singular integral equations

$$\frac{\mu}{2(1-\nu)}\left\{-\frac{1}{\pi}\int_{-c}^{+c}\left[D_{11}^0+\sum_{n=1}^{a_0}(D_{11}^-+D_{11}^+)\right]g_1(t)dt+\frac{1}{2l}\int_{-c}^{+c}\cotan\left(\pi\frac{t-x}{2l}\right)g_1(t)dt\right.$$

$$\left.-\frac{2}{\pi}\int_{-c}^{+c}\left[D_{12}^0+\sum_{n=1}^{a_0}(D_{12}^-+D_{12}^+)\right]g_2(t)dt\right\}=-p,$$

$$\frac{\mu}{2(1-\nu)}\left\{-\frac{1}{\pi}\int_{-c}^{+c}\left[D_{22}^0+\sum_{n=1}^{a_0}(D_{22}^-+D_{22}^+)\right]g_2(t)dt+\frac{1}{2l}\int_{-c}^{+c}\cotan\left(\pi\frac{t-x}{2l}\right)g_2(t)dt\right.$$

$$\left.+\frac{2}{\pi}\int_{-c}^{+c}\left[D_{21}^0+\sum_{n=1}^{a_0}(D_{21}^-+D_{21}^+)\right]g_1(t)dt\right\}=0, \quad (2\text{--}36)$$

where

$$D_{11}^0(t,x)=D_{11}(t,x), \qquad D_{12}^0(t,x)=D_{12}(t,x), \qquad D_{22}^0(t,x)=D_{22}(t,x),$$

$$D_{11}^\pm(t,x)=\int_0^{+\infty}(1+2\xi h+2\xi^2h^2)e^{-2\xi h}\sin\xi(t-x\pm2nl)d\xi,$$

$$D_{12}^\pm(t,x)=D_{21}^\pm+(t,x)=\int_0^{+\infty}\xi^2h^2e^{-2\xi h}\cos\xi(t-x\pm2nl)d\xi, \qquad (2\text{--}37)$$

$$D_{22}^\pm(t,x)=\int_0^{+\infty}(1-2\xi h+2\xi^2h^2)e^{-2\xi h}\sin\xi(t-x\pm2nl)d\xi.$$

We show the calculated mode-I and mode-II SIFs K_{I} and K_{II} in Figure 6. For a small crack spacing in the range $1<l/c<2$, crack interaction significantly influences the SIF solutions. For a larger spacing $l/c>3$, the interaction effect is negligible, and the SIFs tend to the solutions for a single crack, shown in
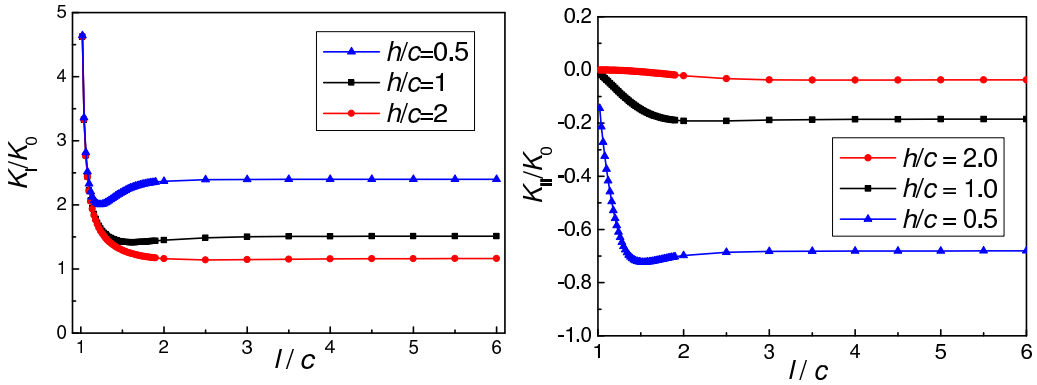
Figure 6. SIFs of a periodic array of subsurface cracks, (a) K_I and (b) K_{II}.

Figure 3. In addition, the crack interaction may shield the SIFs under some combinations of geometric parameters (for example, in the range $1.2 < l/c < 1.6$ with $h/c = 0.5$, as shown in Figure 6), though the interaction effect usually enhances the SIFs [Feng and Yu 2002].

3. Analysis of three-dimensional ion cut

As mentioned in the introduction, the Smart-Cut technology allows production of various SOI wafers with highly uniform thickness. However, metal wires and distributed device elements in integrated circuits require imposing patterns, for example, straight grooves and circular holes, on wafer surfaces. Here, we suggest using the ion cut method to carve three-dimensional surface directly. See Figure 7 for a schema of the basic procedure. The wafer is covered with a specialized metal mask and exposed to an appropriate dose of hydrogen ions at room-temperature [Feng and Huang 2004]. The mask's holes conform to the required wafer surface pattern, and it is thick enough so that hydrogen ions cannot pass
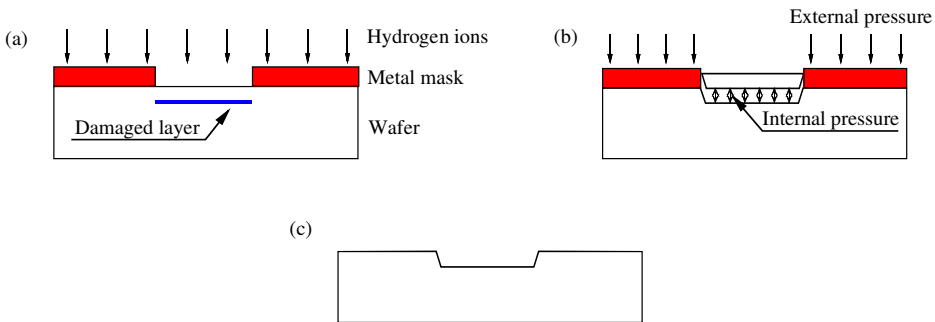
Figure 7. Schematics of the three-dimensional ion cut method: (a) hydrogen ion implantation, (b) thermal annealing and wafer splitting, and (c) the final wafer with a designed surface pattern.

through it, ensuring that hydrogen ions are implanted only in the holes. The masked wafer is next exposed to thermal annealing including two stages of heating, a medium-temperature stage (400–600° C) and a high-temperature stage (about 1100° C). Pressure applied to the mask controls the crack propagation path. During the first stage of annealing, a thin damaged layer appears at the depth of the maximum hydrogen ion concentration. The cracks propagate by kinks, which form as microcrack coalesce within the damaged layer. This removes the unwanted material and creates the desired surface morphology. The subsequent high-temperature thermal treatment removes the remaining hydrogen ions and radiation defects.

Repeating the integral transform methods of Section 2, we next analyze the kink propagation of subsurface cracks and subsequent creation of several representative surface patterns, including shallow circular holes and straight grooves.

3.1. *Ion cut of a circular hole.* To determine how kinks propagate in a mixed-mode crack, we adopt the following fracture criterion, based on the maximum circumferential tensile stress [Lawn 1993]:

$$\frac{1}{2}\left[K_{\mathrm{I}}(1+\cos\alpha)-3K_{\mathrm{II}}\sin\alpha\right]\cos\frac{\alpha}{2}=K_{Ic}, \tag{3–1}$$

where K_{Ic} is the fracture toughness of the material, and α is the kinking angle measured from the crack direction. In the stress fields of a mixed-mode crack, the angle α is determined from

$$K_{\mathrm{I}}\sin\alpha+K_{\mathrm{II}}(3\cos\alpha-1)=0. \tag{3–2}$$

For the configuration in Figure 1, where the upper surface of the system is traction free and the crack is subjected to an internal pressure, the mode-II SIF K_{II} is generally much smaller than that of K_{I}. Substituting the calculated values for K_{I} and K_{II} values (in Figure 2) into Equation (3–2), we conclude that the kinking angle α is generally smaller than 25° if the upper surface of the body is traction free. Therefore, external surface pressure is necessary to produce a hole with a greater α value. Such pressure, applied through the metal mask, can be modeled either as a linear force q distributed along a circle (Figure 8a) or as a distributed surface force. We present only the first case here due to its particular significance, but the second case proceeds similarly.

According to the superposition principle, the crack problem in Figure 8(a) decomposes into sum of the two subproblems of Figures 8(b) and 8(c). In the first, the semiinfinite body has no crack but is subjected to the distributed force q along a circle on the upper surface. The corresponding stress fields can be derived from the well-known Boussinesq solution as

$$\begin{aligned}
\bar{\sigma}_{zz}(r,0) &= -\frac{3ql_0h^3}{\pi}\int_0^\pi \frac{d\theta}{\left(l_0^2+r_0^2-2l_0r\cos\theta+h^2\right)^{5/2}}, \\[2mm]
\bar{\tau}_{zr}(r,0) &= -\frac{3ql_0h^2}{\pi}\int_0^\pi \frac{(l_0\cos\theta-r)d\theta}{\left(l_0^2+r^2-2l_0r\cos\theta+h^2\right)^{5/2}},
\end{aligned} \tag{3–3}$$

where c is the crack radius, l_0 the radius where the linear force q is applied, and h is the distance of the crack from the upper surface. Other axisymmetric problems of a semiinfinite body subjected to surface forces can be solved easily by integrating the stress fields in Equation (3–3). In the second subproblem

(Figure 8c), the upper surface of the body is traction free but the crack surfaces are subjected to the tractions

$$\sigma_{zz}(r,0) = -\bar{\sigma}_{zz}(r,0) - p = \frac{3ql_0h^3}{\pi}\int_0^\pi \frac{d\theta}{\left(l_0^2 + r_0^2 - 2l_0r\cos\theta + h^2\right)^{5/2}} - p,$$

$$\tau_{zr}(r,0) = \bar{\tau}_{zr}(r,0) = \frac{3ql_0h^2}{\pi}\int_0^\pi \frac{(l_0\cos\theta - r)d\theta}{\left(l_0^2 + r^2 - 2l_0r\cos\theta + h^2\right)^{5/2}}.$$

(3–4)

The two cracks in Figures 8(a) and 8(c) share SIF values, but we can solve latter problem more easily using the integral transform method in Section 2.1. Omitting the detailed derivation, we obtain a system of linear equations, similar to Equation (2–20):

$$\frac{\mu}{2(1-v)}\sum_{l=1}^N\left[\frac{1}{t_l-x_m} + \frac{1}{t_l+x_m+2} + \frac{M_1(t_l,x_m)-1}{t_l-x_m} + \frac{M_1(t_l,x_m)-1}{t_l+x_m+2} + \frac{\pi c}{2}D_{11}(t_l,x_m)\right]\frac{H_1(t_l)}{N}$$

$$+\sum_{i=1}^N\frac{\pi c}{2}D_{12}(t_i,x_j)H_2(t_i) = \frac{3ql_0h^3}{\pi}\int_0^\pi \frac{d\theta}{\left(l_0^2 + c^2x_m^2 - 2l_0cx_m\cos\theta + h^2\right)^{5/2}} - p,$$

$$\frac{\mu}{2(1-v)}\sum_{i=1}^N\left[\frac{1}{t_i-x_j} - \frac{1}{t_i+x_j+2} + \frac{M_2(t_i,x_j)-1}{t_i-x_j} - \frac{M_2(t_i,x_j)-1}{t_i+x_j+2} + \frac{\pi c}{2}D_{22}(t_i,x_j)\right]\frac{H_2(t_i)}{N}$$

$$+\sum_{l=1}^N\frac{\pi c}{2}D_{21}(t_l,x_m)\frac{H_1(t_l)}{N} = \frac{3ql_0h^2}{\pi}\int_0^\pi \frac{(l_0\cos\theta - cx_j)d\theta}{\left(l_0^2 + c^2x_j^2 - 2l_0cx_j\cos\theta + h^2\right)^{5/2}},$$

$$H_1(t_N) = 0,$$

$$\sum_{l=1}^N\frac{1+t_l}{2}H_1(t_l) = 0. \qquad (3–5)$$

Using the calculated stress fields, we calculate the SIFs K_I and K_{II} using Equation (2–23), and plot the results in Figure 9 as linear functions of the loading ratio, $q/2cp$. The ratio of SIFs K_{II}/K_I increases with the increase in the externally applied force q. In Figure 10, we show the kinking angle α as a function of $q/2cp$. One may control the propagating kink angle, and hence the shape of the hole, by adjusting the force q. A large kinking angle requires a sufficiently large q; however, since the mode-I SIF decreases linearly with q, the crack will close and cease to propagate if q is too large. We note that the internal pressure p depends mainly upon the dose of implanted hydrogen ions and the temperature [Feng and Huang 2004]. Therefore, in order to cut a circular hole, an appropriate force q should be chosen from Figure 10 to conform to the required hole depth. Finally, we note that the hole's diameter and depth is limited by the ion implantation machine to the order of microns. The hydrogen ion penetration depth varies approximately linearly with the implantation energy and does not depend on the implantation dose [Feng and Huang 2004].
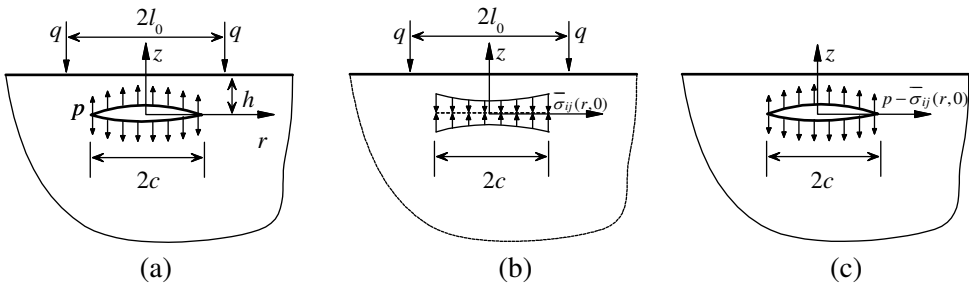
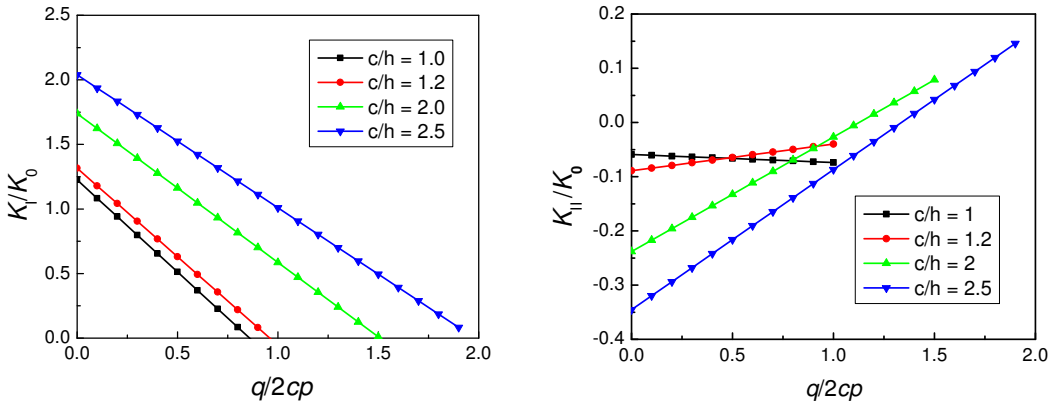**Figure 8.** Superposition method for solving a subsurface crack.

Figure 9. SIFs of a circular subsurface crack subjected to an internal pressure p and a surface force q, where $l_0 = 1.1c$. (a) K_{I} and (b) K_{II}.
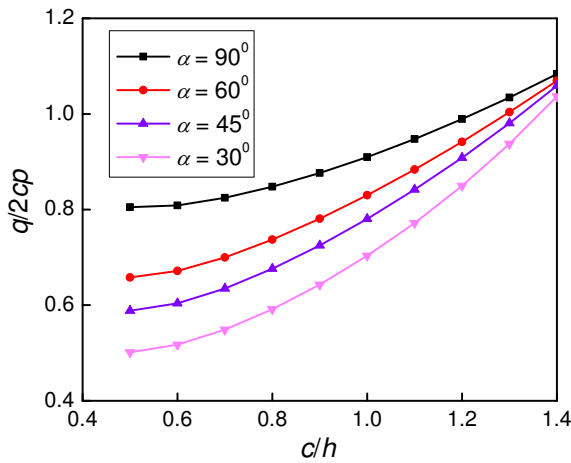

Figure 10. Kinking angle of a circular subsurface crack, where $l_0 = 1.1c$.

3.2. *Ion cut of a long straight groove.* To cut a long, straight surface groove on a wafer, hydrogen ions are implanted into a long square zone left uncovered by a metal mask. We assume that the groove is much longer than its width, c, so the ion cut process simplifies to a plane strain problem. The corresponding crack model can also represented by Figure 8, but without the same plane strain assumption. We again employ superposition. In this case, the tractions on the crack faces in Figure 8(c) become

$$\bar{\sigma}_{yy}(x, 0) = \frac{2qh^3}{\pi} \left\{ \frac{1}{[h^2 + (l_0 + x)^2]^2} + \frac{1}{[h^2 + (l_0 - x)^2]^2} \right\} - p,$$

$$\bar{\tau}_{xy}(x, 0) = \frac{2qh^2}{\pi} \left\{ \frac{l_0 + x}{[h^2 + (l_0 + x)^2]^2} + \frac{x - l_0}{[h^2 + (l_0 - x)^2]^2} \right\},$$

(3–6)

where q is the magnitude of the distributed force per unit length along the z-axis direction. In deriving Equation (3–6), we again used the Boussinesq solution under the plane strain condition [Timoshenko and Goodier 1970].

Substituting Equation (3–6) into the boundary conditions along the crack faces, we obtain the following singular integral equation system, similar to Equation (2–31):

$$\frac{\mu}{2\pi(1-\nu)} \left[-c \int_{-1}^{+1} D_{11}(s, r)g_1(s)ds + \int_{-1}^{+1} \frac{g_1(s)}{s - r}ds - 2c \int_{-1}^{+1} D_{12}(s, r)g_2(s)ds \right]$$

$$= \frac{2qh^3}{\pi} \left\{ \frac{1}{[h^2 + (l_0 + cr)^2]^2} + \frac{1}{[h^2 + (l_0 - cr)^2]^2} \right\} - p,$$

$$\frac{\mu}{2\pi(1-\nu)} \left[-c \int_{-1}^{1} D_{22}(s, r)g_2(s)ds + \int_{-1}^{1} \frac{g_2(s)}{s - r}ds + 2c \int_{-1}^{1} D_{21}(s, r)g_1(s)ds \right]$$

$$= \frac{2qh^2}{\pi} \left\{ \frac{l_0 + cr}{[h^2 + (l_0 + cr)^2]^2} + \frac{cr - l_0}{[h^2 + (l_0 - cr)^2]^2} \right\},$$

$$\int_{-1}^{+1} g_{1,2}(r)dr = 0, \tag{3–7}$$

which we solved easily using the method in Section 2.2. We plot the results for SIFs K_I and K_{II} and the kinking angle α in Figures 11 and 12. As for the circular hole, we find that both the SIF ratio K_{II}/K_I and the kinking angle α increase with the externally applied force q. Therefore, one can direct propagating kinks by varying the force q. If $K_I \leq 0$, the crack will close, not propagate. This limits the kinking angle α to 70°, that is, the shape of the cut groove.

3.3. *Ion cut of an array of periodic grooves.* Finally, we analyze the ion cut method for an array of periodic long straight grooves. We model the ion cut process using the crack configuration in Figure 13. Here q is the distributed force per unit area. We solve by superposition, as shown analogously in
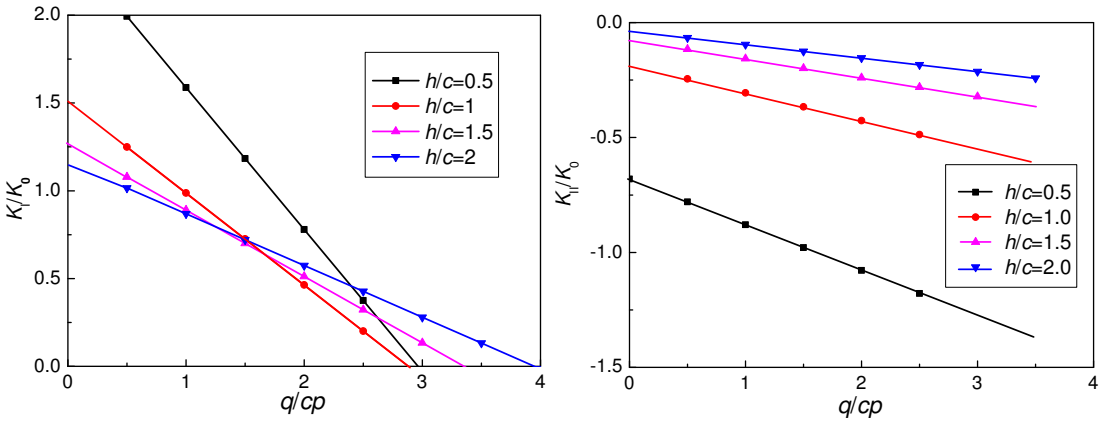
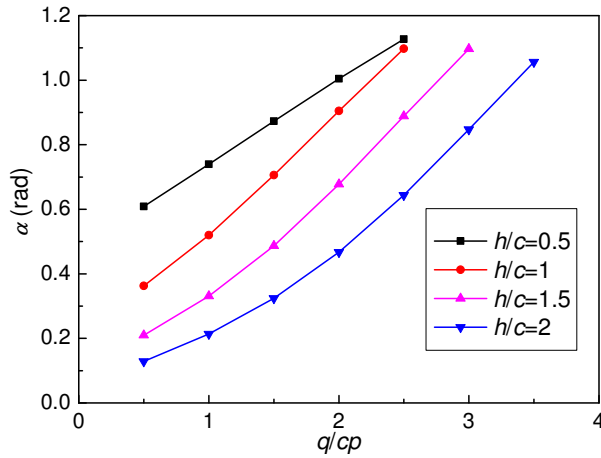**Figure 11.** SIFs of a subsurface Griffith crack, (a) K_{I} and (b) K_{II}.

Figure 12. Kinking angle of a subsurface Griffith crack.

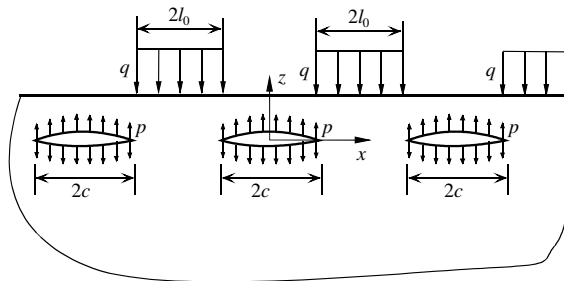Figure 8. Accordingly, the crack SIFs in Figure 13 are those of a semiinfinite space, where the upper

Figure 13. Crack model for cutting of a periodic array of straight grooves.

surface of the body is traction free and the tractions on the crack surfaces are given by

$$
\bar{\sigma}_{yy}(x,0) = \frac{2qh^3}{\pi} \left\{ \sum_{n=0}^{\infty} \int_{-2nl-a}^{-2(n+1)l+a} \frac{dx_2}{[(x-x_2)^2+h^2]^2} + \sum_{n=0}^{\infty} \int_{2nl+a}^{2(n+1)l-a} \frac{dx_2}{[(x-x_2)^2+h^2]^2} \right\} - p,
$$

$$
\bar{\tau}_{xy}(x,0) = -\frac{2qh^2}{\pi} \left\{ \sum_{n=0}^{\infty} \int_{-2nl-a}^{-2(n+1)l+a} \frac{(x-x_2)dx_2}{[(x-x_2)^2+h^2]^2} + \sum_{n=0}^{\infty} \int_{2nl+a}^{2(n+1)l-a} \frac{(x-x_2)dx_2}{[(x-x_2)^2+h^2]^2} \right\},
$$

(3–8)

where we use again the plane-strain Boussinesq solution. The integral transform method leads to a singular integral equation system for the crack configuration in Figure 13:

$$
-\alpha \left(-c \sum_{q=1}^{N_0} \left\{ D_{11}^0(s_q, r_m) + \sum_{n=1}^{a_0} [D_{11}^-(s_q, r_m) + D_{11}^+(s_q, r_m)] \right\} \frac{H_1(s_q)}{N_0} \right.
$$

$$
+ \frac{\pi c}{2l} \sum_{q=1}^{N_0} \left[\cot\left(\pi \frac{s_q - r_m}{2l} c \right) - \frac{1}{\pi \frac{s_q - r_m}{2l} c} \right] \frac{H_1(s_q)}{N_0} + \sum_{q=1}^{N_0} \frac{H_1(s_q)}{(s_q - r_m)N_0}
$$

$$
\left. -2c \sum_{i=1}^{N_0} \left\{ D_{12}^0(s_i, r_m) + \sum_{n=1}^{a_0} [D_{12}^-(s_i, r_m) + D_{12}^+(s_i, r_m)] \right\} \frac{H_2(s_i)}{N_0} \right)
$$

$$
= \frac{2qh^3}{\pi} \left\{ \sum_{n=0}^{\infty} \int_{-2nl-c}^{-2(n+1)l+c} \frac{dx_2}{[(cr_m - x_2)^2 + h^2]^2} + \sum_{n=0}^{\infty} \int_{2nl+c}^{2(n+1)l-c} \frac{dx_2}{[(cr_m - x_2)^2 + h^2]^2} \right\} - p,
$$

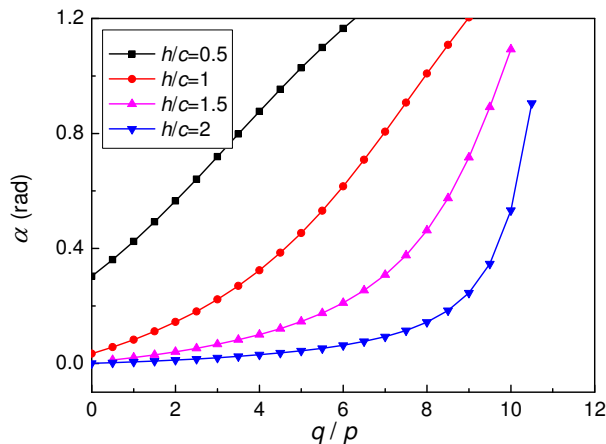**Figure 14.** Kinking angle of a periodic array of subsurface cracks, where $l_0 = 1.1c$.

$$\alpha \Bigg(-c \sum_{i=1}^{N_0} \bigg\{ D_{22}^0(s_i, r_j) + \sum_{n=1}^{a_0} \big[D_{22}^-(s_i, r_j) + D_{22}^+(s_i, r_j) \big] \bigg\} \frac{H_2(s_i)}{N_0}$$

$$+ \frac{\pi c}{2l} \sum_{i=1}^{N_0} \bigg[\cot \Big(\pi \frac{s_i - r_j}{2l} c \Big) - \frac{1}{\pi \frac{s_i - r_j}{2l} c} \bigg] \frac{H_2(s_i)}{N_0} + \sum_{i=1}^{N_0} \frac{H_2(s_i)}{(s_i - r_j) N_0}$$

$$+ 2c \sum_{q=1}^{N_0} \bigg\{ D_{21}^0(s_q, r_j) + \sum_{n=1}^{a_0} \big[D_{21}^-(s_q, r_j) + D_{21}^+(s_q, r_j) \big] \bigg\} \frac{H_1(s_q)}{N_0} \Bigg)$$

$$= \frac{2qh^2}{\pi} \Bigg\{ \sum_{n=0}^{\infty} \int_{-2nl-c}^{-2(n+1)l+c} \frac{(cr_j - x_2) dx_2}{\big[(cr_j - x_2)^2 + h^2 \big]^2} + \sum_{n=0}^{\infty} \int_{2nl+c}^{2(n+1)l-c} \frac{(cr_j - x_2) dx_2}{\big[(cr_j - x_2)^2 + h^2 \big]^2} \Bigg\},$$

$$\sum_{l=1}^{N} H_1(t_l) = 0,$$

$$\sum_{i=1}^{N} H_2(t_i) = 0.$$

Thus we determine the stress fields and the SIFs K_{I} and K_{II}. For brevity, we plot in Figure 14 only the kinking angle α as a function of the loading ratio q/p. This function can be implicitly solved for q, so that, for a desired value of α and internal pressure p (determined by the dose of implanted hydrogen ions), we know the correct force q to apply.

4. Conclusions

We suggest using the ion cut technology to cut directly the surface patterns onto wafers bound for integrated circuits. In the present work, we analyzed the three-dimensional ion cut method using fracture mechanics theory and demonstrated that patterns can be transferred from a mask to an Si or SOI substrate. We presented a convenient method based on integral transforms for calculating the SIFs of subsurface cracks. The Hankel and Fourier integral transforms lent themselves to the axisymmetric and planar-symmetric crack configurations, respectively. Cracks near a surface are generally of mixed-mode because of the nonsymmetric geometry. We gave selected, important solutions for the SIFs of subsurface cracks, but the method can solve many other crack configurations. This method is comparatively easier than the finite element method, and yields the mode-I and II SIFs with higher accuracy. We analyzed the conditions for successfully using the three-dimensional ion cut method. An externally applied force is then required to cut the desired surface morphology. One may vary the kinking direction of subsurface cracks by specifying the ratio of the applied surface force and the internal pressure induced by the implanted hydrogen.

References

[Aspar et al. 1996] B. Aspar, M. Bruel, M. Zussy, and A. M. Cartier, "Transfer of structured and patterned thin silicon films using the Smart-Cut$^{(R)}$ process", *Electron. Lett.* **32**:21 (1996), 1985–1986.

[Aspar et al. 1999] B. Aspar, E. Jalaguier, A. Mas, C. Locatelli, O. Rayssac, S. Pocas, A. M. Papon, J. F. Michaud, and M. Bruel, "Smart-Cut$^{(R)}$ process using metallic bonding: application to transfer of Si, GaAs, InP thin films", *Electron. Lett.* **35**:12 (1999), 1024–1025.

[Bruel 1995] M. Bruel, "Silicon on insulator material technology", *Electron. Lett.* **31**:14 (1995), 1201–1202.

[Bruel 1996] M. Bruel, "Application of hydrogen ion beams to silicon on insulator material technology", *Nucl. Instrum. Meth. B* **108**:3 (1996), 313–319.

[Bunger and Detournay 2005] A. P. Bunger and E. Detournay, "Asymptotic solution for a penny-shaped near-surface hydraulic fracture", *Eng. Fract. Mech.* **72**:16 (2005), 2468–2486.

[Cao 2002] Y. Cao, "Three-dimensional finite element modeling of subsurface median crack in trilayer sandwiches due to contact loading", *Eng. Fract. Mech.* **69**:6 (2002), 729–743.

[Colinge 1991] J.-P. Colinge, *Silicon-on-insulator technology: materials to VLSI*, Kluwer, Boston, 1991.

[Di Cioccio et al. 1997] L. Di Cioccio, Y. LeTiec, C. Jaussaud, M. Bruel, and E. Hugonnard-Bruyere, "Silicon carbide on insulator formation by the Smart-Cut$^{(R)}$ process", *Mat. Sci. Eng. B* **46**:1-3 (1997), 349–356.

[Dyskin et al. 2000] A. V. Dyskin, L. N. Germanovich, and K. B. Ustinov, "Asymptotic analysis of crack interaction with free boundary", *Int. J. Solids Struct.* **37**:6 (2000), 857–886.

[Feng and Huang 2004] X.-Q. Feng and Y. Huang, "Mechanics of Smart-Cut$^{(R)}$ technology", *Int. J. Solids Struct.* **41**:16-17 (2004), 4299–4320.

[Feng and Xu 2006] X.-Q. Feng and M. Xu, "Solutions of stress intensity factors of subsurface cracks", *Key Eng. Mat.* **312** (2006), 83–88.

[Feng and Yu 2002] X. Q. Feng and S. W. Yu, *Damage micromechanics of quasi-brittle solids*, Tsinghua University Press, Beijing, 2002.

[Fleming and Suh 1977] J. R. Fleming and N. P. Suh, "Mechanics of cracks propagation in delamination wear", *Wear* **44**:1 (1977), 39–56.

[Gad et al. 2003] M. A. Gad, J. H. Evans-Freeman, N. Cinosi, and J. Sarma, "Loss measurements of er-doped silicon-on-insulator waveguides", *Mat. Sci. Eng. B* **105**:1-3 (2003), 79–82.

[Goshima and Soda 1997] T. Goshima and T. Soda, "Stress intensity factors of a subsurface crack in a semi-infinite body due to rolling/sliding contact and heat generation", *JSME Int. J. A. Solid Mech. M.* **40**:3 (1997), 263–270.

[Haisma and Spierings 2002] J. Haisma and G. A. C. M. Spierings, "Contact bonding, including direct-bonding in a historical and recent context of materials science and technology, physics and chemistry : historical review in a broader scope and comparative outlook", *Mat. Sci. Eng. R* **37**:1-2 (2002), 1–60.

[Hutchinson and Suo 1992] J. W. Hutchinson and Z. Suo, "Mixed-mode cracking in layered materials", *Adv. Appl. Mech.* **29** (1992), 63–191.

[Jalaguier et al. 1998] A. Jalaguier, B. Aspar, S. Pocas, J. F. Michaud, M. Zussy, A. M. Papon, and M. Bruel, "Transfer of 3 in gaas film on silicon substrate by proton implantation process", *Electron. Lett.* **34**:4 (1998), 408–409.

[Komvopoulos 1996] K. Komvopoulos, "Subsurface crack mechanisms under indentation loading", *Wear* **199**:1 (1996), 9–23.

[Lawn 1993] B. R. Lawn, *Fracture of brittle solids*, Cambridge University Press, Cambridge, 1993.

[Ma and Hwang 1996] C.-C. Ma and L.-R. Hwang, "Dynamic fracture analysis of an inclined subsurface crack subjected to dynamic moving loadings", *Int. J. Fracture* **80**:1 (1996), 1–18.

[Ma et al. 2005] L. Ma, X. Wang, X.-Q. Feng, and S.-W. Yu, "Numerical analysis of interaction and coalescence of numerous microcracks", *Eng. Fract. Mech.* **72**:12 (2005), 1841–1865.

[Spence and Sharp 1985] D. A. Spence and P. W. Sharp, "Self-similar solutions for elastohydrodynamic cavity flow", *P. Roy. Soc. Lond. A Mat.* **400**:1819 (1985), 289–313.

[Srivastava and Singh 1969] K. N. Srivastava and K. Singh, "The effect of penny-shaped crack on the distribution of stress in a semi-infinite solid", *Int. J. Eng. Sci.* **7**:5 (1969), 469–490.

[Timoshenko and Goodier 1970] S. P. Timoshenko and J. N. Goodier, *Theory of elasticity*, 3rd ed., McGraw-Hill, New York, 1970.

[Tong and Bower 1998] Q.-Y. Tong and R. W. Bower, "Beyond "Smart-Cut$^{(R)}$": recent advances in layer transfer for material integration", *MRS Bull.* **23**:12 (1998), 40–44.

[Zhang et al. 2002] X. Zhang, E. Detournay, and R. Jeffrey, "Propagation of a penny-shaped hydraulic fracture parallel to the free-surface of an elastic half-space", *Int. J. Fracture* **115**:2 (2002), 125–158.

[Zhang et al. 2005] X. Zhang, R. G. Jeffrey, and E. Detournay, "Propagation of a hydraulic fracture parallel to a free surface", *Int. J. Numer. Anal. Met.* **29**:13 (2005), 1317–1340.

XI-QIAO FENG: fengxq@tsinghua.edu.cn
Department of Engineering Mechanics, Tsinghua University, Beijing 100084, China

MEI XU: xumei@tsinghua.edu.cn
Department of Engineering Mechanics, Tsinghua University, Beijing 100084, China

XUYUE WANG: wangxuyue@tsinghua.edu.cn
Department of Sciences, Harbin Institute of Technology, Shenzhen Graduate School, Shenzhen 518055, China

BIN GU: bin.gu@aeromech.usyd.edu.au
Centre for Advanced Materials Technology (CAMT), School of Aerospace, Mechanical and Mechatronic Engineering J07, The University of Sydney, NSW 2006, Australia

SUBMISSION GUIDELINES

ORIGINALITY

Authors may submit manuscripts in PDF format on-line. Submission of a manuscript acknowledges that the manuscript is *original and has neither previously, nor simultaneously, in whole or in part, been submitted elsewhere.* Information regarding the preparation of manuscripts is provided below. Correspondence by email is requested for convenience and speed. For further information, write to:

Marie-Louise Steele
Division of Mechanics and Computation
Durand Building, Room 262
Stanford University
Stanford CA 94305

LANGUAGE

Manuscripts must be in English. A brief abstract of about 150 words or less must be included. The abstract should be self-contained and not make any reference to the bibliography. Also required are keywords and subject classification for the article, and, for each author, postal address, affiliation (if appropriate), and email address if available. A home-page URL is optional.

FORMAT

Authors are encouraged to use LaTeX and the standard article class, but submissions in other varieties of TeX, and, exceptionally in other formats, are acceptable. Electronic submissions are strongly encouraged in PDF format only; after the refereeing process we will ask you to submit all source material.

REFERENCES

Bibliographical references should be listed alphabetically at the end of the paper and include the title of the article. All references in the bibliography should be cited in the text. The use of BibTeX is preferred but not required. Tags will be converted to the house format (see a current issue for examples), however, in the manuscript, the citation should be by first author's last name and year of publication, e.g. "as shown by Kramer, et al. (1994)". Links will be provided to all literature with known web locations and authors are encouraged to provide their own links on top of the ones provided by the editorial process.

FIGURES

Figures prepared electronically should be submitted in Encapsulated PostScript (EPS) or in a form that can be converted to EPS, such as GnuPlot, Maple, or Mathematica. Many drawing tools such as Adobe Illustrator and Aldus FreeHand can produce EPS output. Figures containing bitmaps should be generated at the highest possible resolution. If there is doubt whether a particular figure is in an acceptable format, the authors should check with production by sending an email to:

production@mathscipub.org

Each figure should be captioned and numbered so that it can float. Small figures occupying no more than three lines of vertical space can be kept in the text ("the curve looks like this:"). It is acceptable to submit a manuscript with all figures at the end, if their placement is specified in the text by means of comments such as "Place Figure 1 here". The same considerations apply to tables.

WHITE SPACE

Forced line breaks or page breaks should not be inserted in the document. There is no point in your trying to optimize line and page breaks in the original manuscript. The manuscript will be reformatted to use the journal's preferred fonts and layout.

PROOFS

Page proofs will be made available to authors (or to the designated corresponding author) at a web site in PDF format. Failure to acknowledge the receipt of proofs or to return corrections within the requested deadline may cause publication to be postponed.